Optimising the adsorption of bilirubin oxidase using dual polarisation interferometry and an electrochemical quartz crystal microbalance with dissipation analysis

A thesis submitted to the University of Manchester for the degree of

Doctor of Philosophy

in the Faculty of Engineering and Physical Sciences

2015

Trevor McArdle

School of Materials

Table of Contents

University of Manchester
Trevor McArdle
Doctor of Philosophy thesis
Optimising the adsorption of bilirubin oxidase using dual polarisation interferometry and an electrochemical quartz crystal microbalance with dissipation analysis

Abstract

This thesis investigates the adsorption mechanisms and changes in activity of bilirubin oxidase from *Myrothecium verrucaria* immobilised to gold- and silica-modified surfaces. This enzyme is used as an efficient bioelectrocatalyst for the four-electron oxygen reduction in fuel cells. An electrochemical quartz crystal microbalance with dissipation monitoring (E–QCM–D) was used to show how applying a constant potential to bilirubin oxidase adsorbed to a carboxylate-terminated gold electrode resulted in activity loss attributed to structural rearrangement of the adsorbed enzyme layer. When a varying potential was applied, rapid enzyme deactivation occurred, with no mitigation of activity loss through covalent attachment to the electrode.

The E-QCM-D was further used to observe how changing enzyme concentration affects the adsorption mechanics and catalytic activity of the adsorbed layer. An optimum concentration produced greatest activity and stability, with lower concentrations denaturing more readily, and higher concentrations adopting an unfavourable geometry for electron transfer. Surface functionality showed adsorption to hydrophobic methyl-terminated electrodes revealed a rigid layer with reduced catalytic activity. Ammonium terminated surfaces resisted denaturation, but misorientated the enzyme for efficient electrocatalysis. Increasing the chain length of the surface modifiers increased the enzyme–electrode distance; this decreased activity for the carboxylate surface and removed the activity for methyl- or ammonium-terminated surfaces. Dual polarisation interferometry further showed no enzyme denaturation when it was adsorbed to amine and sulfonic acid surfaces.

Enzyme adsorption under an applied constant potential caused a decrease in both mass loading and activity when compared to open circuit potential adsorption. The presence of an applied potential did not cause increased layer denaturation, but changed the orientation of the enzyme in a position unfavourable for electron transfer. Lower applied potential give lower mass loadings, yet similar surface mechanics and activity per adsorbed enzyme.

Chemical modification to pristine graphene showed targeted interactions with biomolecules such as proteins and fluorophores. This surface modification has the potential to be adapted towards adsorption of bilirubin oxidase for fuel cell catalysis and other electrochemical sensing applications.

The observations in this thesis show how the E–QCM–D and DPI can provide a more expansive picture of the applicability of redox enzymes in fuel cell systems. Preventative steps need to be taken in order to maintain an enzyme's structural integrity and in turn its catalytic competency. Without such provisions the observations above suggest that redox enzymes have a finite lifetime when under conditions approximating fuel cell systems.

Declaration

I, the author Trevor McArdle, declare that no portion of the work referred to in this thesis has been submitted in support of an application for another degree or qualification in this, or any other, university or other institute of learning.

i. The author of this thesis (including any appendices and/or schedules to this thesis) owns certain copyright or related rights in it (the "Copyright") and s/he has given The University of Manchester certain rights to use such Copyright, including for administrative purposes.

ii. Copies of this thesis, either in full or in extracts and whether in hard or electronic copy, may be made only in accordance with the Copyright, Designs and Patents Act 1988 (as amended) and regulations issued under it or, where appropriate, in accordance with licensing agreements which the University has from time to time. This page must form part of any such copies made.

iii. The ownership of certain Copyright, patents, designs, trademarks and other intellectual property (the "Intellectual Property") and any reproductions of copyright works in the thesis, for example graphs and tables ("Reproductions"), which may be described in this thesis, may not be owned by the author and may be owned by third parties. Such Intellectual Property and Reproductions cannot and must not be made available for use without the prior written permission of the owner(s) of the relevant Intellectual Property and/or Reproductions.

iv. Further information on the conditions under which disclosure, publication and commercialisation of this thesis, the Copyright and any Intellectual Property and/or Reproductions described in it may take place is available in the University IP Policy (see http://documents.manchester.ac.uk/DocuInfo.aspx?DocID=487), in any relevant Thesis restriction declarations deposited in the University Library, The University Library's regulations (see http://www.manchester.ac.uk/library/aboutus/regulations) and in The University's policy on Presentation of Theses.

Acknowledgments

I would like to thank Dr Christopher F. Blanford for his continuous support and guidance throughout my research and write up. His positive attitude and dedication have been invaluable and am truly grateful. I would also like to thank both my co-supervisors, Prof. Robert Dryfe and Prof. Ian Kinloch for their guidance and support throughout.

A special thank to Kulveer Singh for his time, knowledge and friendship. Thanks go to past and present Blanford group members, all of whom have contributed in someway to success of this thesis and to making the lab a great working environment.

I would also like to thank the Engineering and Physical Sciences Research Council for their funding of my project and the NOWNANO DTC management team for creating a diverse and enjoyable program.

A huge thank you to my Mum and Dad, for their continued support through all of my education. There is no question I am where I am today because of all your hard work. To my brother and sisters, thanks for always being there and supportive.

To my wife’s family, thank you all for making visiting home so enjoyable.

A very special thank you to my wife Jane, for her continued patience, words of encouragement and loving nature in helping me through the past four years.

Abbreviations

AFM	Atomic force microscopy
BSA	Bovine serum albumin
CA	Chronoamperometry
CE	Counter electrode
Cu–T1	Type 1 copper centre
Cu–T2	Type 2 copper centre
Cu–T3	Type 3 copper centre
CV	Cyclic voltammetry
DET	Direct electron transfer
DPI	Dual polarisation interferometry
E-QCM-D	Electrochemical quartz crystal microbalance with dissipation monitoring
ET	Electron transfer
E°	Equilibrium redox potential
HOPGE	Highly ordered pyrolytic graphite
ITO	Indium tin oxide
J_i	Flux of ionic species
LUMO	Lowest unoccupied molecular orbital
MCO	Multicopper oxidases
MFC	Microbial fuel cell
*Mv*BOx	*Myrothecium verrucria* bilirubin oxidase
ORR	Oxygen reduction reaction
OWLS	Optical waveguide lightmode spectroscopy
PFE	Protein film electrochemistry

PGE	Pyrolytic graphite edge
PEMFC	Proton exchange membrane fuel cell
QCM	Quartz crystal microbalance
QCM-D	Quartz crystal microbalance with dissipation monitoring
RE	Reference electrode
RI	Refractive index
RSA	Random sequential adsorption
SAM	Self-assembled monolayer
SCE	Saturated calomel electrode
SHE	Standard hydrogen electrode
SPR	Surface plasmon resonance
TE	Transverse electric (polarisation mode)
TM	Transverse magnetic (polarisation mode)
TNC	Trinuclear cluster
TST	Transition state theory
*Tv*L	*Trametes versicolor* laccase
WE	Working electrode

List of Figures

Chapter 1

Introduction

1 Introduction

1.1 Oxygen reduction

Almost all living things need oxygen to create energy in living cells. Animals use it as the final electron dump for the respiration reaction converting sugar to energy plus water and carbon dioxide (via glycolysis, the citric acid cycle and oxidative phosphorylation). In photosynthesis, this reaction is reversed, using carbon dioxide and water to produce dioxygen and sugars.[1]

The oxygen reduction reaction (ORR) occurs via two main routes: a four–electron reduction of dioxygen to water, or a two–electron reduction of dioxygen to hydrogen peroxide, which can further be reduced to water. The standard reduction potentials are give in Table 1.1 for each of the three reaction sat 298 K.

Table 1.1 Standard electrode potentials and temperature coefficents in water at 298.15 K for oxygen reduction.[2]

Reaction	**Standard electrode potential *E*° (V)**	**d*E*°/dT (mV/K)**
$O_2+4H^++4e^-\rightarrow H_2O$	1.2291	-0.8456
$O_2+2H^++2e^-\rightarrow H_2O_2$	0.695	-0.993
$H_2O_2 + 2H^+ + 2e^- \rightarrow 2H_2O$	1.763	-0.698

In biological processes, the ORRs are used in energy conversion reactions. The four-electron reduction is particularly important in fuel cells, where current is generated at the fuel cell cathode.[3] Oxygen reduction from a two-electron reaction is undesirable due to it's generation of hydrogen peroxide as a destructive by-product and also for only utilising two electrons worth of current as opposed to four.

Due to cathode activation polarisation, which is caused by limits in the kinetics of the reaction at the electrode, this thermodynamic potential can rarely be achieved.[2] This overpotential, which is the difference between the thermodynamic potential and the actual potential at which reduction begins, means there is a loss of theoretical energy available from the fuel oxidation. This drop in voltage relates to a loss in overall power from the fuel cell. In order to deal with this efficiency loss, the oxygen reduction reaction is catalysed, bringing the reduction potential towards to the thermodynamic value.[2]

1.1.1 Inorganic catalysis

There have been a range of materials investigated as inorganic catalysts to improve the efficiency of the ORR reaction, as listed in

Table 1.2. However these metal catalysts exhibit slow oxygen reduction due to how much overpotential they require.

The most commonly used materials are platinum (Pt) based due to its lower overpotential (0.77 V) and good stability.[4] For use in fuel cells, platinum's lack of specificity can cause electrochemical short circuits so a membrane is normally required. Economically, Pt is ultimately unfavourable as it is a rare resource and can be costly.[5]

Platinums overpotential requires high material loading due to sluggish reaction kinetics.[6] Therefore inorganic catalysts used as cathodes for oxygen electrocatalysts are the major limiting factor for energy conversion in fuel cells. For these reasons we turn to biology for inspiration to either use or mimic their superb catalytic ability.

Table 1.2. Inorganic catalysts currently being investigated for the use in the ORR.

Inorganic catalyst	Type	Reaction details	Active site/Metal	Additional info
Titanyl phthalocyanines[7]	Metal macrocycles	Rich redox behaviour allows for catalysis of a range of target species. Reduction potentials able to be tuned dependent on substituents.	Titanium	Show ORR in both protic and aprotic solutions. Prone to demetallation of macrocycle ring leading to a decrease in stability.
Cobalt(II) meso–tetraethynylporphyrins (supported on carbon nanotubes)[8]	Metal macrocycle	Adsorption of metal porphyrin onto sidewalls of carbon nanotubes. Showed greater stability and ORR activity.	Cobalt	Not completely 4 electron reduction, some hydrogen peroxide produced which degrades carbon support.
Manganese dioxide nanoflakes [9]	Metal oxide	47 nm MnO nanoflakes allow for high mass to activity for the ORR.	Magnesium	Use in both acidic and alkaline solutions.
Nitrogen–doped activated carbon.[8]	Carbon	Greater levels of N doping has exhibited outstanding electrocatalytic activity for the ORR. Is comparable with a 10% Pt/C catalyst.	Carbon	Oxygen reduction produced hydrogen peroxide.
Iridium–decorated palladium–platinum [10]	Platinum group elements	A palladium core, platinum shell with iridium decorated catalyst showed improved activity ORR than for just Pd–Pt. Catalysis showed good stability.	Palladium Platinum Iridium	Platinum group metals are an expensive route for efficient electrocatalysts.

1.1.2 Biological catalysis

In biology, the ORR plays an important part in the final stage of electron-transport chains. Cytochrome *c* oxidase, which contains atoms of copper with two haem prosthetic groups, reduces dioxygen to water. This process creates an proton gradient which in turn releases energy.[11] Catalytic centres of numerous dioxygen reducing enzymes are made up of copper and/or iron (haem) centres.[12] Copper-containing enzymes that activate or bind dioxygen have a wide variety of biological functions as described in Table 1.3. A common feature of these enzymes is they all bind oxygen to a reduced Cu(I) species and produce no unwanted intermediate oxidation states such as hydrogen peroxide during the reduction of oxygen to water (does not apply to enzymes that produce peroxide).

Many of the copper-containing enzymes listed in Table 1.3 have a lower overpotential than that of platinum, such as tyrosinase, laccase and bilirubin oxidase.[5]

Table 1.3. Catalytic enzymes with copper centres that bind or activate dioxygen.

Enzyme	**Reaction details**	**Type of copper centre involved in O_2 activation**	**Additional roles**
Amine oxidase[13-14]	Coupled oxidation of amines to aldehydes and reduction of dioxygen to peroxide	Mononuclear	Regulation of amine levels in higher eukaryotes
Galactose oxidase[15]	Coupled oxidation of alcohols to aldehydes and reduction of dioxygen to peroxide	Mononuclear	Hydrogen peroxide generation
Dopamine β–monooxygenase[16]	Coupled conversion of dopamine to norepinephrine by hydroxylation of benzylic position of ethylamine side chain, oxidation of ascorbate and reduction of dioxygen to water	Mononuclear	Controls levels of hormones and also dopamine and norepinephrine levels
Peptidylglycine α–amidating monooxygenase[17]	Coupled hydroxylation of glycine at α–position, oxidation of ascorbate oxidase and reduction of dioxygen to water	Mononuclear or non–coupled binuclear	Regulation of peptide hormones
Hemocyanin[18]	Reversible binding of O_2	Coupled binuclear	Oxygen transport in invertebrates
Tyrosinase[16]	Hydroxylation of aromatic ring and reduction of dioxygen to water	Coupled binuclear	Aromatic ring oxidation
Cytochrome c oxidase[19]	Coupled oxidation of cytochrome c and reduction of dioxygen to water	Binuclear Cu–Fe(haem)	Proton pump in electron transport chain
Laccase[20]	Coupled oxidation of phenols and reduction of dioxygen to water	Trinuclear	
Bilirubin oxidase[21]	Coupled oxidation of bilirubin to biliverdin and reduction of dioxygen to water	Trinuclear	
Ceruloplasmin[22]	Oxidation of Fe(II) to Fe(III) with the reduction to water	Trinuclear	Iron homeostasis in humans
Fet3p[23]	Oxidation of Fe(II) to Fe(III) with the reduction of water	Trinuclear	Iron homeostasis in yeast

This lower overpotential makes these catalysts a more attractive alternative to the inorganic catalysts. Proteins also have the ability to operate in physiological conditions where oxygen solubility and diffusivity is high, giving higher current densities. This makes them more advantageous than platinum, which has a tendency to corrode and cause dissolution at pH 7.[5, 24]

1.2 Multicopper oxidases

Multicopper oxidases (MCOs) are a family of enzymes that can catalyse the one–electron oxidation of a range of organic substrates in nature.[25] These enzymes typically contain four copper ions, which are classified into three distinct types denoted as Cu–T1, Cu–T2 and Cu–T3 based on their spectroscopic signatures.[26] There are other copper type classifications that are less common such as binuclear copper A and B centres.[19] These have different coordination geometries, which alter their reduction potentials. The Cu–T1 site is a lone copper ion whereas the Cu–T2 and two Cu–T3 form a copper centre, which is referred to as the trinuclear cluster (TNC).

The mechanism for oxygen reduction follows three stages.[26] First is electron transfer from a reduced species (homogenous catalysis) or from an electrode (artificial heterogeneous catalysis) to the Cu–T1 site. A second stage involves the intramolecular electron transfer (ET) from the Cu–T1 to the TNC via a highly conserved Cu–T1–Cys–His–His–Cu–T3 pathway.[27] The third stage is the dioxygen reduction to two water molecules.

The coordination of the Cu-T1 is characterised by two histidine residues and one cysteine. The remaining coordination sites are occupied by non-coordinating residues or weakly bound ligands.[27-28] There is an intense cysteine to Cu(II) charge transfer that appears at around 600 nm, which is responsible for its deep blue colour of the enzyme seen in solution. The Cu–T1 is the first catalytic centre, where the oxidation of the electron donor is carried out. The redox potential of the Cu–T1 site can vary between 0.12V up to

0.8V vs. SHE which further classifies the enzymes as either low, middle or high redox–potential enzymes that is governed by the coppers coordination. [29]

The Cu–T2 sites are normally located in the second catalytic domain part of the enzyme, away from the electron transfer sites and are coordinated by N or N/O ligands. The Cu–T2 are accompanied by a pair of Cu–T3 copper ions, forming the TNC where dioxygen is bound and reduced to water. Each of the Cu–T3 are coordinated by three histidine residues.

The rate–determining step for the overall mechanism is generally the oxidation of the substrate at the Cu–T1 site, which is explained later (Mass transport, 1.3.4.1) and is the reasoning for immobilisation techniques mentioned (Surface immobilisation of bilirubin oxidase, 1.2.2).[30] The ET and oxygen reduction are both said to be fast process, > 1000 s^{-1}. [31] However it has been shown that the ET for certain forms of MCOs, e.g., inhibited or resting form, which can result in the rate determining step becoming the ET between the Cu–T1 and the TNC.[32-33]

1.2.1 Bilirubin oxidase

This thesis focuses on one MCO enzyme, bilirubin oxidase from *Myrothecium verrucaria* (*Mv*BOx), which has shown promise for fuel cell applications.[34-35] What makes BOx an attractive alternative to other MCOs such as laccases is that it posses a high stability and activity at near neutral pH and has a high tolerance towards chloride.[21] It was first used in 1981 by Tanaka for detection of bilirubin,[25] its natural substrate, which it oxidises to biliveridin with the concomitant reduction of dioxygen to water.[36] The crystal structure is shown in Figure 1.1.[28]

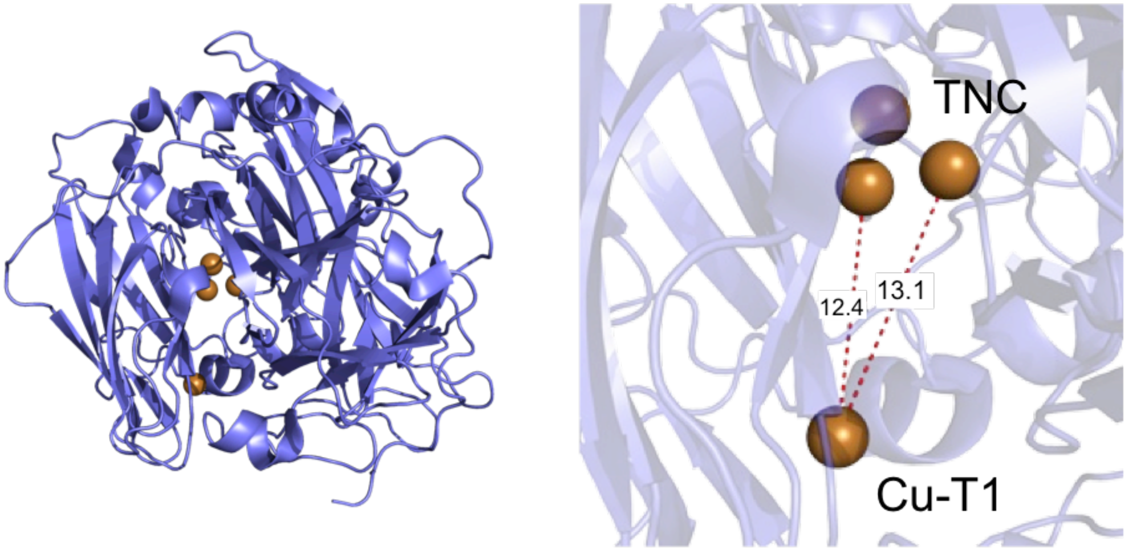

Figure 1.1. A cartoon representation of the X–ray determined crystal structure of *Mv*BOx (PBD code 2XLL) shows the full protein structure and a zoomed section of the copper sites and labelled distances.

The structure resembles many other MCOs with four copper ions. As seen in the crystal structure, the Cu–T1 site is located towards the surface of the protein in a specifically positioned binding pocket.[37] The crystal structure shows an unusual environment around the Cu–T1 of two non-coordinating hydrophobic amino acids, asparagine and threonine.[28] For effective heterogeneous catalysis, positioning of the Cu–T1 and its binding pocket to an electrodes surface is critical in facilitating fast direct electron transfer (DET) for the ORR. Fast intermolecular DET rate decreases exponentially with distance,so positioning of Cu–T1 should ideally be less than 14 Å.[26, 38]

1.2.2 Surface immobilisation of multicopper oxidases to surfaces

The structure of three-domain MCOs are all highly homologous, which allows similar immobilization techniques to be used across the species, whether they come from plant, fungi or bacteria.[26] Because MCOs with two-domains tend to form dimers and have different structures upon adsorption, their immobilisation techniques can be different and are not covered in this thesis. Immobilisation methods tends to fall into two groups. Those that rely on DET, and those that require mediated electron transfer (MET). As these two methods are affected by enzyme orientation and attachment, only immobilisation for DET will be covered within this thesis.

The first use of DET between a redox-active protein and an electrode was shown by Eddowes and Hill in 1977.[39] They successfully showed DET between cytochrome *c* immobilised on bis(5-pyridyl) modified gold electrodes. Yeh and Kuwana also showed the reversible electrochemistry of cytochrome *c* just a few weeks later, this time supported on indium–doped tin oxide (ITO).[40] Berezin et al. showed the DET could be used to detect the enzymatic activity of larger proteins. DET was shown for adsorbed laccase on to modified carbon electrodes in the presence of oxygen, but showed no signal in oxygen-free buffer.[41] The ability to remove macromolecular diffusions away from electrochemical measurements allowed for thermodynamic and kinetic studies of biological redox process to be studied. Analysis of these process were able to be carried out on sub–picomole amounts and thus became known as protein film electrochemistry (PFE) (Protein film electrochemistry, 1.3.9).[42]

1.2.2.1 Self assembled monolayers for protein adsorption

A widely used technique for tuning the surface functionality of an electrode before protein adsorption is to modify the surface with a self-assembled monolayer (SAM). This can allow the surface properties and characteristics to vastly change. SAM are selected dependent on the properties desired, such as a change in hydrophobicity, positive, negative or neutral groups, specific functional groups for covalent linkage, or to produce an electron blocking layer. They are readily used in surface science due to easy formation, as displayed in Figure 1.2. Here reactive species from solution adsorbed to the surface and rearrange themselves to form highly order dense monolayers. The coverage, composition and quality of SAMs are important to understand for there use in many applications. An example of a SAM often used in surface science is functionalised thiolates. These molecules will have a thiol head groups, which readily reacts with gold to produce a monolayer, leaving the rest of the molecules, the spacer and tail. These can produce well–structured and stable chemical interfaces that can specifically tune the surface functionality and film thickness.[43-44] These become important when electron transfer through the SAMs is required (Interfacial electron transfer, 1.3.6). Other forms of SAMs can be made from organosilanes, which have a standard formula of X-R-Si(OR'), where X is and organic, such as amino or alkyl, R is and Aryl or Alkyl $(CH_2)_n$ with n = 0,1 or 3, and R' is a methyl ethyl etc. The alkoxy group is hydrolysable and can react with metals to act as a bridge between organic and inorganic substrates.

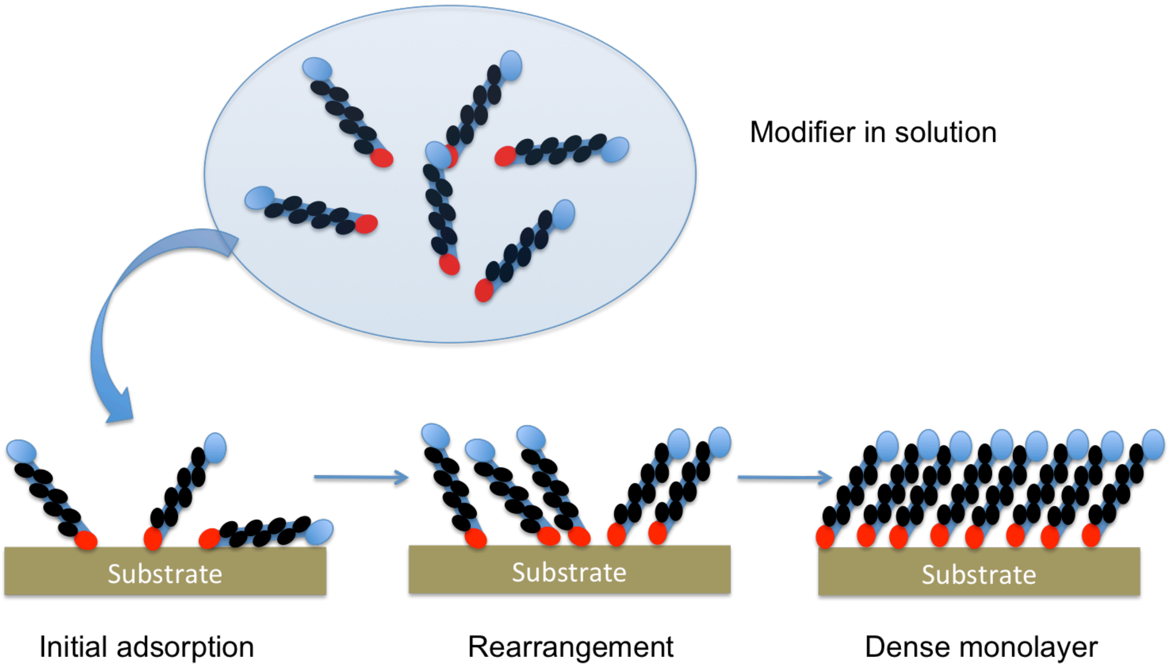

Figure 1.2 SAM formation onto a substrate from solution.

There are several methodologies which are used to determine characteristics of the SAMs on a surface such as: infrared spectroscopy, X-ray spectroscopy and scanning probe microscopy.[45] Another way to determine the surface coverage of a monolayer that has formed on the surface is via voltammetric measurements of the charge passed for the one electron-reductive desorption.[46] Integration of the current passed, corresponding to the reductive peak, given as

$$Q = \int_{E_A}^{E_D} \frac{i}{v} dE \qquad \text{Eq.1.1}$$

where Q is the amount of charge passed, E_A is the potential at which reductive peak starts, E_D, is the potential at which desorption ends, and v is the scan rate. For a one-electron reduction of a thiolate, each electron passed is representative of an previously adsorbed thiol. This allows for the monolayer coverage Γ to be calculated from:

$$\Gamma = \frac{Q}{nF} \qquad \text{Eq.1.2}$$

where F is the Faraday constant and n is the number of electrons for the reduction (usually 1). The spacing of individual adsorbed species is dependent on the interactions of the head groups and of the linker molecules. For alkane spacer molecules, between SAM head and tail groups, pi-pi interactions help to form a dense monolayer, whereas mixed monolayers can form relatively low-density films due to group repulsion. Studies of the structure of alkanethiols on Au (111) with molecular-level resolution reported substrates, with molecule–molecule spacing up to 5 Å and an area per molecule of 21.6 $Å^2$ (about 4.6 molecules nm^{-2}).[47-48]

1.2.2.2 Immobilisation via physical adsorption

The first methods to immobilise redox active proteins used simple physical adsorption onto different surfaces. The first reported immobilisation of laccase was by Tarasevich et al. in 1979, here laccase was adsorbed onto carbon black electrodes. In the presence of oxygen-saturated buffer, the electrochemical reduction of oxygen to water was increased along with a positive shift in reduction potential.[49] Several studies use unmodified pyrolytic graphite edge (PGE) electrodes that allows fast adsorption of enzymes.[32, 50] Adsorption is attributed to the interaction with oxygen-containing surface groups allowing for non-specific adsorption. However the variability in electrochemical responses from using PGE electrodes has led to alternative electrodes being investigated

A more reproducible surface for physical adsorption of enzymes is to use gold. Pankratov et al. looked at the immobilisation of *Mv*BOx and laccase adsorbed to bare gold surfaces. Clear electrochemical responses were seen for *Mv*BOx, whereas the laccase showed no activity due to mis-orientation.[21]

Immobilisation of MCOs too thiol-modified gold surfaces have been extensively research.[28, 51-53] These immobilisations are usually governed by electrostatic interactions. Olejnik et al. show the how the orientation of adsorbed laccase was governed by electrostatic interactions between amino and carboxyl-terminated thiol modified gold electrodes.[51] A lack of activity was seen when adsorbed on the amino-modified surface. Electrostatic immobilisation of cytochrome *c* (Table 1.2) on a carboxylic acid terminated thiol on gold was also studied by de Groot et al.[54] A dependence on pH was observed, showing adsorption only at pH less the 5.5, showing the need for the protein to be positively charged.

Immobilisation has more recently been studied where specific parts of an enzyme are targeted. Blanford et al. used amino–anthracene to target a electron entry binding pocket of laccase from *Trametes versicolor,* which was shown to increase the catalytic efficiency and lifetime of the adsorbed layer.[55]

1.2.2.3 Immobilisation via covalent attachment

An alternative from of attachment is immobilising MCOs to electrodes via covalent linkage. Generally, methods for covalent attachment are by activating the surface groups of the electrode and reacting with nucleophilic groups and the protein. [56]

Balland et al. showed oriented immobilisation of a active monolayer of histidine-tagged *Trametes versicolor* laccase (*Tvl*) that was all in the correct orientation for electron transfer.[57] Here a nitrilotriacetic acid was used as the functional group of an organothiol-modified surface, and covalently bound through copper coordination to the histidine sites. Ramirez et al. have covalently attached bilirubin oxidase from *Trachyderma tsunodae* to 3-mercaptopropanoic acid modified gold electrodes using EDC–NHS chemistry.[53] The attached enzymes orientation showed a reduction in catalytic ability, due to increased distance of the T1 copper site to the electrode. Recently Singh et al. showed how *Mv*BOx covalently attached via an amide linkage between a thiol-modified surface and a lysine residue on the enzymes surface did not change mitigate the observed activity loss.[58]

1.3 Electrochemistry

Electrochemistry is the study of chemical reactions that involve electron transfer between the electroactive species and an electrodes surface. In this thesis electrochemistry is used to study redox enzyme catalysis by measuring the flow of electrons between an electrode and enzyme as a function of applied potential. Electrochemistry is a broad technique that has applications ranging from fuel cells, batteries and chemical sensing. Electrochemical theory is also important for understanding process such as corrosion or electroplating. Electrochemistry can also be used to study redox enzyme catalysis, by measuring electron transfer from an electrode to the metal centres of the proteins that are attached to the enzyme otherwise known as protein film electrochemistry (Protein film electrochemistry, Section 1.3.9) [59-60]

Within this thesis, focus is specifically given towards electron transfer between an electrode and a species in solution. Electrochemistry allows us to determine a range of information regarding these processes, such as reduction potentials (Protein film electrochemistry, 1.3.9), diffusion coefficients (Mass transport, 1.3.4.1), and electron transfer rate constants (interfacial electron transfer, 1.3.6).[61] An electrode can act as both an electron donor and acceptor, moving redox-active species between different oxidation states. This is normally controlled externally by control equipment called a potentiostat.

Experimentally in order to study electrochemistry, two or more interfaces need to be compared to give a full description of a process, and these make up one complete electrochemical cell. For an electron transfer between a metal electrode and a species in solutions, a charge separation must develop. This charge separation creates a potential difference, which will be fixed for a given system. Experimentally this potential difference can't directly be measured as it does not complete an electrical circuit so a second electrode needs to be introduced to act as a reference.[4]

1.3.1 Reference electrodes

An applied potential at an electrode|electrolyte interface, can be measured between two electrodes but to be able to compare it to other potentials, you need a reference electrode (RE). This enables a standardised known potential to be applied to any reaction. The normal RE used by convention is the standard hydrogen electrode (SHE) and is conventionally set at $E° = 0$ V (° symbolised standard conditions). The SHE is based on the reduction of protons to form gaseous hydrogen given as:

$$2H^+(aq) + 2e^- \rightarrow H_2(g)$$

however due to experimental impracticalities, secondary reference electrodes are used with a known potential difference from the SHE. The two common types of references are silver|silver chloride (Ag|AgCl) or saturated calomel electrode (SCE).

1.3.2 Nernst equation

The Nernst equation shows allows the calculation of a that the potential at an electrode when it is at equilibrium, and is given as:

$$E = E^{\circ} - \frac{RT}{nF} \ln Q \qquad \text{Eq.1.3}$$

where E° is the equilibrium redox potential measured experimentally, R is the gas constant, T is the temperature, n is the number of electrons transferred Q is the reaction coefficient given as:[4]

$$Q = \frac{B^b}{A^a} \qquad \text{Eq.1.4}$$

Where A and B are the concentration of the oxidised and reduced species respectively, and a and b are the stoichiometric coefficients. In a reduction reaction, the amount of reduced species increases and the amount of oxidised species decreases until the equilibrium is reached and Gibbs free energy for the reaction approaches zero.

1.3.3 Three-electrode system

Dynamic electrochemistry is where there is a change in the concentration of the oxidised or reduced species due to an applied potential, and is measured by a change in current. In a two–electrode system, the counter electrode also acts as the reference, this lowers accuracy due to difficulty of maintain a constant potential. A three–electrode set up consists of a working electrode (WE), a counter electrode (CE), which provides or collects the current and a RE, as shown in Figure 1.3.

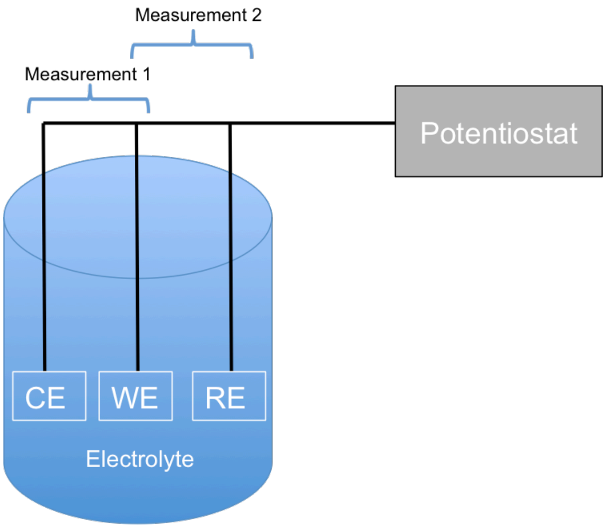

Figure 1.3. A typical three–electrode system showing the typical measurements recorded. First measurement is between the working electrode (WE) and counter electrode (CE), which measures the flow of electrons. The second measurement is between and the WE and the reference electrode (RE), which records the potential. The applied potential and the measured current are controlled by the potentiostat.

The reference electrode measures a single redox reaction (at the WE), so it needs to have no current passing through it otherwise the potential that defines it would change as the reaction proceeded. For this reason, dynamic experiments require the use of a third electrode, CE.

1.3.4 Dynamic electrochemistry

1.3.4.1 Mass transport

Mass transport concerns the transport of reactants from the bulk phase to the electrode surface, and the removal of products away from the electrode. Along with the electron transfer step for a chemical reaction, these three processes determine the overall rate of a reaction, with the slowest being the rate limiting reaction step.[4] In the case of *Mv*BOx electrocatalysis, transport processes, which involve transport of oxygen and protons to the catalytic centre of the enzyme, the catalytic reduction of oxygen to water, which in itself involves internal electron transfer, chemical rearrangements and other molecular motions, could all be the rate limiting step.

The movement of ions in solution can occur through one of three mechanisms: diffusion due to concentration gradients of the ions, convection due to movement of the solution and electrophoretic migration due to the electrostatic field present acting on the ions in the solution.[62] The total flux of ionic species is therefore a combined effect of these three processes shown as:

$$J_i = f\ (Diffusion, \mathrm{C}onvection, Migration) \qquad \text{Eq. 1.5}$$

For a system that follows steady state diffusion, that is, a controlled concentration gradient between the electrolyte at the interfaces and electrolyte in the bulk, the flux of the species can be approximated using Fick's first law of diffusion:

$$J_{DIFFUSION} = -D\left(\frac{\partial C}{\partial x}\right) \qquad \text{Eq. 1.6}$$

where J is the diffusion flux (mol m^{-2} s^{-1}), D is the diffusion coefficient (m^2 s^{-1}), C is the concentration (mol m^{-3}) of species in solution at location x.

Convection of ions can be either a natural process caused by thermal or density gradients in solutions, or by external forces such as bubbling, pumping or stirring. Natural convection causes a solution to mix in a random unpredictable manor. To avoid this, forced convection can be used to remove this unpredictability allowing for reproducible environments over longer time scales.[63] This works by creating a stable flowing direction that resists mixing laterally, known as laminar flow.[63] When laminar flow is achieved the mass transport for convection can be predicted by:

$$\frac{\partial C}{\partial t} = -v\frac{(\partial C)}{\partial x} \qquad \text{Eq. 1.7}$$

where C is the concentration (mol m^{-3}) of species in solution, t (s) is the time, v represents the velocity (m s^{-1}) of the solution and x represents the distance (m). This integrates with Equation 1.5, where the forced velocity replaces the diffusion coefficient.

Migration of ions due to an electric field produced at the electrode/solution interface can induce the movement of ions either towards or away from the electrode. These migration effects can be important electrochemical reaction, where the migration flux is given as:

$$J_{MIGRATION} = -\mu C \frac{\partial \phi}{\partial x} \qquad \text{Eq. 1.8}$$

where μ is the ionic mobility, C is the concentration, ϕ is the electrostatic potential and x is distance. This means the change in buffer solutions with different ions and different sizes can influence the electrostatic potential and thus the migration flux.[4] Experimentally to minimise the effects of migration, redox-active ions are normally screened with counter ions. When selecting the electrolyte, inert ions under experimental conditions are chosen at concentrations at least 100 times great than the redox species concentration.[4]

1.3.5 Electrical double layer

The electrical double layer (EDL) is found in a region between the electrode and the bulk electrolyte in solutions. At the EDL, any transfer in charge either to of from the electrode is balanced by a rearrangement of ions from the solutions. This caused the electrode to become polarised and creates a different electrostatic potential than that of the bulk electrolyte solution, due to screening of ions.[62] Charges are either attracted or repelled within the solution close to the electrode surface.

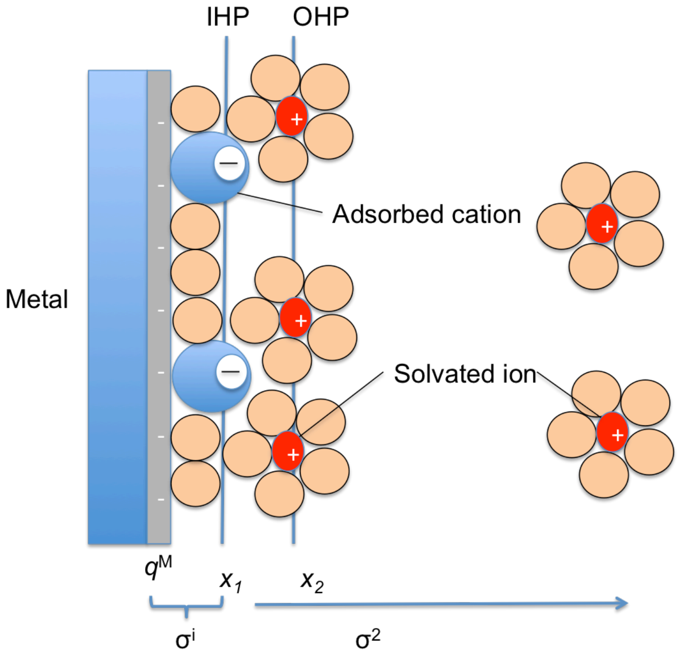

Figure 1.4 Typical model of the double layer region between an electrode and electrolyte.

Helmholtz first proposed a theoretical model that considered a layer of counter ions at the electrode surface to balance the charge presented from the electrode. In Figure 1.4 the electrical double layer is shown that is made up of several layers. After the electrode, there is an inner layer, which is referred as the inner Helmholtz plane (IHP) that contains solvent molecules and specifically adsorbed ions. The location of the specifically adsorbed species is given as x_1, and has a charge density denoted as σ^1. Solvated ions can only approach the surface to distance x_2, known as the Outer Helmholtz plane (OHP). Due to the larger distance between solvated ions and the electrode surface, only long-range electrostatic forces can occur, so chemical properties of the ions does not affect the interaction. These solvated ions are adsorbed non-specifically, meaning they are free to move around in a three-dimensional region called the diffuse layer, which extends from the OHP, to the bulk electrolyte. In this diffuse layer, the net charge density decreases with increasing distance from the electrode. This causes a potential drop across the layer that does not decrease linearly. The excess charge density on the solution side of the double layer, is required to cancel the charge density at the electrode surface, and is given as:

$$\sigma^S = \sigma^i + \sigma^d = -\sigma^M \qquad \text{Eq. 1.9}$$

by varying electrode potential, the concentration and thickness of the diffusion layer will change. In general, for ionic concentrations of greater than 10^2 M, the thickness will be less than 100 Å.[4]

1.3.6 Interfacial electron transfer

When a reduction or oxidation reaction occurs for a single electron transfer between and two species, as shown below:

$$\mathrm{O_{(aq)}} + ne^- \underset{k_{oxidation}}{\overset{k_{reduction}}{\leftrightharpoons}} \mathrm{R_{(aq)}} \qquad \text{Eq. 1.10}$$

the individual current flows can be calculated using:

$$i_{reduction} = -nFAk_{reduction}[\mathrm{O}] \qquad \text{Eq. 1.11}$$
$$i_{oxidation} = nFAk_{oxidation}[\mathrm{R}] \qquad \text{Eq.1.12}$$

where n is the number of electrons pre reduction or oxidation, F is Faraday's constant and $k_{\mathrm{oxidation}}$ and $k_{\mathrm{reduction}}$ are the rate constants for the forward and reverse reactions respectively, and A is the surface area of the electrode. At equilibrium the net conversion rate is zero where the forward and backward rates are equal, by convention, negative rates are used for the reduction. The rate constants of solution-phase reaction vary with temperature given by the relationship ln k is linear with 1/T. This was first proposed by Arrhenius and expressed the rate constant as:

$$k = Ae^{\frac{-E_A}{RT}} \qquad \text{Eq. 1.13}$$

where E_{A} is the activation energy and A is a frequency factor. The exponential therefore gives the probability of using thermal energy to overcome an initial energy barrier. This is shwon using Figure 1.5, where a reaction proceeds as a function of potential energy. The reactants and products are shown as energy parabolas, to denote all energy states of potential energy that the species can occupy, and the point at which they cross is where they share the same energy.

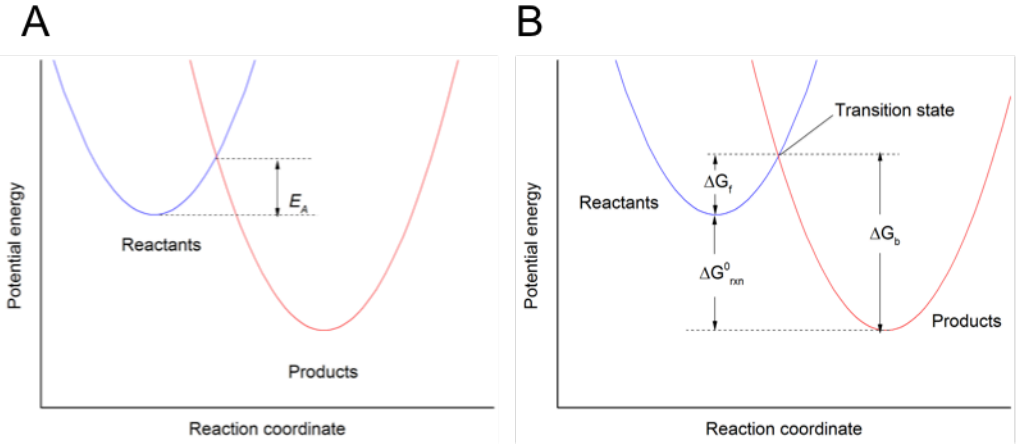

Figure 1.5. Representation of reaction pathway in terms of potential energy Panel A. Panel B shows the transition state theory free energies during a reaction

As a reaction proceeds, the coordinates of the reaction change from the reactants on the left, to the products on the right. The reaction path starts at minimum for the reactants before surpassing an energy maximum to give a lower overall energy for the products. We can also look at E_{A} as being the change in standard internal energy from the minimum to the maximum and so an equivalent statement of the Arrhenius equation Eq.1.13, can be written as:

$$k = Ae^{\frac{-\Delta G_f}{RT}} \qquad \text{Eq. 1.14}$$

where ΔG_f is the standard free energy of activation. This is the base of transition state theory (TST), which predict values of A and E_A for specific chemical systems. This TST approach is that a reaction will proceed via a well-defined transition state (also known as activated complex) from reactants to products.

1.3.6.1 Marcus theory

Marcus theory was the first microscopic theory developed for electron-transfer reactions in which only outer spheres were involved, i.e. a change in charge (e.g., oxidation of Fe^{2+} to Fe^{3+}), through electron jumping, with little to no structural changes and no broken bonds.[4] Outer-sphere reactions, involve two species which undergoing electron transfer, without altering their coordination. This occurs by an electron being transferred from one primary bond system to another. In outer-sphere reactions, the reactant does not strongly interact with the electrode, and is normally separated by at least a solvation layer.[62] Later on the theory was used to include inner-sphere electron transfer.[64] In these cases electron transfer occurs where the reactants and products share a ligand with each other, this is said to be ET within a primary bond system. Unlike outer-sphere reactions, inner-sphere reactions have a strong interaction with an electrode surface and thus require specific adsorption onto the electrode surface.

For the most part, outer-sphere ET reactions are easier to analyse, and where most of the theory has been developed.[65-66] For an electron transfer reaction, given by:

$$R + e^{-} \rightarrow P \qquad \text{Eq. 1.15}$$

with the assumption that the reactants does not change its configurations during the actual transfer step. This is governed by the Frank-Condon principle, which states the nuclear momenta and positions do not change on the time scale of electron transitions.[4] A second assumption is that the electron being transferred must travel from the electrode state to the product state of the same energy. This means that the electron transfer process is radiationless and occurs when the two parabolas of the reactant and electrode overlap.

If we take the standard free energy of Eq.1.14, but account more for the nature of the reaction coordinate, we can define the rate constant for k^0 as:

$$k^0 = \kappa_{\mathrm{el}} K_{\mathrm{p}} v_{\mathrm{n}}\ e^{(-\frac{\Delta G^\ddagger}{RT})} \qquad \text{Eq. 1.16}$$

where κ_{el} is the electronic transmission coefficient (the probability of electron tunnelling) K_p is the equilibrium constant, v_n (s^{-1}) is the nuclear frequency factor (frequency of crossing the free energy barrier) and $\Delta G^\ddagger$ is the activation energy. The tunnelling probability is given as:

$$\kappa_{el} = e^{(-\beta x)} \qquad \text{Eq. 1.17}$$

where x is the distance over which tunnelling occurs and β is a factor dependent on the height of the energy barrier and the nature of the medium. From this an expression to give the electronic transmission coefficient κ_{el} can be given as:

$$\kappa_{el}(x) = \kappa_{el}^0 e^{\,(-\beta x)} \qquad \text{Eq. 1.18}$$

where κ_{el} tends to 1 when x is at a distance where the interaction between the reactant and the electrode is sufficiently strong enough to be adiabatic. [4]

Like the TST, the reaction can be considered in terms of nuclear coordinates. The reacting species are defined as electron donor and electron acceptor. Two assumptions are made, i) that the acceptor has a fixed distance from the electrode and ii) that the standard free energies of the donor and acceptor, ΔG^0_D and ΔG^0_A depend quadratically on the reaction coordinate q, as given by:

$$G_D^0(q) = (\tfrac{k}{2})(q^\ddagger - q_0)^2 \qquad \text{Eq. 1.19}$$

$$G_A^0(q) = (\tfrac{k}{2})(q^\ddagger - q_D)^2 + \Delta G^0 \qquad \text{Eq. 1.20}$$

where q_D and q_A are the values of the coordinate for the reactants and products. For a reaction at an electrode, ΔG^0 is equal to $F(E–E°)$ and is dependent on the electrode potential (Butler-Volmer effects of potential on energy barriers,

1.3.6.2).

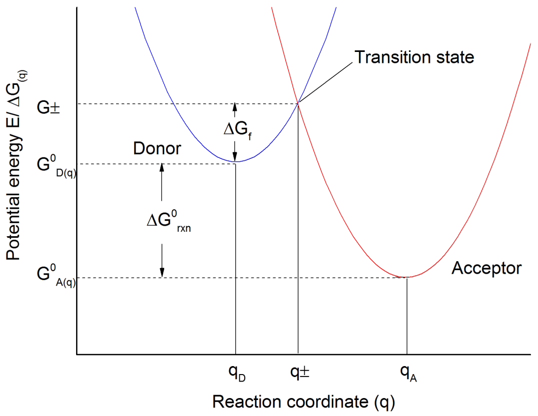

Figure 1.6. Standard free energy as a function of reaction coordinate q for an electron transfer reactions from an electron donor to and electron acceptor.

Figure 1.6 shows the reaction coordinate of a reaction form D to A. As already discussed, the assumption is that the free energies at the transition state of the reactant and products are equal to zero therefore, Eq.1.19 is equal to Eq.1.20 and we can solve for $q^{\ddagger}$. Substituting an expression for q back in to Eq.1.19 and giving the reorganisation energy, λ, to equal $(k/2)(q_R - q_P)^2$, we can define the standard free energy for the electron transfer reaction as:

$$\Delta G_f^0 = \frac{\lambda}{4}\left(1 + \frac{F(E-E^{\circ})}{\lambda}\right)^2 \qquad \text{Eq. 1.21}$$

showing the overall rate of ET is potential dependent, but also dependent on the reorganisation energy λ. The reorganisation energy represents the energy required to transform the nuclear configuration in the reactant and the solvent to those in the product state.[4]

1.3.6.2 Butler-Volmer effects of potential on energy barriers

The potential of an electrode strongly affects the kinetics of a reaction occurring on the surface. An understanding of how potential affects k_{ox}/k_{red} (Eq. 1.10) is therefore required in order to predict reactivity. In Figure 1.7 the reaction coordinate for a one electron reduction is shown. In order to measure the effects of potential change, we use a reference point within the reaction, which is set as the reaction pathway when the potential is at equilibrium, defined as $E°$. For the reaction coordinate at $E°$, both the cathode and anodic activation energies are shown and denoted as $\Delta G_{0c}^{\ddagger}$ and $\Delta G_{0a}^{\ddagger}$ (0 symbolises at equilibrium, '*c'* and *'a'* denote cathode and anodic respectively). If the potential of the system were to change by ΔE, to a new value E, then the resident energy of the electron on the electrode, which changes the $O + e$ curve to move up or down. The lower curve shown in Figure 1.7 shows the effect of a positive ΔE, and shows that the barrier for oxidation $\Delta G_a^{\ddagger}$ and the new potential has become less than $\Delta G_{0a}^{\ddagger}$, meaning the reaction with thermodynamically proceed.

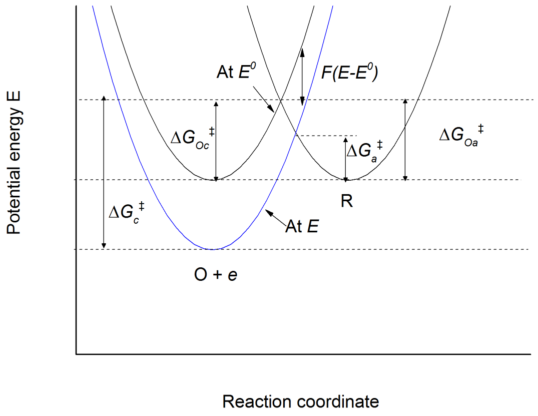

Figure 1.7 Effects of potential change on the standard free energies of activation for oxidation and reduction.

1.3.7 Electrochemical techniques

1.3.7.1 Cyclic Voltammetry

Voltammetry is a technique that measures the specific current flowing through a working electrode as a function of an externally changing potential. Cyclic voltammetry (CV) gives information such as current, potential, reaction rates of reversible electron transfer processes occurring.[62]

In cyclic voltammetry the electrode potential is ramped at a constant rate from a starting potential, E1 to a final potential, E2 before returning back to E1 to complete one cycle. This gives a triangular wave potential profile as shown in Figure 1.8A. The rate at which the potential is changed is known as the scan rate, v (V s^{-1}). Figure 1.8B shows an idealised CV of an oxidation and reduction of a redox active couple in solution. From E1 to E2 voltammogram shows the oxidation of the species in solution, given by the oxidation peak current at i_p^{ox} at the potential E_p^{ox}. On the reverse8 scan from E2 to E1, the species is reduced back to its starting material shown at E_p^{red} with a peak reduction current at i_p^{red}.

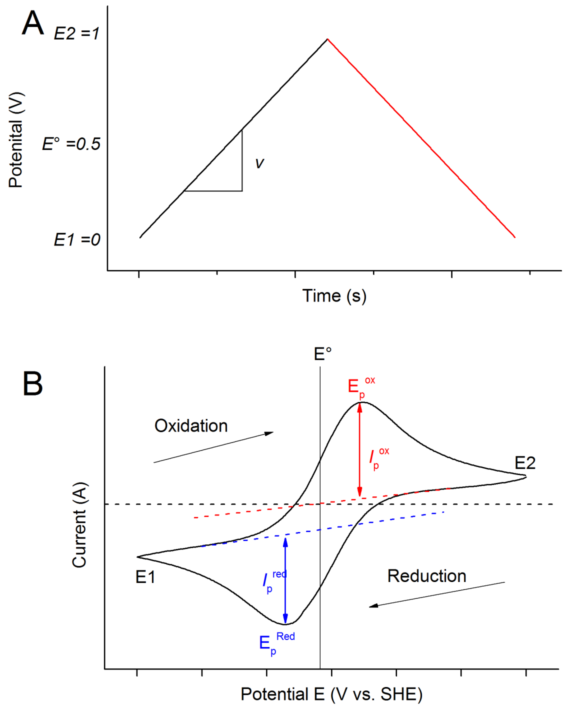

Figure 1.8. Schematic representation of a voltammetric sweep between electrode potentials E1 and E2 against time, panel A. Typical schematic of a cyclic voltammetry sweep where a soluble, reversible, one-electron redox-active species is being reduced and oxidised between sweeping generating catholic and anodic currents, panel B.

The reason for the shape of the curve can be described due to mass transport limitations and due to the driving force available for reduction or oxidation. As the potential is ramped, the Fermi level of the electrode has greater energy than the lowest unoccupied molecular orbital (LUMO) of the species in solution the oxidation reaction begins to occur.

Once E_p^Ox is reached, the potential is sufficiently high enough to instantaneously oxidise all the reactants at the electrode surface. At this point the reaction is diffusion limited, and the current reduces. Upon the reverse scan a similar scenario occurs with the reduction of the species back to its starting state.

For the one–electron reversible reaction, the peak separation between E_p^Ox and $E_\mathrm{p}^\mathrm{Red}$ is given as:

$$\Delta E = E_p^{Ox} - E_p^{Red} = \ln \frac{RT}{nF} \qquad \text{Eq. 1.22}$$

where n is the number of electrons. The 59 mV peaks separation (298 K) is governed by the Nernst equation, which includes a conversion factor of 2.303 for a natural log to $\log_{10}$.[4]

1.3.7.2 Chronoamperometry

Chronoamperometry is a complimentary technique to cyclic voltammetry where instead of sweeping the potential, it is fixed, and the current is measured with time. This can allow for diffusion coefficients to be determined.[4]

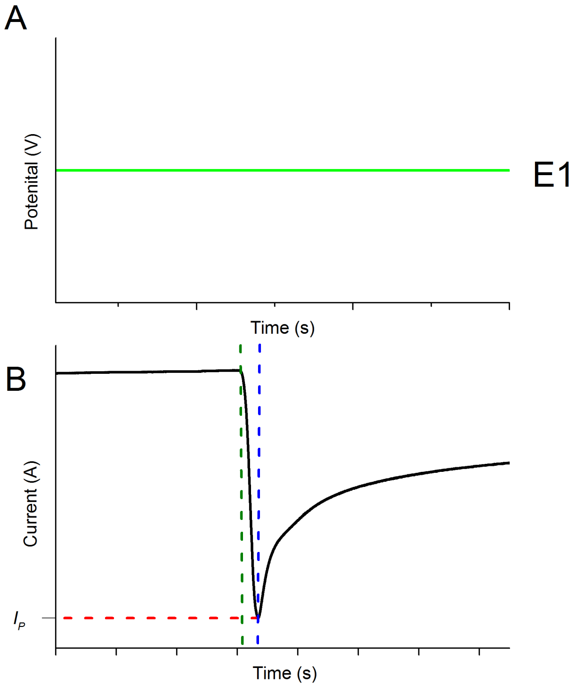

Figure 1.9. Schematic representation of chronoamperometry experiment. Panel A shows the potential held at E1 against time. Panel B shows the cathodic current response against time when a redox-active protein is added to a system. The green dashed lines indicate injection and the blue dashed the blue dashed indicates time taken after injection to reach maximum catalytic current, and red dashed line show the maximum current response before decay.

In Figure 1.9, a constant potential is held at a suitable reduction potential for an electroactive species. The green dashed lines show the addition of the electroactive species and it can be seen in B that an increase in current is observed due to a catalyst being added which is reducing reactants in solution. As the reactants approach the surface the current increases until a maximum, shown as $i_{p.}$ is reached. The time taken to reach i_p is a mixture of reactant diffusion, polarisation of the electrode–solution interface and reorganisation of the ions to form an electrochemical double layer.[67] The time taken therefore can be attributed to the size, charge and concentration of the reactants in solution. Once i_p is reached, the current then begins to decay with time because the flux of electroactive species to the electrode is proportional to the concentration gradient at the electrode surface, and the concentration gradient diminishes with time as a result of the increasingly thickening region of depleted species. This allows the calculation of diffusion coefficients since they are proportional to the current decay.

1.3.8 EC and EC' mechanisms

The EC mechanism relates to a chemical reaction that occurs immediately after an electrode reaction. An example could be a reduced species reacting with the solvent to produce a species that is not electroactive at the potentials where the initial reduction took place. The rate of electron transfer is then governed by Fick's 2nd law of diffusion, however because the reduced species is used up, the rate for the generation of the reduced species is given by:

$$\frac{\partial[R]}{t} = D_0\left(\frac{\partial^2[R]}{\partial x^2}\right) - [R]k_{EC} \qquad \text{Eq.1.23}$$

where k_{EC} is the chemical rate constant which can be studied by increasing scan rate during cyclic voltammetry.[4]

The EC' mechanism is a special type of EC process that involves the reaction of the species involved in the electron transfer, with a species in solution, to regenerate the starting material as shown by:

$$\mathrm{O} + ne \rightleftharpoons \mathrm{R} \qquad \text{Eq.1.24}$$

$$\mathrm{R} + \mathrm{Z} \rightarrow_{k_{EC}} \mathrm{O} + \mathrm{Y} \qquad \text{Eq. 1.25}$$

In MCO catalysis, dioxygen is reduced to water by an EC' mechanism, reforming the active center of the enzyme each cycle. In order to study these reactions, a technique known as protein film electrochemistry is used.

1.3.9 Protein film electrochemistry

Protein film electrochemistry (PFE), also known as protein film voltammetry, is a technique used to quantify the catalytic ET through an enzyme and yield information on thermodynamics and kinetics of the protein under investigation.[42] The technique requires adsorption of a protein onto an electrode as a stable mono or sub-monolayer. Importantly, due to the size and nature of proteins, orientation is crucial for fast ET.[68] The advantage of PFE is that the immobilisation of the protein on an electrode surface removes relatively slow macromolecular diffusion from the electrochemical measurements which allows for easier analysis of the electrochemical measurements and removal of otherwise limiting processes.[69] This also improves the sensitivity of the electrochemical measurements, meaning sub-picomole amounts of protein are required.[42, 55]

PFE allows for the thermodynamic driving force of a redox-active enzyme to easily be measured. By varying the potential (using cyclic voltammetry) and observing the resulting current flow, reduction potentials for enzymatic active sites can be observed. PFE also allows investigation of enzyme turnover conditions, such as pH, temperature and electrolyte.[42] Figure 1.10 shows a typical PFE experiment using cyclic voltammetry to measure the catalytic ability of the MCO *Mv*BOx to reduction dioxygen to water. The starting potential at 0.7 V vs. Ag|AgCl has too small a driving force for ET to occur and as a result there is no flowing current. As the potential decreases, the onset of catalysis is observed by a change in magnitude of the negative current (negative due to a reduction process). The potential at which the ET occurs gives details on the reduction potential of the copper active site. For *Mv*BOx, the onset reduction potential is seen at 0.55 V vs. Ag|AgCl and classifies *Mv*BOx as a high redox potential enzyme.[60] The first scan shows the largest current, however after reaching a maximum at ~0.37 vs. Ag|AgCl, before mass transport limitations result in a decrease in the current.

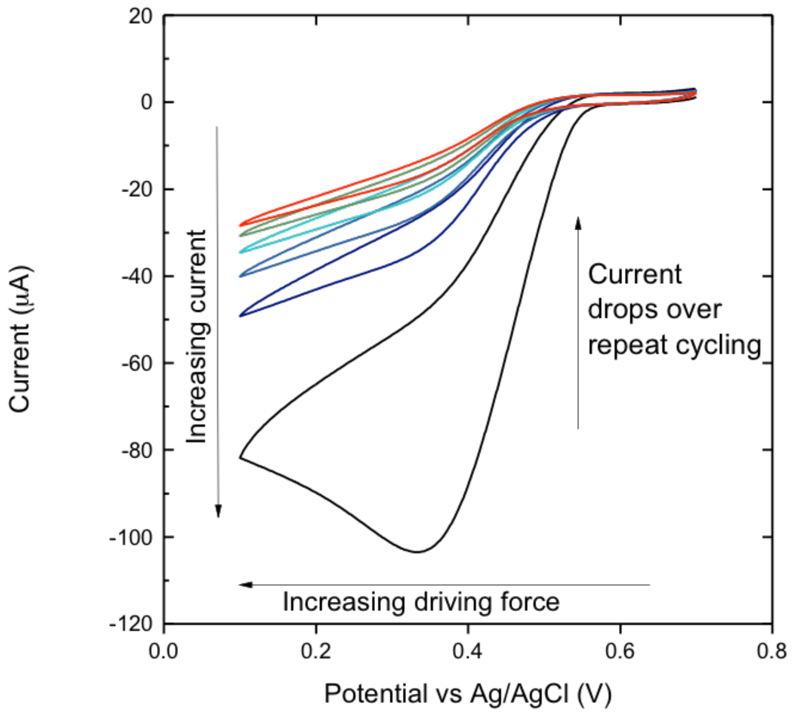

Figure 1.10. Typical electrocatalytic wave of *Mv*BOx gold QCM electrode. Conditions: 0.1 M sodium phosphate, pH 6.0, 25 °C, 100% O_2 (pre–saturated for 20 min), scan rate 10 mV s^{-1} 0.1 ml min^{-1}

Subsequent scans shows a decrease in enzyme activity due to enzyme deactivation and desorption.[58] As the current drops, mass transport becomes less of an issue, and the rate determining step now becomes limited by something intrinsic to the enzyme, and may also be affected by the enzyme turnover frequency (k_{cat}).[60]

1.3.10 Catalytic voltammetry of MCOs

Catalytic voltammetry of MCOs is normally carried out on either graphite electrodes or gold electrodes modified with SAMs (Surface immobilisation of multicopper oxidases**,** 1.2.2).

Table 1.4 gives summaries of the key studies of either *Mv*BOx or closely related plant and fungal laccases. For *Mv*BOx, catalysis is generally highest around pH 7, which is close to its optimum activity. Laccases typically show voltammetry at lower pH ranges of 3–5.

1.4 Protein adsorption

Overall protein structure is determined by numerous factors, such as pH, hydrogen bonding, electrostatic interactions, conformational entropy and van der Waals forces.[70] When a protein comes into contact with a surface, external and individual protein properties will ultimately determine the outcome of adsorption: conformation rearrangements or protein unfolding.[71] Due to the large size of proteins with unique amino acid sequences, this becomes a difficult task to predict. This section will focus on each of the contributing factors.

1.4.1 Factors controlling protein adsorption

1.4.1.1 External considerations

Temperature can play a role in protein adsorption in two ways. Firstly at increased temperatures, the diffusivity of the protein towards a surface will be increased, therefore increasing the rate of adsorption.[72] A secondary effect of increased temperature is entropy gain from the replacement of bound water molecules and protein structural rearrangements. When protein–surface bonds are formed, the internal, non-covalent bonds

Table 1.4. Catalytic MCOs which are involved in the four-electron dioxygen reduction that have been studied by PFE

Enzyme	Electrode surface	Voltammetry details	Catalysis	Experimental conditions
Bilirubin oxidase from *Myrothecium verucaria*[73]	Highly ordered PGE (HOPGE)	650– (200) vs Ag/AgCl/sat. KC	Sigmoidal wave E^{cat}: 460 vs Ag/AgCl/sat. KCl	pH 4,7 O_2 saturated buffer stirred buffer: 0.1 M phosphate
Bilirubin oxidase from *Myrothecium verucaria*[74]	Spectroscopic PGE	1000–0 mV, 10 mV s^{-1}	Sigmoidal wave E^{cat} approx 700 mV	pH 4 0.26 mM O_2 0.1 M citrate phosphate buffer
Bilirubin oxidase from *Myrothecium verucaria*[21]	Bare gold	1100–0.2 mV vs. NHE	Sigmoidal wave E^{cat} approx. 650 mV	pH 7.4 0.1M phosphate
Bilirubin oxidase from *Myrothecium verucaria*[58]	Gold modified 3mercaptopropanoic acid	910–210 mV	Sigmoidal wave E^{cat} approx. 650 mV	pH 6 0.1M phosphate
Bilirubin oxidase from *Trachyderma tsunodae*[53]	Gold modified 3mercaptopropanoic acid	650–150 mV	Sigmoidal wave E^{cat} approx 500 mV	pH 7 0.1 M phosphate
Laccase from *Trametes hirsuta*[21]	Bare gold	1100–200 mV vs. NHE	No catalysis observed	pH 4 0.1M citrate
Laccase from *Trametes hirsuta*[20]	Gold nanoporous	700–100 mV	Sigmoidal wave E^{cat} approx. 650 mV	pH 4 0.1M phosphate 20 °C
Laccase from *Trametes hirsuta*[51]	Gold modified aminoethyl	800–0 mV vs. Ag/AgCl	Sigmoidal wave E^{cat} approx. 600 mV	pH 4.5 0.1 citrate
Laccase from *Trametes hirsuta*[51]	Gold modified carboxyethyl	800–0 mV vs. Ag/AgCl	Sigmoidal wave E^{cat} approx. 560 mV	pH 4.5 0.1 citrate
Laccase from *Trametes hirsuta*[75]	Gold modified cysteine, cystamine, aminothiophenol	400–(–600) mV vs Ag/AgCl	Sigmoidal wave E^{cat} approx. 100 mV for aminothiophenol only	pH 5 0.1 M phosphate

In this table E^{cat} is used in order to describe the position of the catalytic wave and corresponds approximately to the halfway point of the steepest part of the wave. Silver/silver chloride reference electrode, $E_{SHE} = E_{Ag/AgCl} + 0.209$ V at 25 °C can be broken, increasing the conformational entropy, which is temperature dependent. In general with increasing temperatures, an increase in surface-bound protein is observed which implies that ΔS binding > 0.[76]

Electrostatic interactions are controlled by pH and ionic strength of the buffered protein solutions.[77] At pH values near the isoelectric point (pI), the number of negative and positive charges from the amino acid residues are equal, resulting in a overall neutrally charged protein (assuming that all charges are +1 or -1). When the pH is lower than the pI, the resulting protein is positively charged, and for higher pH, the protein is negatively charged. When substrate and protein have oppositely charged surfaces, protein attraction is high and results in faster protein adsorption. In contrast, the highest surface densities are seen when the protein is at its isoelectric point.[77] This is due to protein–protein interactions being minimised. Dissolved ions in solutions determine the ionic strength of the solution, therefore, at higher concentrations, a larger dampening of the attractive electrostatics is seen.[78] Electrostatics can also play a role in protein orientation.[79] This is due to a negative or positive protein still retaining regions of oppositely charges areas, which maybe influence overall position the protein adopts on the surface.

1.4.1.2 Protein structure

Proteins can be classified into types of interfacial behaviours when you take into consideration their size, compositions and structural stability. Small and rigid proteins (~15 kDa) tend to have little propensity to undergo structural changes upon adsorption and are classed as hard proteins.[80] Intermediate sized proteins (60 kDa) undergo some degree of conformational restructuring upon surface adsorption. The magnitude of conformational changes depends on the surface, environment conditions, but also on the type of protein domains available. The local composition of amino acids on a protein divide up the domains into areas of hydrophobic/hydrophilic, polar/non-polar and charged/uncharged regions.[72] Due to the complexity of these larger proteins, multiple states of adsorption are available with different adhesion energies, such as a active, relaxed or denatured state.[81-82] On hydrophilic surfaces, proteins will direct their hydrophilic regions towards the surface to minimise surface energy. In the case of hydrophobic surfaces, proteins inner hydrophobic core will expose itself to the surface. The conformational entropy therefore is increased during the adsorption phase, which plays a major driving force in protein adsorption.[82]

1.4.1.3 Surface properties

The properties of a surface can vastly affect the tendency for protein adsorption. Characteristics such as surface energy, polarity, charge and morphology can increase/decease the rates of desorption, the rates of surface spreading, protein orientation or protein unfolding.[82-83] The energy of a surface is a measure of how much the surface will repel or attract surface adsorption for a protein. High surface energy have a greater attractive tendency for protein adsorption, as to minimise the energy; an example of high surface energy materials is bare metals, such as gold or platinum.[84] Polarity of the surface can have two profound effects. As the surface becomes more non-polar, an increase in overall adsorption is observed.[83] A non-polar surface also increases the conformational reorganisation of a protein, due to reducing the unfolding energy barriers.[83] This can explain why generally proteins show an increase tendency to bind to hydrophobic surfaces over hydrophilic.[85]

Surface selection for protein adsorption is generally selected in order to investigate a certain scientific questions. Surfaces for protein adsorption can consist of unmodified substrates such as glass, mica, noble metals or graphite. However it is also extremely common to modify surfaces to give a specific surface functionality. One way of modifying surface is to produce SAMs (Immobilization of MCOs at surfaces, 1.2.2) that can give a monolayer on the surface with a different surface functionality.[86-87] Noble metal such as gold, are easily modified with organothiols to give a range of different end functional groups such as carboxylic acids, amines or methyl-terminated.[88] Another surface modification is to use silanization through organosilanes with specific functional groups such as hydroxyl terminated.[89] These forms of monolayer modifications are normally performed on silica-based materials.

1.4.2 Protein interactions at solid surfaces

In free solutions, a protein can move freely and has no constraints on orientation unless aggregation occurs. However as a protein approaches a surface it will adopt a certain position upon adsorption, which will ultimately determine which parts of the protein are available to the bulk solutions and which parts are surface bound. For proteins with specific bioactivity, the orientation becomes an important issues, as is the case with MCOs.[51] Successful DET is determined by *Mv*BOx adopting a favourable orientation, which promotes facile electron transfer, which in turn is dependent on the distance between the electrode and the primary electron entry point on the enzyme.[21, 68]

Most proteins have either elliptical or rod-like geometry and as long as the protein remains structurally stable, the proteins orientation can normally be described as side-on or end-on. In the end-on state, the protein layer will be thicker and have a higher overall adsorbed mass that the side-on. After protein adsorption, the overall geometries of the protein maybe hindered, although observed work has seen they are still able to alter the orientation if the local surrounding conditions change. For continuous adsorption, protein-

protein interactions become more dominant and can lead to a change in the adopted energy free minimum of the protein layer.[90]

1.4.2.1 Structure of adsorbed layers

Not all protein adsorption results in the same saturated surface coverage. Highly ordered dense monolayers, loosely packed sub–monolayers or even multilayer coverage is possible. Generally, unless near the pI of the protein, electrostatic charge repulsions of individual proteins will resist aggregation that can lead towards multilayer formation. Therefore proteins away from the pI generally form less dense layers. Surface density can also be affected by protein concentration. At low concentrations, full surface coverage takes longer and can there give adsorbing proteins more time to spread on the electrode surface.[91] At higher concentrations there is a higher competition for adsorption sites and adsorption occurs more rapidly. As each protein is more densely packed, further conformational changes are limited i.e., spreading is limited.[82]

1.4.2.2 Protein–protein interactions

Protein–protein interactions normally result in repulsive forces since the overall charges are the same.[92] This forces adlayers to be less than saturated. This is not however strictly true if the protein is near its pI. This has been seen in several studies comparing adsorption at pH values next to, and away from the proteins pI. Zhao et al. showed BSA adsorption on to a silica surface showed a five-fold increase when adsorbed at the pI compared with pH 3 (pI BSA 4.7).[93]

Table 1.5. Weak intermolecular interactions.[94]

Force	Strength (kJ/mol)	Interaction distances (nm)
Van der Waals	0.4-4.0	0.30.6
Hydrogen Bonds	12-30	0.3
Ionic Interactions	20	0.25
Hydrophobic Interactions	<40	varies

Protein–protein interactions forces are however only short range interactions, and do not play a major role until a critical surface coverage forces proteins to interact with each other.[82] Different types of weak intermolecular interactions are given in Table 1.5 along with the strength and distances. The protein-protein interactions therefore depend on the composition of surface groups of each individual protein. Higher rates of desorption have been seen once a critical surface coverage had been met.[95] An opposite cooperative effect can actually increase surface coverage due to protein-protein interactions. Studies have hypothesised cooperative adsorption to be due complex electrostatic fields in the circumference of adsorbed proteins, inducing a kind of electrostatic self assembly.[96]

1.4.2.3 Protein adsorption overshooting

Overshoot refers to a phenomenon that occurs where the adsorption process goes beyond a surface saturation maximum, before returning an expected saturation level, as shown in Figure 1.11A.

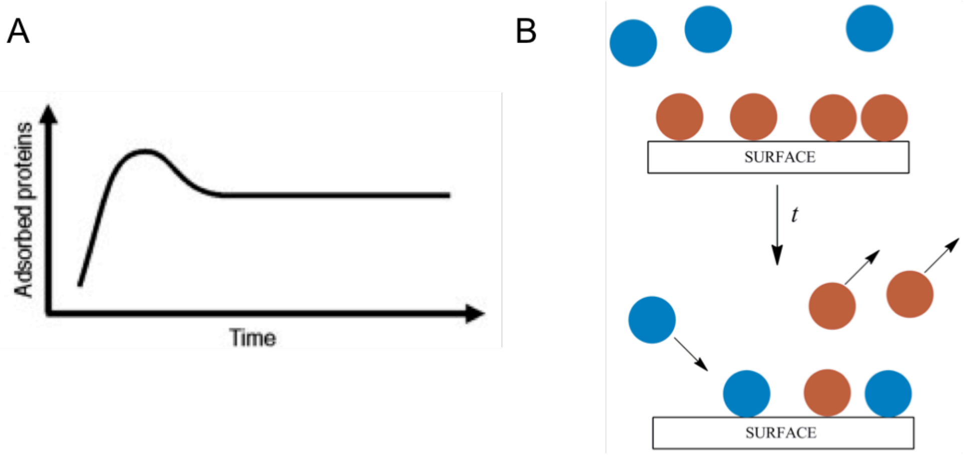

Figure 1.11 Diagram showing the overshoot during adsoption. Panel A shows the overshoot of adsorbed protein before forming a stable layer. Panel B shows the Vroman effect where faster adsorbed protein is being replaced by proteins with a higher surface affinity.

Several studies have observed this process, however it still remains unclear which processes are responsible, as not all proteins exhibit this effect and can be condition dependent. A time-delay model was proposed whereby an overshoot occurs when the surface is temporarily oversaturated and equilibrium is reached later on, through desorption.[97]

Vroman expanded this theory as different properties and shapes of overshoots were being observed.[98] After studying the adsorption of fibrinogen, he noticed that a maximum adsorption was observed initially as the fast adsorbing protein saturated the surface, but then at lower surface coverage was seen as the fibrinogen was replaced by other proteins of higher surface affinity, as shown in Figure 1.11B.[98-99]

1.4.3 Kinetic models for protein adsorption

A general way to try to understand complex protein adsorption is the use of simple kinetic models, which take into account adsorption phenomena such as structural rearrangements, overshooting, cooperative effects, etc. Kinetic models are normally constructed from rate equations. In this section the different adsorption models, which have been developed, are compared, along with their advantage/disadvantages, assumptions and limitations.

1.4.3.1 Langmuir adsorption model

The first such model to be established was the Langmuir adsorption model given as:

$$\frac{\mathrm{d}\theta}{\mathrm{d}t} = k^{\mathrm{on}} C_S \left(\frac{1-\theta}{\theta_{\mathrm{max}}}\right) - k^{\mathrm{off}}\theta \qquad \text{Eq. 1.26}$$

where θ is the frational coverage, θ_{max} is the maximum surface coverage, k^{on} and k^{off} are the on/off rate constants and C_S is the adsorbate concentration.[100] The Langmuir model was originally designed to study adsorbing small gas molecules, which bind reversibly. Therefore several assumptions are made:

1. The surface sites are all flat and can hold only one molecule per site (up to monolayer coverage only)
2. There are no interactions between other adsorbed molecules
3. All sites are equivalent.

This is not normally the case with proteins, since adsorption is generally an irreversible process due to the favourable gain in entropy and interactions between adsorbents do occur and surfaces are never completely flat. This model is still applied today due to its simple formula, however the general consensus is that it inadequately describes protein adsorption.

1.4.3.2 Random sequential adsorption model

The random sequential model develops the Langmuir model further and takes into account more realistic protein adsorption behaviour, most importantly the ability to bind to random surface sites.[101-102] It also assumes adsorbed species act as hard particles and are completely immobilised onto a surface. This creates an exclusion zone around them, which prevents further adsorption. Once a particle has adsorbed, it is fixed in position and therefore an irreversible process. This therefore creates a situation where as the surface coverage increases, the rate of adsorption decreases. The RSA model predicts that adsorption will asymptotically approach a 2D jamming limit, where no further adsorption will take place, given by:[103]

$$M_\infty - M = t^{-\frac{1}{\eta}} \qquad \text{Eq. 1.27}$$

where M_∞ is the jamming limit, η is the number of degrees of freedom. Initially this model give agreed results towards explaining why you see an over estimation in adsorption when using the Langmuir adsorption model.[101] The assumption that the particles are rigid and irreversibly bound doesn't give a complete picture of protein adsorption because it does not account for conformational changes of the protein after adsorption.

1.4.3.3 Three-state model

The idea that proteins can adopt different adsorbed states, such as compact (smaller size than normal), expanded (spreading to a large area), monomer or dimer, side-on or end-on has been suggested in several models.[104] These models tend to separate the two different processes (adsorption and conformation changes) into rate equations where parameters such as concentration or coverage may affect different rate equations differently.

Rabe et al. suggested a recent model, illustrated in Figure 1.12, where there were three states of protein adsorption given as

1. Irreversible initial state that resists desorbing upon rinsing
2. Reversible state, which is only observed after a critical surface coverage
3. Relaxation of a reversible state into a final irreversible state.[104]

Their model was supported by experimental data of adsorbing β–lactoglobulin, which showed transitions for different states at critical surface coverage or time constants and is allowing rate constant for the adsorption and subsequent transformation of different states.

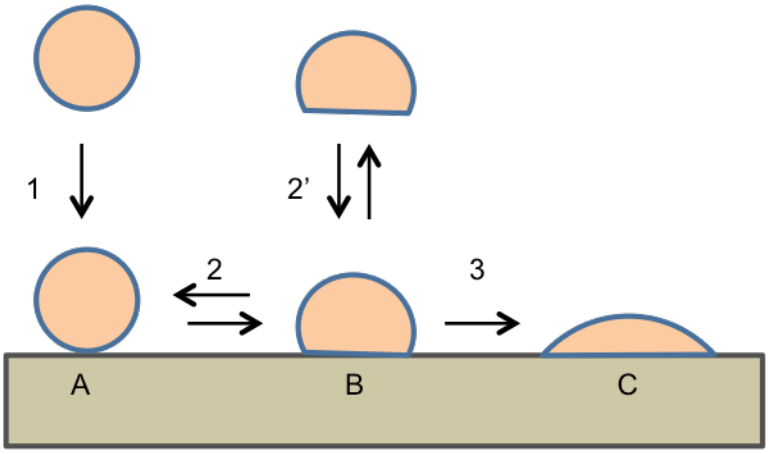

Figure 1.12 Diagram of a three-state model adsorption model. A shows an initial irreversibly bound state that resists desorbing. B shows a reversible state and C shows relaxation from a reversible state into an irreversible sate.

1.5 Quartz crystal microbalance

The quartz crystal microbalance is an acoustic technique that is sensitive to inertial mass. It can measure minute changes in adsorbed mass in solution by a change in frequency of a resonating quartz crystal. This resonance is a direct result of the quartz crystal's piezoelectric properties, which are described in more detail further on. A special addition that can accompany mass detection, it also measuring energy dissipation of the oscillating crystal, relating information about the viscoelastic properties, viscosity changes, structural rearrangements and molecular interactions of the adsorbate.[105]

1.5.1 Background

Pierre and Jacques originally discovered back in 1880 that an external electric field has the ability to induce a mechanical strain in a material. They also showed that changing the cut angle of a crystal, with respects to its crystal structure, meant that the direction of the induced strain could be controlled. Many materials exhibit this piezoelectric effect, such as

Rochelle salt, tourmaline, lithium niobate, etc. The most common material is quartz (crystalline silicon dioxide), because it has low damping, is easily synthesised and comes largely defect free. The mechanical strain can be controlled dependent on the angle cut with respect to the crystalline axes. When quartz crystals are used for mass detection devices, such as the QCM, an AT–cut is used by slicing a quartz rod at an angle of 35°15’ with respect to the crystalline axis, as shown in Figure 1.13.

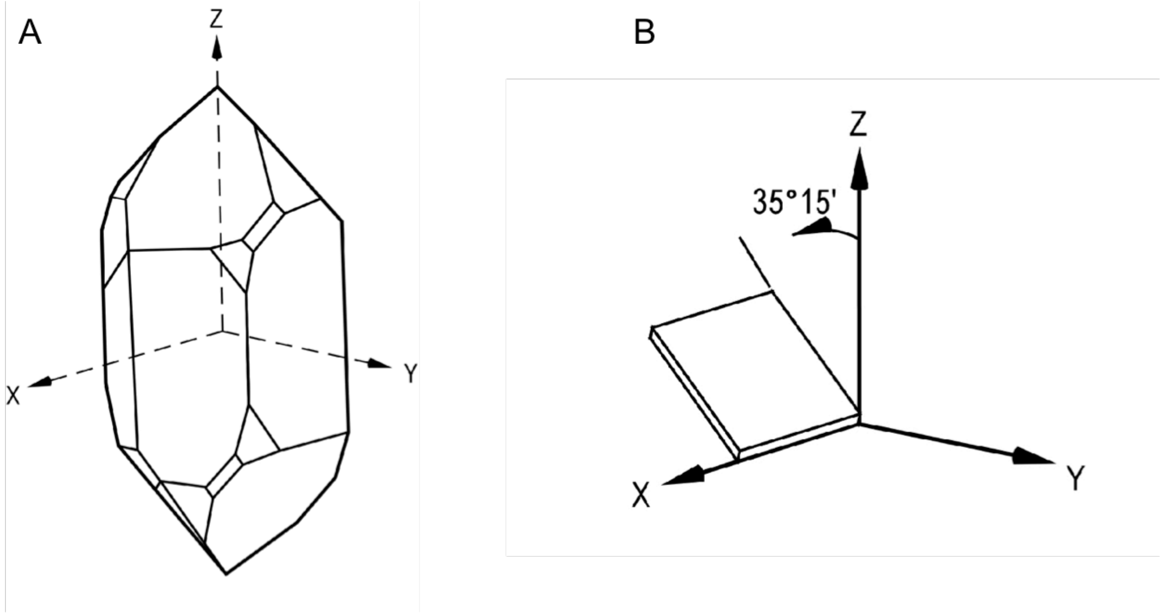

Figure 1.13. Diagram of quartz crystal. Panel A shows a quartz crystal which has been grown in the z plane. Panel B shows the angle required to cut from the z plane for a AT–cut crystal.

This cut is selected due to its near-zero temperature coefficient, which is the proportionality constant relating the oscillation frequency of the crystal in vacuum to the temperature. It also only generates shear mode oscillations.

QCM uses quartz as a piezoelectric resonator with thin layers of gold sputtered or evaporated on to both sides of the crystal, which act as electrical connections to drive the crystal oscillation. When the applied electrical voltage across an AT-cut crystal is alternated, vibrations in two directions are created. The primary vibration runs parallel to the crystal surface. Energy losses of this oscillation are small and mainly due to friction or vibrational dampening. This energy dissipation can yield important information about adsorbed material (Energy dissipation, 1.5.4). The secondary vibration occurs through the thickness of the crystal known as a transverse shear wave and can be seen in Figure 1.14.

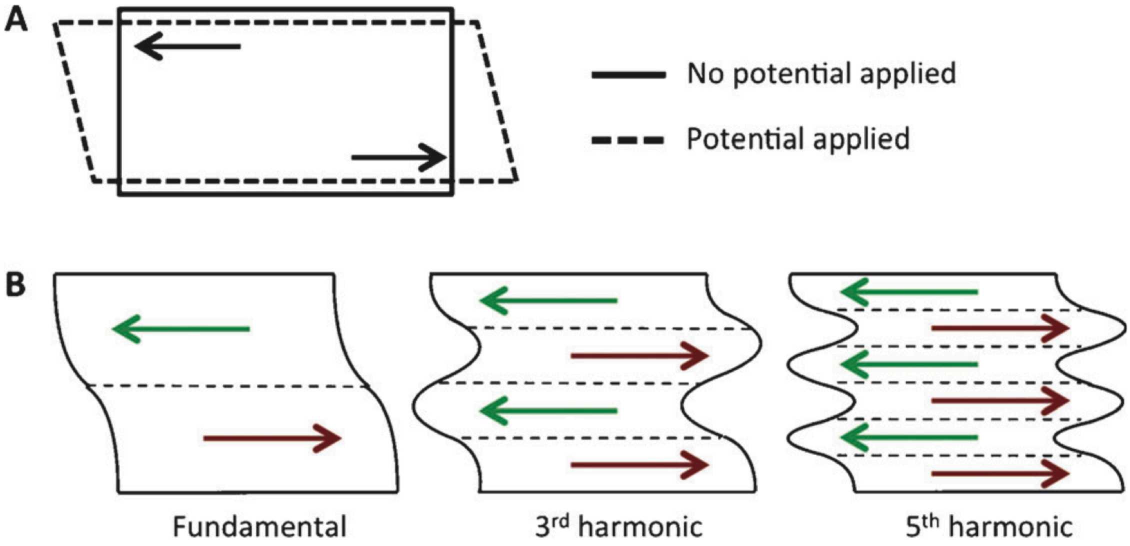

Figure 1.14. Schematic showing the mechanical shear strain caused as a result of the applied potential. Panel A shows the mechanical strain when an potential is applied. Panel B shows the transverse waves propagating though in the thickness direction of the crystal for the fundamental overtone, the 3rd and the 5th harmonic. Figure adapted from ref.[106]

A standing shear wave condition is achieved when the thickness of the crystal is twice the acoustic wavelength. The fundamental frequency (f_0) of the acoustic wave can therefore be given as:

$$f_0 = \frac{v}{2t} \quad \text{Eq. 1.28}$$

where v is the wave velocity ($3.34\ 10^4\ \text{ms}^{-1}$) and t is the thickness of the resonator. Resonance of the wave can occur at integers of half wavelengths of the induced wave, with the oscillation anti nodes at each of the crystal surfaces for increasing harmonics. For a 5 MHz crystal, Eq.1.27 shows the thickness will be 0.33 mm, for a 15 MHz crystal, the thickness will be reduced to 0.11 mm. Thinner crystals with a higher fundamental frequency give greater mass sensitivity but thin crystal are more fragile. A compromise is made by using thicker crystal with a lower fundamental frequency giving stronger crystal, but driving the crystal at higher harmonics for increased sensitivity. Different harmonics have different levels of sensitivity with regards to what they are sampling. Lower harmonics are more sensitive to bulk changes and external mechanical vibrations. Higher harmonics are better for the analysis of mass adsorption, due to a lower penetration depth. This arises as a result of a shear wave being created in the solution above the oscillating crystal. For a Newtonian fluid, the decay length of the wave, δ, is given as:

$$\delta = \sqrt{\frac{\eta_{fluid}}{\pi N f_0 \rho_{fluid}}} \qquad \text{Eq. 1.29}$$

where η_{fluid} is the shear viscosity of the fluid (0.9 MPa.s for water at room temperature), ρ_{fluid} is the density (1×10^3 kg m^{-3}). For the fundamental frequency, the decay length is approximately 0.24 µm. For the seventh harmonic, this decay length drops to 0.09 µm, creating the higher surface sensitivity.[58]

One issue which occurs with using higher harmonics is that overlap between unwanted anharmonic side bands (nodes that are perpendicular to the plane of the resonator) which results in a lower signal-to-noise ratio.[107]

1.5.2 Mass sensitivity

The fundamental frequency (Eq.1.28) shows that as the thickness of the quartz increases, the overall amplitude of the frequency decreases. Therefore as mass is adsorbed, the thickness of the crystal will increase and the new material will act as the antinodes of the acoustic wave. From Eq.1.28, an increase in thickness will result in a decrease in the frequency.[108]

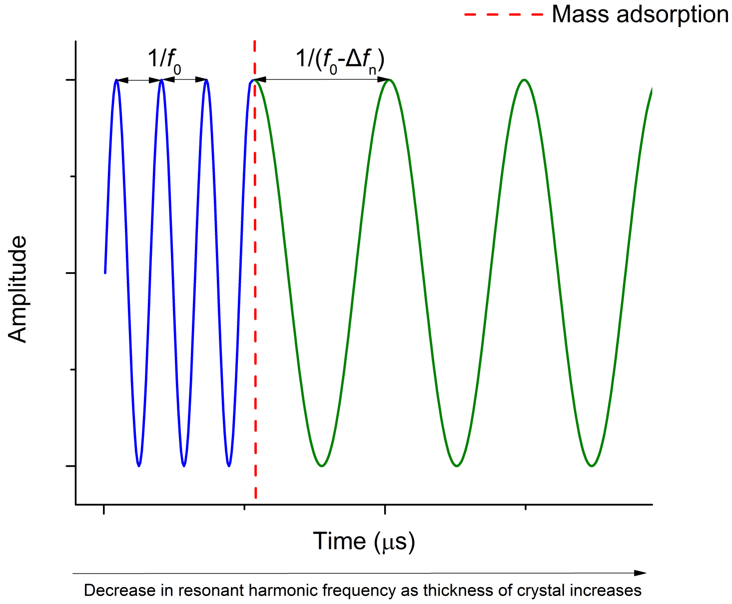

Figure 1.15. Schematic showing the frequency change of the fundamental harmonic when mass is adsorbed to the surface of the quartz crystal

It is this relationship that allows the QCM to act as a mass sensor because the frequency change (Δf) is calculated based on a presumed thickness increase. This gives the mass per area of the crystal (m) is given as:

$$m = t\rho \qquad \text{Eq. 1.30}$$

where ρ is the density of the quartz and t is the thickness. We can then differentiate Eq.1.29 to give:

$$\mathrm{d}f = -\frac{f}{m}\mathrm{d}m \qquad \text{Eq. 1.31}$$

Changing df to Δf we can substitute in m to give the Sauerbrey equation:

$$\Delta f = -\frac{f}{t\rho}\Delta m = -n\frac{2f_0^2}{v\rho} = -n\frac{1}{C}\Delta m \qquad \text{Eq. 1.32}$$

where t and ρ are the thickness and density respectively of the adsorbed mass and n is the harmonic number. For a 5MHz AT-cut quartz crystal, $\rho = 2650$ kg m^{-3} and v is 3.34×10^4 m s^{-1}.

1.5.3 Sauerbrey limitations

When calculating the adsorbed mass using the Sauerbrey equation, three assumptions are made for the calculation to hold true.[108] Because the added mass is seen as an extension of the quartz crystal itself, it is said to need:[109]

1. To be relatively small in comparison to the overall weight of the crystal
2. The adsorbate must be rigidly adsorbed
3. There must be an evenly distributed mass over the entire crystal.

This therefore means, experimentally, the precise measurements of soft biological materials limit the QCMs ability to act as a microbalance. The frequency relationship with the Sauerbrey equation underestimates the adsorption of soft biomolecules due to the shear wave oscillation being dampened. This arises due the nature of biological materials being hydrated and having a flexible structure. For large proteins, conformational changes are possible upon adsorption, which do no longer meet the above criteria of being rigidly adsorbed. A second limitation is the hydration effect. Proteins can have different levels of bound and entrapped water. Therefore the QCM is better suited to measure the dynamic (hydrated) mass of biological systems.[110] For this reason a second parameter is introduced to measure the adsorbate's ability to store mechanical energy from the oscillating crystal, a notion termed its viscoelasticity.[105]

1.5.4 Energy dissipation

When a viscoelastic film adsorbs to a QCM crystal, frictional dissipative losses due to their viscoelastic nature occur. These vibrational losses are termed the 'dissipation' of a system and quantifies the energy loss of a crystal after rapid excitation close to its resonant frequency.[105] The decay rate of the vibrational energy will depend on the dampening of surrounding medium. For small, tightly adsorbed layers, inelastic collisions between molecules are small so the energy dissipation is low. For larger bound soft species, such as proteins, inelastic collisions are a lot more common, and due to bound and trapped water, energy dissipation is much higher.[109, 111] This can allow for dissipation measurements to probe composition of bound species, their hydration levels, their stability and overall structure–function relationship immediately upon adsorption and over time.

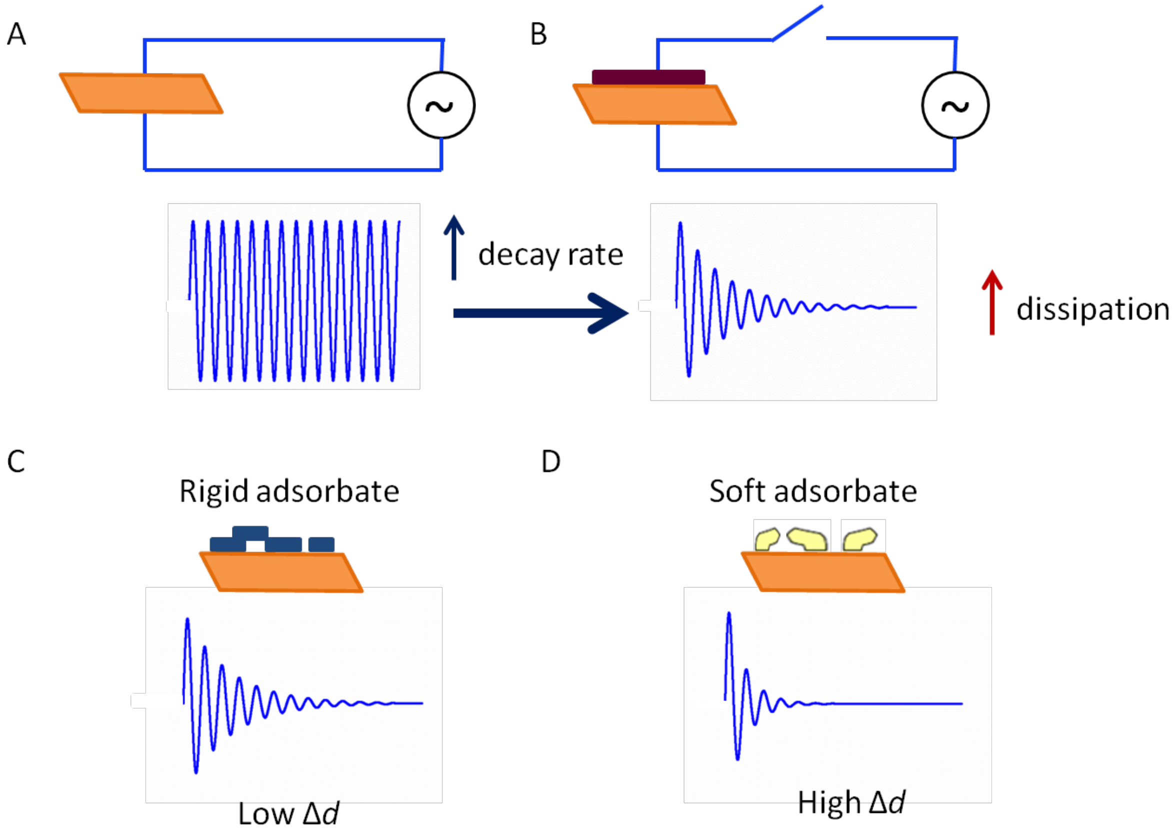

Figure 1.16. Schematic showing how the oscillating frequency decay varies between rigid and soft adsorbed layers. Panel A shows a standard oscillation. Panel B shows the driving force for the oscillation is turned off. The voltage amplitude will decay exponentially with time, with the decay time constant inversely proportional to the dissipation. Panel C shows the oscillation decay for a rigidly adsorbed layer, with a slow decay constant and low dissipation. Panel D shows a soft adsorbed layer with fast decay constant and a high dissipation. Figure adapted from ref.[106]

Dissipation is measured as decay in the amplitude of the oscillating crystal once the driving force has been turned off as shown in Figure 1.16. The amplitude (A) of the oscillation is fitted to an exponentially dampened sinusoidal from the point where the driving force is turned off at $t = 0$, given as:

$$A(t) = A_0 e^{\frac{1}{\tau}} \sin(2\pi f t + \theta) \qquad \text{Eq.1.33}$$

where τ is the decay time constant, f the frequency, θ is the phase angle. The decay constant is related to the energy dissipation, *d*, by

$$d = \frac{1}{\pi f \tau} \qquad \text{Eq. 1.34}$$

which can be expressed dimensionless as

$$d = \frac{E_{\text{Dissipate per cycle}}}{2\pi E_{\text{Stored}}} = \frac{1}{Q} \qquad \text{Eq. 1.35}$$

where *Q* is known as the quality factor, which is a measure of the strength of damping of the resonator oscillation. Resolution of frequency and dissipation in liquids is on the order of ± 0.1 Hz and 1×10^{-7}, respectively, and approximately one order of magnitude better in air or vacuum. Typical *f* and *d* responses for protein adsorption are on the order of tens to hundreds of Hz and tens of ppm respectively.

1.5.5 QCM-D for biomolecular studies

The softer and more viscous the biological species, the more the adsorbed layer does not follow the sensor's oscillation, leading to an increase in inelastic collisions and thus increased dissipation.[109] Considering only analysis of the frequency increase with time, information can be gathered on the rates of adsorption and overall surface coverage. This can identify which models of protein adsorption best fit with a particular system (Kinetic models of protein adsorption, 1.4.3). Considering the energy dissipation of these systems, further investigate of the conformation, orientation and structural evolution can be studies with time. By plotting Δ*d* and Δ*f*, the relationship between conformation and mass changes can be extracted, which allows us to suggest a reaction mechanisms of what is happening on the surface.[111] Monitoring Δ*d* and Δ*f* for different harmonics also allows for modelling of viscoelastic variables, such as surface and bulk viscosity effects, as different harmonics have different penetration distances.[106, 112]

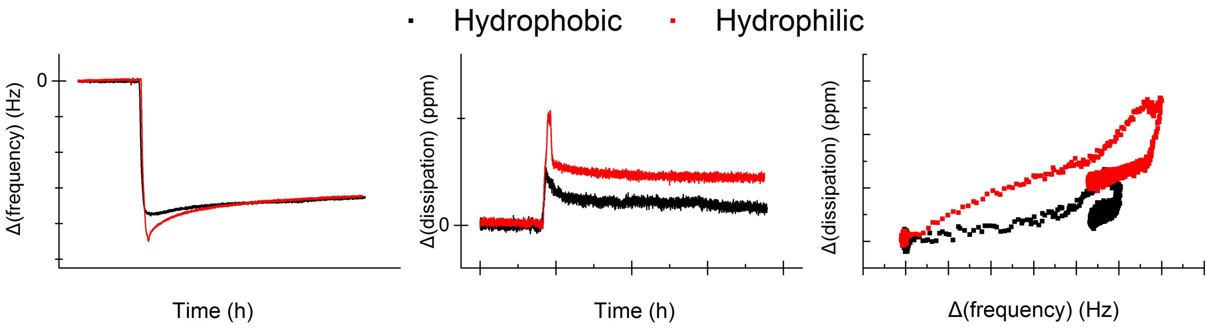

Figure 1.17. Frequency, dissipation and Δ*f* vs. Δ*d* plots for *Mv*BOx adsorbed onto a hydrophobic surface in black, and a hydrophilic surface in red. Panel A shows an irreversibly bound surface for hydrophobic one and a overshoot for the hydrophilic one. Panel B shows lower dissipation on the hydrophobic compared to the hydrophilic. Panel C shows different changes in the Δ*f* vs. Δ*d* gradients for the two different adsorptions.

Figure 1.17 compares two different scenarios for protein adsorption. In red, the hydrophilic surface shows the enzyme adsorption overshoots, giving a increase in magnitude of the frequency maximum response, before returning to a stable layer, this is seen in both the Δ*f* and Δ*d* traces. In black, the hydrophobic surface shows enzyme adsorption occurs in an irreversible form, where a stable layer is formed straight away, albeit with same final mass as the hydrophilic. The dissipation traces show a large overshoot for the hydrophilic surface and a higher final dissipation. This shows that the enzyme is able to remain in a more flexible state. The low dissipation for the hydrophobic layer suggests conformational changes have led to a move rigid layer being formed. The Δ*d* vs. Δ*f* plots show different gradients for the initial adsorption stages followed by different regions which account for overshooting, re-orientation, denaturation or desorption. Therefore it is possible to use the normalised the dissipation response to the change in frequency, and plot Δ*d* vs. Δ*f* to investigate the structural mechanisms of protein adsorption in different situations.

1.5.6 Electrochemical QCM–D

A E-QCM-D allows the simultaneous measurement of mass adsorption, dissipation analysis and electrochemical response, and is able to correlate the effect each has on the other. The first use of a electrochemical cell along with QCM measurements was to measure the frequency response as cadmium was electrodeposited.[113] This was further developed to assess the deposition of a range of metals at different adsorption voltages.[114]

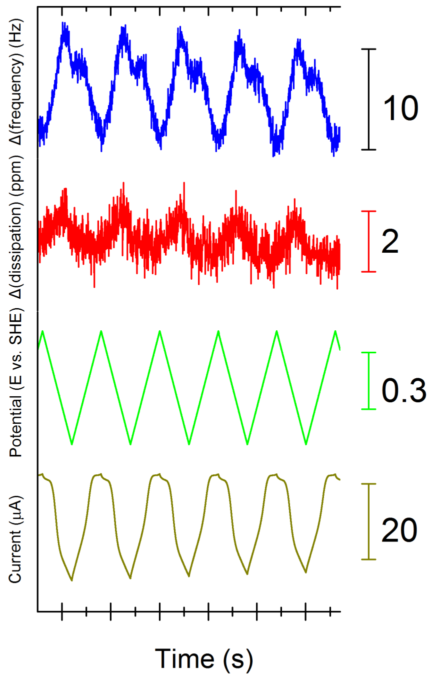

Figure 1.18. E-QCM-D response for an adsorbed layer *Mv*BOx on gold. Traces show how frequency, dissipation and current changes as a function of time in the presence of a cycling potential Conditions: 0.1M sodium phosphate buffer pH 6.0 at 25 °C with continuous O_2 bubbling, 25 mg ml^{-1}, 25 µl *Mv*BOx sample volume, seventh harmonic shown. Flow rate 0.1 ml min^{-1}

Figure 1.18 shows how frequency, dissipation and current changes with time in the presence of an cycling potential (CV experiment). In this case the E-QCM-D showed how the cycling of potential (producing a reductive current in this case) from an adsorbed *Mv*BOx layer as well as disturbing the frequency and dissipation traces due to the applied electric field.

1.5.6.1 E–QCM–D in redox enzyme catalysis

The use of the E–QCM–D technique has several advantages over other surface techniques used to measure protein adsorption. The most prominent is the ability to measure bioelectrocatalytic activity as a function of adsorbed mass and enzyme adlayer viscoelasticity. Surface orientation and conformational changes can also be investigated as a function of biocatalytic efficiency. It also allows the more fundamental electron transfer mechanisms of biomolecules to be probed. Such studies have investigated the use of spaces to allow for electron hopping and the ability to fine-tune DET length dependence.[115]

The E–QCM–D also allows for protein adsorption onto different functionalised surfaces via chemical modification (Paper I, 3, Paper II, 4). Allowing the ability to measure surface adsorption and biocatalytic efficiency that can be correlated to protein–surface interactions.

1.6 Dual polarisation interferometry

Another technique for measuring molecular systems at the solid/liquid interface is dual polarisation interferometry (DPI). The function of any biomolecule adsorbate layer is ultimately governed by its own structure, the environment under which it adsorbs, and molecular arrangement.[80] This has created an increasing need for sensitive equipment, which has the ability to measure important parameters such as the refractive index (RI), thickness, mass and density accurately. These parameters are important as it can give an understanding to how conformational changes occur after adsorption. DPI is a surface analytical optical technique that can be used complementary to QCM as it provides information on molecular dimensions and surface packing, amount of surface loading, dry mass amounts and adsorbate stoichiometry[116]. The measured dry mass is directly complimentary to the QCM, which measures the hydrated mass of the adsorbed layers.

1.6.1 Background

An interferometer is a device with two optical paths that can detect minute changes in optical path length affected by an optical field passing through a sensing waveguide. Typical optical interferometers are configured using the Mach–Zehnder format, by etching waveguide regions in the top surface of an optical dielectric stack.[117] DPI uses a simplified slab waveguide configuration where two waveguides (sensing and reference) are stacked on top of each other.[118] The waveguide is made up of five thin films of silicon oxynitride stacked on top of a silicon wafer as shown in Figure 1.19.

The layers alternate in low/high RI, starting with the bottom cladding layer. The reference layer is surrounded by two cladding layers, which effectively shield it from the influence of the sensing waveguide. The sensing waveguide has a cladding layer below but has an exposed area above it, which has been etched away so the sensing waveguides surface can interacts with the sample. The length of the etched away cladding top layer determines the interaction length of the sensing waveguide with the sample.

Coherent light broadly illuminates the end face of the device as shown in Figure 1.19 A, which excites all modes equally (guide and radiation) into the structure, however only the guide modes of light propagate for more than 50 µm. As the light exits the sensor, the light diffracts into free space and due to the close proximity of the sensing and reference waveguide (roughly 4 µm), the diffracted light generates Young's interference fringes in the far-field only a few millimetres from the end of the waveguide.[119] A sample solution is flowed over the top of the waveguide, allowing for surface contact of the protein with the sensing surface (Figure 1.19 B). As molecules adsorb and desorb, changes in the optical properties of the sensing waveguide are detected by either phase changes or light adsorption, that is. This translates into changes in both intensity and phase of the interference patterns (Figure 1.19 C).

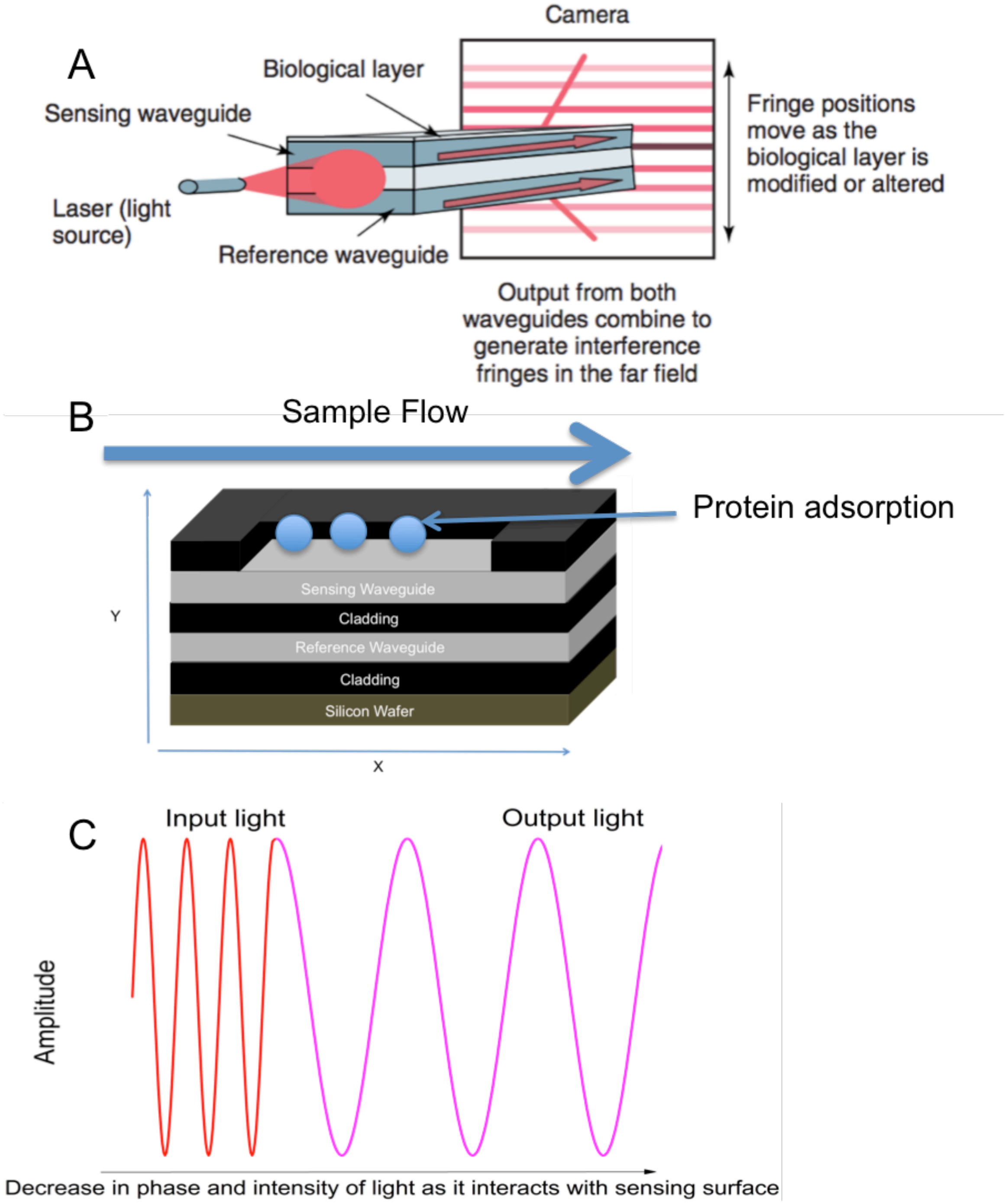

Figure 1.19. Schematic showing the DPI set up. Panel A shows a sensor being illuminated with laser light, which produce youngs fringe patterns on a camera as light propagates from the end of the chip. Panel B shows the layers of the waveguide and the interaction of the adsorbate with the sensing surface. Panel C shows the phase and intensity change of the input light from the sensing waveguide after interaction with the adsorbed protein. Image adapted from ref.[119]

DPI design allows for the propagation of two polarisations of light, transelectric (TE$_0$ single mode) and transmagnetic (TM$_0$ single mode), through both the reference and sensing waveguides (Figure 1.20). This allows for two optical phase change measurements to be made by switching the polarisation between the two on a 2 ms cycle. In order to measure a direct phase change, the relative phase position of both TE_0 and TM_0 are continuously monitored.

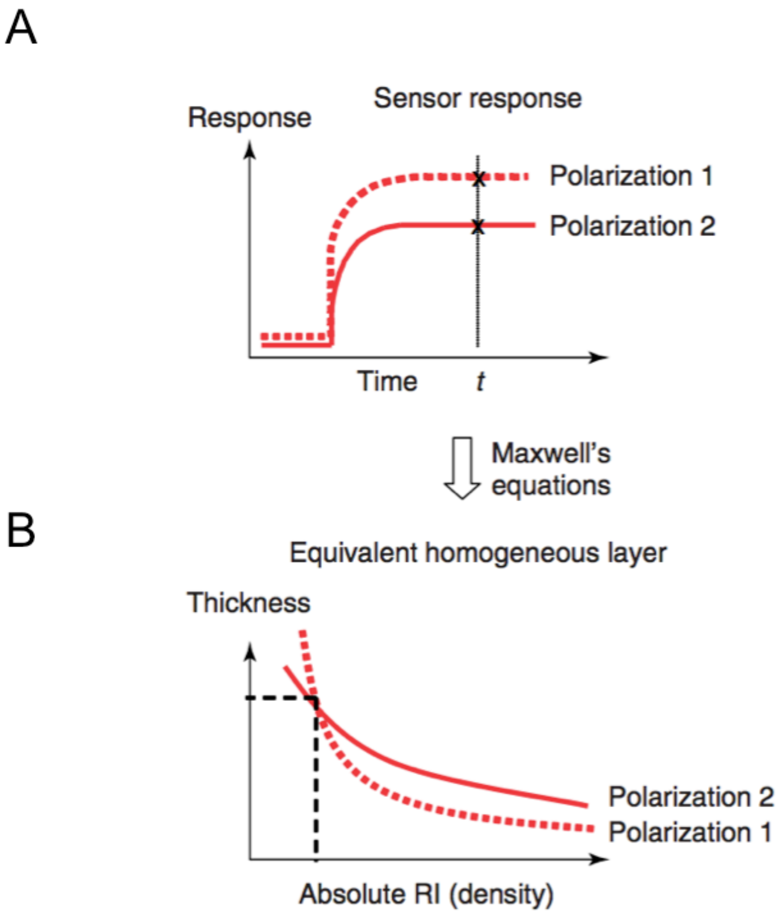

Figure 1.20 Phase change difference for both TE and TM polarisations of light. Panel A shows the response of the two polarisations with the addition of an adsorbate onto the sensing waveguide. Panel B shows resolved data for the two polarisations give one solution.[119]

By performing a numerical Fourier transform of the Young's fringe patterns, phase and contrast can be calculated simultaneously. The phase change is calculated based on the vertical position change of interference fringes as seen in Figure 1.21A.

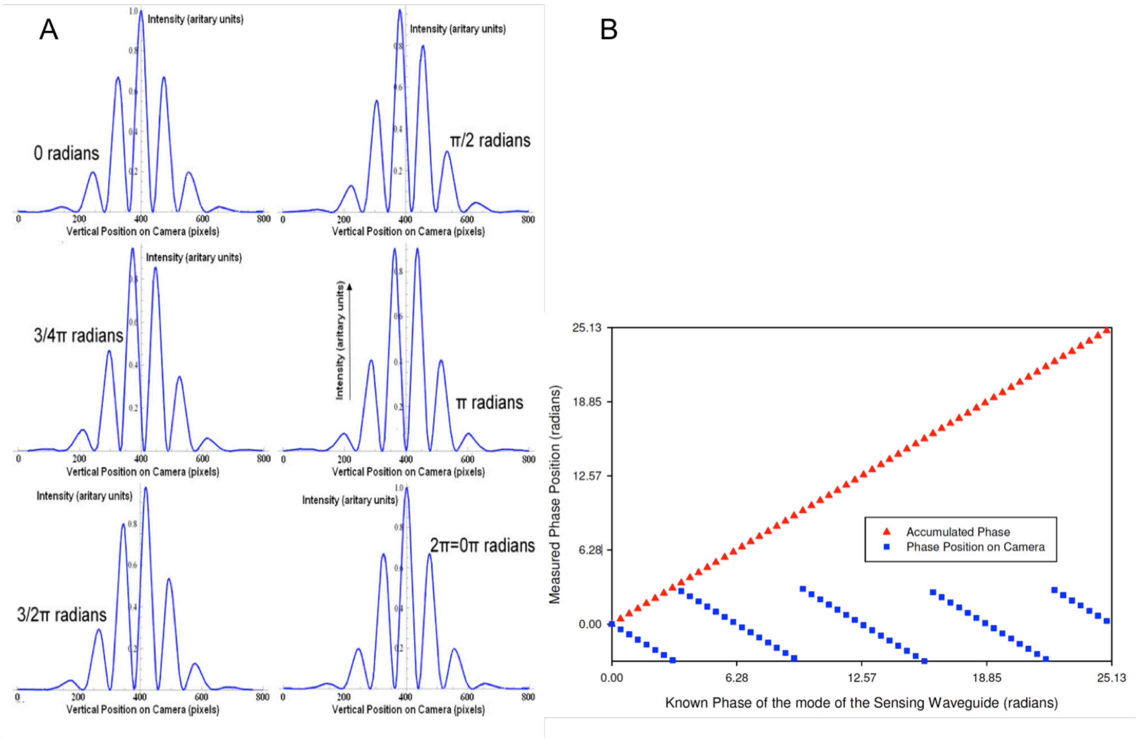

Figure 1.21. DPI interference pattern for phase changes. Panel A shows different phase positions as the DPI cycles through 2π radians. Panel B shows the accumulation of the phase change as the interference pattern repeats itself. Image adapted from ref.[120]

As the fringe patterns cycle through 2π radians before returning to their original positions, the phase change needs to be constantly tracked and a total phase change accumulated based on the number of cycles.

Constructive interference occurs when the two light sources are said to be in phase by:

$$\psi_S - \psi_R = \frac{2\pi dx}{\lambda L} = 2\pi n$$

Eq. 1.36

where ψ_S and ψ_R are the phase of the sensing and reference waves respectively, *d* is the distance separating the reference and sensing waveguides, *n* is an integer and *x* is the fringe spacing. λ represents the wavelength of the illumination light (helium–neon laser, 632.6 nm) and *L* is the distance of end of the waveguide to the detection camera. As the light propagates through the waveguide, an evanescent field is produced above and below, which decays exponentially from the surface normal to the direction of light. This evanescent wave interacts with the sample and is what is responsible for changing the effective RI of the sensing waveguide, leading to a phase change, given by $\Delta\psi$. This phase change alters the interference fringe patterns by Δx given by:

$$\Delta x = \frac{\lambda L}{2\pi d}\Delta\psi = \frac{x\Delta\psi}{2\pi} \qquad \text{Eq.1.37}$$

This fringe shift allows the effective refractive index of the sensing waveguide to be solved using Maxwell's equations. Maxwell's equations allow for the production and interrelation of electric fields and magnetic fields in a material.[80] This allows a complete description of how different modes propagate in a dielectric waveguide. Once the equations are solved, a set of all possible solutions for the layer is calculated for both the TE_0 and TM_0. These possible solutions discount any high order modes because the structure of the DPI does not support them, so only the zero order modes are used.[119] To determine the optical and geometrical properties of an adsorbed layer, an iterative approach is taken. The thickness, RI, and extinction coefficient of the deposited material is adjusted until the guided modes within the sensing waveguide produce propagation constants that lead to the experimentally determined phase and contrast changes in both the TE_0 and TM_0. This is represented graphically in Figure 1.19B, a continuous range of thickness and RI values are calculated, but only one pair of solutions exist for both mode simultaneously.

1.6.2 Data analysis

The RI increments, given by d*n*/d*c* are consistent for proteins allowing for the determination of the density and mass of the adsorbed species given by:

$$\rho_L = \frac{\rho_P(n_L - n_S)}{(n_P - n_S)} \qquad \text{Eq.1.38}$$

$$m_L = \rho_L \tau_L \qquad \text{Eq. 1.39}$$

where ρ_L is the density of the layer, ρ_P is the density of the protein, n_L is the RI of the layer, n_S is the RI of the solution, n_p is the RI of protein, m_L is the mass loading per unit area of the layer and $\tau_L$is the thickness of the adsorbed species. This can then allow for the molecular footprint (area of one molecule) to be calculated using:

$$A = \frac{M_W}{N_A m_L} \qquad \text{Eq. 1.40}$$

where A is the area per molecule, M_W is the protein molecular weight and N_A is Avogadro's number. The volume fraction of the adsorbed protein, ϕ_p is given by:

$$\phi_p = \frac{n_L^2 - n_S^2}{n_p^2 - n_S^2} \qquad \text{Eq.1.41}$$

Once the thickness and RI are resolved the density, mass molecular footprint and volume fraction are calculated. Assumptions about protein structure, orientation, stability, surface interactions, and protein–protein interactions can start to be inferred.

1.6.3 DPI protein adsorption studies

Since DPI was introduced in 2004, it has seen increasing interest in many biological solid/liquid interface studies. For instance, DPI has been used to study the interactions between adsorbed antigens and antibodies to give information on dissociation constants and binding stoichiometry.[121] Protein displacement studies using DNA were carried out showing how shorter DNA strands can be reversibly adsorbed, and displaced when longer DNA was introduced. A direct correlation between DNA length and displacement efficiency could be observed.[122]

Studies have shown the effects of environmental conditions such as pH and protein concentration on the adsorption of globular proteins to DPI sensors. Freeman et al. studied lysozyme adsorption at pH 4 and pH 7 with increasing concentrations of 0.03 to 4.0 g dm-^{3}.[123] At low pH, the increasing concentration changed thickness from 14–43Å and mass from 0.21 to 2.36 mg m^{-2}. At this pH there was a large deformation of the monolayer at low concentrations and almost all of the adsorbed protein took on a side-on adsorption at high concentrations. At pH 7, initial adsorption again indicated side–on orientation, but resulted in bilayer formation.

Globular protein adsorption models have been investigated using DPI alongside neutron reflectivity.[103] In this study BSA adsorption using the standard Langmuir adsorption isotherm was compared to a random sequential model using experimental data. DPI showed that until a critical surface coverage was exceeded, adsorption followed Langmuir adsorption. However above a concentration of 0.5 mg ml^{-1}, the RSA model give a better fit. This however is not too surprising, given as the Langmuir adsorption isotherm was not intended for use of soft materials (Langmuir adsorption model, 1.4.3.1), nor is RSA fully suited for protein adsorption. DPI measurements on surface coverage and thickness were also compared with NR and give good agreement over larger concentration ranges.

1.7 Other experimental techniques

There are many experimental approaches for studying protein adsorption onto surfaces each with there own advantages. Below is a selection of complimentary techniques that can compliment that of E–QCM–D and DPI.

1.7.1 Ellipsometry

Ellipsometry is an optical technique that measures the changes in polarisation of an incident light, which is reflected onto a sample. It allows thickness measurements of an adsorbed layer to an accuracy of 1 nm. In ellipsometry the RI is not calculated and is assumed to be the same of the bulk solution, for this reason it is not as sensitive as DPI, which give resolutions to 1 Å.[124-125]

1.7.2 Surface plasmon resonance

Surface plasmon resonance (SPR) measures the interaction of proteins as well as adsorption kinetics. Light from a single polarisation is used to create an electron charge density waves (surface plasmon) that interact with adsorbed molecules on a surface (typically gold or silver). It has a accuracy of 0.1– 1 ng cm^2.[126-127] However, one of SPR main restrictions is cannot measure both the thickness and the refractive index simultaneously.

1.7.3 Neutron reflectometry

Neutron reflectometry (NR) shows resolution comparable to X-ray reflection. Detailed analysis of a proteins film's structure can be obtain through the use of deuterium to enhance the overall scattering contrast. Two disadvantages to NR is the need for travel to a synchrotron where beam time is limited, and the sample size required is normally large.

1.7.4 Atomic force microscopy

In atomic force microscopy (AFM), information is obtained by scanning a small probe across a samples surface. As the probe interacts with the surface, a laser light is reflected of the back of the cantilever probe which can give information on the topography, chemical properties and tip–protein attraction forces. Lateral resolution of < 1 nm and height resolution of < 1 Å can be obtained. In protein studies, distribution, conformation and degree of denaturation can be obtained.[89, 128]

1.7.5 Optical waveguide lightmode spectroscopy

Optical waveguide lightmode spectroscopy (OWLS) uses an optical grating for the coupling of a He–Ne laser into a planar waveguide. Both transverse electric (TE) and transverse magnetic (TM) modes are used and allow for the measurements of thickness and refractive index of thin layers to be obtained.[125, 129] Experimental set up limits the rate at which data collection can be performed (typically 2 seconds), which is slower that DPI. Typically the mechanical setup and temperature control requirement also limits the achievable sensitivity of the measurement.[116]

Chapter 2

Materials and Methods

2 Materials and Methods

2.1 Materials

2.1.1 Chemicals

All chemicals are listed in Table 2.1 and were used as received without further purification. Water was purified via reverse osmosis and ion exchange to a resistivity of 18.2 MΩ cm at 25 °C using a MilliQ water purifier.

Table 2.1. List of chemicals used, supplier and specification

Chemical	**Supplier**	**Purity**
1-heptanethiol	Sigma Aldrich	98 %
1-propanethiol	Sigma Aldrich	99 %
2-2’-azino-bis(3-ethylbenzonthiasonline-6-sulfonic acid) diammonium salt (ABTS)	Sigma Aldrich	
2-aminoethanethiol hydrochloride	Acros Organics	98 %
3-(trihydroxysilyl)propane-1-sulfonic acid 35% in water	Fluorochem	
3-aminopropyltriethoxysilane	Acros Organics	99 %
3-mercaptopropionic acid (3MPA)	Fluka	> 99 %
6-aminohexanethiol hydrochloride	Sigma Aldrich	>99%
6-mercaptophexanoic acid (6MHA)	Fluka	>99%
buffer solutions pH 4 (phthalate)	Fisher	
buffer solutions pH 7 (phosphate)	Fisher	
dihydrogen orthophosphate dihydrate	Fisher	99.0–101.0 %
disodium hydrogen orthophosphate anhydrous	Fisher	> 99.5 %
hexamethyldisilazane	Sigma Aldrich	> 99 %
hydrochloric acid	Fisher	37 %
hydrogen peroxide	Scientific Laboratory Supplies	(30% w/v)
sulfuric acid	Fisher	>95 %
toluene anhydrous	Alfa Aesar	99.8 %
trimethoxypropylsilane	Sigma Aldrich	97 %
tris(carboxyethyl)phosphine hydrochloride (TCEP)	Sigma Aldrich	> 98 %

2.1.2 Buffers

Buffers were made up using respective solutions of their acid and bases. Individual buffers were titrated to desired pH at 25 °C and recorded using an Accumet 950 pH meter (Fisher Scientific). All buffers were stored at 4 °C. For dual polarisation interferometry (DPI), buffers were passed through 0.44 µm pore filters and degassed via vacuum sonication to remove air bubbles.

2.2 Bilirubin oxidase purification

Bilirubin oxidase from *Myrothecium verrucaria (Mv*BOx) was purchased from Amano Enzyme (Chipping Norton). Lyophilised *Mv*BOx powder was dissolved in 0.1 M sodium phosphate buffer pH 6.0 at 4 °C. The solution was centrifuged through a polyethersulfone membrane to removed small molecular-weight contaminants (Vivaspin, GE healthcare, 30 kDa MWCO). The protein concentration of the filtrate was determined from its UV-visible absorption, measured with a Nanodrop (Thermo Scientific), based on A_{280} measured from 2 µl aliquots and using $\varepsilon_{280\text{ nm}} = 9.52 \times 10^4$ M^{-1} cm^{-1}, calculated from the enzyme amino acid sequence by the online software ProtParam Expasy Proteomics Server (http://www.expasy.ch/tools/protparam.html).[130] A full UV spectrum was also taken of every new batch of protein. Bovine serum albumin (BSA) was dissolved in 0.1 M sodium phosphate pH 6.0 concentration was calculated using a Bradford assay.

2.2.1 ABTS assay

Activity of purified enzyme was measured using an ABTS assay. The formation of the cation, ABTS^{2-} formed after oxidation (colourless to green solution), allows UV adsorption to measure the rate of oxidation.

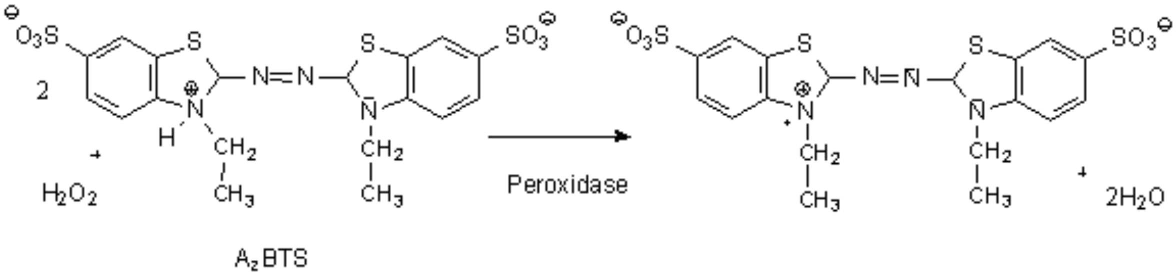

Figure 2.1 Oxidation of ABTS to generate the radical ABTS^{-} cation

ABTS 1 mM solutions were prepared by dissolving an ABTS (10 mg) tablet into 18.2 ml deionised water. Aliquots of enzyme (~0.005 mg ml^{-1}) were made in 0.1 M sodium phosphate buffer pH 6 with 1mM ABTS (300 µl) at 25 °C. The solution was divided up into 1 ml cryovials and stored in a vapour phase liquid nitrogen dewar. If A_{410} > 0.16 cm^{-1} the ABTS solution was discarded. Aliquots of enzyme (~0.005 mg ml^{-1}) 1 ml solutions were made in 0.1 M sodium phosphate buffer pH 6 with 1mM ABTS (300 µl) at 25 °C.

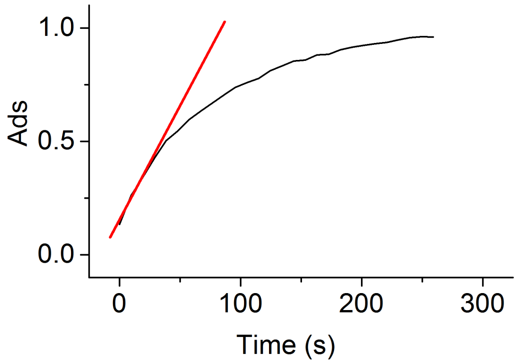

Figure 2.1. Typical plot of ABTS assay with increasing adsorption at 410 nm. Maximum slope was used to calculate catalytic turnover for the enzyme. Conditions 0.005 mg ml^{-1} *Mv*BOx 1 mM ABTS. Adsorption recorded every 5 seconds for 5 minutes.

Concentrations of oxidised ABTS were measured in a 96-well plate reader at 410 nm ($\varepsilon = 3.6 \times 10^4$ cm^{-1} M^{-1}).[131] One unit of enzyme activity (U) is given as the amount of enzyme required to oxidise 1 µmol ABTS min^{-1}. Concentrations were monitored for 5 min, at 410 nm every 5 seconds and the maximum slope was used to record activity as shown in Figure 2.1. The pathlength was calculated from the volume and area of plate well used. Concentrations of ABTS were in excess so that the concentration can be assumed to be constant. The calculated activity of the sample of *Mv*BOx shown in Figure 2.1 is 1280 U mg^{-1}.

2.2.2 Gel chromatography

Sodium dodecyl sulfate-polyacrylamide gel electrophoresis (SDS-PAGE) was used to test protein purification and storage stability of *Mv*BOx based on molecular weight separation against a known weight ladder. Three batches of *Mv*BOx were compared and shown in Figure 2.2. Batch A is freshly purified, batch B is protein stored in liquid nitrogen vapor phase for 3 months, batch C is freshly purified enzyme from an old batch stored at 4 °C for 12 months. *Mv*BOx, 20 µl 2.5 mg ml^{-1} was mixed with 20 µl Laemmli buffer (solution contains 4% SDS, 20% glycerol, 10% 2-mercaptoethanol, 0.004% bromphenol blue and 0.125 M Tris HCl, pH approx. 6.8) and heated to 100 °C for 5 minutes. As a result, the protein denatures and each subunit of the protein takes on a negative charge. This allows for the subunits to be separated based on size.

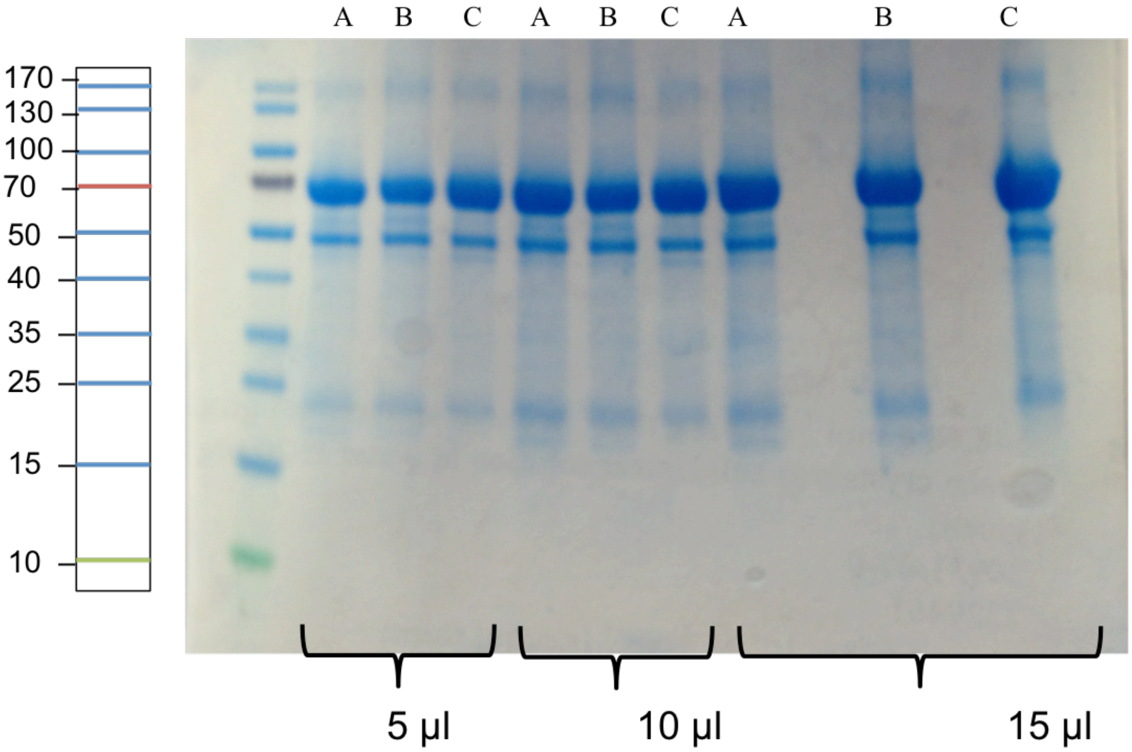

Figure 2.2. SDS page showing different batches of *Mv*BOx A-C. Batch A is freshly purified, batch B is protein stored in liquid nitrogen vapour phase for 3 months, batch C is freshly purified enzyme from an old batch stored at 4 °C for 12 months. Each batch has 3 increasing volumes of 1.25 mg ml^{-1} to obtain correct loading. The prestain ladder indicates molecular weight cut offs from 10–70 kDa.

A PageRuler prestain protein ladder (Thermo Scientific No.26616) was used with molecular weight stains for 10–170 kDa. Figure 2.2 shows several bands from 23–170 kDa which correspond to breaks in the monomeric protein. The expected molecular weight for *Mv*BOx is 68 kDa, which shows an intense band for all three batches. Therefore the different storage for the three batches has not been shown to alter the structure of the proteins in a way that can be detected by SDS-PAGE.

2.3 Quartz crystal microbalance

2.3.1 Operation

The quartz crystal microbalance (QCM) model used was a Q-Sense E1 (Biolin Scientific). For QCM with dissipation monitoring (QCM-D), a regular QFM 401 flow module (total internal volume of 140 µl, 40 µl sample chamber) is used, shown in Figure 2.3A. The wettable materials which were exposed other than the sensor surfaces was either titanium or Viton. The measured temperature of the QCM cell was held constant ± 10 mK. Buffer entered and exited the flow module through 0.5 mm Teflon tubing. Buffer was stored in a sealed glass bottle as shown in Figure 2.3B. Buffer was flowed through the cell using a peristaltic pump set at an arbitrary value of 2 (ca.0.1 ml min^{-1}).

The E-QCM-D is shown in Figure 2.3B, with red arrows indicating flow direction of the buffer. For electrochemical QCM with dissipation monitoring (E-QCM-D), a modified QEM 401 flow module, with a replaced internal flow unit made from poly(oxomethylene) (Delrin) was used, with a sample chamber volume of 100 µl. This modification by a previous student improves the internal fluidic flow path and wettability, in addition to housing a 5.7 mm OD reference electrode (Ag|AgCl|3M NaCl reference electrode, BASi RE-6, $E_{\mathrm{SHE}} = E_{\mathrm{ref}} + 0.209$ V) as shown in Figure 2.4.[58, 132] This modification removed poor electrochemical communication between the reference and the counter electrode which was a constant source of failure with the standard microreference, rather than the new fitted regular sized reference.[132] Both cells have the ability to measure either flowing or stagnant liquids.

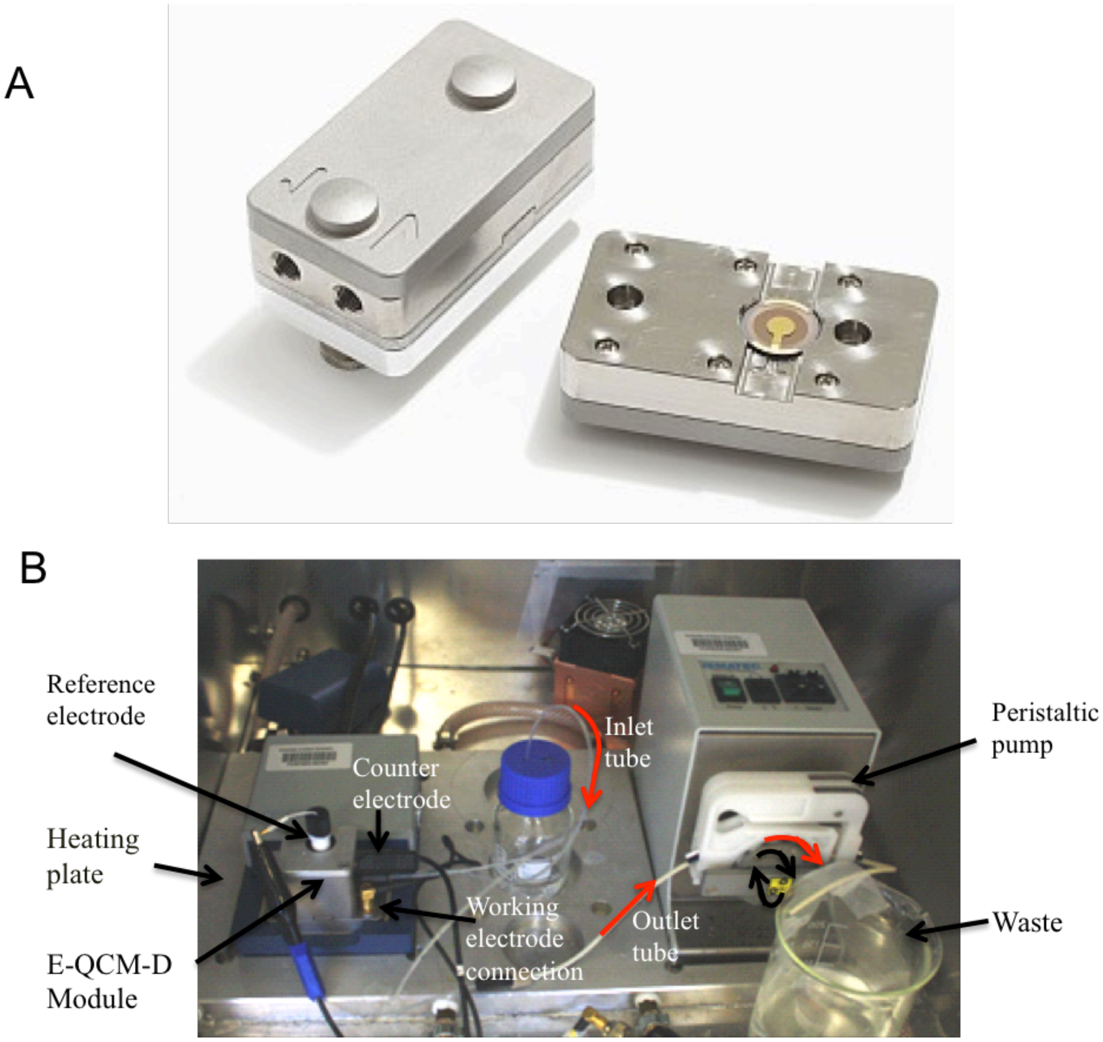

Figure 2.3. Images of QCM flow module and experimnetal set up. Panel A shows a standard QFM 401 flow module, Panel B shows a typical QCM set up with a modified E-QCM-D flow module inside a metal house unit.[133-134]

The QCM is housed in a temperature-controlled insulated cupboard, with a fan to help regulate the temperature. Temperature stability of both instruments is ± 0.02 °C.[134] Samples are heated on an aluminum plate to maintain a constant temperature, controlled by a water recirculation pump set to 25 °C.

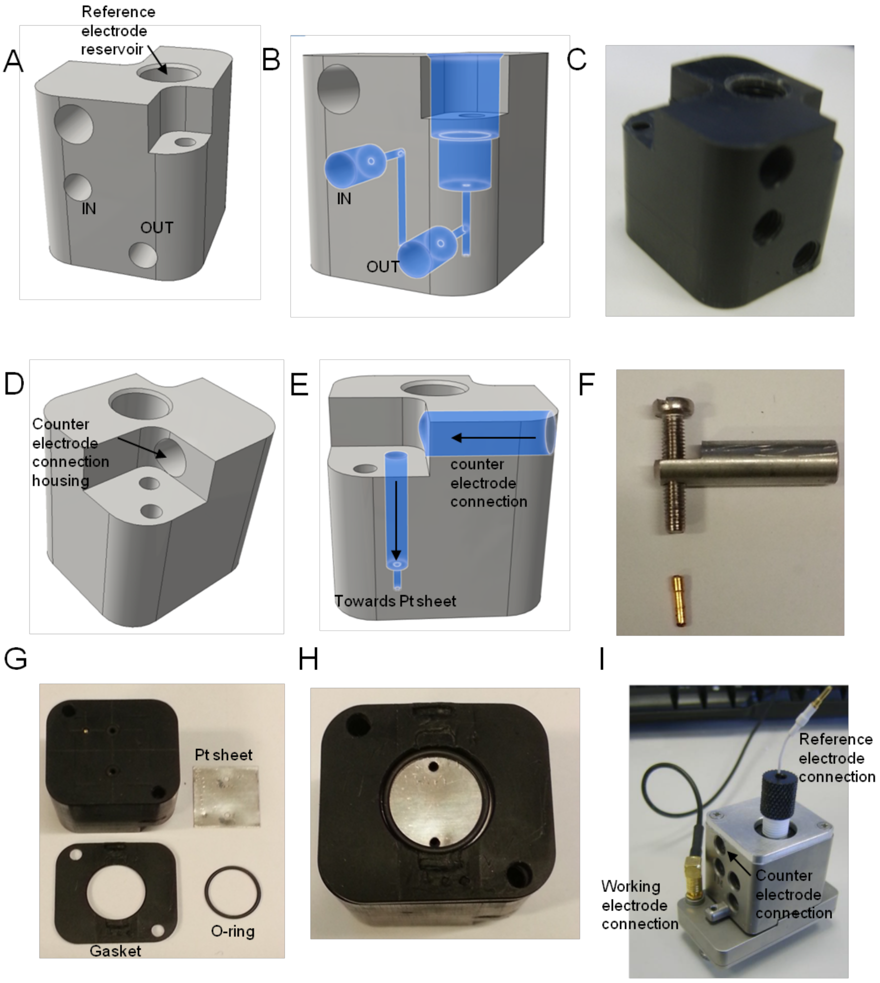

Figure 2.4. Images showing modification of E-QCM-D flow module. Panel A shows the side view of the redesigned cell detailing the fluid inlet and outlet holes along with the new reference electrode reservoir at the top of the module. Panel B shows the fluid flow path for the inlet and outlet and how the new reference reservoir maintains an ionic connection with the fluid. Panel C shows a photograph of the real module machined out of delrin. Panel D shows the opposite side view to panel A with an arrow indicating where the counter electrode connection is housed. Panel E shows the upper counter electrode housing where the metal contact sits and the lower housing which contains the screw and gold contact pin, which makes contact with the platinum sheet. Panel F shows how the counter electrode connection is constructed. Panel G shows the individual components for assembling the cell including the platinum sheet which is positioned to align the two holes above the inlet and outlet holes. This allows fluid to pass over the platinum sheet. The gasket sits on top of the sheet and an O-ring is placed in the spacing (shown in Panel H). Panel I shows an assembled module with working electrode and reference electrode connections in place. The pin for the counter electrode from the potentiostat fits in the hole marked. The images in A, B, D and E were designed using AutoCAD 2013 and Inventor Fusion 2013. Images designed by Kulveer Singh, previous Ph.D student.[132]

The thermal coupling between the flow modules and QCP101 chamber platform was improved with thermal conducting paste (RS components, RS 217-3835). Fluidic driving force is provided by a peristaltic pump (Ismatech), which is controlled via a windows interface driving a LabJack U3-HV ADC/DAC.

Figure 2.4 describes the housing unit for the modified E-QCM-D flow module. The counter electrode shown in Figure 2.4G is 0.2 mm thick, 2.25 cm^2 square platinum plate running parallel to the sensor surface as the counter electrode. The distance between the working electrode and counter electrode was 0.7–0.8 mm; the distance between working and reference electrode was 0.9–1.0 mm.

2.3.2 Sensors

QCM sensors were made from AT–cut crystals with a fundamental frequency of 4.95 ± 0.05 MHz (Q-sense). The crystal was coated in a thin homogeneous film with a Ti adhesion layer between crystal and surface material. Each sensor has an outer diameter of 14 mm, exposed area of 10.1 mm diameter, a thickness of 0.3 mm and wraparound electrodes, as shown in Figure 2.5.

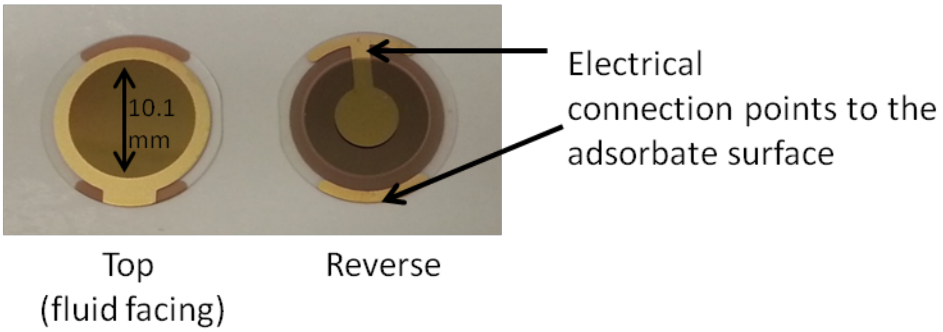

Figure 2.5. QCM gold–coated AT–cut sensor with diameter dimensions and wraparound electrical connection points

The sensor surfaces are polished to give r.m.s. surface roughness of less than 3 nm.[58] All measurements have the 3^{rd}, 5^{th}, 7^{th} and 9^{th} harmonic recorded. The 3^{rd} harmonic was used specifically for calibration of the chip to ensure correct mounting and wetting. A dissipation value of 182 ppm for 0.1 M phosphate buffer is normal for a clean sensor; deviation of 2% of this value suggests an issue. If the crystal is mounted incorrectly, is damaged or buffer is not wetting the entire surface, lower than expected dissipation value will be observed. The reason for some small changes in this value amount from repeated piranha cleaning (see 2.4.1) of the sensor surfaces. For experimental analysis, the 7th harmonic is used throughout this thesis due to its good signal-to-noise ratio.[58] Higher harmonics are also less sensitive to the interference during sample loading. Sensors were normally used 3-5 times before becoming damaged.

2.3.3 Electrochemical set up

For the E-QCM-D a standard three-electrode setup is used. The QCM sensor doubles as a working electrode for electrochemical measurements. The counter electrode platinum sheet is sandwiched between the main house unit of the QCM and the working electrode. A silver–silver chloride (Ag|AgCl|3M NaCl) (BASi RE-6, $E_{SHE} = E_{ref} + 0.209$ V at 25 °C) reference electrode is fitted inside the E-QCM-D main housing unit. Connections to the working electrode were from a copper wire, which attached directly to the base plate of the QCM, Figure 2.4I. The counter electrode connection was made through a spring-loaded gold pin connected to a steel screw, Figure 2.4F. The reference electrode was connected using a crocodile clip.

A Compactstat potentiostat (Ivium Technologies) was used to apply the potential and measure resulting current. IviumSoft software used to record data (Ivium Technologies).

2.3.4 Sample loading

A set volume of sample was pipetted into a 1 ml vial and allowed to equlibrate to 25 ºC on a heated aluminium plate. Enzyme was introduced to the cell by stopping the pump, reversing the flow for a few seconds to produce a suspended drop at the end of the entry tube, placing the tube in the enzyme solution and restarting the pump in the forward direction. After enzyme was introduced, the procedure was repeated to flow buffer through the cell. Typical volumes for protein injections were 25 µl. The sample adsorption was recorded approximately 2 minutes after injection.

2.4 QCM sensor surface preparation

2.4.1 Cleaning

New sensors were washed with ethanol, dried under nitrogen and then placed under a ozone-generating UV lamp for 20 minutes, at a distance of 1 cm. A used sensor was cleaned using a 3:1 ratio of sulfuric acid and hydrogen peroxide (piranha solution, 30 ml) respectively for 15 minutes at 80 °C before being ozone cleaned. This process oxidises the surface to remove contaminants, however it also etches gold from the surface of the crystal, which results in a gradual destruction of the gold coating and thus a limited number of cleaning cycles.

2.4.2 Organothiol surface modifications

Cleaned sensors were placed into 10 ml of 10 mM solution of the organothiol. The solution was left for 15 hours to grow a thiol layer under a nitrogen atmosphere. The sensors were then removed, rinsed with water then ethanol before being dried under a stream of nitrogen.

2.4.3 Reductive desorption of thiol layer

Reductive desorption of thiol was carried out to show the sensor had previously been coated with an organothiol and to quantify the coverage. In Eq.2.1 the reduction of gold-thiol bond is shown, which results in desorption of the organothiol. By measuring the potential and current for the reductive deposition process via cyclic voltammetry, the surface coverage of the layer can be calculated.[46]

$$\mathrm{Au-SR+\ e^- \ \rightarrow Au(0)+\ RS^-} \qquad \text{Eq.2.1}$$

Reductive desorption was carried out in 0.1M NaOH to avoid interference from dihydrogen evolution from solvent reduction. The reduction peak potential is influenced by two parts, first the thiolated head group and the second to the hydrocarbon chain of the remaining organothiol. The desorption potential is related to the potential-induced penetration of ions through the self-assembled monolayer (SAM).[46] Therefore a more positive reduction potential is seen for thinner, less densely packed layers. Figure 2.6 shows that for a gold crystal that has been modified with 6-mercaptohexanoic acid, a reductive peak at –0.55 V vs. SHE is seen. There is no oxidation peak on the return oxidative scan (–1 Vto 0 V) and no subsequent reduction peak on the second scans reductive sweep, indicating the removal of the thiol layer. Assuming reductive desorption is a one–electron process, as given by equation Eq.2.1 the area surface density of the thiol layer can be calculated by integrating the area underneath the reductive desorption peak seen in Figure 2.6.

By measuring the number of electrons transferred between the thiol layer and the electrode, we can determine the number of thiol groups using:

$$\Gamma = \frac{\int \mathrm{i} dE}{nvFA} \qquad \text{Eq.2.2}$$

where Γ is the surface density of the thiol layer, *i* is the current, *E* is the applied potential, *n* is the number of electrons transferred, *v* is the scan rate, *F* is the Faraday constant and *A* is the area of the electrode.[46]

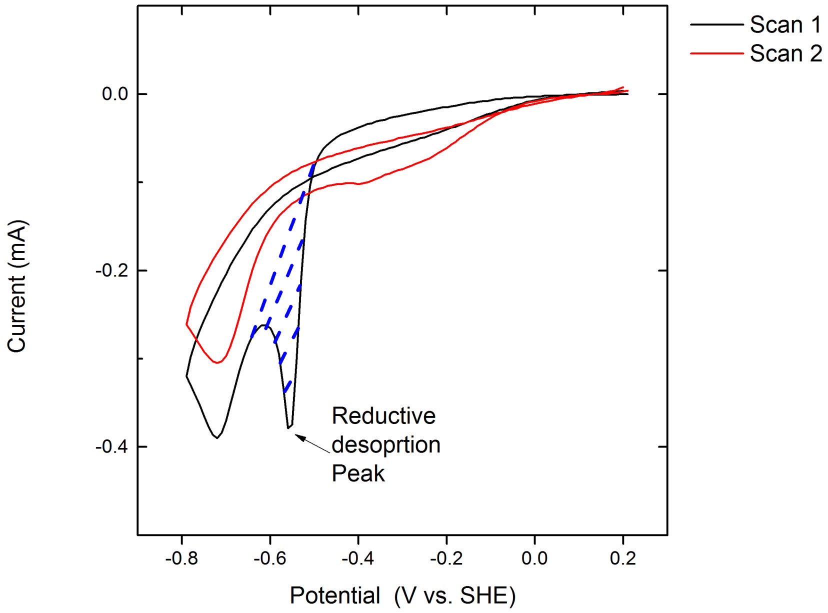

Figure 2.6. Cyclic voltamagram of reductive desoprtion of gold QCM sensor modified with 6-mercaptohexanoic acid. The black first scan shows a reductive peak at -0.55 V vs. SHE. The red second scan does not show this peak. The peak seen at –0.72 is water electrolysis. Conditions: scan rate 50 mVs^{-1} 10 mV Estep 0.21–0.79 V vs SHE 0.1M NaOH saturated with nitrogen

2.4.4 Organosilane surface modifications

With one exception, organosilane solutions (5% w/w) were made up in 10 mL anhydrous toluene. For the water-based the silane agent, 10 mL ethanol was used instead of toluene. Silane modification was carried out for 15 hours in a nitrogen atmosphere onto silica-coated QCM sensors. After modification, sensors were washed with fresh toluene, rinsed in DMF and rinsed with ethanol before being dried under a stream of nitrogen.

2.5 Dual polarisation interferometry

2.5.1 Operation

All dual polarisation interferometry (DPI) measurements were carried out using an Analight 4D (Farfield, Biolin Scientific), which is shown in Figure 2.7. The fluidic system was driven using a mechanical syringe pump (Harvard). Flow rate can be varied from 1 µl – 100 µl min^{-1} during operation and up to 1 ml min^{-1} for cleaning.

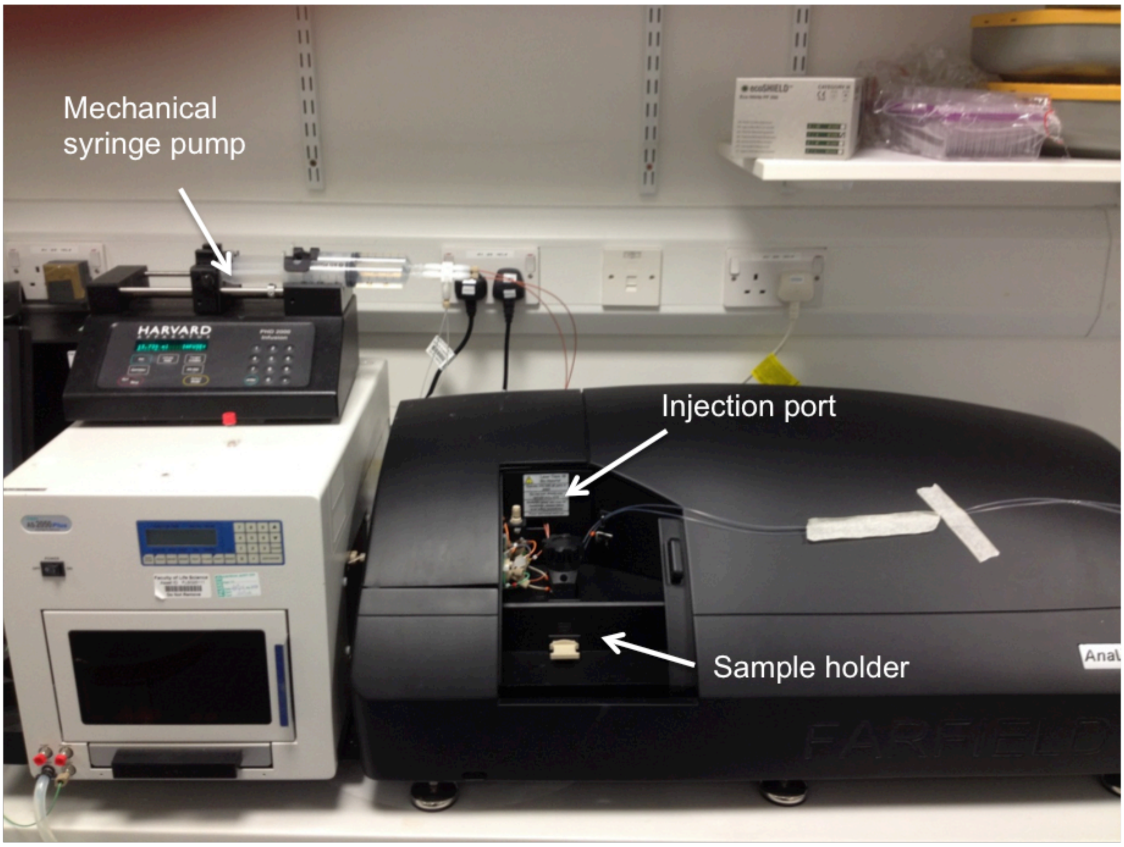

Figure 2.7 Photo of Analight 4D dual polarisation interferometer. This picture shows the housing for the enclosed optics, fluidic and temperature control.

The temperature was maintained at 20 °C and controlled to ± 0.0001 K. The fluidic system uses HPLC–type components, with a computer controlled 6–port valve which injects the samples on to the sensor's surface.[135]

2.5.2 Sensors

Silicon oxynitride FB80 AnaChips (Farfield) are dual slab waveguide, meaning the reference and sensing guides are stacked on top of each other. Sensors are made up of five silicon oxynitride with different doping levels of nitrogen to control the refractive index (RI) of each layer. There are three cladding layers, one at the bottom middle and top, which separate the reference and sensing layers, Figure 2.8. The top layer has etched slices through the cladding to expose the sensing surface to the sample solution. The sensing surface is 89% SiO_x and 11% SiN_y produced using plasma–enhanced chemical vapor deposition (PECVD). PECVD produces an amorphous SiO_xN_y surface.

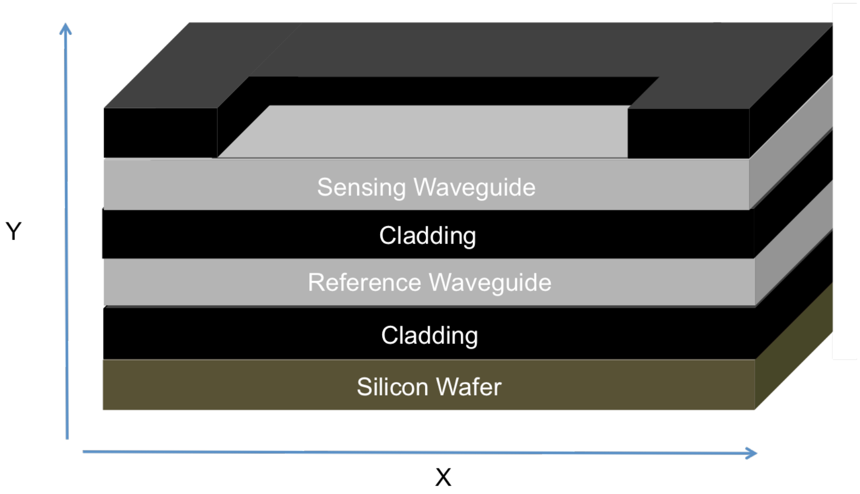

Figure 2.8 Schematic of DPI sensor. Image shows five PECVD layers on top of a silicon wafer. The top cladding layer has an etched channel, which allows the fluid flowing over top of the sensors to come into contact with the sensing waveguide. X denotes the length of the sensor and the direction of confined light and Y denotes the height of the sensor. In actual DPI sensors, there are two etched channels.

Sensors are 24 mm × 6 mm and have a fluorosilicone mask clamped onto the surface of the chip. The mask creates two separate channels on the sensor, labelled channel 1 and channel 3, where the sample solutions are flowed over the sensing surface, with a dead volume of 10 µl.[136] Each channel can have the sample injection controlled individually using a 6 port injector. In between the two channels lies 'channel 2', which does not have an etched away surface, so does not come into contact with the solution. This is used in the calibration of the sensor.

2.5.3 Calibration

Although PECVD produces very precise layers of silicon oxynitride, the effects of cleaning can change the thickness and RI of the sensing layer. To correct for these changes, a chip calibration is required, which uses two solutions of known RI.

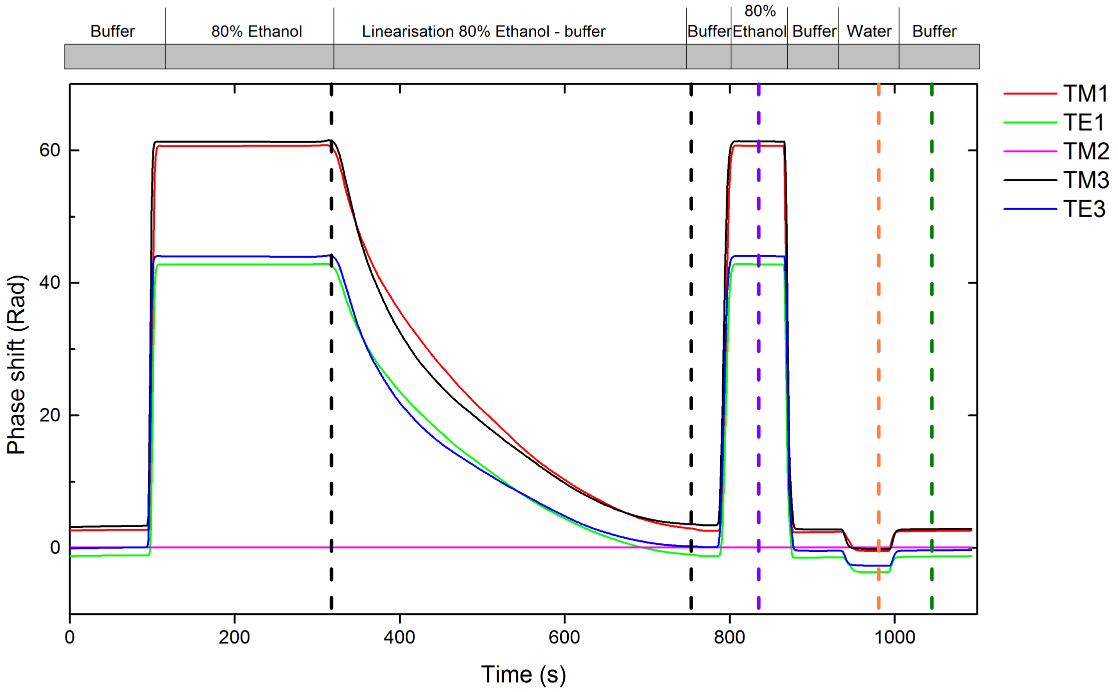

Figure 2.9. Calibration section of a typical DPI experiment. The linearisation region is shown as the area between the two black dashed lines. Chip calibration, using a transition from 80% ethanol to water is shown as purple and orange dashed lines respectively. Bulk calibration from water to running buffer is shown as orange to green dashed lines. The resolver program uses the data points from all five dashed lines to calculate RI and thickness of sensor and the bulk buffer solution's RI. Transmagnetic (TM) and transelectric (TE) are the two different polarisations, with the number symbolizing the channel number.

Both solutions are treated as an infinitely thick adsorbed layer that cause changes in both polarisations modes. Comparison of these changes, with the expected changes in polarisation for a standard sensor allows the actual RI and thickness of each used sensor to be determined.

A typical experiment will have a linearisation region, and chip calibration transition, e.g., a transition from water to 80% ethanol/water (w/w), and at a bulk calibration e.g., from water to buffer. Figure 2.9 shows a typical calibration section of a DPI experiment. For linearisation 80% ethanol is loaded and linearised with running buffer at a rate of 20 µl min^{-1}. After linearization, 80% ethanol and then water are injected to allow for the chip calibration and bulk calibration. The data points are selected and the resolver software calculates the RI and thickness.

2.5.4 Sample loading

Standard injection loops for each channel holds 200 µl of sample. The sample is loaded through a plastic syringe, first filling channel one then channel three. To fill both injection loops, 600 µl is added to remove any air bubbles. This was done because air bubbles disrupt the constant tracking of the phase shifts. Once the sample has been loaded, the computer-operated six port valve can be opened to either one or both channels. Sample speed injection is controlled using the mechanical syringe pumps.

2.5.5 Cleaning

New sensors were washed with ethanol, dried under nitrogen and then placed under a UV ozone generator for 20 minutes. Sensor cleaning used the same procedure as in 2.4.1 The DPI was cleaned after each run using 2 % SDS in water, 2 % Hellmanex in water, and 100 % isopropanol. The injection loops were flushed at an increased flow rate of 1ml min^{-1} to remove any contaminants that remained after cleaning.

2.5.6 Organosilane surface modification

Surface modification of the DPI sensors followed the same procedure for silica QCM sensors (Organosilane modification, 2.4.4).

2.5.7 Data analysis

AnaLight Explorer V1.5 software was used for data analysis. The first calibration of the chip and bulk solution was calculated. TE and TM phase response were selected for each calibration stage, as shown in Figure 2.9. Then, the beginning and end of ethanol linearisation responses are selected, followed by responses for ethanol to water, to calibrate the chip, and finally response for water to buffer, to calculate the bulk buffer RI. After calibration, the computer software then resolves the recorded phase shifts and contrast change as the sample adsorbs to the surface, to give RI and thickness values. Density and mass were calculated once RI and thickness had been resolved.

2.6 Protein structure

Protein crystal structure for *Mv*BOx (pdb 2xll) was sourced from the Protein Data Bank at http://www.rcsb.org/pdb/home/home.do and the molecular modelling program PyMOL was downloaded from http://pymol.sourceforge.net/ and used to show protein crystal structures and the coordination of the copper sites in bilirubin oxidase (*Mv*BOx).

Chapter 3

Sources of activity loss in the fuel cell enzyme bilirubin oxidase

3 Sources of activity loss in the fuel cell enzyme bilirubin oxidase[58]

In this paper, the activity of a high-potential multicopper oxidase, bilirubin oxidase, was studied under typical operating conditions for oxygen reduction. When applying an alternating potential, enzyme electrocatalysis for the four-electron reduction of O_2 to water rapidly decreases. Using an electrochemical quartz crystal microbalance, decreases in activity were shown to coincide with rapid structural changes upon adsorption. Using a common stabilisation method via covalent attachment of the enzyme to the electrode, a lower catalytic efficiency was observed along with no added stability benefit.

My contribution to the published work included measuring the effect on changing CV scan parameters, including potential ranges, scan rates, substrate surface, variations in oxygen saturation, azide inhibition, and relating our findings to a second multicopper oxidase, laccase. I also helped write and edit the final manuscript.

Energy &
Environmental Science

RSC Publishing

COMMUNICATION

View Article Online
View Journal | View Issue

Sources of activity loss in the fuel cell enzyme bilirubin oxidase†

Kulveer Singh,[ab] Trevor McArdle,[b] Patricia R. Sullivan[a] and Christopher F. Blanford*[b]

Cite this: *Energy Environ. Sci.*, 2013, **6**, 2460

Received 6th January 2013
Accepted 19th June 2013

DOI: 10.1039/c3ee00043e

www.rsc.org/ees

Electrochemical quartz crystal microbalance measurements with energy dissipation monitoring (E-QCM-D) show that the catalytic lifetime of the O_2-reducing multicopper oxidase bilirubin oxidase from *Myrothecium verrucaria*, adsorbed on or covalently attached to a organothiol-modified gold electrode, is shortened from days to hours when the applied potential is cycled to below a critical potential (0.6 V *vs.* SHE at pH 6.0)

Broader context

The multicopper oxidases are a family of copper-containing enzymes that includes laccases and bilirubin oxidases. They have been studied as efficient replacements for platinum and its compounds to catalyse the four-electron reduction of O_2 to H_2O in low-temperature, enzymatically catalysed fuel cells. Enzymes' specificity, selectivity against inhibition, and ability to function at near-neutral pH values mean they can generate power in living plants or animals. One of the barriers to the practical use of redox enzymes in fuel cells—as well as biosensors and industrially useful enzymatic transformations—is the proteins' slow loss in activity with time. We simultaneously measured electrocatalytic activity, adsorbed mass of enzyme, and the stiffness of this protein adlayer and concluded that structural rearrangements and water loss are the primary culprits in activity loss in these cathodes. The effect was most pronounced when we simulated a changing power load by cycling the potential. Covalent attachment did not mitigate activity loss. Enzyme-coated cathodes that receive their electrons directly from an electrode, rather than *via* redox mediators, will need additional stabilisation before they will be durable enough for miniature fuel cells from which a sustained power output is required.

Immobilised oxidoreductases show a loss in electrocatalytic activity with time, colloquially termed 'film loss', which limits their applicability to technological applications such as heterogeneous biocatalysis, biosensor development and fuel cells.[1–4] We used the multicopper oxidase (MCO) bilirubin oxidase from *Myrothecium verrucaria* (*Mv*BOx) as a model protein to dissect the mechanisms of film loss, using an electrochemical quartz crystal microbalance with dissipation measurement (E-QCM-D). This technique allows us to simultaneously measure the hydrated mass of the enzyme adsorbed on the sensor surface, its mechanical coupling to the sensor and its catalytic competence.

MCOs have been advanced as catalysts for the four-electron reduction of O_2 to water, a key reaction in low-temperature fuel cells.[5] Bilirubin oxidases carry out this reaction at near-neutral pH values, at a lower overpotential than Pt,[6,7] and can produce currents limited only by transport of O_2 into solution.[6]

Many methods exist for preparing oxidoreductases for heterogeneous electrocatalysis, including uses in enzyme-catalysed fuel cells.[2] A common and relatively straightforward method is *via* direct adsorption on graphite electrodes.[8] The roughness and heterogeneous surface chemistry of abraded graphite supports many enzymes for analytical protein film electrochemistry,[9] but complicates any analysis of activity loss mechanisms. Immobilising enzymes in redox-active polymers,[6] within porous electrodes[10] or on high surface-area dispersions[11,12] creates a reservoir of surplus enzyme that can mask underlying activity loss. In this work, the electrode is the surface of the QCM sensor, a flat, polished gold surface modified with the short-chain thiol 3-mercaptopropionic acid (3MPA) to produce a chemically homogeneous surface for stable adsorption of *Mv*BOx and efficient direct electron transfer to it.[13,14]

An E-QCM has been used previously to follow the adsorption and electrocatalysis of *Mv*BOx on bare gold sensors,[15] but their work was carried out in static conditions with dilute enzyme solutions, did not include dissipation analysis, and presented adlayer masses equivalent to ~10 layers of enzyme. Moreover, we have found the simultaneous energy dissipation analysis, which they could not do, is crucial to understanding the

---

[a] *Inorganic Chemistry Laboratory, Department of Chemistry, South Parks Road, Oxford, OX1 3QR, UK*

[b] *School of Materials and Manchester Institute of Biotechnology, 131 Princess Street, Manchester, M1 7DN, UK. E-mail: christopher.blanford@manchester.ac.uk*

† Electronic supplementary information (ESI) available: Materials and methods; calculations; images of bare sensor surface; controls with bare gold, azide-inhibited *Mv*BOx, BSA and *Tv*L; variations in scan parameters and oxygenation; plots of Δd_7 *vs.* Δf_7. See DOI: 10.1039/c3ee00043e

mechanisms of activity degradation, particularly when the applied potential is not constant. Also, Olejnik *et al.* used an E-QCM to study the activity and lifetime of covalently bound laccase, a related MCO, but they measured activity only under constant applied potential.[16]

Fig. 1 shows a typical adsorption of *Mv*BOx on a 3MPA-modified gold-coated sensor. Buffer saturated with O_2 was passed continually through the measurement cell except at *ca.* 15 min when the enzyme was injected. For thin, rigid and evenly distributed layers, the mass adsorbed on a QCM sensor is proportional to the change in the resonant frequency of the crystal's shear vibration modes;[17] in this work the proportionality constant equals −17.9 ng cm^{-2} Hz^{-1} for the fundamental frequency and −2.55 for the seventh harmonic, which was used for its sensitivity to changes close to the surface and insensitivity to variations in sensor mounting (see ESI†). The 300 Hz drop in the resonant frequency of the seventh harmonic (Fig. 1A) is consistent with the formation of a hydrated enzyme monolayer of protein on the sensor surface (see ESI†). At the same time, the energy dissipation of the crystal increased to a maximum of about 3 ppm (Fig. 1B).

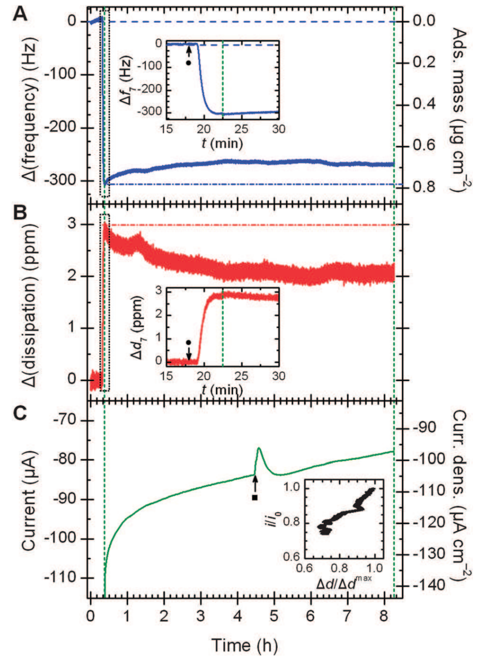

Fig. 1 E-QCM-D response (7th harmonic) with time for bilirubin oxidase adsorbed non-covalently on a 3-mercaptopropionic acid layer: (A) frequency change, (B) energy dissipation change, and (C) O_2 reduction current. Insets in (A) and (B) highlight sensor response after adding 25 μl 24 mg ml^{-1} enzyme (●). Green dashed lines show when a potential of 0.21 V *vs.* SHE was applied. Inset in (C) shows the correlation between dissipation value and electrocatalytic activity. *Conditions*: 0.1 M sodium phosphate pH 6.0 (pre-saturated with O_2), 25 °C, 0.1 ml min^{-1}, projected electrode area 0.80 cm^2. Flow rate of O_2 lowered for 10 min at ■.

Dissipation is the sum of all energy losses in the system per oscillation cycle.[18] Adsorption of proteins contributes towards this dissipated energy and this change can give insight into conformation changes during protein monolayer formation.[19] Softer films experience more inelastic collisions than more rigid films. The formation of softer films, therefore, produces higher Δ*d* values.

The surface of the QCM sensor also serves as a working electrode to quantify the catalytic activity of the protein film and any resistance to electron transfer from the sensor to the proteins' metal centres. The current is proportional to the areal density of the enzyme on the surface and its turnover frequency (see ESI†), thus providing a sensitive method to monitor catalytic activity at the same time as changes in mass and stiffness of the adlayer.

To probe how enzyme activity changes with time under conditions approximating constant load in a fuel cell, a potential of 0 V *vs.* Ag|AgCl|3 M NaCl was applied 7.5 min after the enzyme was injected and held constant for *ca.* 8 h. The applied potential is low enough to drive enzymatically catalyzed O_2 reduction, but too high for O_2 to be reduced on bare gold. An initial steady-state current of −110 μA (Fig. 1C) was observed in comparison to near-zero reduction current in the presence of buffer saturated with argon (see ESI†). The current magnitude was up to 30 μA larger for the first 1.0–1.5 min while dissolved O_2 near the sensor surface was depleted. The initial turnover frequency of the enzyme (k_{cat}) under constant potential conditions is about 35 s^{-1} (see ESI†), about 7× lower than values presented for *Mv*BOx in the absence of mass-transport limitations,[7] but more than 10× higher than previous work using an EQCM setup.[15] Over the course of the measurement, the current decayed to about 30% of its initial value.

Although the initial adsorbed mass of enzyme correlates with the initial magnitude of the catalytic current, subsequent changes in adsorbed mass with time do not parallel changes in catalytic activity. The trace in Fig. 1A is typical: the mass dropped by about an eighth over the first 2.5 h, then remained stable for the next 5 h at (0.68 ± 0.01) μg cm^{-2}. In contrast, changes in energy dissipation with time show an almost linear correlation with catalytic activity (Fig. 1C inset). Like the current magnitude, the dissipation also drops by about 30% over time.‡ The changes of *Mv*BOx on bare gold sensors are almost identical (see ESI†).

Thus, the term 'film loss' is not strictly accurate here: the slow loss of activity in *Mv*BOx must be due to some non-desorptive process like structural changes or copper loss. The strong correlation between adlayer stiffness (inversely related to Δ*d*) and activity implicates structural changes as the primary source of activity loss. The effect of applied potential on protein structure also appears in the plot of Δd_7 *vs.* Δf_7 (see ESI†), which normalises dissipation to adsorbed mass to quantify visco-elastic losses.[19,20] The magnitude of $\partial d_7/\partial f_7$ is more than two times higher when a potential is applied: the protein layer stiffens substantially under applied potential.

To simulate the effect of a variable load on an enzymatic biofuel cell, complementary E-QCM-D measurements were

KS

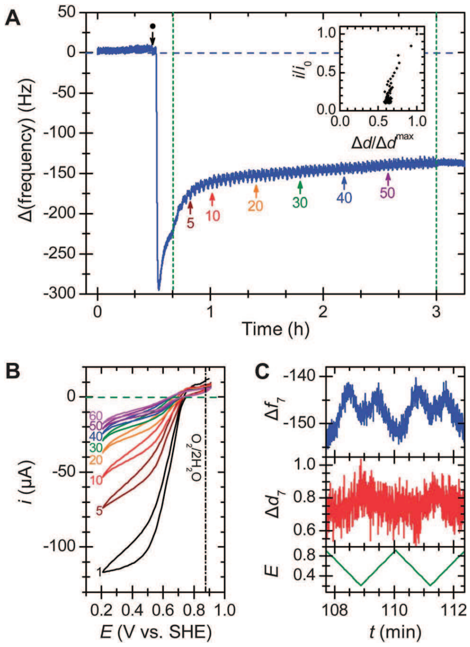

Fig. 2 Effect of potential cycling on bilirubin oxidase adsorbed on a 3-mercaptopropionic acid layer. (A) Frequency response from the addition of 24 mg ml^{-1} *Mv*BOx (●) followed by 60 potential cycles between 0.91 and 0.11 V *vs.* SHE at 10 mV s^{-1} (green dashed lines); arrows mark the start of numbered cycles. Inset shows the relationship between enzyme activity (current at the lowest potential for that scan) and energy dissipation for each scan, normalized to values from scan 1. (B) Selected scans from the cyclic voltammetry. (C) Frequency (Hz) and dissipation (ppm) responses with applied potential (V *vs.* SHE) for scans 30 and 31. *Conditions*: O_2-saturated 0.1 M sodium phosphate buffer pH 6.0 at 25 °C flowing at 0.1 ml min^{-1} with continuous O_2 bubbling; 7th harmonic.

TM

recorded with the potential cycling (Fig. 2). In contrast to the relatively stable mass when the applied potential is held constant, cycling the potential causes an immediate drop in adsorbed mass (Fig. 2A): the mass typically drops by 20–25% over *ca.* 15 min. The catalytic current degrades simultaneously, falling by about a third in the same period (Fig. 2B).§ As in the constant potential cases, the correlation between activity and dissipation (Fig. 2A inset) was nearly linear, albeit with a non-zero intercept.

If the scan range is kept above 0.6 V *vs.* SHE, the pattern of mass and activity loss is like that for chronoamperometry. Decreasing the scan rate to 1 mV s^{-1} led to the same mass loss but only about half the activity loss. Changing the step size had no significant effect on either current loss or mass loss (see ESI†).

After about 10–20 potential cycles, the frequency trace stabilises, but the O_2 reduction activity approaches zero. A QCM measures hydrated mass and about 45% of the protein's mass is entrained water (see ESI†) that contributes to frequency changes of the sensor,[19–21] suggesting that the enzyme adlayer extensively dehydrates during potential cycling. However, in this case some desorption cannot be ruled out.

When the potential was cycled, both the frequency and dissipation traces showed periodic changes that were slightly out of phase with the applied potential (Fig. 2C). The frequency traces showed multiple peaks and a maximum peak-to-peak amplitude of *ca.* 9 Hz (0.02 μg cm^{-2}), about 3% of an enzyme monolayer. The varying potential or electric field near the surface may repeatedly distort the adsorbed protein, causing it to repeatedly expel mass in the form of water or ions, and hastening its denaturation. This hypothesis is consistent with STM observations on single molecules of another MCO, laccase from *Streptomyces coelicolor*, that showed different heights for reduced and oxidised enzyme on a thiol-modified gold electrode.[14]

To control for the possibility that diminishing activity is due to enzyme desorption, *Mv*BOx was covalently linked to a thiol-modified gold crystal *via* an amide linkage between an activated carboxylate on the surface and one of the lysine side chains on the protein's exterior (Fig. 3), identical to EDC–NHS-type coupling reactions. After uncoupled enzyme was washed away, the potential was cycled. Unlike the adsorbed samples, the mass dropped by only 6% in the first 7 cycles then stabilised between 0.68 and 0.70 μg cm^{-2}. Despite this, the catalytic activity still

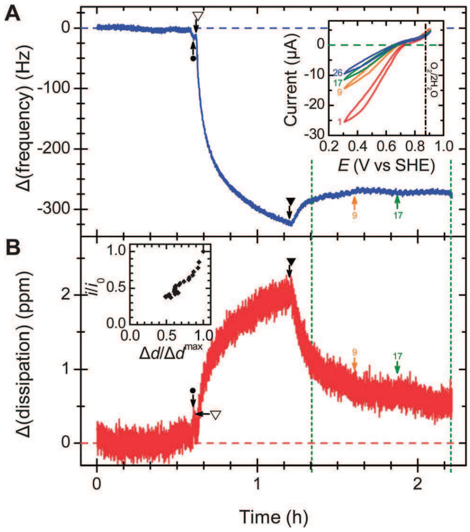

Fig. 3 Effect of potential cycling on (A) frequency response and (B) dissipation response for bilirubin oxidase covalently bound *via* an amide linkage to a thiol-modified QCM sensor. After addition of 25 μL of 24 mg ml^{-1} *Mv*BOx (●), buffer flow stopped (▽) to allow adsorption and reaction with surface layer (reaction adapted from the literature)[22] then resumed (▼) for *ca.* 10 min before voltammetry. Potential cycled 26 times between 0.91 and 0.31 V *vs.* SHE (green dashed lines). Arrows indicate start of selected cycles and correspond to numbering in top inset. Lower inset relates activity and dissipation as in Fig. 2. Other conditions as in Fig. 2.

KS

dropped off rapidly (Fig. 3A inset), diminishing by 80% in less than 1 h. The activity *versus* dissipation trace (Fig. 3B inset) displayed the same characteristic correlation, again suggesting that structural changes are responsible for activity loss, even if they are not accompanied by a large mass loss.

Covalent attachment did not stabilise the catalytic activity. It also decreased the efficiency of electron transfer from the electrode to the enzyme. The position of E_{cat}, a characteristic potential defined by the maximum of the change in current with potential on a swept-potential voltammogram, shifts by −0.1 V, meaning that the covalently attached enzyme needs a greater driving force (~10 kJ mol^{-1}) to drive electrocatalysis compared to the adsorbed sample. The increased charge-transfer resistance is also evident in the shape of the voltammograms in the inset of Fig. 3A: a more linear, ohmic response dominates the sigmoid shape characteristic of electrochemical–chemical (EC) reactions (compare to Fig. 2B).

Reactive dye labelling measurements identified three reactive lysine side chains on *Mv*BOx through which the enzyme could couple to the surface (see ESI†). All of these groups position both of the enzyme's electron acceptors more than 2 nm from the electrode surface, too far for interfacial electron transfer rate compatible with biochemical processes.[23]

Controls using catalytically inactive bovine serum albumin (BSA) on 3MPA-layers showed stable frequency and dissipation traces when the potential was cycled.

The structures of the high-potential MCOs used for fuel cell cathodes are similar,[24] so the patterns of activity loss are likely to be the similar for all three-domain MCOs. For example, laccase from *Trametes versicolor* (*Tv*L) showed similar patterns of mass and activity loss, though the magnitudes differed (ESI†). The observed behaviour depends on protein structure and electrode composition, however. For example, covalent attachment by amide linkage stabilised a [NiFe] hydrogenase over 2 h in response to potential steps up to 250 mV,[25] and covalently bound [FeFe] hydrogenases showed activity decay time constants ranging from hours to days depending on immobilisation method.[1] in activity that was attributed to fast desorption and slower denaturation processes.

Also, an enzyme can be stabilised by its immediate environment: surface modifications and buffered polyelectrolytes let some fuel cell enzymes retain some activity for months.[3,26] The current goal, therefore, is to relate extended catalytic stability to enzyme structure and the enzyme's interface with the electrode and other surroundings.

Conclusions

We applied E-QCM-D as a real-time probe of the potential-dependent stability of enzymes used as catalysts in fuel cell cathodes. The catalytic activity of *Mv*BOx drops rapidly when the applied potential is cycled to simulate variable loads on a fuel cell cathode. Although this activity loss was accompanied by some loss of mass from the adlayer, covalent attachment did not improve catalytic stability and also resulted in lower power output because of longer distances for interfacial electron transfer. Catalytic activity decreased even when the adlayer's mass remained stable, such as when the applied potential was constant. Decreasing catalytic activity always correlated with increasing layer stiffness, implicating structural rearrangements over desorption as the primary mechanism of activity loss. These observations suggest that without additional treatment or overpotential limits, MCO-coated cathodes may be unsuitable for long-term power generation in enzymatically catalysed fuel cells.

Acknowledgements

The authors thank Hannah Roberts and Ivana Sardzikova for assistance with protein digestion and mass spectrometry, Tom McNamara for protein purification, Robert A.W. Dryfe for valuable discussions, and the mechanical and electronics workshop at the University of Oxford's Department of Chemistry for help with design and construction of the E-QCM-D insert and ozone generator. The authors gratefully acknowledge funding from the UK's Engineering & Physical Sciences Research Council (EP/G00434X/2).

Notes and references

‡ The dissipation trace for enzyme loadings greater than about 0.6 mg (10 nmol) initially spikes but returns to a stable baseline in about 10 min, indicative of loosely bound protein (ESI†). The value of $\Delta d^{\max}$ is taken from the post-spike baseline.

§ Reduction current magnitudes above 110 μA produced CV scans with a flattened shape indicative of mass-transport polarisation, so the current at 0.4 V *vs.* SHE on the reductive sweep was used for activity loss calculations.

1 C. Baffert, K. Sybirna, P. Ezanno, T. Lautier, V. Hajj, I. Meynial-Salles, P. Soucaille, H. Bottin and C. Léger, *Anal. Chem.*, 2012, **84**, 7999–8005.
2 X.-Y. Yang, G. Tian, N. Jiang and B.-L. Su, *Energy Environ. Sci.*, 2012, **5**, 5540–5563.
3 C. F. Blanford, C. E. Foster, R. S. Heath and F. A. Armstrong, *Faraday Discuss.*, 2009, **140**, 319–335.
4 H. C. Angove, J. A. Cole, D. J. Richardson and J. N. Butt, *J. Biol. Chem.*, 2002, **277**, 23374–23381.
5 M. T. Meredith and S. D. Minteer, *Annu. Rev. Anal. Chem.*, 2012, **5**, 157–179.
6 N. Mano, J. L. Fernandez, Y. Kim, W. Shin, A. J. Bard and A. Heller, *J. Am. Chem. Soc.*, 2003, **125**, 15290–15291.
7 L. dos Santos, V. Climent, C. F. Blanford and F. A. Armstrong, *Phys. Chem. Chem. Phys.*, 2010, **12**, 13962–13974.
8 F. A. Armstrong, H. A. O. Hill, B. N. Oliver and N. J. Walton, *J. Am. Chem. Soc.*, 1984, **106**, 921–923.
9 C. F. Blanford and F. A. Armstrong, *J. Solid State Electrochem.*, 2006, **10**, 826–832.
10 U. Salaj-Kosla, S. Pöller, W. Schuhmann, S. Shleev and E. Magner, *Bioelectrochemistry*, 2013, **91**, 15–20.
11 K. Murata, K. Kajiya, N. Nakamura and H. Ohno, *Energy Environ. Sci.*, 2009, **2**, 1280–1285.
12 S. Krishnan and F. A. Armstrong, *Chem. Sci.*, 2012, **3**, 1015–1023.
13 M. Tominaga, M. Ohtani and I. Taniguchi, *Phys. Chem. Chem. Phys.*, 2008, **10**, 6928–6934.

14 V. Climent, J. Zhang, E. P. Friis, L. H. Østergaard and J. Ulstrup, *J. Phys. Chem. C*, 2012, **116**, 1232–1243.

15 Y. Kamitaka, S. Tsujimura, T. Ikeda and K. Kano, *Electrochemistry*, 2006, **74**, 642–644.

16 P. Olejnik, B. Palys, A. Kowalczyk and A. M. Nowicka, *J. Phys. Chem. C*, 2012, **116**, 25911–25918.

17 G. Sauerbrey, *Z. Phys.*, 1959, **155**, 206–222.

18 M. Rodahl, F. Höök, A. Krozer, P. Brzezinski and B. Kasemo, *Rev. Sci. Instrum.*, 1995, **66**, 3924–3930.

19 M. Rodahl, F. Höök, C. Fredriksson, C. A. Keller, A. Krozer, P. Brzezinski, M. Voinova and B. Kasemo, *Faraday Discuss.*, 1997, **107**, 229–246.

20 F. Höök, M. Rodahl, B. Kasemo and P. Brzezinski, *Proc. Natl. Acad. Sci. U. S. A.*, 1998, **95**, 12271–12276.

21 U. B. Jensen, E. E. Ferapontova and D. S. Sutherland, *Langmuir*, 2012, **28**, 11106–11114.

22 B. Ge, T. Meyer, M. J. Schöning, U. Wollenberger and F. Lisdat, *Electrochem. Commun.*, 2000, **2**, 557–561.

23 C. C. Page, C. C. Moser, X. X. Chen and P. L. Dutton, *Nature*, 1999, **402**, 47–52.

24 C. J. Rodgers, C. F. Blanford, S. R. Giddens, P. Skamnioti, F. A. Armstrong and S. J. Gurr, *Trends Biotechnol.*, 2010, **28**, 63–72.

25 A. A. Hamdan, B. Burlat, O. Gutiérrez-Sanz, P.-P. Liebgott, C. Baffert, A. L. De Lacey, M. Rousset, B. Guigliarelli, C. Léger and S. Dementin, *Nat. Chem. Biol.*, 2013, **9**, 15–17.

26 C. M. Moore, N. L. Akers, A. D. Hill, Z. C. Johnson and S. D. Minteer, *Biomacromolecules*, 2004, **5**, 1241–1247.

Electronic Supplementary Material (ESI) for Energy & Environmental Science
This journal is © The Royal Society of Chemistry 2013

Electronic Supplementary Information for

Sources of activity loss in the fuel cell enzyme bilirubin oxidase

Kulveer Singh, Trevor McArdle, Patricia R. Sullivan and Christopher F. Blanford

Table of contents

Section S1 Material sources

Bilirubin oxidase from *Myrothecium verrucaria* (*Mv*BOx) was obtained from Amano Enzyme. The enzyme was purified as for protein crystallization.[1] Lyophilized *Mv*BOx powder was dissolved in 10 mM sodium phosphate, pH 7.0 at 4 °C, then centrifugally dialyzed to remove small-molecular-weight contaminants (Vivaspin, 30 kDa MWCO PES). This was then further purified by weak anion exchange (DEAE Sepharose) and by hydrophobic interaction (HiTrap Phenyl Sepharose) chromatography at 4 °C. The protein was eluted using 10 mM sodium phosphate, pH 7.0 at 4 °C, with a 0–0.4 M ammonium sulfate gradient for the anion exchange, and 50 mM sodium phosphate, pH 6 at 4°C, with a 1.25–0 M ammonium sulfate reverse gradient for hydrophobic interaction. Typical yields of purified protein were ≈ 3% by mass. Protein concentrations were determined using the Beer-Lambert law based on $A_{280\text{nm}}$ measured from enzyme aliquots and using $\varepsilon_{280\text{nm}} = 9.52 \times 10^4\ \text{M}^{-1}\ \text{cm}^{-1}$, calculated from the enzyme amino acid sequence by the online software ProtParam – Expasy Proteomics Server (http://www.expasy.ch/tools/protparam.html).

Laccase from *Trametes versicolor* (TvL) was obtained as a crude powder from Sigma. The crude powder was dissolved in 10 mM sodium acetate, pH 5.5 at 5 °C, then filtered through two filters (GFA, 0.45 µm, 0.22 µm). This was then centrifugally dialyzed to remove small-molecular-weight contaminants (Vivaspin, 30 kDa MWCO PES). This was then further purified by weak anion exchange (Q Sepharose, 10 mM sodium acetate, pH 5.5 at 5 °C, with a 0–0.1 M ammonium sulfate gradient) followed by hydrophobic interaction (HiTrap Phenyl Sepharose, 20 mM sodium phosphate, pH 4.7 at 5 °C, with a 1.65–0 M ammonium sulfate reverse gradient) at 5 °C.

Dimethyl sulfoxide (DMSO, ≥99.9%, Fisher), hydroxylamine hydrochloride (>97%, Fisher), hydrochloric acid (37%, Fisher), sodium dihydrogen orthophosphate dihydrate (99.0–101.0%, Fisher), disodium hydrogen orthophosphate anhydrous (99.5+%, Fisher), trisodium citrate dihydrate (≥99%, Sigma), citric acid monohydrate (≥99%, Sigma), ammonium bicarbonate (≥99.5%, Sigma), iodoacetamide (≥99%, Sigma), dithiothreitol (DTT, ≥99.5%, Sigma), trypsin (from porcine pancreas, >10,000 units/mg, Sigma), pepsin (from porcine gastric mucosa, ≥250 units/mg, Sigma), tris(2–carboxyethyl)phosphine hydrochloride (TCEP, >98%, Sigma), sulphuric acid (1.83 g ml^{-1} specific gravity, >95%, Fisher), hydrogen peroxide (30% w/v, Scientific Laboratory Supplies), 3-mercaptopropionic acid (3MPA, >99%, Fluka), 3-mercapto-1-propanol (3MPOL, 95%, Sigma), 3,3′-dithiobis(sulfosuccinimidylpropionate) (DTSSP, >98%, ProChem Inc.). The *N*-hydroxysuccinimide ester of fluorescein-5-EX (F5EX, CAS no. 1196157-68-2) was purchased from Sigma Aldrich, stored in the dark at –20 °C. All chemicals were used as received without further purification. All water was purified via reverse osmosis and ion exchange to a resistivity of 18.2 MΩ cm at 25 °C using a MilliQ water purifier.

Section S2 Equipment

QCM-D data were acquired using a Q-Sense E1 system with accompanying Q-Soft data acquisition software. QCM-D measurements without concurrent electrochemical analysis used a Q-Sense Flow module 401 (total volume ~140 µl, volume above sensor surface ~40 µl, non-sensor surfaces Ti or Viton). E-QCM-D measurements used a modified Q-Sense QEM401 module (volume above sensor surface ~100 µl). The PTFE insert on the electrochemistry module was replaced by a custom-made insert made of poly(oxomethylene) (Delrin) for better wettability, to accommodate a standard 5.7 mm OD reference electrode, and to provide a more robust seal when liquid was pulled through the cell. The manufacturer's value for typical mass sensitivity in liquid is 1.8 ng cm^{-2},[2] equivalent to <0.3% of a monolayer of *Mv*BOx.

The sensors (Q-Sense) were 14mm diameter, gold-coated, AT-cut quartz crystals with a Ti adhesion layer and a fundamental frequency of (4.95 ± 0.05) MHz. All the frequency and dissipation changes presented are from the seventh harmonic of the fundamental frequency (35 MHz, $C = 125$ ng cm^{-2} Hz^{-1}). This harmonic is less affected by crystal mounting and small mechanical vibrations when changing solutions, is more surface sensitive, and still gives a good signal-to-noise ratio compared to the higher frequencies. The measured temperature of the QCM cell was constant within 10 mK. The dependence of the fundamental frequency on temperature (i.e., $d(\Delta f/f)/dT$) of AT-crystals at 25 °C is -3.3×10^{-7} K^{-1},[3] so temperature variations should not lead to frequency variations greater than 16 mHz. In practice, however, we observed larger variations in frequency and dissipation, usually in the range of ±7–14 Hz and ±0.5 ppm for Δf_7 and Δd_7, respectively. The sensor surface is remote from the point at which the E1 system measures the temperature, so the entire liquid handling system (cell, reservoir, tubing and pump) was placed on top of an aluminium plate through which water held at 25 °C was circulated, then surrounded by an insulated box in which the air was circulated by an electric fan. The thermal coupling between the flow modules and QCP101 chamber platform was improved with thermal conducting paste (RS components, RS 217-3835). Other sources of variation arise from the mounting of the crystal in the cell and the effect of the repeated cleaning procedure on the gold surface.

Enzyme was introduced to the cell by stopping the pump, reversing the flow for a few seconds to produce a suspended drop at the end of the entry tube, placing the tube in the enzyme solution and restarting the pump in the forward direction. After enzyme was introduced, the procedure was repeated to flow buffer through the cell. Each exchange took less than 1 min. The dead time for liquids to flow from the inlet to the cell was 2 min.

The electrochemical cell used a three-electrode configuration: the gold-coated QCM sensor (exposed geometric area of 0.80 cm^2) as the working electrode; a 0.2mm thick, 2.25cm^2 square platinum plate running parallel to the sensor surface as the counter electrode; and a Ag|AgCl|3M NaCl reference electrode (BASi RE-6, $E_{\mathrm{SHE}} = E_{\mathrm{ref}} + 0.209$ V). The distance between the working electrode and counter electrode was 0.7–0.8 mm; the distance between working and reference electrode was 0.9–1.0 mm. The potential was set and the current was measured by an Ivium CompactStat, using the accompanying IviumSoft control software.

Buffer was kept in a sealed glass bottle and oxygenated for 20 min before each experiment. Increasing the pump speed produced moderate increases in current. For example, an O_2-reduction current of –69 µA at 0.1 ml min^{-1} increased by 9% when the flow rate was increased to 0.3 ml min^{-1}. No significant current increase was seen upon increasing the flow rate to 0.5 ml min^{-1} and flow rates greater than 0.5 ml min^{-1} mechanically disrupted the stability of the electrochemical cell. (Conditions for example: 25 µl of 12 mg ml^{-1} *Mv*BOx, 25 °C, 0.1 M sodium phosphate pH 6.0, 0 V vs. reference.)

Section S3 QCM sensor surface treatment and protein adsorption

Section S3.1 Cleaning

Residual contamination on new QCM sensors was removed by placing them under a ozone-generating UV lamp in air for 30 min. Sensors were reused by oxidizing the surface with piranha solution (3:1 v:v conc. H_2SO_4:30 wt% H_2O_2) for 20 min with constant heating at 60°C, followed by rinsing in water. The crystals were dried under a stream of house nitrogen from boil-off, then ozone treated as described.

Section S3.2 Organothiol surface modification

Surface modification solutions consisted of either 10 mM DTSSP, 10 mM 3MPA or 10 mM 3MPOL mixed with 1.3 mM TCEP in ethanol. Solutions were sonicated for 20 min. before freshly cleaned sensors were immersed for 15 h under a nitrogen atmosphere (for 3MPA) or 3 h in air (for DTSSP). (Consistent with the reports of Z. Cao and co-workers, we have observed gold dissolution by QCM from oxygenated thiol solutions.)[4, 5] Surface coverage of the thiol layer was determined by reductive desorption in basic anaerobic aqueous solution,[6] giving surface coverages between 9.6 x10^{-11} and 6.7 x10^{-10} mol cm^{-2}, depending on the size and length of the thiol layer. After surface modification, the crystals are rinsed with water and ethanol, dried in a stream of nitrogen gas, then mounted in the E-QCM cell.

Section S3.3 Introduction of protein to the cell

The fluid flow through the cell is controlled via peristaltic pump located and operated outside the cell, at a rate of 0.1 ml min^{-1}. The pump was stopped and the inlet tubing switched to a microcentrifuge tube containing 25µL of protein at the desired concentration. After addition, the pump was temporarily switched to flow in an anticlockwise to eliminate air bubbles from the flow path. At this point the pump was turned back to clockwise and the fluid flow was resumed.

Section S3.4 DTSSP coupling

The addition of protein was done in the same way however upon the QCM-D response in the frequency and dissipation traces, the peristaltic pump was turned off for 45 min to allow for the succinimidyl groups to react with the lysine residues of *Mv*BOx. After the reaction had proceeded the pump was turned back on and fluid flow resumed.

Section S4 Relating electrocatalytic current to enzyme activity

Electrocatalytic activity is related to the areal density of the enzyme on the surface and its turnover frequency according to Eqn. S1:

$$i = -n\,F\,A\,\Gamma\,k_{\mathrm{cat}} \tag{S1}$$

where i is the catalytic current (negative for reductive processes by convention), n is the number of electrons involved in the reaction (4 for the reduction of O_2 to $2H_2O$), F is Faraday's constant, A is the electroactive surface area of the electrode accounting for surface roughness ($0.80\ \mathrm{cm}^2 \times 1.6$, see Section S7), Γ is the coverage of the enzyme ($4.2\ \mathrm{pmol\ cm}^{-2}$ for a saturated monolayer, see Section S8), and k_{cat} is the enzyme's intrinsic rate constant/turnover frequency.

Section S5 Degree of labelling and reactive lysine determination

Section S5.1 Methods

Section S5.1.1 Fluorescein 5-EX (F5EX) labelling

*Mv*BOx was labelled with an amine-reactive fluorophore based on a procedure from Molecular Probes (now Invitrogen).[7] Aliquots of 15.2 mM F5EX in DMSO were mixed with aliquots of 0.24–0.25 mM *Mv*BOx in 0.1 M sodium bicarbonate pH 8.3 to give dye:protein molar ratios of up to 72. The total volume of the reaction mixture was 110 to 200 µl. The mixture was incubated in the dark with stirring at room temperature for 1 h, then 0.1 ml of freshly prepared 1.5 M hydroxylamine pH 8.5 was added to conjugate to unreacted F5EX and stop further reaction with the protein. The protein was separated from unconjugated dye by dialysis through a 30 kDa MWCO filter (Vivaspin, GE Healthcare).

The degree of labelling (DoL) was determined spectrophotometrically ($\lambda_{\mathrm{max}}^{\mathrm{F5EX}} = 494$ nm) in a 1cm path length quartz cuvette and Eqn. S2:

$$\mathrm{DoL} = \frac{A_{494\ \mathrm{nm}}^{\mathrm{mix}}\ \varepsilon_{280\ \mathrm{nm}}^{Mv\mathrm{BOx}}}{\left(A_{280\ \mathrm{nm}}^{\mathrm{mix}} - \mathrm{CF}\ A_{494\ \mathrm{nm}}^{\mathrm{mix}}\right)\varepsilon_{494\ \mathrm{nm}}^{\mathrm{F5EX}}} \tag{S2}$$

where $A^{\text{mix}}_{280\text{ nm}}$ and $A^{\text{mix}}_{494\text{ nm}}$ are the recorded optical densities for the labelled protein at 280 nm and 494 nm, respectively, $\varepsilon^{\text{F5EX}}_{494\text{ nm}} = 6.8 \times 10^4\ \text{M}^{-1}\ \text{cm}^{-1}$, $\varepsilon^{\text{protein}}_{280\text{ nm}} = 9.2 \times 10^4\ \text{M}^{-1}\ \text{cm}^{-1}$, and the correction factor (CF) = 0.30. The correction factor is the ratio of the absorbance of the free dye at 280 nm to its absorbance at $\lambda_{\max}$ (i.e., $\varepsilon^{\text{F5EX}}_{280\text{ nm}}/\varepsilon^{\text{F5EX}}_{494\text{ nm}}$). The values for the dye were recorded at pH 8.0.

Section S5.1.2 Trypsin digest

Solutions of 1 mg ml^{-1} *Mv*BOx, 100mM dithiothreitol (DTT, for reduction of disulphide bonds in the protein), 100mM iodoacetamide (to cap free cysteine thiolates), and 20 µg ml^{-1} trypsin were made in 50mM ammonium bicarbonate. 2.1 µl of the DTT solution was added to 50 µl of the protein solution, the mixture was vortexed then incubated for 45 min at 37 °C. After the solution returned to room temperature, 8.7 µl of the iodoacetamide solution was added, the mixture vortexed again, then incubated in the dark for 45 min. at room temperature. A further 2.2 µl of DTT solution was added, the mixture vortexed, then incubated at 37 °C for 10 min. 20 µl of trypsin solution was added to the mixture, which was then incubated for 12 h at 37 °C. Final solution frozen at –21 °C and stored for 7 d until mass spec analysis.

Section S5.1.3 Pepsin digest

50 µl *Mv*BOx (15 mg ml^{-1}, 0.1M sodium phosphate buffer pH 6.0) was acidified with 20 µl 0.04M HCl. To this solution, 20 µl 0.3 mg ml^{-1} pepsin in water was added (71:1) and the mixture vortexed briefly. The mixture was incubated for 12 h at 37 °C, heated to 95 °C for 15 min. then cooled to room temperature and frozen at –21°C.

Section S5.1.4 MALDI mass spectrometry

All MALDI mass spectrometry experiments were carried out on an Ultraflex II instrument (Bruker Daltonics) in positive reflectron mode. A solution of matrix (α-cyano-4-hydroxycinnamic acid) matrix was applied to the protein sample and allowed to dry before analysis.

The spectra taken of the protein after the trypsin digest are plotted in Figure S1. Peaks were labelled according to the conventions of Roepstorff and Fohlman[8] and Johnson and co-workers,[9, 10] guided by the tutorial article from Wysocki and co-workers.[11] These assignments are summarized in Table S1 and Table S2. No differences were observed in the peak positions after the pepsin digest.

Section S5.2 Results and Analysis

At a dye-to-protein molar ratio of ca. 25, the degree of labelling saturated at about one dye molecule per protein molecule (DoL = 1.09 ± 0.10, Figure S1 inset). The main new contributions to the mass spectrum of the labelled protein were the peaks shown in Figure S1**B**, which correspond to Lys408 and Lys118. Small peaks appeared in fragments containing labelled Lys181 (Figure S1**E**) and Lys21 or Lys214 (Figure S1**F**). Small peaks disappeared from the spectrum of the unlabelled protein corresponding to Lys429 (Figure S1**D**) and Lys44 (Figure S1**E&G**). Trypsin cleaves at Arg and Lys residues, so the F5EX labels will always be at the C-terminus of any peptide fragment. So, with the exception of the doubly charged a21 fragment in Figure S1**F**, a, b and c ions are not labelled. There was no definitive pair of labelled peaks corresponding to the appearance of one shifted by 475.07 Da and the disappearance of its parent.

Most of the lysines can be ruled out: of the 11 lysines in the sequence of *Mv*BOx (Figure S2), three do not appear differently in the labelled and unlabelled samples: Lys220, Lys251 and Lys314. Lys118 and Lys429 have <2.5 Å^2 of their atoms on the protein surface (using the FindSurfaceResidues.py algorithm on PyMOLwiki).[12] Although Lys118 is accessible to react with dye molecules, it is too buried to couple to surface groups.

The strongest evidence points to the most reactive exposed lysine side chain being Lys408, with some reactivity in Lys 21 and Lys181. All three groups are more than 1.5 nm from the enzyme's active sites, too far for tunnelling rates compatible with biological processes:[13] Lys408 is 2.59 nm from the type 1 copper (considered the primary electron acceptor)[14] and 2.15 nm from the type 2 copper; Lys21 is 3.23 nm from the type 1 and 2.03 from a type 3 copper; and Lys181 is 1.94 nm from the type 1 copper. These distances were measured from the terminal nitrogen atom.

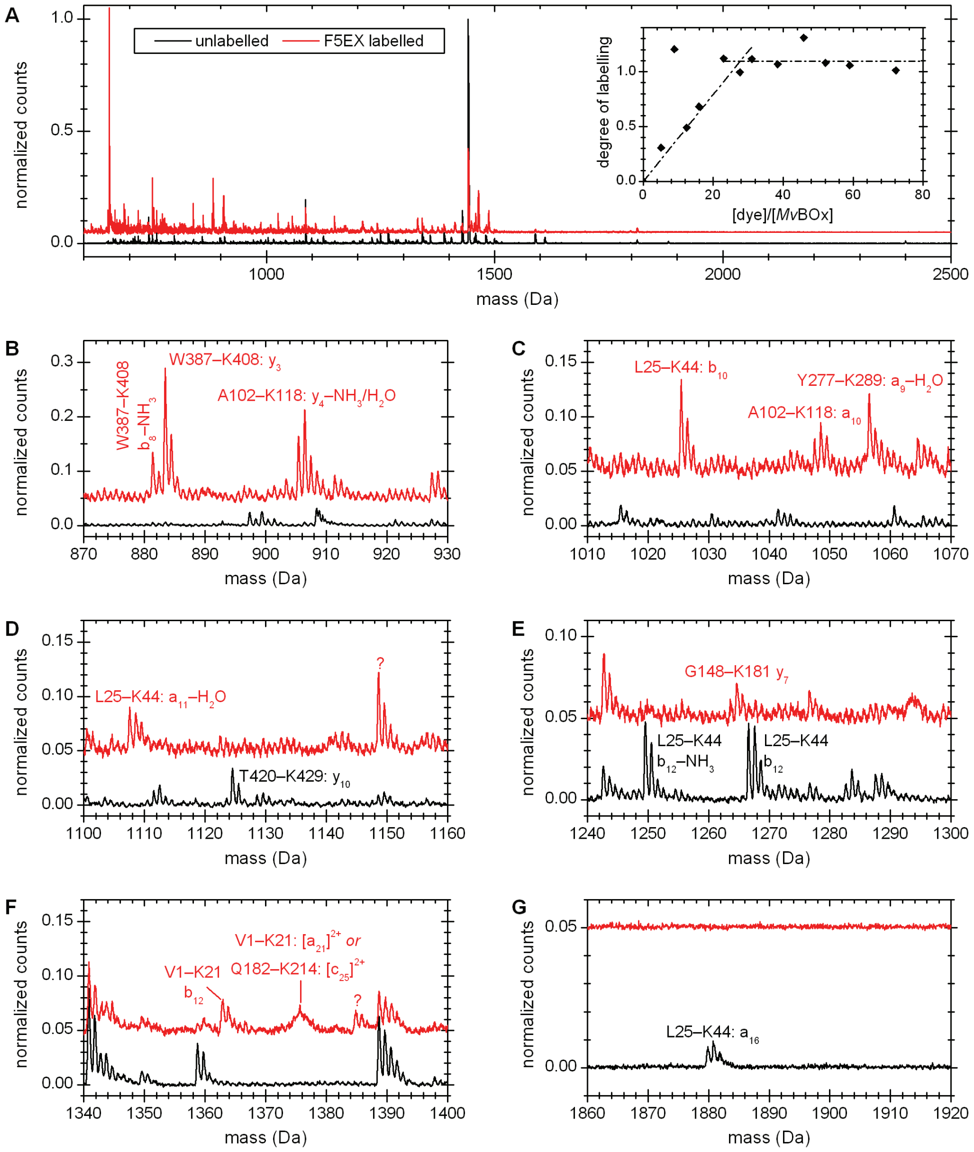

Figure S1. Determination of the location of reactive lysine side chains in *Mv*BOx by reaction with fluorescein 5-EX (F5EX). Panel **A** compares the full MALDI mass spectra of enzyme that has been labelled with F5EX (red) and that which has not (black). The inset shows the degree of labelling as a function of enzyme concentration. The lines are to guide the eye. Panels **B**–**F** show specific regions where the two mass spectra differ. Peak labels give the peptide sequence and ion type.[8-10] The full scale for the unlabelled and labelled spectra are 2.9×10^4 and 1.9×10^4 counts, respectively.

e KS

Table S1. Additional peaks in MALDI mass spectrum of fluorescein 5-EX–labelled *Mv*BOx compared to unlabelled *Mv*BOx after trypsin digest

Mass (Da)	Fragment	Assignment
881.4	W387–K408	b_8–NH_3
884.4	W387–K408	y_3
905.4	A102–K118	y_4–H_2O/NH_3
1025.5	L25–K44	b_{10}
1048.5	A102–K118	a_{10}
1056.5	Y277–K289	a_9–H_2O
1107.6	L25–K44	a_{11}–H_2O
1148.5	unknown	
1264.6	G148–K181	y_7
1362.8	V1–K21	b_{12}
1374.	V1–K21 Q182–K214	a_{21}^{2+} c_{25}^{2+}
1384.9	unknown	

Table S2. Missing peaks in MALDI mass spectrum of fluorescein 5-EX–labelled *Mv*BOx compared to unlabelled *Mv*BOx after trypsin digest

Mass (Da)	Fragment	Assignment
1124.5	T420–K429	y_{10}
1249.5	L25–K44 Q182–K214	b_{12}–NH_3 c_{25}^{2+}
1266.6	L25–K44	b_{12}
1879.9	L25–K44	a_{16}

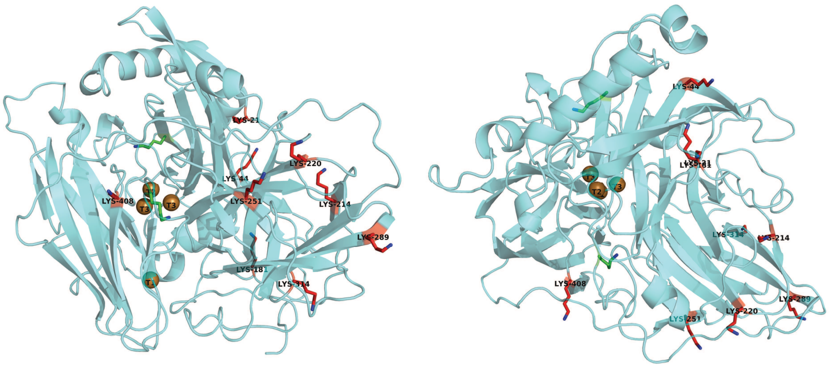

Figure S2. PyMOL visualization of the location of the lysine residues in *Mv*BOx (PDB code 2xll).[1] The polypeptide backbone is shown as the cyan cartoon. The coppers are shown as spheres labelled with their spectroscopic designation. The nine lysine side chains that have at least 2.5 Å^2 on the surface are in red; the two that do not are in green. The image on the right is rotated 90° along a horizontal axis.

KS

Section S6 Effect of protein concentration on protein adsorption isotherm

Oxygenated buffer was flowed over gold-coated crystals modified with 3-mercaptopropionic acid (Figure S3) and those with no surface modification (Figure S4) until a steady baseline was observed in the frequency and dissipation traces. For each concentration, 25 µL of enzyme was flowed through the cell. Both sets show a maximum frequency change for the seventh harmonic of 275–325 Hz (0.70–0.83 µg cm^{-2}, cf. Section S8) The dissipation traces are markedly different: the adlayer on bare gold initially has a much higher viscoelasticity (i.e., higher dissipation) then stiffens within 1–2 min. There is also a much sharper decrease in mass after adsorption on bare gold. These are both characteristics of substantial dehydration and denaturation of the protein.

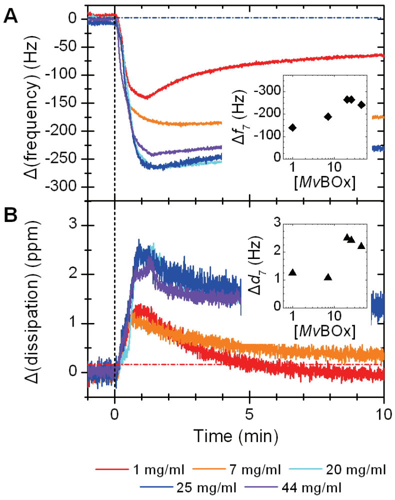

Figure S3. The effect of enzyme concentration on adsorption onto 3-mercaptopropionic acid–modified gold-coated quartz crystals. Panel **A** shows the frequency change at different concentrations of enzyme. Panel **B** shows dissipation change at different concentrations. The insets show the relationship between concentration and highest magnitude of frequency and dissipation change. Conditions: 7th harmonic, 0.1 M sodium phosphate pH 6.0 (pre-saturated with O_2), 25 °C, 0.1 ml min^{-1}

`KS`

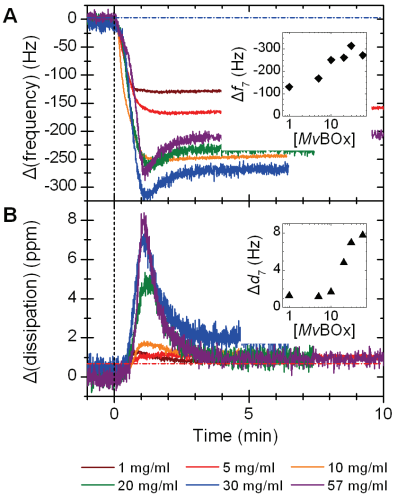

Figure S4. The effect of enzyme concentration on adsorption onto bare gold-coated quartz crystals (i.e., without organothiol modification). Panel **A** shows the frequency change at different concentrations of enzyme. The inset in panel **A** shows the relationship between concentration and peak frequency change. Panel **B** shows the dissipation change at different concentrations. The insets show the relationship between concentration and highest magnitude of frequency and dissipation change. Conditions: 0.1 M sodium phosphate pH 6.0 (pre-saturated with O_2), 25 °C, 0.1 ml min^{-1} TM

Section S7 Electroactive area (surface roughness) determination

The accessible surface area of the gold-coated QCM sensors was determined by the electrochemical formation and stripping of a gold oxide monolayer in solution according to an IUPAC method.[15] The QCM crystal was suspended in 0.1 M H_2SO_4, typically immersing 90 mm^2 of the gold surface. The potential was cycled at 50 mV s^{-1} from 0.45 V to 1.6 V (vs. Ag|AgCl|3 M NaCl) until a stable voltammogram was recorded (30 cycles). The potential was then cycled once over the same range at 10 mV s^{-1} and the charge transferred was calculated from the stripping peak at about 1.08 V vs. ref, corrected with a linear baseline (Figure S5). Backscattered electron images of the sensor surface (Figure S6) appeared to show a polycrystalline surface with a profusion of 5μm-wide cracks. We used the IUPAC-recommended value of 390 ± 10 μC cm^{-2} to relate the area of the stripping peak to the surface area of the gold accessible to oxygen.[15] The ratio of the electrochemically accessible surface area to the geometric surface area (roughness factor) was 1.5–1.6. These roughness factors are consistent to those reported by Kamitaka et al. for their Seiko sensors (1.5–1.7).[16]

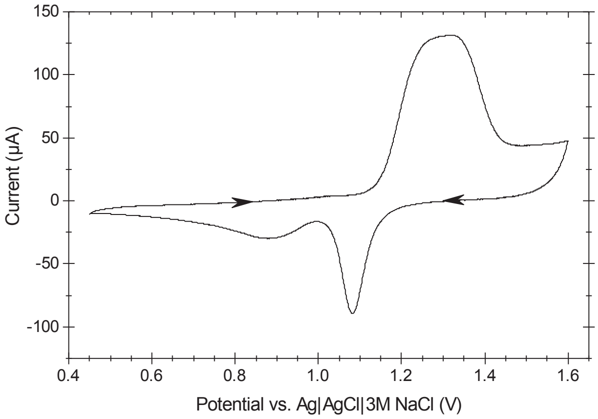

Figure S5. A representative example of the final cyclic voltammogram associated with gold oxide formation and stripping on a Q-Sense QCM sensor.

KS

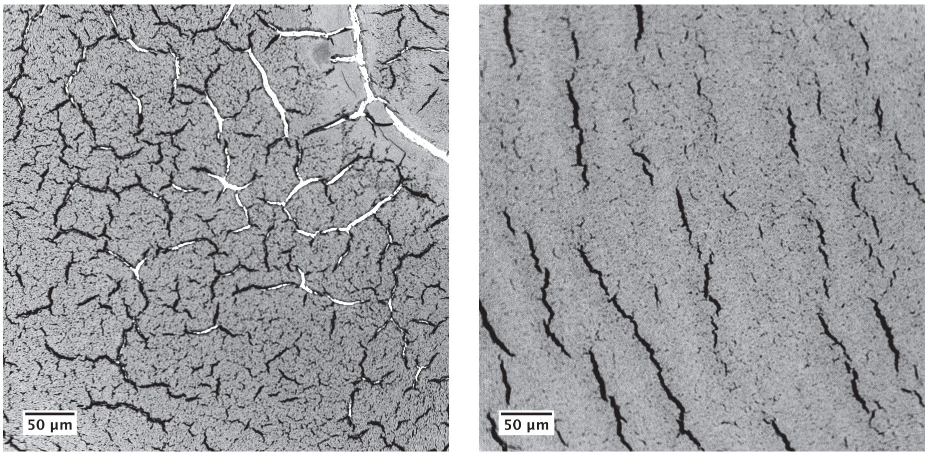

Figure S6. Representative scanning electron micrographs taken of the surface of a Q-Sense gold-coated QCM sensor. The image on the left was taken near the crystal centre and the right image was taken toward the edge of the crystal. The crystals were new and were prepared by leaving under an ozone-generating lamp for 20 min. The above images are from a backscattered electron SEM (Phenom Pro G2 desktop SEM).

TM

Section S8 Estimation of the mass required for surface saturation

A first estimate of the frequency change expected from a saturated monolayer of *Mv*BOx can be obtained by simply dividing the QCM sensor's active area by the macromolecule's footprint (ca. 40 nm^2, based on PDB 2xll),[1] then applying the Sauerbrey equation:[3]

$$\Delta m = -\frac{\sqrt{\rho_q \mu_q}}{2 f_1^2 N} \Delta f_N \tag{S3}$$

$$\Delta m = -\frac{C}{N} \Delta f_N \tag{S4}$$

where Δm is the mass adsorbed, ρ_q and μ_q are the density and shear modulus of AT-cut quartz (2.648 g cm^{-3} and 2.947×10^{11} g cm^{-1} s^{-2}, respectively), f_1 is the fundamental frequency of the sensor (4.95 ± 0.05 MHz), N is the harmonic of the sensor, and Δf_N is the frequency change of that harmonic. For the Q-Sense E1, the proportionality constant, C, is 17.87 ng cm^{-2} Hz^{-1}.

Table S3. Contributions to the hydrated mass of *Mv*BOx

Component	Mass (Da)
peptide chain	59955
copper ions four per macromolecule	254
ordered glycans four *N*-linked *N*-acetylglucosamines per macromolecule	812
water V_{cell} = 631.75 nm^3, 4 macromolecules/cell assumes 53.3% solvent, $\rho_{\text{water}} = 10^{-21}$ g nm^{-3} (of which there are 316 ordered water molecules per macromolecule = 5922 Da)	50520
total	*111541*

Monolayer coverage of close-packed *Mv*BOx macromolecules on a perfectly smooth sensor surface is 4.2 pmol cm^{-2}. Corrections must be applied for the roughness of the sensor surface (Section S7) and the mass of the water that is mechanically coupled to the protein. We assumed that solvent content of the three-dimensional X-ray structure could approximate the mass of water in a closely packed monolayer of the protein to calculate a hydrated mass of 111.5 kDa (Table S3). This gives a maximum adsorbed mass on a smooth electrode of 0.47 µg cm^{-2} (Δf_1 = –26.0 Hz, Δf_7 = –182 Hz), and 0.78–0.80 µg cm^{-2} on our electrodes (Δf_1 = 44 Hz, Δf_7 = –306–308 Hz, 7.2 pmol cm^{-2}). The latter values are consistent with the observations presented in the main text.

Section S9 Enzyme adsorption on a bare gold sensor

The measurements shown in Figure S7 parallel those shown in Figure 1 in the main text. The change in frequency occurring here is to a lesser extent than with the 3MPA-modified gold surface and the magnitude of catalytic current is also lower, within the normal range of variation we observed. When a chronoamperometric potential is applied (~28 min) there is a large apparent mass loss (~25 Hz, 0.06 µg cm^{-2}) which may be due to removal of loosely bound enzyme or mechanical effects (cf. Figure 2 in the main text). The short, horizontal portion of the current vs. dissipation trace (Figure S7 inset) arose from a short increase in dissipation after the potential was turned on, after which the trace returned to its more typical linear correlation with a slope near 1. The first-order time constant for current loss was 2.2 h.

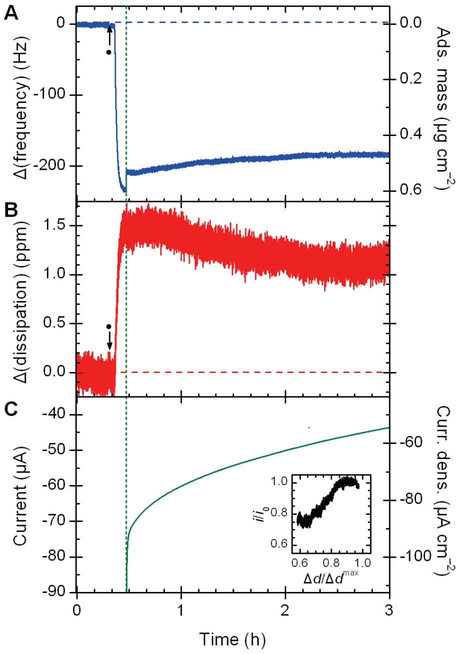

Figure S7. E-QCM-D response (7th harmonic) with time for bilirubin oxidase adsorbed on a bare gold crystal surface: **A** frequency change, **B** energy dissipation change, **C** O_2 reduction current. Circle (●) indicates when 25 µl 24 mg ml^{-1} *Mv*BOx was injected. Green dashed line shows when a potential of 0.21 V vs. SHE was applied. Inset in C shows the correlation between dissipation and electrocatalytic current. Conditions: 0.1 M sodium phosphate pH 6.0 (pre-saturated with O_2), 25 °C, 0.1 ml min^{-1}. Current density based on geometric area of 0.80 cm^2. `TM`

Section S10 Combined effects of cyclic voltammetry and chronoamperometry

We compared the effects of constant and variable potentials on the same layer of *Mv*BOx (Figure S8). After *Mv*BOx adsorption, the potential was cycled five times (Figure S8B, scan time 124 s) causing a 25% mass loss (ca. 0.15 µg cm^{-2}) and an activity loss of about a third (44 µA). The shape of the first reductive scan shows flattening that is characteristic of mass-transport limitations, which would mask the true activity of the protein layer, so the actual activity loss is probably higher. At 0.45 V, the activity loss is about 60%. The potential was then held constant at 0 V for ca. 7 h. During this time the frequency trace remained relatively stable between –146 and –132 Hz, but the current dropped by 52%. Turning the potential on and off caused momentary fluctuations in the frequency trace, similar to that seen in Figure S7. Finally, the potential was cycled 10 more times (Figure S8C) during which the activity dropped by about a third and the mass dropped by about a tenth to about 60% of its value before the start of the voltammetry.

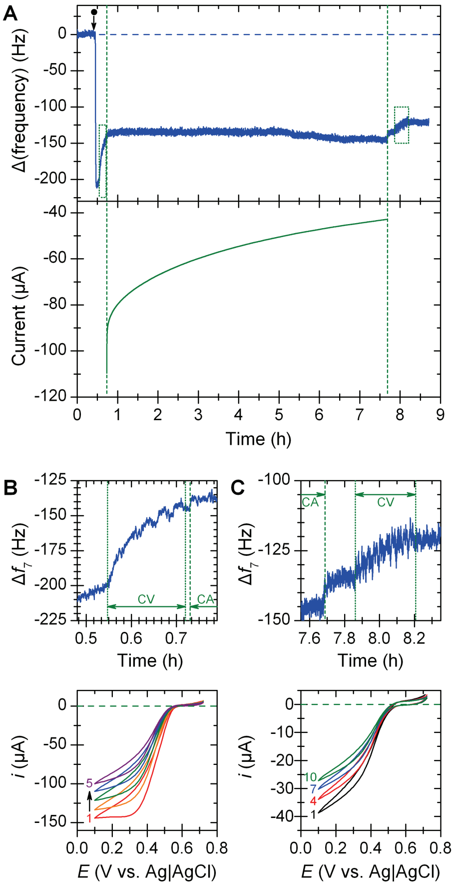

Figure S8. Frequency and current responses with time for *Mv*BOx adsorbed on a gold-coated QCM sensor modified with 3-mercaptopropionic acid. The top part of panel **A** shows the frequency change. Circle (●) indicates when 25 μl 24 mg ml^{-1} *Mv*BOx was injected. The periods when the potential was cycled (panels **B** and **C**) are indicated by dotted green boxes. The period when a constant reducing potential was applied is indicated by dashed green vertical lines. The bottom part of panel **A** shows current response to constant potential. Panel **B** shows frequency and current responses to five potential cycles before a constant potential was applied. Panel **C** shows this data for 10 potential cycles after a constant potential was applied. Data for frequency traces averaged over 21 points (6 s). Conditions: 0.1 M sodium phosphate pH 6.0 (pre-saturated with O$_2$), 25 °C, 0.1 ml min^{-1}, seventh harmonic shown. Cyclic voltammetry (CV): 0.72 → 0.10 → 0.72 V vs. Ag|AgCl|3M NaCl, 10 mV s^{-1}. Chronoamperometry (CA): constant applied potential of 0 V vs. Ag|AgCl|3M NaCl.

KS

Section S11 QCM measurements in the absence of electrocatalysis

Cycling the potential on thiol-modified gold crystals without enzyme (Figure S9) produces oscillations in the Δf & Δd traces as for Figure 1, but with an amplitude about three times higher than when *Mv*BOx or BSA is adsorbed. The traces in panel C show the onset of O_2 reduction around 0.5 V vs. SHE. A bump on the oxidative scan appears around 0.72 V vs. SHE after the first scan.

Bovine serum albumin (BSA), a globular protein with similar dimensions to *Mv*BOx, was adsorbed on a 3MPA-coated QCM sensor (Figure S10). Unlike the rapid mass loss observed for an *Mv*BOx adlayer when the potential was cycled (Figure 2), the frequency response for the BSA adlayer increased slightly to a value about 80% of its initial magnitude. The frequency response of an azide-inhibited *Mv*BOx adlayer (Figure S11) was closer to that of the uninhibited enzyme, with a large, rapid drop in adsorbed mass. As expected, no electrocatalytic activity was observed for either BSA or azide-inhibited *Mv*BOx.

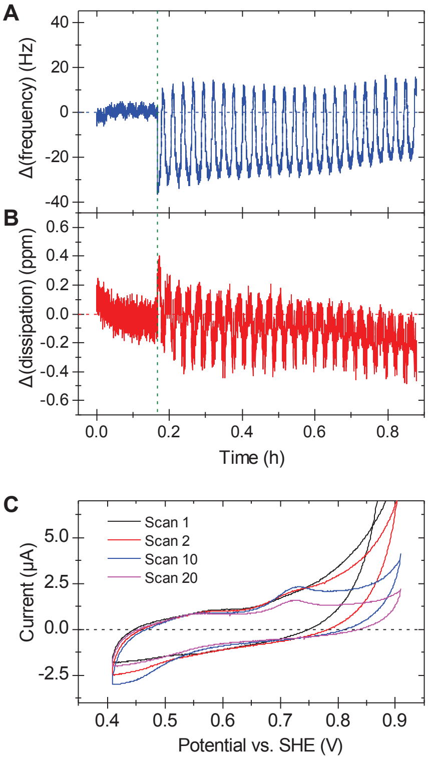

Figure S9. Frequency, dissipation and cyclic voltammetric responses with time for a gold-coated QCM sensor modified with 3-mercaptopropionic acid. Panel **A** shows the frequency change, panel **B** shows the dissipation response and panel **C** shows selected CV traces. The vertical green dashed line indicates the start of the voltammetry. Conditions: 0.1 M sodium phosphate pH 6.0 (pre-saturated with O_2), 25 °C, 0.1 ml min^{-1}, seventh harmonic shown. Cyclic voltammetry: 0.7 → 0.2 → 0.7 V vs. Ag|AgCl|3M NaCl, 10 mV s^{-1}.

TM

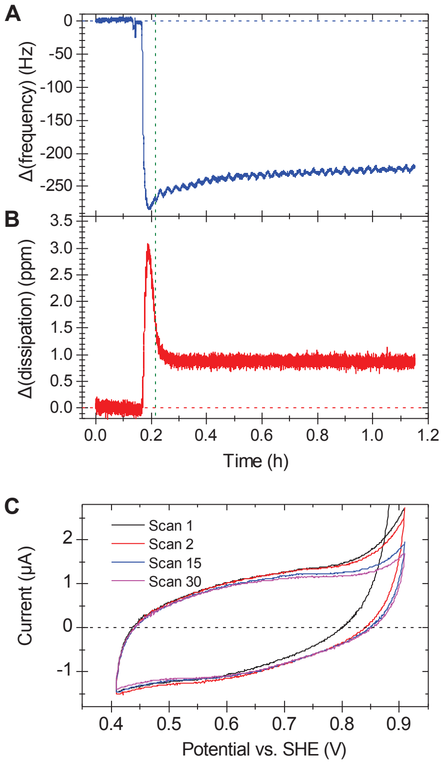

Figure S10. Frequency, dissipation and cyclic voltammetric responses with time for bovine serum albumin (25 µl 24 mg ml^{-1}) adsorbed on a gold-coated QCM sensor modified with 3-mercaptopropionic acid. Panel **A** shows the frequency change, Panel **B** shows the dissipation response, and Panel **C** shows selected CV scans. The vertical green dashed line indicates the start of the voltammetry. Conditions: 0.1 M sodium phosphate pH 6.0 (pre-saturated with O_2), 25 °C, 0.1 ml min^{-1}, seventh harmonic shown. Cyclic voltammetry: 0.70→ 0.20 → 0.70 V vs. Ag|AgCl|3M NaCl, 10 mV s^{-1}. TM

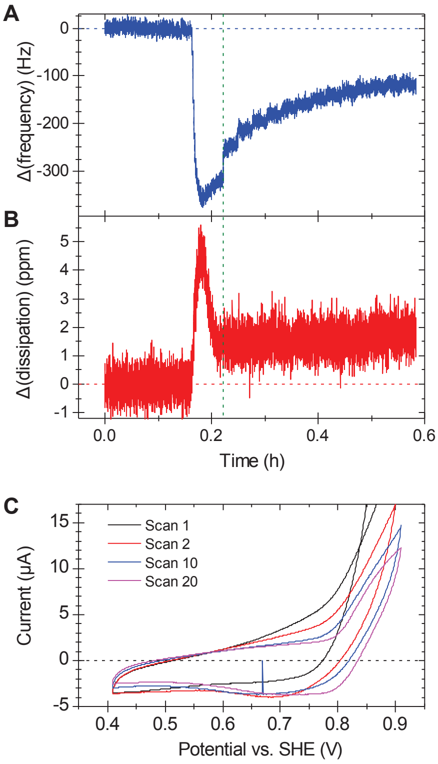

Figure S11. Frequency and current responses with time for *Mv*BOx inhibited with 0.1 mM azide (25 μl 24 mg ml^{-1}) adsorbed on a gold-coated QCM sensor modified with 3-mercaptopropionic acid. Panel **A** shows the frequency change, Panel **B** shows the dissipation response, and Panel **C** shows selected CV scans. The vertical green dashed line indicates the start of the voltammetry. Conditions: 0.1 M sodium phosphate pH 6.0 (pre-saturated with O_2) with 0.1 mM sodium azide, 25 °C, 0.1 ml min^{-1}, seventh harmonic shown. Cyclic voltammetry: 0.70 → 0.20 → 0.70 V vs. Ag|AgCl|3M NaCl, 10 mV s^{-1}.

TM

Section S12 Effect of changing CV scan parameters

Changing to potential range over which the cyclic voltammetry significantly affected both mass and activity loss (Figure S12). Lower the value of the high-potential vertex made no difference to stability, while raising the potential of the low-potential vertex above ca. 0.6 V vs. SHE significantly improved stability and changed the pattern of inactivation to be closer to that of the chronoamperometry case.

Mass and activity are also sensitive to scan rate. Lower scan rates (e.g., Figure S13) lead to much larger losses in activity even though the mass losses are comparable to those from faster scan rates (Table S4).

There was no appreciable difference in the QCM traces when the size of the potential steps for the CVs was varied between 0.1 mV and 10 mV.

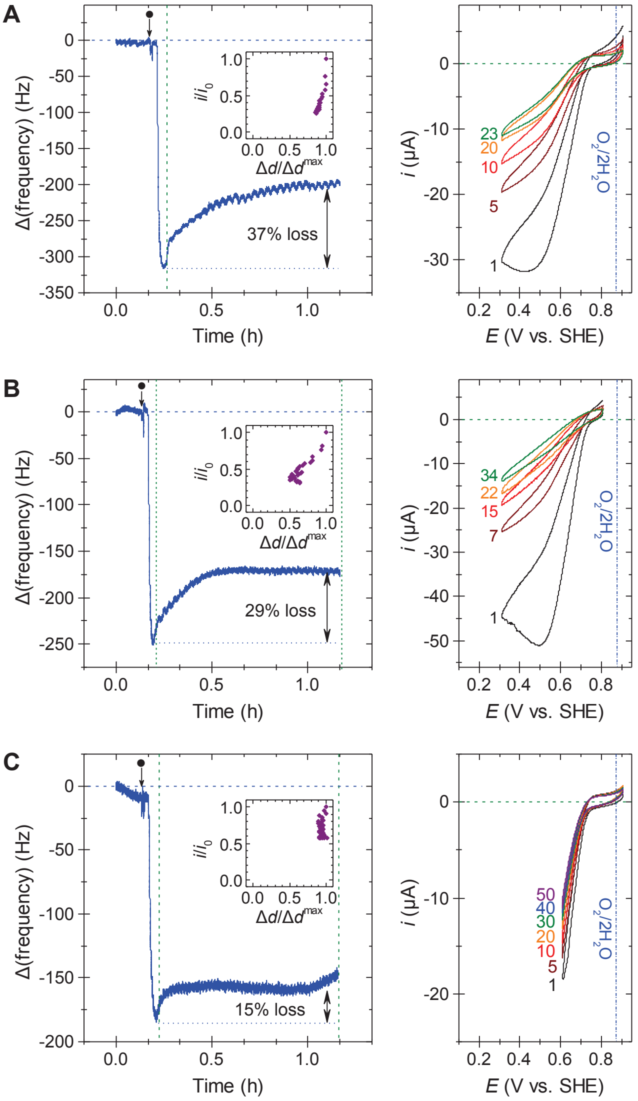

Figure S12. Frequency and electrochemical response to *Mv*BOx adsorbed on a gold-coated QCM sensor modified with 3-mercaptopropionic acid. Panel **A**: 0.70 to 0.10 V vs. Ag|AgCl|3M NaCl (full range); Panel **B**: 0.60 to 0.10 V vs. reference (keeping below potential for four-electron O_2 reduction); Panel **C**: 0.70 to 0.40 V vs. reference (keeping above potential where some reduction occurs in the absence of protein, cf. **Figure S9**). Green dashed lines indicate the period over which cyclic voltammetry scans were run. Circle (●) indicates when 25 μl 24 mg ml^{-1} *Mv*BOx was injected. The insets show the relationship between dissipation and electrocatalytic current. Conditions: 0.1 M sodium phosphate pH 6.0 (pre-saturated with O_2), 25 °C, 0.1 ml min^{-1}, seventh harmonic shown. Scan rate: 10 mV s^{-1}.

TM

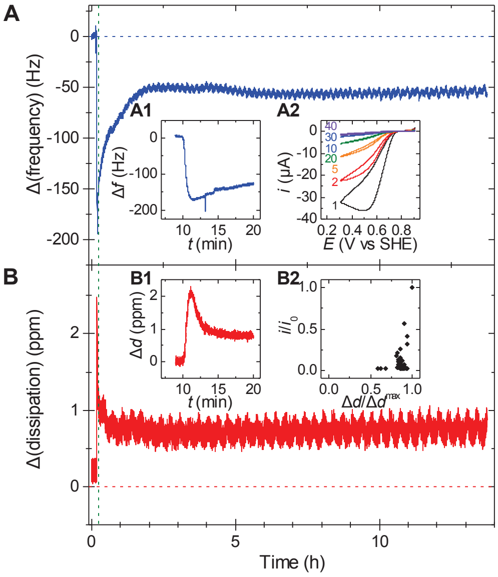

Figure S13. Frequency, dissipation and current responses to *Mv*BOx adsorbed on a gold-coated QCM sensor modified with 3-mercaptopropionic acid when the applied potential is scanned 10× more slowly than the case shown in Figure 2. Panel **A** shows the frequency change. The insets **A1** and **A2** show, respectively, a zoom of frequency during adsorption and cyclic voltammetry scans 1, 5, 10, 20, 30 and 40 of 46 scans. Panel **B** shows the dissipation response. Inset **B1** shows a zoom of the dissipation trace during adsorption. Inset **B2** shows the relation between current and dissipation during the experiment. The green dashed line indicates when cyclic voltammetry was started. Conditions: 0.1 M sodium phosphate pH 6.0 (pre-saturated with O_2), 25 °C, 0.1 ml min^{-1}, seventh harmonic shown. Cyclic voltammetry: 0.70 → 0.10 → 0.70 V vs. Ag|AgCl|3M NaCl, 1 mV s^{-1}.

TM

Table S4. Effect of scan rate on adlayers of *Mv*BOx. Fractional losses are based on readings taken immediately cyclic voltammetry began and 20 minutes after.

scan rate (mV s^{-1})	no. scans	current loss	mass loss
0.1	100	66%	30%
0.01	10	57%	24%
0.001	1	31%	27%

Section S13 Effects of variations in oxygen saturation

The effect of swapping between oxygen and argon flow during constant potential experiments is illustrated in Figure S14. The trace shows a typical pattern of a peak in the dissipation from the formation of a loosely bound layer that washes away quickly, followed by a steady frequency response and an exponential decrease in catalytic current. Changing the buffer purge gas to argon causes the current magnitude to decrease with a first-order time constant of about 780 s; switching back to oxygen causes the current magnitude to increase with a first-order time constant of about 450 s. As indicated by the dotted line in panel **C** (a first-order exponential extrapolation of the current measured before the argon flush), the current magnitude after reoxygenation is slightly higher than would be expected in the absence of an argon purge.

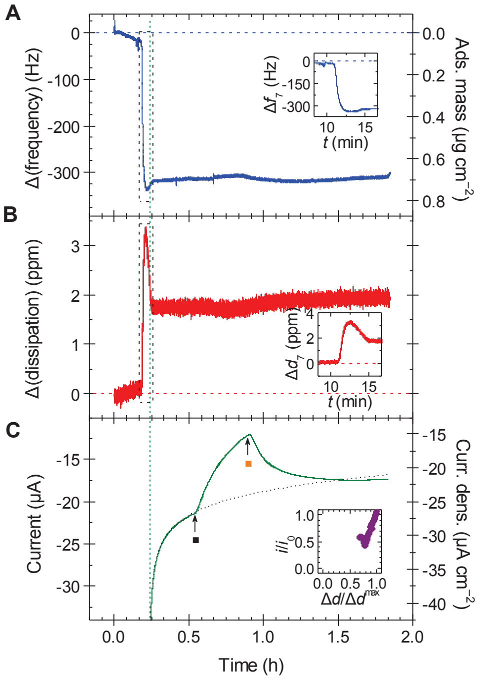

Figure S14. Frequency, dissipation and current response with time for *Mv*BOx adsorbed onto a gold-coated QCM sensor modified with 3-mercaptopropionic acid. The green dashed line shows when a potential of 0 V vs. Ag|AgCl|3M NaCl was applied. Inset in **A** and **B** shows zoomed trace of enzyme adsorption. Square (■) indicates the switch to argon gas saturated buffer solution and (🟧) indicates the switch back to oxygen-saturated solution. Conditions: 0.1 M sodium phosphate pH 6.0 (pre-saturated with O_2), 0.1 M sodium phosphate pH 6.0 (pre-saturated with O_2), 25 °C, 0.1 ml min^{-1}, seventh harmonic shown. Current density based on projected electrode area of 0.80 cm^2.

TM

A ‘mixed mode’ measurement, in which both constant and cycled potentials were used, is shown in Figure S16. After protein adsorption, the applied potential was held constant, then argon-saturated buffer was flowed through the cell. While the oxygen was being displaced, the measurements swapped to cyclic voltammetry. Toward the end of the potential cycling, the oxygen-saturated buffer was reintroduced; some activity remained. After 25 cycles, the potential was again held constant. Both the current and frequency response at this stage were very stable.

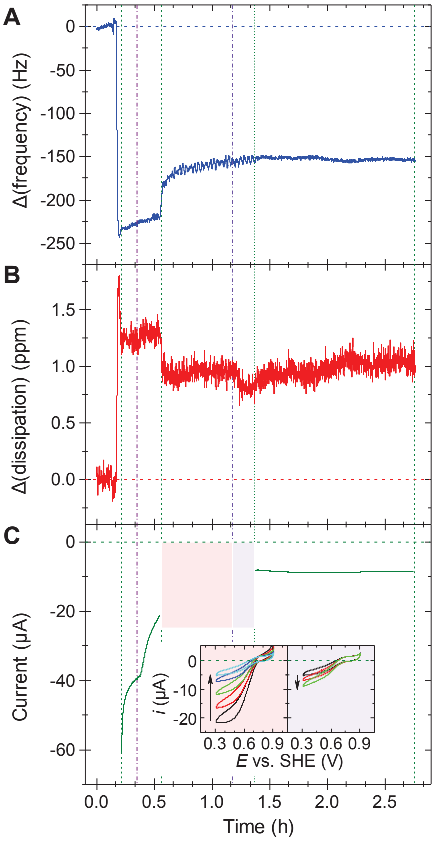

Figure S15. The effect of oxygen on the (**A**) frequency, (**B**) dissipation and (**C**) current response with time for *Mv*BOx adsorbed onto a gold-coated QCM sensor modified with 3-mercaptopropionic acid. The vertical green dashed lines represent the start and end of chronoamperometry measurements (0.1 V vs. Ag|AgCl|3M NaCl). The vertical green dotted lines represent the start and end of cyclic voltammetry (0.70 → 0.10 → 0.70 V vs. reference). The vertical purple dash-dot lines indicate when the solution flowing through the cell was changed to argon saturated buffer. The insets in Panel **C** show the decay in electrocatalytic current as O_2-satured buffer is displaced by argon-saturated solution (left inset; scans 1, 3, 6 and 19 shown) and the partial recovery of current after the argon-saturated buffer is replaced by O_2-saturated solution (right inset, scans 19, 21 and 24 shown). Conditions: 0.1 M sodium phosphate pH 6.0 (pre-saturated with O_2), 25 °C, 0.1 ml min^{-1}, seventh harmonic shown.

KS

Section S14 Measurements on a second multicopper oxidase

We also used a second commercially available multicopper oxidase, laccase from *Trametes versicolor* (*Tv*L). The protein was adsorbed to a gold-coated quartz crystal modified with 3-mercapto-1-propanol, with the adsorption and subsequent cyclic voltammetry performed as for Figure 2 from the main text. Figure S16 shows 50 potential cycles and E-QCM-D responses that parallel those observed for *Mv*BOx.

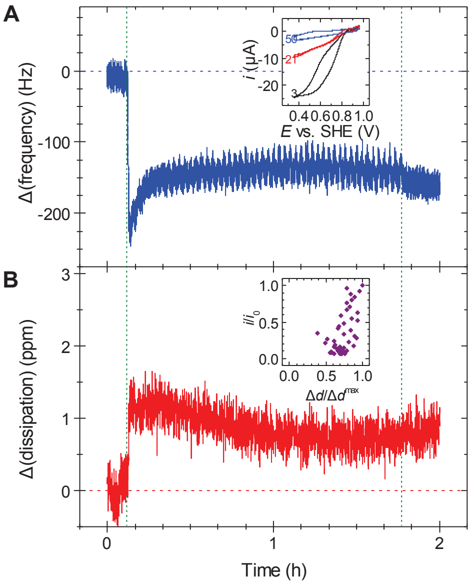

Figure S16. Frequency (Panel **A**) and dissipation (Panel **B**) response to *Tv*L adsorbed on a gold-coated QCM sensor modified with 3-mercapto-1-propanol. The green dashed line indicates when cyclic voltammetry was started and ended. Inset: Cyclic voltammetry of *Tv*L on 3-mercapto-1-propanol. Inset in **A** shows scans 3, 21 and 50; inset in **B** shows the relationship between current and dissipation at each low-potential vertex. Conditions: 25 °C, 0.1 M sodium citrate pH 4.0 (pre-saturated with O_2), 0.1 ml min^{-1}, seventh harmonic. Potential range: 0.75 → 0.15 → 0.75 V vs. Ag|AgCl|3M NaCl, 10 mV s^{-1}.

KS/TM

To compare the effect of covalent attachment to enzymes other than *Mv*BOx (Figure 3, main text) we attached *Tv*L to a DTSSP-modified gold crystal. The covalent attachment occurs through a single reactive lysine residue, Lys174,[17] which is ~32 Å away from the T1 centre, too far for efficient electron transfer from the electrode.[13] The loss of activity is further highlighted in the near absence of a catalytic wave upon potential cycling (panel **A** inset). In contrast to the observations for *Mv*BOx in Figure 3, the frequency magnitude increased when the potential was cycled, though the current vs. dissipation trace (panel **B** inset) was similar.

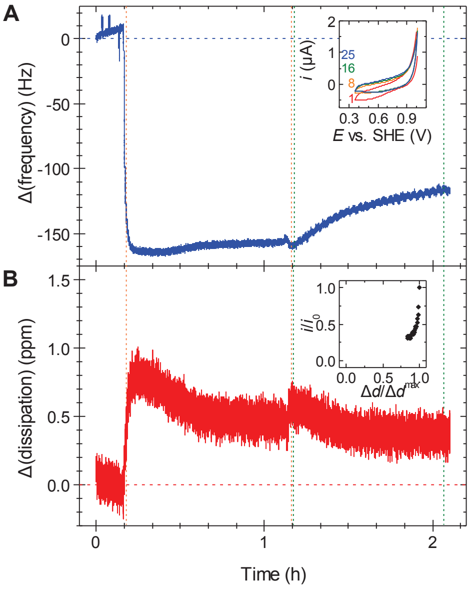

Figure S17. Frequency and dissipation response with time for *Tv*L covalently bound via an amide linkage to a DTSSP-modified QCM sensor. The orange dashed lines represent the time left for enzyme to react with surface layer (reaction adapted from the ref. 18) during which time the peristaltic pump was turned off. The green dashed line shows when potential cycling began with the inset in **A** showing the cyclic voltammograms from scans 1, 8, 16 and 25 of 25 scans. **B** shows the dissipation during enzyme adsorption and the subsequent change on potential cycling. Conditions: O_2-saturated 0.1 M sodium phosphate buffer pH 6.0 at 25 °C flowing at 0.1 ml min^{-1} with continuous O_2 bubbling, seventh harmonic shown. Cyclic voltammetry (CV): 0.80 → 0.15 → 0.80 V vs. Ag|AgCl|3M NaCl, 10 mV s^{-1}.

`TM`

Section S15 Additional Δd_7 vs. Δf_7 traces

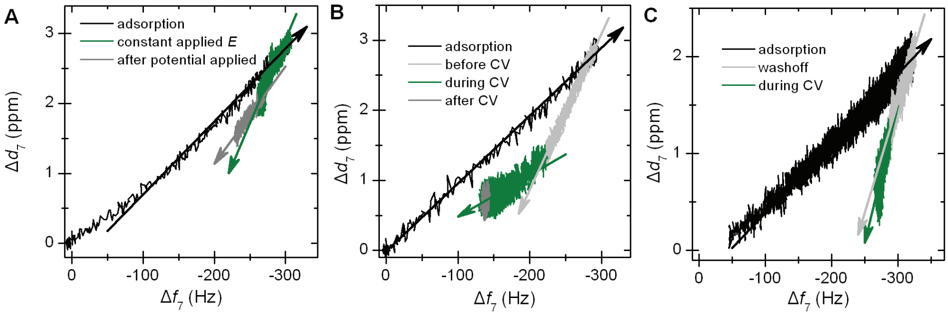

Figure S18. Plots showing correlation between energy dissipation and frequency change for the data plotted in **A** Figure 1, **B** Figure 2 and **C** Figure 3 in the main text.

`KS`

Section S16 References

1. J. A. Cracknell, T. P. McNamara, E. D. Lowe and C. F. Blanford, *Dalton Trans.*, 2011, **40**, 6668-6675.
2. Q-Sense, Q-Sense E1 Module, http://www.q-sense.com/file/q-sense-e1-folder.pdf.
3. G. Sauerbrey, *Z. Phys.*, 1959, **155**, 206-222.
4. Z. Cao, Z. L. Xiao, N. Gu, S. Shimada, T. Fukuda and H. Matsuda, *Solid State Phenom.*, 2007, **121–123**, 385–388.
5. Z. Cao, L. Zhang, C.-Y. Guo, F.-C. Gong, S. Long, S.-Z. Tan, C.-B. Xia, F. Xu and L.-X. Sun, *Mater. Sci. Eng. C*, 2009, **29**, 1051-1056.
6. C. A. Widrig, C. Chung and M. D. Porter, *Journal of Electroanalytical Chemistry and Interfacial Electrochemistry*, 1991, **310**, 335–359.
7. Invitrogen, Amine-Reactive Probe Labeling Protocol | Life Technologies, http://www.invitrogen.com/site/us/en/home/References/protocols/cell-and-tissue-analysis/Labeling-Chemistry-Protocols/Amine-Reactive-Probe-Labeling-Protocol.html.
8. P. Roepstorff and J. Fohlman, *Biol. Mass Spectrom.*, 1984, **11**, 601-601.
9. R. S. Johnson, S. A. Martin, K. Biemann, J. T. Stults and J. T. Watson, *Anal. Chem.*, 1987, **59**, 2621-2625.
10. R. S. Johnson, S. A. Martin and K. Biemann, *Int. J. Mass Spectrom. Ion Processes*, 1988, **86**, 137-154.
11. V. H. Wysocki, K. A. Resing, Q. Zhang and G. Cheng, *Methods*, 2005, **35**, 211-222.
12. FindSurfaceResidues, http://www.pymolwiki.org/index.php/FindSurfaceResidues.
13. C. C. Page, C. C. Moser, X. X. Chen and P. L. Dutton, *Nature*, 1999, **402**, 47-52.
14. E. I. Solomon, U. M. Sundaram and T. E. Machonkin, *Chem. Rev.*, 1996, **96**, 2563-2605.
15. S. Trasatti and O. A. Petrii, *J. Electroanal. Chem.*, 1992, **327**, 353-376.
16. Y. Kamitaka, S. Tsujimura, T. Ikeda and K. Kano, *Electrochemistry*, 2006, **74**, 642-644.
17. J. Sobek, M.Chem. thesis, University of Oxford, 2005.
18. C. M. Moore, N. L. Akers, A. D. Hill, Z. C. Johnson and S. D. Minteer, *Biomacromolecules*, 2004, **5**, 1241-1247.

Chapter 4

Combining electrochemical quartz crystal microbalance with dissipation monitoring and dual polarisation interferometry analyses to optimise the mass-specific activity of bilirubin oxidase adlayers

4 Combining electrochemical quartz crystal microbalance with dissipation monitoring and dual polarisation interferometry analyses to optimise the mass-specific activity of bilirubin oxidase adlayers

In this paper, electrochemical quartz crystal microbalance and dual polarization interferometry were paired in order to study deposition conditions of a multicopper oxidase (MCOs). The selective and efficient biocatalysts of the high-potential MCO bilirubin oxidase was compared with changes in concentration and surface charge. Changes in activity were linked with the adsorption mechanisms, structural rearrangements and desorption.

I wrote the paper and completed all experimental work. Kulveer Singh was responsible for modification of the E-QCM-D flow module. Thomas McNamara contributed to the computer modelling sections for *Mv*BOx adsorption on QCM and DPI. Christopher Blanford helped write and edit the paper.

Optimizing the mass-specific activity of bilirubin oxidase adlayers through combined electrochemical quartz crystal microbalance and dual polarization interferometry analyses

Trevor McArdle,† Thomas P. McNamara,† Kulveer,†,‡ Christopher F. Blanford†,*

†School of Materials and Manchester Institute of Biotechnology, 131 Princess Street,
Manchester, M1 7DN, UK.

‡Department of Chemistry, Inorganic Chemistry Laboratory, University of Oxford, South
Parks Road, Oxford, OX1 3QR, UK.

E-mail: christopher.blanford@manchester.ac.uk

Abstract

This study paired two surface analysis techniques, dual polarization interferometry (DPI) and analysis by an electrochemical quartz crystal microbalance with dissipation capability (E-QCM-D) to find the deposition conditions that give the highest and most stable electrocatalytic activity per adsorbed mass of enzyme. Layers were formed by adsorption from buffered solutions of bilirubin oxidase from *Myrothecium verrucaria* at pH 6.0 to planar surfaces, under high enzyme loading (≥ 1 mg ml^{-1}) for contact periods up to 2 min. Both unmodified and carboxylate-functionalized gold-coated sensors showed that a deposition solution concentration of between 10–25 mg ml^{-1} gave the highest activity per mass of adsorbed enzyme with an effective catalytic rate constant (k_{cat}) of about 40 s^{-1}. The densification of adsorbed layers observed by DPI correlated with reduced bioactivity seen from E-QCM-D. Post-adsorption changes in thickness and density observed by DPI were incorporated into Kelvin-Voigt models of the QCM-D response. The modeled response matched experimental observations when the adlayer viscosity tripled after adsorption. Methyl-terminated surfaces produced rapid loss of enzyme activity, attributed to denaturation and dehydration. Positively charged surfaces produced adlayers with comparable physical properties to those formed on negatively charged surfaces, but with a much lower activity, which was ascribed to unfavorable enzyme orientation for rapid electron transfer. Increasing the chain length of the modifier on carboxylate-terminated surfaces produced a reduction in activity per adsorbed mass, but increased stability to potential cycling.

Introduction

Enzymes used in biotechnological processes are often immobilized to create heterogeneous catalysts that are readily isolated from a reaction mixture.[1, 2] A persistent challenge in enzyme immobilization is maintaining catalytic activity in spite of energetic and steric effects that render some of the immobilized enzyme inactive or ineffective.[3] For example, a protein may spread and denature on adsorption, or be oriented so that access to substrate binding sites is blocked.[4, 5] The situation is more complex in bioelectrocatalytic systems: oxidoreductases, enzymes that catalyze electron-transfer reactions, must also be encapsulated or positioned in a way that ensures that electron transfer does not limit the overall reaction rate.[6-8] Solutions to these challenges include entrapment of enzyme in hydrogels containing tethered electron-transfer mediators that surround the enzyme[9] and the use of substrate mimics to orient and stabilize enzymes.[10]

This study follows from observations that the most stable and active enzyme adlayers were formed from concentrated protein solutions, often in excess of 10 mg ml^{-1}. Here we present a systematic investigation into the origin of these observations using bilirubin oxidase from *Myrothecium verrucaria* (*Mv*BOx), a 64kDa multicopper oxidase (MCO). MCOs are a family of copper-containing enzymes that includes laccases, ascorbate oxidase and ceroluplasmin and can catalyze the four-electron reduction of O_2 to water with a higher thermodynamic efficiency (lower overpotential) than platinum.[11, 12] For this reason, MCOs have been extensively researched as real or inspirational catalysts for cathodes on low-temperature fuel cells.[7, 8, 13]

Bilirubin oxidase contains four copper atoms in two active sites. Dioxygen is reduced to water at a buried trinuclear cluster of copper ions. Electrons for this reduction enter the enzyme through a lone "Type 1" copper separated from the protein's surface by a single histidine residue. In nature, these electrons are typically supplied by the oxidation of organic substrates or ferrous iron.[14] When bilirubin oxidase is immobilized on an electrode, the lone copper needs to be no more than 1–2 nm from the electrode surface to avoid interfacial electron transfer being the rate-limiting step in oxygen-reduction electrocatalysis.[15, 16] Therefore to obtain the highest current density for a given amount of enzyme, enzyme adsorption must promote correct orientation.

Larger proteins do not behave like rigid particles and deform on adsorption depending on pH, temperature, concentration, surface chemistry.[4, 5, 17] While many studies exist for the adsorption of model proteins such as lysozymes and albumins, publications on how adsorption affects biocatalytic function are rarer.[18]

Pankratov et al. showed a direct comparison between laccase and bilirubin oxidase adsorbed onto bare gold surfaces.[7] They observed laccase to be completely catalytically inactive, even after direct addition of an electron donor (ABTS) suggesting rapid enzyme denaturation upon adsorption. Bilirubin oxidase showed a similar turnover frequency for the adsorbed enzyme, as for the enzyme in solution. However, the catalytic activity dropped to less than 50% in only 3 hours, which they attributed to conformational changes of the enzyme.

Herrera et al. investigated the surface coverage of D-amino acid oxidase and its relationship to surface bio-activity.[18] Surface filling and relaxation times of the adsorbing protein were monitored for different experimental conditions using *in situ* amperometry and *ex situ* spectrophotometry. On silica, when the substrate and enzyme are oppositely charged, the relaxation step occurred at the same rate of surface filling. For unfavorable electrostatic conditions, the relaxation time occurred over larger time. Bio-activity was irrespective of the surface coverage in both cases. Adsorption to gold showed the relaxation step was driven by hydrophobic interactions and highly dependent on surface coverage. Therefore surface activity was only maintained at high surface coverages.

Surface modifiers such as organothiols and organosilanes offer a straightforward method to control the surface chemistry of electrodes. Long-chain alkylthiols, in particular, can produce highly organized monolayers, allowing the terminal groups to change the properties of the surface.[19, 20] Olejnik et al. studied laccase adsorption on functionalized gold electrodes of phenyl groups ending with aminoethyl or carboxyethyl entities.[6] In this case, the aminoethyl functionality increased the oxygen reduction activity of laccase. This was ascribed to the closer proximity of the T1 site to the electrode. Singh el al. investigated physical adsorption and covalent attachment of *Mv*BOx onto carboxylate-terminated SAMs. They showed how rapid enzyme deactivation occurred during cycling of the potential and that covalent attachment failed to increase activity or stability.[8] Ulyanova et al. evaluated immobilization methods for two MCOs by comparing the catalytic response in the presence and absence of an electron-transfer mediator.[21]

An electrochemical quartz crystal microbalance with dissipation analysis (E-QCM-D) is a device that can simultaneously measure adsorbed mass (through a drop in resonant frequency), provide information on layer rigidity (through the rate of dissipation of stored energy in the resonator), and quantify catalytic activity (through electrochemical measurements).[22] The maximum mass sensitivity is given as 0.5 ng cm^{-2},[23, 24] about 0.1–0.2% of a saturated layer of *Mv*BOx. The E-QCM-D probes the *hydrated* mass of the adsorbed layer due to coupling of water within and around the proteins.[25] Dissipation is a measurement of how much vibrational energy from the oscillating crystal is lost per cycle.[26] Energy loss relays information about the rigidity of the adsorbed layer and how its changes with time, i.e., structural changes or dehydration.[27]

Dual polarization interferometry (DPI) complements E-QCM-D measurements by probing the *dry* mass of an adlayer.[28] An adlayer on a sensing waveguide changes the refractive index (RI) phase of light relative to a reference waveguide. The use of two polarizations of incident light allows these two parameters to be resolved and from there, the density, mass and thickness of the adlayer can be calculated.[29]

Studies combing the QCM with similar optical techniques, such as surface plasmon resonance (SPR) can give complementary hydrated and dry adsorbed masses of proteins. Caruso et al.[30] showed the advantage of using QCM with SPR to give the wet and dry mass of ferritin. However, in SPR, light of only one polarization (TM) is used to determine the mass per unit area of adsorbed films. SPR cannot determine both the thickness and the refractive index simultaneously.[31] There have been several studies relating QCM-D to DPI,[32, 33] such as comparing the lysozyme adsorption on silica surfaces at different coverage values.[34] Low coverage showed an irreversibly adsorbed layer being formed, increasing coverage showed reorganization effects leading to monolayer coverage. This study, however, only deduced the orientation as a function of layer thickness, rather than give any quantitative measurements of conformational changes. QCM-D has also been used to study the adsorption of bovine serum albumin (BSA) on gold sensors in the presence and absence of NHS alkane thiol SAMs.[35] They observed that protein concentration during the immobilization step change the morphology and subsequent ligand bind of the adlayer, yet had little effect on surface saturation.

This current work follows non-equilibrium surface adsorption of *Mv*BOx to bare and SAM-modified surfaces using QCM and DPI. The first aspect of this study establishes how the mechanics and catalytic activity of an adlayer are affected by deposition solution concentration. The second shows how surface charge and chemistry affect mass-specific catalytic activity. The optimization method developed here can be applied to other oxidoreductases to improve the sensitivity and range of experiments available for analytical protein film electrochemistry[36] and to enable enzymatically catalyzed generation of fine chemicals (industrial biotechnology).[22]

Experimental

Materials and reagents

Lyophilized *Mv*BOx powder (Amano Enzyme EU, Chipping Norton, UK) was dissolved in 0.1 M sodium phosphate buffer pH 6.0 at 4 °C. The solution was purified by centrifugation through polyethersulfone membrane (Vivaspin, 30 kDa MWCO) to remove small-molecular-weight contaminants. Protein concentration was calculated by UV absorption, using $\varepsilon_{280\ \mathrm{nm}} = 9.52 \times 10^4\ \mathrm{M^{-1}\ cm^{-1}}$, calculated from the enzyme amino acid sequence.[37] Bovine serum albumin (BSA) (lyophilized powder, crystallized, ≥98.0% Sigma Aldrich) was dissolved in 0.1 M sodium phosphate pH 6.0.

Solutions of *Mv*BOx were prepared from dilutions of higher concentration stock solutions, which were stored in the gaseous phase above liquid nitrogen. BSA solutions were made up fresh to the desired concentration and stored at 4 °C. For *Mv*BOx, concentrations range from 1 mg $\mathrm{ml^{-1}}$ to 50 mg $\mathrm{ml^{-1}}$, for BSA 0.1 mg $\mathrm{ml^{-1}}$ to 100 mg $\mathrm{ml^{-1}}$.

Silica surfaces were functionalized with 5wt% solutions of trimethoxy(propyl)silane (TMOPS, ≥97%Sigma), (3-aminopropyl)triethoxysilane (APTES, ≥98% Sigma), dissolved in toluene and 3-(trihydroxysilyl)propane-1-sulfonic acid (THSPS, Flurochem) dissolved in ethanol. Gold surfaces were modified with 10 mM ethanolic solutions of 3-mercaptopropionic acid (3MPA, >99%, Fluka), 6-mercaptohexanoic acid (6MHA, Sigma 98%), 2-aminoethanethiol (2AE, Acros Organics >98%), 6-aminohexanethiol, propanethiol (Sigma 98%) and heptanethiol (Sigma 98%).

All further chemicals listed were used with in general surface preparation and buffers: hydrochloric acid (37%, Fisher), sodium dihydrogen orthophosphate dihydrate (99.0–101.0%, Fisher), disodium hydrogen orthophosphate anhydrous (99.5+%, Fisher), trisodium citrate dihydrate (≥99%, Sigma), citric acid monohydrate (≥99%, Sigma), sulfuric acid (1.83 g ml^{-1}, >95%, Fisher), hydrogen peroxide (30% w/v, Scientific Laboratory Supplies) 3,3ʹ-dithiobis(sulfosuccinimidylpropionate) (DTSSP, >98%, ProChem Inc.). For buffer were prepared from weak acid and complementary base, rather than titrating with strong acid or base

All chemicals were used as received without further purification. Water was purified via reverse osmosis and ion exchange to a resistivity of 18.2 MΩ cm at 25 °C using a MilliQ water purifier.

Electrochemical quartz crystal microbalance with dissipation analysis

A Q-sense E1 system was used to measure protein adsorption along with Q-soft data acquisition software (version 2.5.18.682). For QCM-D measurements, a standard Q-sense flow module 401 was used (140 µl total volume, 40 µl sample chamber over sensor). E-QCM-D measurements used a modified Q-Sense QEM401 module with a 0.1 ml sample chamber volume (see SI). Sensors (Q-Sense) were 14mm-diameter AT-cut quartz crystals with a fundamental frequency of 4.95 ± 0.05 MHz. Sensors were coated with gold or silica on gold, both with a titanium adhesion layer. The flow module and fluid handling system were positioned on an aluminum plate maintained at 25 °C using an internal water flow. The temperature of the flow module was stabilized to within 10 mK using the E1's integrated Peltier device.

QCM measurements started with a flow of buffer until a stable response was obtained, typically 30 minutes for the QCM-D and longer for the E-QCM-D. Liquids were pulled through the cell with a peristaltic pump at 0.1 ml min^{-1}. Aliquots of *Mv*BOx and BSA solutions were introduced to the cell by pausing the flow to swap between buffer and protein solution. Time between sample loading and sensor interaction was approximately 2 minutes.

Adsorbed mass (typically shown as secondary *y*-axes) was estimated using the Sauerbrey equation:

$$\Delta m = -\frac{C}{N}\Delta f_N \tag{1}$$

where Δm is the adsorbed mass, N is the harmonic number, Δf_N is the frequency response associated with that harmonic, and C a proportionality constant equal to 17.9 ng $\mathrm{cm^{-2}\ Hz^{-1}}$).

The catalytic current (i_{cat}) is proportional to both the surface coverage (Γ) and turnover frequency (k_{cat}) (Equation 2),

$$i_{\mathrm{cat}} = -nFA\Gamma k_{\mathrm{cat}} \tag{2}$$

where n is the stoichiometric number of electrons transferred (4 for O_2 reduction to water), F is the Faraday constant, and A is the electrode area. The negative sign indicates reduction.

For films with low dissipation values and a constant hydrated protein mass (M_{H}), the ratio of catalytic current to frequency change is directly proportional to the average catalytic rate for the adsorbed enzymes (Equations 3a and 3b),[22] with a proportionality constant of 1.1×10^{-8} C s for *Mv*BOx.[8] This mass-specific catalytic activity is the key parameter for adlayer optimization.

$$\frac{i_{\mathrm{cat}}}{\Delta f_N} = \frac{C\,n\,F\,A}{N\,M_{\mathrm{H}}}\,k_{\mathrm{cat}} \tag{3a}$$

$$\frac{i_{\mathrm{cat}}}{\Delta f_N} \propto k_{\mathrm{cat}} \tag{3b}$$

The 7th harmonic was used for data analysis. Frequency changes presented in the manuscript have not been divided by the harmonic number except where noted; this differs from the harmonic-normalized frequency response that Q-Sense software displays.

An Ivium CompactStat potentiostat was used for electrochemical measurements. A three-electrode system was used: the gold-coated QCM sensors acted as the working electrode (0.8 $\mathrm{cm^2}$), a 0.2 mm thick 2.25 $\mathrm{cm^2}$ rectangle of platinum located 0.7–0.8 mm from the working electrode acted as counter electrode and a Ag|AgCl|3M NaCl reference electrode (BASi RE-6, $E_{\mathrm{SHE}} = E_{\mathrm{ref}} + 0.21$ V).[8] Buffer was pre-oxygenated with industrial-grade O_2 (BOC) for at least 20 minutes prior to any electrocatalytic measurements. The potential for cyclic voltammetry measurements was swept between 0.7 and 0.1 V vs. reference at 10 mV $\mathrm{s^{-1}}$. A surface area of 0.8 $\mathrm{cm^2}$ was used for current density calculations.[8]

Dual polarization interferometry

An *Ana*Light 4D (Farfield Group Ltd., Manchester, UK) was used to measure protein interaction with ~1s time resolution. The sensor chip is a dual slab, which is made of silicon oxide slightly doped with nitrogen. A HeNe 632.8 nm laser is used to illuminate the optical waveguide.

Protein was adsorbed on silicon oxynitride FB80 *Ana*Chips (dimensions 24 mm × 6 mm, Farfield Group Ltd.) clamped inside a temperature-controlled housing. Two flow paths were defined by a fluorosilicone mask set on the chip (10µl sensing volume, 15mm^2 sensing area). The instrument was maintained at 25 °C. The chip surface was calibrated with bulk buffer (0.1M sodium phosphate pH 6.0), solutions of ethanol:water (80:20 w/w) and water, all at 25 °C. The flow rate was controlled by a mechanical syringe pump (Harvard). The injection loops were cleaned with 200 µl each of 2wt% SDS in water, 2wt% Hellmanex in water, then isopropanol. Data was analyzed using *Ana*light Explorer Software (Farfield Ltd.) to calculate RI, mass, thickness and density.

Surface modification

Sensors for QCM and DPI were cleaned in piranha solution (3:1 v:v H_2SO_4 and H_2O_2) for 15 minutes at 80 °C. The crystal was washed with water then dried under nitrogen and exposed to UV/ozone treatment for 15 minutes. Bare crystals were stored for 16 hours under ambient conditions before being used. Chemically modified DPI and QCM sensors were placed in the modification solution then stored under a house nitrogen atmosphere for 16 hours before being dried under nitrogen and used.

Protein solution viscosity and density measurements

Viscosity measurements were recorded using a AMVn Automated Microviscometer (Anton Paar). Buffered protein solutions of 1–30 mg ml^{-1} were prepared and measured twice. Intrinsic viscosity was calculated using both the Huggins and Kraemer approach. Solution densities were calculated gravimetrically using 100 and 1000 µl aliquots.

Frequency and dissipation modeling

Modeling the QCM-D response of the protein adlayer was based upon a Kelvin-Voigt model and used equations derived by Voinova et al.[26] and Rodahl,[38] and implemented in Matlab. The introduction of the protein solution into the QCM cell was modeled as an instantaneous change from buffer to 15 mg ml^{-1} enzyme solution, a residence time of 30 s in which the protein concentration remained constant, followed by a drop in concentration modeled as a first-order exponential with a time constant of 60 s. Enzyme absorption was modeled by the Langmuir equation using a finite-time difference method with the coverage being proportional to the average thickness. The time steps were decreased to 10 ms when convergence was observed. The density of a 64kDa protein (1 450 kg m^{-3}) was based on a published correlation between molecular weight and density.[39] The adlayer shear and viscosity values were estimated using QTools and based upon the frequency and dissipation responses from harmonics 5, 7 and 9 for a 15 mg ml^{-1} adlayer on a 3MPA-coated sensor 15 min. after adsorption. For models which described the behavior of pre-absorbed layers undergoing a physical change, time constants for the increase in density and decrease in thickness were derived from the DPI data in Figure 6.

Results and Discussion

Concentration effects on bare gold and carboxylate-terminated surfaces

Adsorption on QCM sensors

The effects of increasing concentration on adsorption and bioactivity of *Mv*BOx adsorbed to bare gold and carboxylate–terminated surfaces have been investigated. E–QCMD measurements were recorded for concentrations ranging from 1–50 mg ml^{-1}. A typical QCM-D experiment is shown in Figure 1A, where the frequency and dissipation responses are given for 25 μl of 25 mg ml^{-1} *Mv*BOx adsorbing onto a 3MPA-modified sensor.

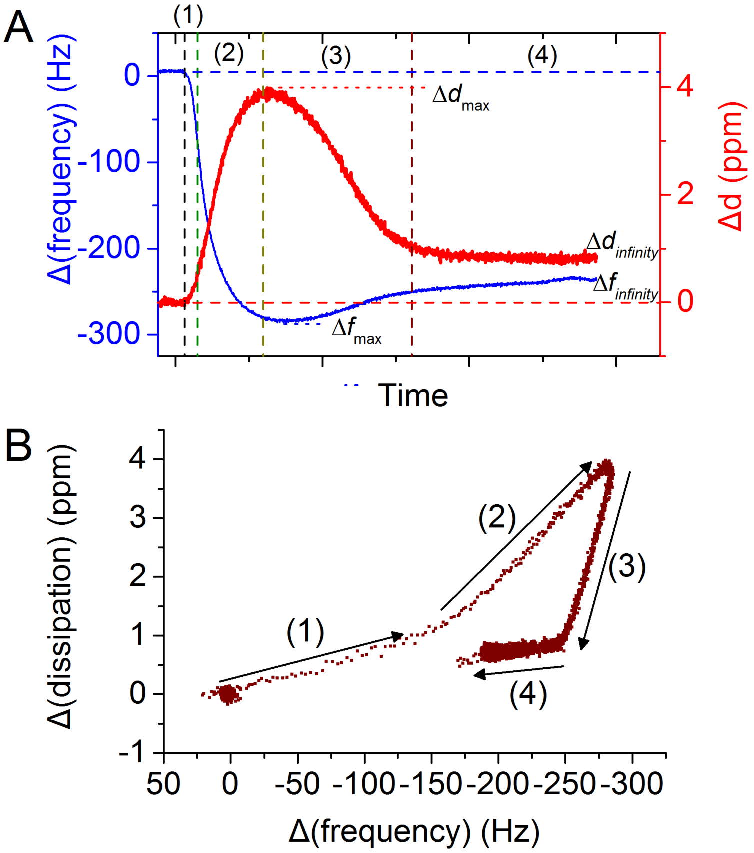

Figure 1. Typical QCM-D response for *Mv*BOx adsorbed onto a 3MPA-modified gold-coated QCM sensors. Panel A shows frequency and dissipation response. Panel B shows Δ*d* vs. Δ*f* plots labeled into four distinct regions which correlate to regions of adsorption shown in A. Conditions: 0.1M sodium phosphate buffer pH 6.0 at 25 °C with continuous O_2 bubbling, 25 mg ml^{-1}, 25 µl *Mv*BOx sample volume, seventh harmonic shown. Flow rate 0.1 ml min^{-1} TM

The adsorption process showed a consistent pattern with four distinct regions. These region are also mapped by plotting Δ*d* vs. Δ*f* (Figure 1B) which normalizes the amount of energy lost from non-rigid adlayer to the adsorbed mass. To a first approximation, steeper slopes correspond to less rigid layers.

In region (1), an initial decrease in frequency (Δ*f*) and a concomitant increase in dissipation (Δ*d*) are observed as the protein begins to adsorb onto the sensor. This initial adsorption is ascribed to the formation of an irreversible rigid layer. Once a critical surface coverage point is reached, the magnitude for Δ*f* and Δ*d* increases, to give a second stage of adsorption region (2), until a maximum is observed for both frequency and dissipation, labeled Δf_{max} and Δd_{max}, respectively and indicative of the formation of a less rigid layer of protein. Once the maximum magnitude change passes, a rapid reverse is observed for dissipation in region (3) along with a small magnitude increase for frequency (mass loss) until a stable layer is formed. A final region shows a slow decrease in frequency and dissipation observed over a longer time scale, labeled region (4). This is due to slower relaxation and resulting dehydration and desorption.[22] Final frequency and dissipation values of the adsorbed layers are designated Δf_∞ and Δd_∞.

The QCM response for enzyme loading at high concentration of *Mv*BOx on to a 3MPA-coated sensor (comparable data for bare gold are shown in the SI) is shown in Figure 2. Roughly 5 minutes after adsorption, cyclic voltammetry (CV) wass started to assay the bioelectrocatalytic activity of the protein film, which is discussed further on.

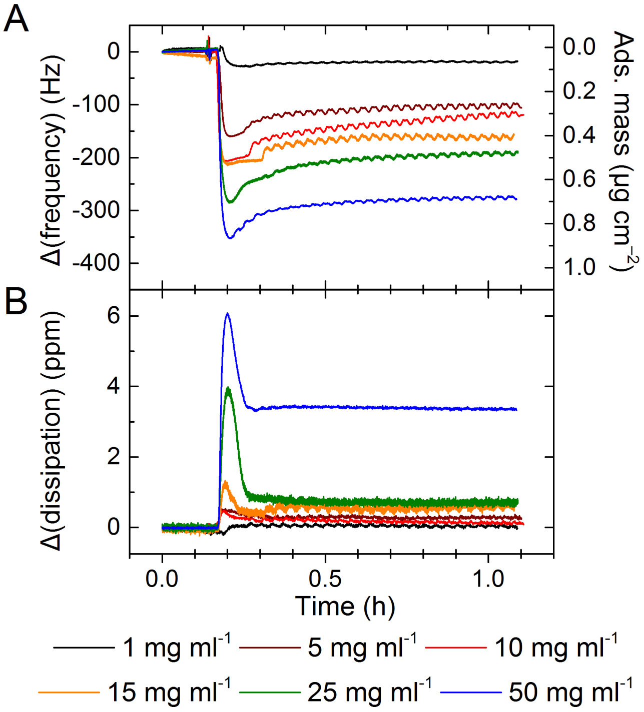

Figure 2. Effect of varying *Mv*BOx concentration on 3MPA-modified gold-coated QCM sensors. The top panel shows the QCM frequency response, and the bottom panel shows the dissipation response. Oscillations on the traces are from cyclic voltammetry being run. Conditions: 0.1M sodium phosphate buffer pH 6.0 at 25 °C with continuous O_2 bubbling, 0.1 ml min^{-1}, 25 μl *Mv*BOx sample volume, seventh harmonic shown. CV potential cycled between 0.91–0.31 V *vs*. SHE at 10 mV s^{-1} TM

The CV causes oscillations in both frequency and dissipation traces as a result of an alternating electric field. As the concentration increases, the surface coverage increases as shown be the magnitude change in frequency. For a saturated monolayer, based on the molecular footprint of *Mv*BOx (SI) the magnitude of a monolayer's theoretical frequency shift for the seventh harmonic is ca. 300 Hz.[8]

As the concentration was increase, the frequency and dissipation responses both increased for adsorption to unmodified gold and carboxylate-terminated surfaces (Figure 3A & B). The "normalized" dissipation ($\Delta d/\Delta f$) increased with the deposition solution concentrations above 5 mg ml^{-1} for adsorption stages (1) and (2) on 3MPA-coated surfaces (Figure 3C & D), whereas unmodified gold surfaces only showed a concentration dependence for adsorption stage (2). As the concentration increased, the amount of frequency and dissipation "overshoot" of frequency and dissipation also increased.[5] In order to test how much of the overshoot was due to bulk solution changes, rather than surface-bound protein measurements with longer solution contact times of 45 seconds (75 µl, three times larger) were carried out. QCM-D data for concentrations ranging 5–25 mg ml^{-1} are given in the SI.

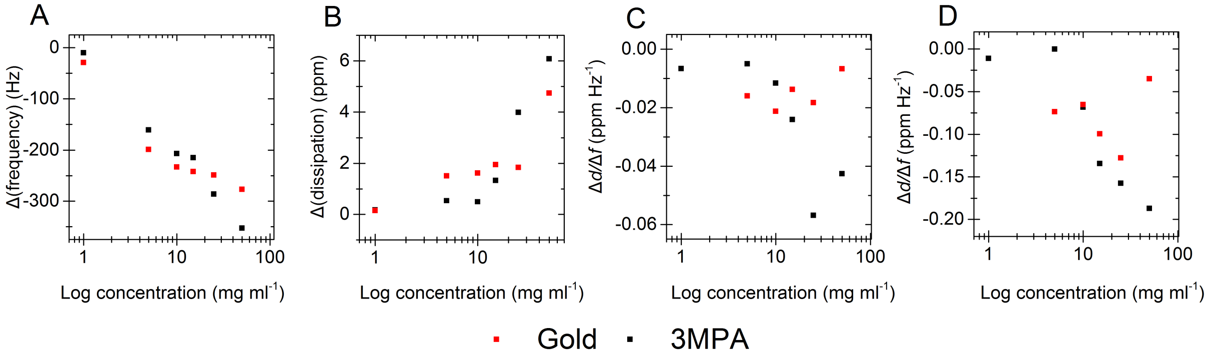

Figure 3. QCM analyses for *Mv*BOx adsorption to bare gold and 3MPA-modified QCM sensors for concentrations ranging from 1–50 mg ml^{-1}, shown on semilog plots. A Δf_{max}, B Δd_{max}, C $\Delta d_{max}/\Delta f_{max}$ for stage (1) of adsorption, D $\Delta d_{max}/\Delta f_{max}$ for stage (2) of adsorption. TM

Comparing adsorption between 15 and 45 seconds, the $\Delta d / \Delta f$ regions (1) and (2) on gold and 3MPA are much lower for 45 seconds indicating a more rigid layer being formed. Region (1) adsorption for longer contact times on 3MPA showed a dependence on the concentration, whereas gold did not. Longer contact times did not indicate any different significant increases in frequency or dissipation responses for maximum or final layers for concentrations on both 3MPA and gold.

To compare the adsorption mechanisms of increasing deposition concentrations of a similarly sized globular protein, BSA, was adsorbed onto bare silica QCM sensors (SI). A different adsorption mechanism was observed for BSA. The Δd vs. Δf plots for BSA did not show distinct regions (1) and (2) for adsorption like *Mv*BOx. Instead one single stage was observed with increasing $\Delta d/\Delta f$ as the concentration increased. Over the range of concentrations investigated (0.1–100 mg ml^{-1}), the magnitude of $\Delta f_{\max}$ for BSA was approximately a third lower than for *Mv*BOx on unmodified gold or 3MPA-modified sensors. Dissipation responses for BSA increased linearly with increasing concentrations and were higher than the same concentrations of *Mv*BOx.. Although this is not a direct comparison to increasing concentrations of *Mv*BOx on gold, *Mv*BOx adsorbed to bare silica (SI) still shows a distinct two-stage adsorption process suggesting it is a protein- and surface-specific characteristic, and not just surface dependent.

Changes in adsorbate–surface interactions were compared using $\Delta d/\Delta f$ values for the first two-adsorption regions as shown in Figure 1B. Increasing the concentration of *Mv*BOx on 3MPA-coated sensors showed that above 10 mg ml^{-1} an increase in the $\Delta d/\Delta f$ was observed for region (1). This was not the case for gold, which showed no concentration dependence on the adlayer being formed during the initial stage of adsorption. This shows that the $\Delta d/\Delta f$ values are not just a bulk solution affect, rising with increased concentration, but an enzyme-surface interaction.

At concentrations below 10 mg ml^{-1}, the low $\Delta d/\Delta f$ value suggests a rigid layer is initially formed, which can be attributed to a higher rate of the protein spreading on the surface to the rate at which fresh protein is adsorbed. At lower concentrations, the adsorbed protein has time to relax on the surface and form a more rigid layer. As the solution concentration is increased, the rate of adsorption will also increase, therefore reducing the amount of enzyme relaxation due to neighboring protein electrostatic repulsion and steric hindrance.[18] *Mv*BOx has a pI or around 4.1, so at pH 6, will have a overall negatively charged surface.[40] It is hard to generalize the surface charge of gold under experimental conditions, but the carboxylate-terminated surface will be negatively charged. This will therefore generate electrostatic repulsion between the adsorbing enzyme, and could reducing the rate surface spreading. For stage (1) adsorption to bare gold surfaces, protein spreading will be governed by a hydrophobic effect and occurred on different time scales to the electrostatic spreading seen for the carboxylate surface.[7, 18] This could mean that at higher concentrations (and the rate of surface adsorption is proportional to solution concentration), you may be slowing down this rate through these charge effects.

Fraser et al. observed for cubosome adsorption to avidin biotin at concentrations above a 0.1 mg ml^{-1}, rapid binding kinetics lead to chaotic and disordered adlayers. QCM-D measurements showed reduced surface coverage and higher levels of surface reorganization with increasing concentration.[41] This would be reflected by smaller slightly smaller Δf but larger Δd peaks. This matches the data observed for final layers on bare gold, but not to 3MPA. This study was from equilibrium adsorption, and cubosomes were on the size order of 150 nm, compared with 5-6 nm enzymes. It could be suggested that 3MPA inhibits chaotic binding, due to a slower binding kinetics, which in turn produce a more stable ordered layer.

The magnitude of $\Delta d/\Delta f$ is larger for adsorption to unmodified gold for region (1) (Figure 1B) than for 3MPA for concentrations 10 mg ml^{-1}, which is evidence for a more rigid. However, as the concentration of the deposition solution increases, this swaps, and gives a more flexible layer for the 3MPA surface. The magnitude of $\Delta d/\Delta f$ for stage (1) on gold does not show a dependence on concentration, suggesting the rate of spreading is not influenced by the increased protein–protein interactions at the surface. Similar trends were shown for the larger injections volumes (SI). Region (2) $\Delta d/\Delta f$ increased for both 3MPA and gold showed an increase with increasing concentration to form a mostly reversibly bound adlayer.

For similar concentrations, adsorption stage (2) on gold showed a lower $\Delta d/\Delta f$ than for 3MPA, (Figure 3D) meaning the adlayer being formed was much more rigidly bound. This can be accounted for by increased surface spreading on bare gold for the first initial stage. This can also explain why above a concentration of 5 mg ml^{-1} of *Mv*BOx adsorbed to gold, there is much smaller variation in the adsorbed mass when compared with 3MPA adlayers due to less free space available.

Longer contact times showed Δd vs. Δf plots still followed a two-stage adsorption profile, however, the viscoelasticity of the layers at longer contact time were more rigidly bound. The Δf_{max} and Δd_{max} increase with concentration as for the short contact times, which show these values to have dependence on the bulk solution, since overall mass loading was lower.

Effect of *Mv*BOx concentration on specific activity

In order to assess the mass-specific oxygen reduction activity for *Mv*BOx films, cyclic voltammetry was performed for 25 scans between 0.31 and 0.91 V vs. SHE. The potential sweep in CV measurements has been shown to destabilize adlayers of *Mv*BOx and was used here to accelerate the desorption of any loosely bound protein and to quickly reach a steady-state frequency response.[8]

A comparison of first CV scan for *Mv*BOx adsorbed onto unmodified and 3MPA-coated sensors from solutions with concentrations from 1 to 50 mg ml^{-1} is shown in Figure 4.

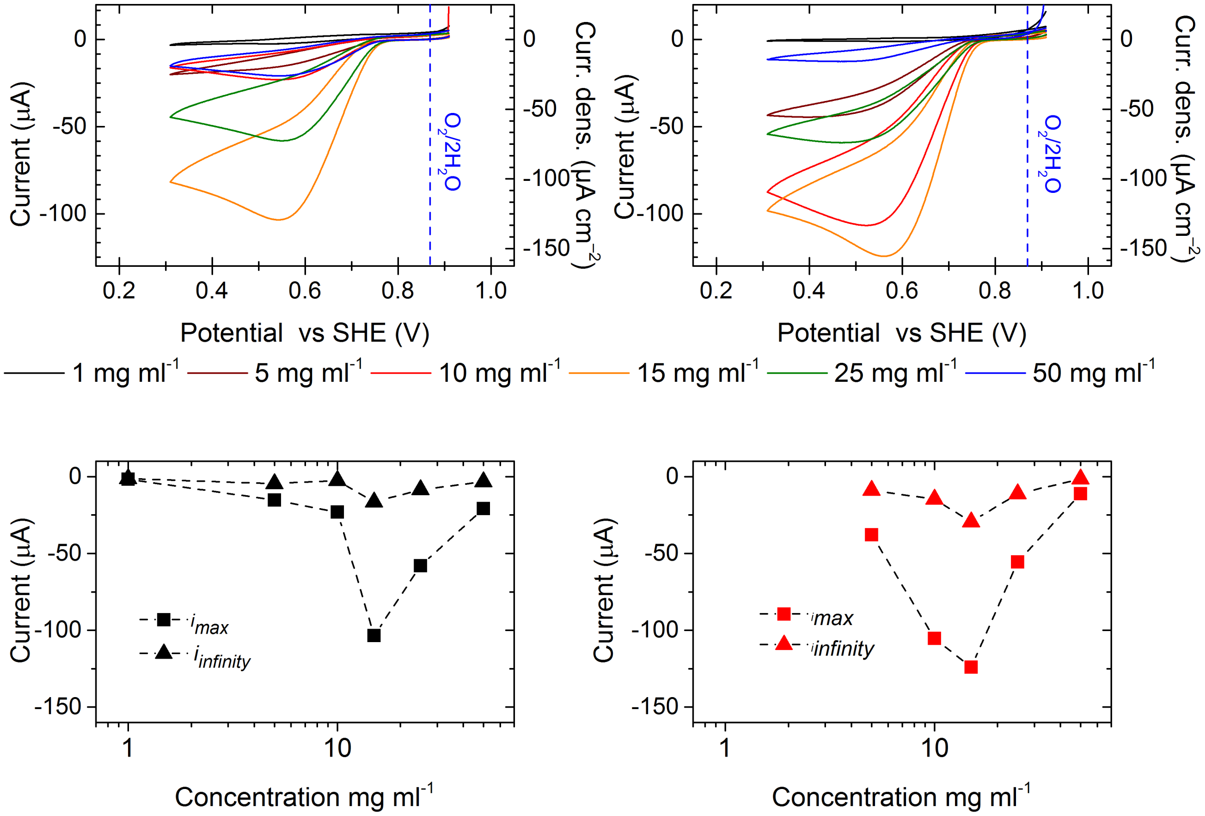

Figure 4. Electrocatalytic O_2 reduction current from adlayers of *Mv*BOx formed on a QCM sensor from concentrations ranging 1–50 mgml^{-1}. Left: bare gold, right: 3MPA. A. First CV scan (of 25). B. The maximum and final current from the reductive scan at 0.55 V vs. SHE. Conditions: 0.1M sodium phosphate buffer pH 6.0 at 25 °C with continuous O_2 bubbling, flow rate 0.1 ml min^{-1}; *Mv*BOx sample volume 25 µl; potential cycled between 0.91–0.31 V *vs*. SHE at 10 mV s^{-1}. TM

*Mv*BOx activity is shown by an increase in reductive (negative) current from the cyclic voltammograms. Scans started at a high (more oxidizing) potential where there is not enough driving force for the electron transfer to the copper complex in the enzyme. At ca. 0.7 V, enzyme-catalyzed O_2 reduction starts to occur and the current magnitude increases. This current increases with increasing driving force (lower potentials) until processes such as mass transport limit the reaction rate. For the CV scans in Figure 4A, the concentration of O_2 near the surface is depleted enough to cause the magnitude of the reductive current to peak around 0.55 V and preclude the reverse (oxidative) scan from overlapping with the scan in the reductive direction. The change between the $i_{\max}$ and i_{∞} traces in Figure 4B shows how the catalytic activity decay for all concentrations between the first scan to the 25th.

The highest and most persistent (i.e., highest $i_{\infty}/i_{\max}$) catalytic activity was observed on both unmodified gold and 3MPA-coated surfaces from adlayers formed from 15 mg ml^{-1} (Figure 4) solutions. Concentrations of 25 and 50 mg ml^{-1} both have similar current densities for gold and 3MPA surfaces, but the lower concentrations, in particular 10 mg ml^{-1} show increased catalytic current on 3MPA.

The most *efficient* use of enzyme (i.e., highest mass-specific activity) was determined by taking the ratio of current to frequency change (Equation 3). In Table S2,the initial and final turnover frequency estimates are given for concentrations ranging 1–50 mg ml^{-1}. For both initial and final layers, the highest relative turnover frequency is seen to be 15 mg ml^{-1}. Anomalous results were obtained from the 1 mg ml^{-1} sample because frequency traces were affected by oscillations caused by an alternating electric field, and are not shown in Figure 5. A similar optimum concentration for the specific activity for *Mv*BOx adsorbed onto gold (SI), but final current densities was about two times greater for *Mv*BOx adsorbed on 3MPA. Longer protein contact times show a reduction in overall specific activity per adsorbed mass unit, yet still give maximum activity per adsorbed mass at a concentration 15 mg ml^{-1}.

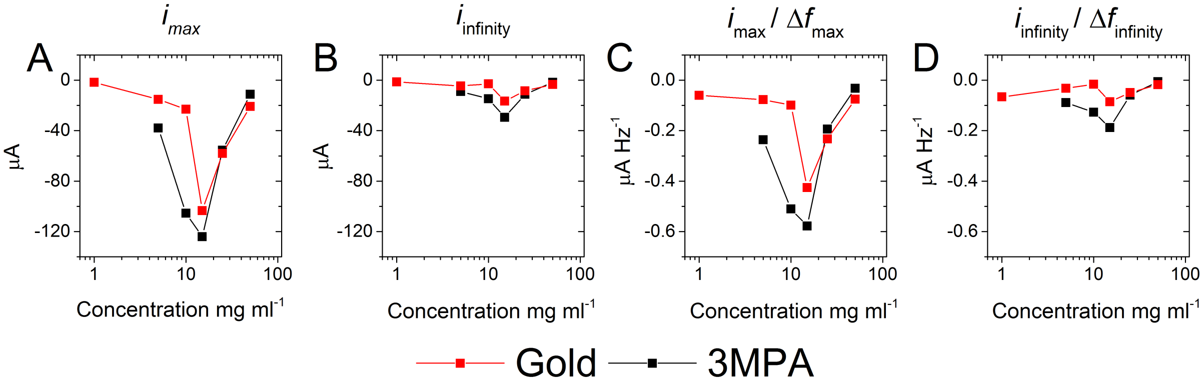

Figure 5 *Mv*BOx specific activity for adsorption to bare gold and 3MPA-modified QCM sensors for concentrations ranging from 1–50 mg ml^{-1}, shown on semilog plots. A $i_{\max}$, B $i_{infinity}$, C $i_{\max}$/ $\Delta f_{\max}$ and D i_{infinity}/ $\Delta f_{\text{infinity}}$ (I_{max} shows the reductive current at 0.55V vs. SHE)

TM

Mass loss with time can be related to activity loss by normalizing current to the adsorbed mass (SI). The change in $\Delta f_{\infty}/\Delta f_{max}$ vs. i_{∞}/i_{max} plots for both gold and 3MPA surfaces show that 15 mg ml^{-1} has the lowest activity loss per adsorbed enzyme regardless of surface. Activity loss on bare gold generally showed greater current loss after the 1st scans and after 25 scans when compared to on 3MPA . Gold surfaces show a much faster decay and lower final current densities compared to 3MPA.

The mass loss from protein desorption has previously been shown not to be the main cause for loss of bioelectrocatalytic activity.[8] The changes in activity from increasing the concentration can be assumed to be a result of how the enzyme adsorbs and is positioned on the surface. We hypothesise that the adlayer formed at an optimum concentration results in a adsorbed layer that is not overcome by steric hindrance from to much adsorbed material, but equally has not had time to form a relaxed state on the surface due to an ideal surface coverage.

Dual polarization interferometry analysis

DPI measurements of enzyme adsorption from 0.1–15 mg ml^{-1} *Mv*BOx solutions were carried out to independently measure thickness and density changes of the adsorbing layers. The results from a typical DPI measurement for *Mv*BOx adsorbed on a silicon oxynitride sensor is shown in Figure 6. Assuming plug flow, where the velocity of the fluid is the same for any entire cross section, the protein solution remained in the cell for 1 minute, compared to 15 s for the QCM measurements. At pH 6, the silicon oxynitride has a zeta potential of about –50 mV,[42] giving a surface that is electrically similar to the negatively charged 3MPA-coated surface used for QCM measurements.

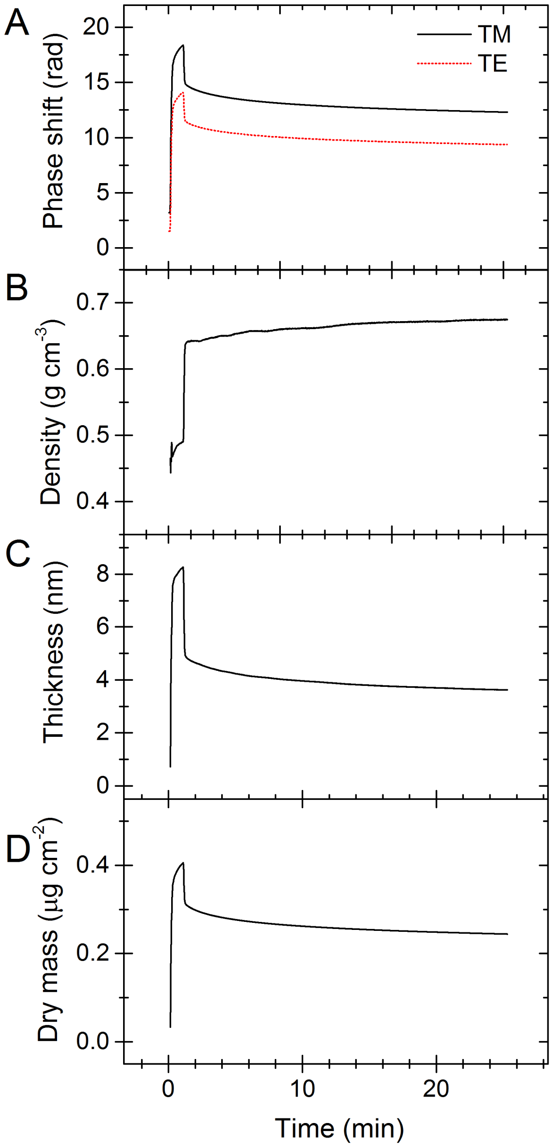

Figure 6. Typical *Mv*BOx adsorption to an un-modified silicon oxynitride DPI sensor. A. Phase shift, B. resolved data for density, C. thickness, and D. adsorbed dry mass. Conditions: 0.1M sodium phosphate buffer pH 6.0 at 25 °C flowing at 0.05 ml min^{-1}; injection: 50 µl of 15 mg ml^{-1} *Mv*BOx. TM

Upon injection of protein, a large phase shift is seen in both polarizations (Figure 6A). This response reflects both the protein adsorption, and the bulk effects of the concentrated protein solution. After injection the protein sample is then flushed out of the sensor chamber and a sharp decrease is seen as the solution returns to the bulk buffer. After this point the phase shift decreased, indicating layer thinning, and the refractive index increased, indicating layer densification (Figure 6B & C). The density values are those of the protein in the absence of buffer, so are below 1 g cm^{-3}.[43] The dry mass of the layer also decreases with time (Panel D), indicating that some desorption was also occurring.

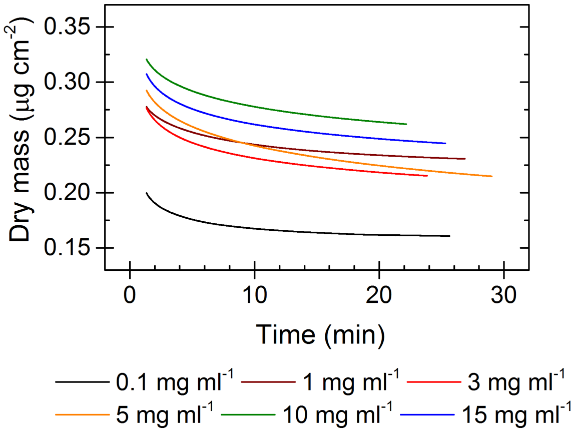

Figure 7 Resolved adsorbed mass DPI data for *Mv*BOx adsorbed onto silicon oxynitride DPI sensors. Conditions: 0.1M sodium phosphate buffer pH 6.0 at 25 °C, flow rate 0.05 ml min^{-1}, injection: 50 µl *Mv*BOx. TM

DPI data, for concentrations ranging between 0.1–15 mg ml^{-1} was collected and the resolved adsorbed mass data is shown in Figure 7. Mass changes with time are small for the low concentrations. The data was fitted to a first-order exponential decay to give values for the density, thickness and mass and time constants for each of these changes (SI). Adlayers of 1 mg ml^{-1} and above showed similar thickness, mass and density formed on the silicon oxynitride surface, with time constants in the hundreds of seconds. At the lowest concentrations, the thinnest and densest layer is produced. Increasing the concentration of the layer-forming solution did not produce a clear trend in surface density.

Increasing the *Mv*BOx concentration shows that there are small changes in adsorbed protein layer. As the concentration increases, did not seem to show any clear trends in density, mass and thickness. All layers undergo some degree of densification, mass loss and thinning. A possible explanation could be that over time surface spreading still occurs which forces some enzyme desorption. This means above a critical concentration, the structural change of the adsorbed layer becomes slower, which may allow for great stability and could explain the increase in specific activity observed in E-QCM-D measurements.

Modeling adsorption behavior

We modeled the QCM-D response of the protein adsorption and layer evolution to discover how bulk solution properties might affect some of the sensor response and to determine whether the densification and mass loss observed in the DPI measurements would match the QCM responses we observed. First, we aimed to replicate the “overshoot” in Δf and Δd in regions (1) and (2) at protein concentrations greater than 5 mg ml^{-1}. These responses are affected by changes in the viscosity and density of the bulk solution. The model response for the seventh harmonic as a function of protein concentration is shown in Figure 8, which shows the model response under conditions similar to those in Figure 2.

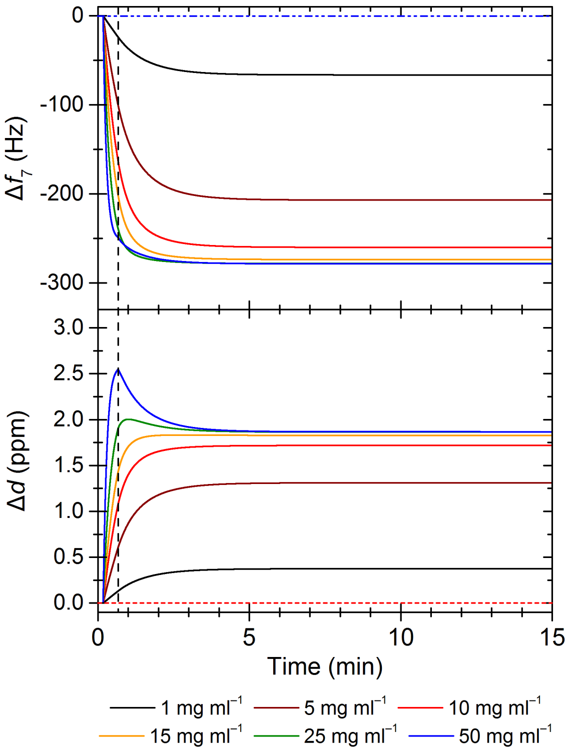

Figure 8. Simulated frequency and dissipation response from protein absorption onto a QCM sensor surface. The model includes an initial 10s baseline where just buffer is present, the solution is then changed to a protein solution for 30 seconds before the solution is changed back to buffer (black dashed line) and the concentration of the enzyme in the bulk solution decreases as a first-order exponential with a time constant of 60s. The inset shows an enlarged section of the frequency response where the solution is changed back to buffer. The properties of the layer are: adlayer viscosity 3.2 × 10^{-3} Pa s; adlayer shear modulus 3.2 × 10^{5} Pa; adlayer density 1 450 kg m^{-3}; fundamental frequency 4.95 MHz; solution density 1.0 × 10^{3} kg m^{-3}; solution viscosity 8.5 × 10^{-4} Pa s.

`TMcN`

The simulations assume irreversible adsorption with no change in mechanical properties after formation and the formation of a continuous homogeneous film rather than one comprised of discrete protein units. The simulation shows a small overshoot only on the Δd_7 trace for the 25 mg ml^{-1} and 50 mg ml^{-1} solutions. None of the traces shows an overshoot on the Δf_7 trace, suggesting that some of the overshoot may be due to the formation of additional layers of weakly and reversibly bound protein. Other factors that may contribute to this overshoot is a potential rocking motion by the bound enzyme within an incomplete layer.[44, 45] This model however requires the absorbed species to be able to pivot around a single point, resulting in a true rocking motion. In reality while this motion can contribute to a transient peak, due to the likely multiple points of contact between the enzyme and the surface this rocking motion and so contribution to the transient peak is likely to be greatly reduced. This interpretation contrasts with the three-state model proposed by Rabe and co-workers to explain overshoot. However, they used much lower protein concentrations in their studies than we used in this work (~10^{-8}–10^{-6} M vs. ~10^{-5}–10^{-3} M). Interestingly, the magnitude of Δf_7 *increased* slightly after the protein slug left the chamber (SI). The only way to duplicate the decrease in the magnitude of Δf_7 was by including mass loss in the model (Figure 9).

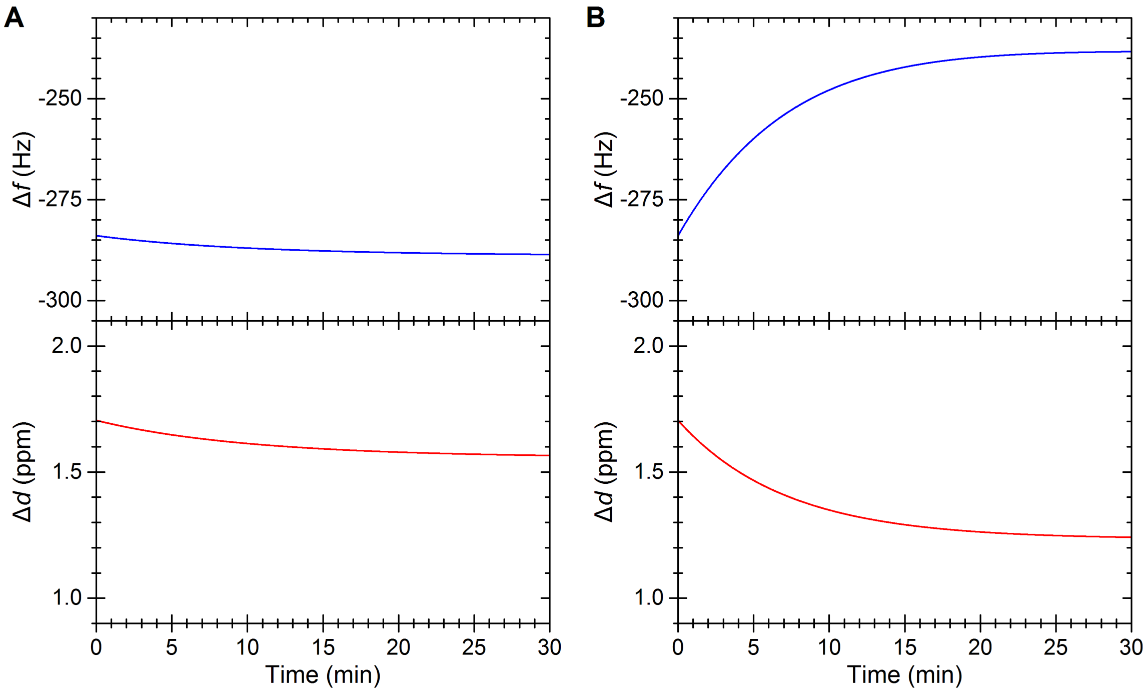

Figure 9. Simulated frequency and dissipation responses from a QCM-D that would result from the thinning of an absorbed protein layer like that generated from a 15 mg ml^{-1} solution of *Mv*BOx. The adlayer viscosity and shear modulus remain constant. Panel A shows the response where the surface protein concentration remains constant (i.e., adlayer thinning is matched by densification). Panel B shows the response when thinning is accompanied by mass loss. Adlayer changes are modeled as first-order exponentials. Adlayer properties: viscosity 3.2 × 10^{-3} Pa s; shear modulus 3.16 × 10^{5} Pa; initial density 1 450 kg m^{-3}; final density 1 595 kg m^{-3}; densification time constant 660 s; initial thickness 6 × 10^{-9} m; final thickness 4.5 × 10^{-9}; thinning time constant 440 s; fundamental frequency 4.95 MHz; solution density 1 × 10^{3} kg m^{-3}; solution viscosity 8.5 × 10^{-4} Pa s. TMcN

Combining information from the DPI about thickness and density changes to the film after adsorption with the shape of regions (3) and (4) from the QCM-D traces allows general conclusions to be drawn about the changes in the mechanical properties of the adlayer; further quantitative analysis would require more modeling because of the non-monotonic behavior of the QCM-D responses.[23] Figure 10 shows how the Δd_7 vs. Δf_7 plots would appear with mass loss densification and a change in the viscoelastic properties of the film, i.e. increases or decreases in the adlayer's viscosity and/or shear moduli. The shape of the traces with increasing layer viscosity most closely matches the shape of regions (3) and (4) shown in Figure 1B, but cannot determine how the shear modulus is changing with time.

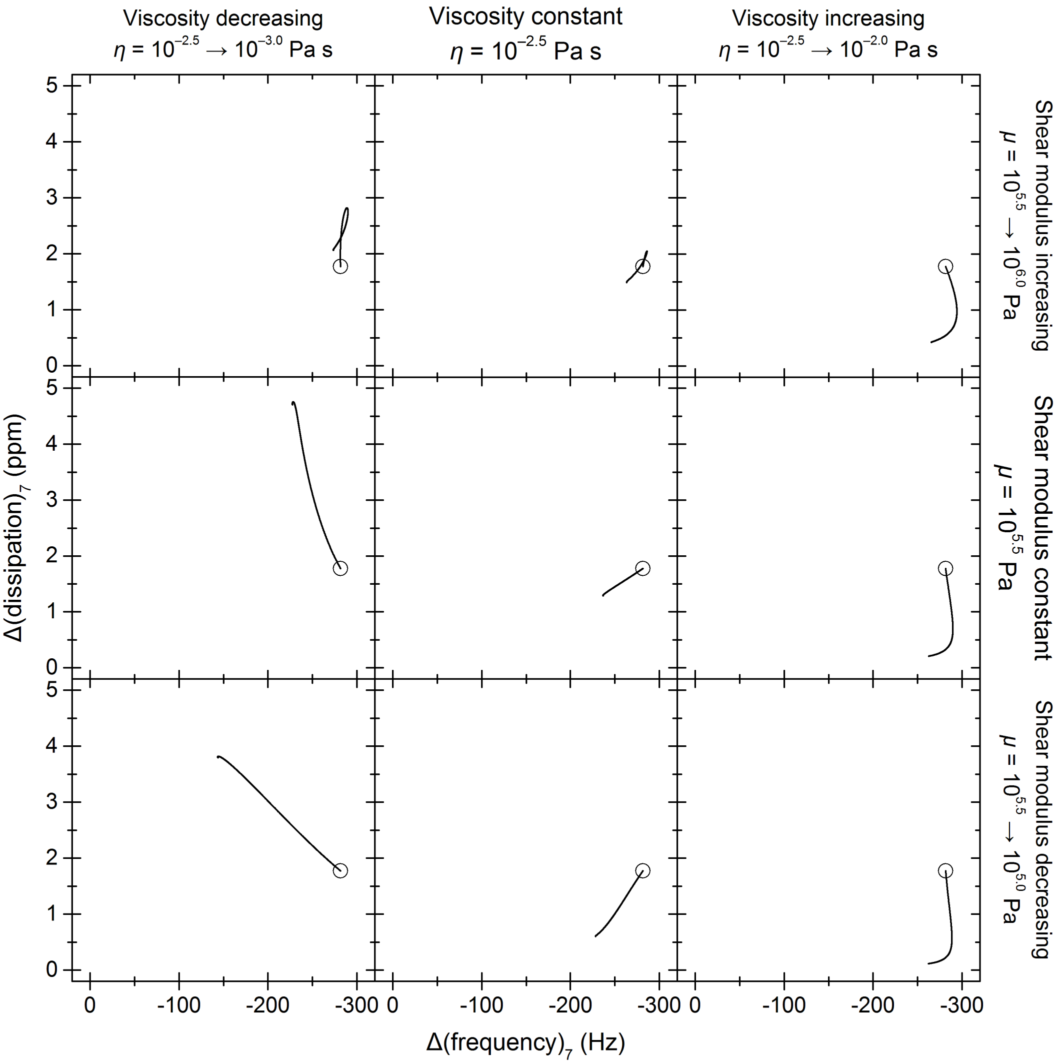

Figure 10. Simulated Δd vs Δf plots for an absorbed protein layer on a QCM sensor surface undergoing physical property changes. The circle shows the starting response. In all simulations the layer undergoes a 25% thickness reduction (τ_h = 440 s) and a density 10% increase (τ_ρ = 660 s) consistent with the DPI analysis of an adlayer formed from 15 mg ml^{-1} *Mv*BOx. The graphs in the left column have a decreasing viscosity (τ_η = 250 s) by a factor of $10^{0.5}$ during the simulation, the center column graphs have a constant viscosity and the graphs in the right column have an increasing viscosity during the simulation by a factor of $10^{0.5}$. The rows follow a similar trend with shear values increasing or decreasing (τ_μ = 250 s) by a factor of $10^{0.5}$ ordered in rows. The plots show the response for the seventh harmonic. The starting properties of the adlayer are: viscosity 3.16×10^{-3} Pa s; shear modulus 3.16×10^{5} Pa; density 1 450 kg m^{-3}; thickness 6 nm; fundamental frequency 4.95 MHz; solution density 1×10^{3} kg m^{-3}; solution viscosity 8.5×10^{-4} Pa s.

TMcN

Surface charge and chain length effects on adsorption and specific activity

E-QCM-D analysis

*Mv*BOx was adsorbed on surfaces terminated with positive ammonium groups, negative carboxylates and neutral methyl groups to compare adsorption behavior as a function of surface charge and hydrophobicity. The specific activity of adsorbed *Mv*BOx layers onto these function groups was also investigated, along with the effect of increasing the modifier carbon chain length.

Carboxylate-terminated surfaces were generated from 3-mercaptopropanoic acid (3MPA) and 6-mercaptohexanoic acid (6MHA), methyl-terminated surfaces from 3-mercaptopropane (3MP) and 6-mercaptohexane (6MH), and ammonium surfaces-terminated surfaces from 2-aminoethanethiol (2AE) and 6-aminohexanethiol (6AH).

Figure 11 shows the QCM-D response to *Mv*BOx adsorption from 25 mg ml^{-1} solution on these six linkers. Protein adsorption was higher and more stable on the longer-chain surface modifiers. Analysis of the adsorption of *Mv*BOx for the different stages is given in SI. Adsorption on to methyl-terminated surfaces showed very similar adsorption patterns in Δd vs. Δf for both lengths and similar normalized gradients. Carboxylate-terminated surfaces showed very similar Δd vs. Δf to the ammonium surfaces, although overall surface adsorption was greater on the carboxylate modification.

Ammonium-, sulfonate-, and methyl-terminated organosilanes were used to modify silica-coated QCM sensors (SI) to facilitate comparison to functionalized DPI sensors. Adsorption behavior for both negatively charged modifiers (sulfonate on silica and carboxylate on gold) was comparable. Methyl-terminated silane produced a more rigid adlayer than for the thiol modification, but still followed the similar trend for two-stage adsorption. The ammonium-terminated silane only showed one adsorption region instead of two. The attractive forces between the protein and surface during adsorption are greater than repulsive forces from protein–protein interactions from once neighboring surface sites are filled, preventing surface reorientation.

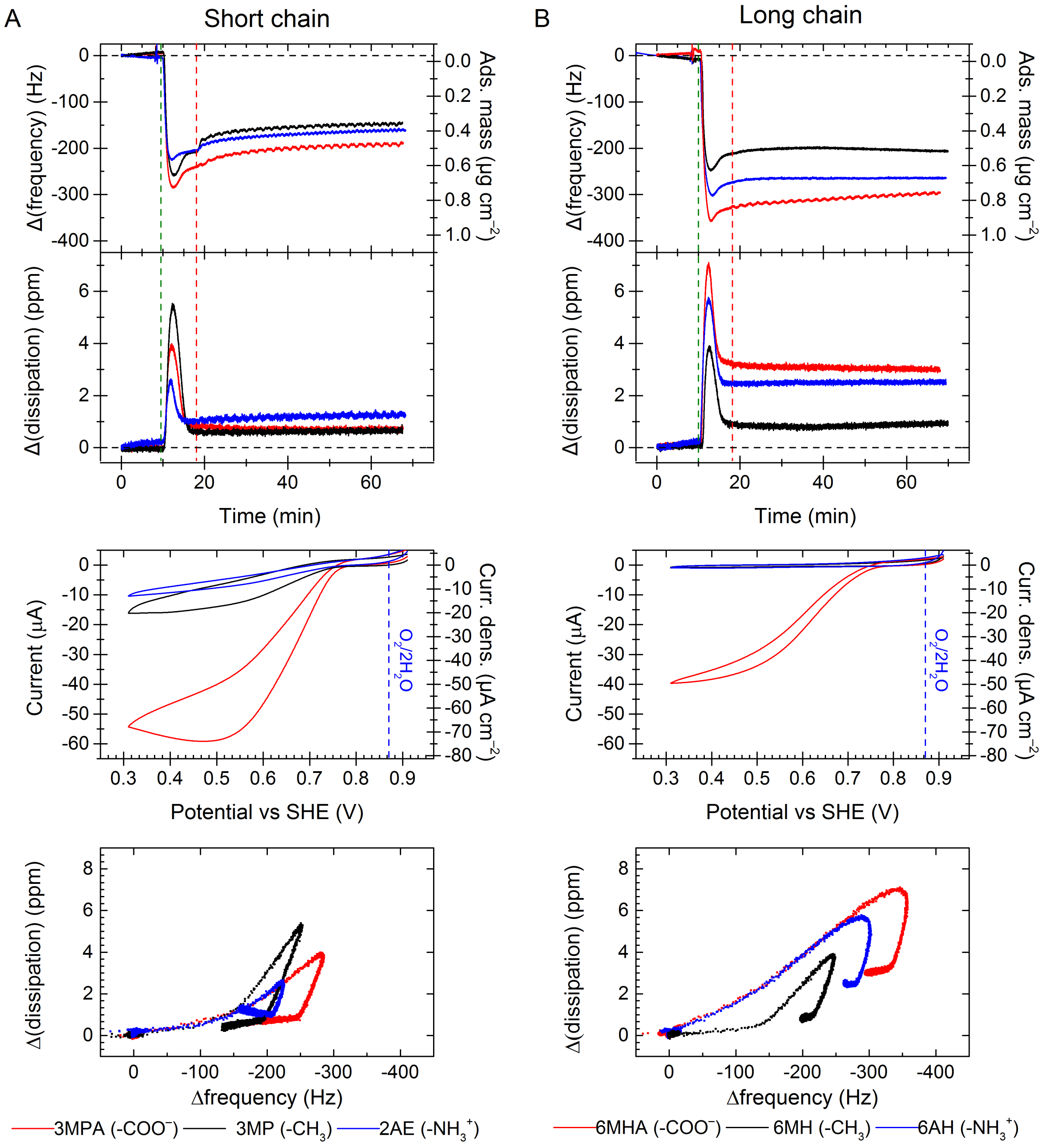

Figure 11. Effect of changing the terminal functional group and chain length of organothiol surface modifiers on E-QCM-D responses to *Mv*BOx adsorption for shorter (column A) and longer (column B) modifiers. From top to bottom, each column shows frequency response, dissipation response, first CV trace, and Δ*d* vs. Δ*f* plot. Column B shows the same responses for longer-chain modifications. Potential cycled between 0.91–0.31 V *vs*. SHE at 10 mV s^{-1}. On the frequency and dissipation traces, green dashed lines show the start of the adsorption of *Mv*BOx and red dashed lines show the start of CVs and associated oscillations caused by varying the potential. Conditions: oxygen-saturated 0.1M sodium phosphate buffer pH 6.0 at 25 °C flowing at 0.1 ml min^{-1} with continuous O_2 bubbling, traces are for the seventh harmonic; injection: 25 μl, 25 mg ml^{-1} *Mv*BOx. TM

Surface adsorption onto different length modifiers has shown that *Mv*BOx only behaves in a similar manner for a hydrophobic methyl-terminated surface. This can be attributed to proteins generally undergoing fast conformational changes upon hydrophobic surfaces, due to the enzyme's inner hydrophobic pocket being compromised.[4]

The ammonium and carboxylate surfaces both showed increased surface adsorption along with a less rigid adlayer. The hydrophobic nature of the methyl-terminated surface showed much greater change for region (2) than for region (1) suggesting the similar rigid layer formed during the initial stage, but different interaction with the bulk during stage two. Based on the magnitude of $\Delta d/\Delta f$, longer-chain modifiers showed a less rigid layer being formed in region (1) than for their shorter-chain analogues, although region (2) showed similar slopes irrespective of chain length, only surface modification. This seems to indicate that the smaller the initial rigid layer build up during region (1), the greater the overall stability of the adsorbed layer. This was also observed for films deposited on bare gold and 3MPA at increasing concentrations.

Effect of surface modification for *Mv*BOx specific activity

The effect of modifier on absolute and specific catalytic activity is summarized in Table 1. Longer-chain modifiers consistently produced a lower catalytic current, as expected for a system with a longer electron tunneling distance; no bioelectrocatalytic response was observed for films on 6AH or 6MH.[15] Negatively charged surfaces (3MPA and 6MHA) consistently produced higher activity films. Catalytic stability was greatest for 2AE, which lost roughly a third activity over 25 scans, however, this modifier showed the lowest initial specific activity. This could both be explained by an increase in distance between the catalytic center of the enzyme and the electrode. The increased distance will slow the rate of electron transfer, however, the catalytic center is further away from the alternating electric field produced at the electrodes surface, reducing the detrimental affects observed. The short-chain carboxylate surface (3MPA) showed the largest initial specific activity, although the long-chain carboxylate had higher specific activity after 25 scans. Destabilizing effects due to the potential cycling seems to also be greatly reduced on the longer-chain modifications. This suggests the potential cycling plays less of a role in dehydrating the enzyme layer due to a reduced influence of the alternating electric field near the electrode's surface.[46, 47]

Table 1. *Mv*BOx specific activity for adsorption onto carboxylate-, ammonium- and methyl-terminated QCM sensors with modifier lengths of 3 and 6 bond lenghts. i_{max} is the current at 0.55V vs. SHE on the first reductive scan.

Surface modifier	$i_{max}/\Delta f_{max}$ μA Hz^{-1}	$i_\infty/\Delta f_\infty$ μA Hz^{-1}
3MPA	−0.194	−0.059
2MP	−0.029	−0.029
2AE	−0.048	−0.026
6MHA	−0.081	−0.081
6MH	−0.001	−0.001
6AH	−0.002	−0.002

DPI analysis

DPI measurements were carried out to provide complementary adsorption analysis onto different surface modifications. Silicon oxynitride sensors were modified with organosilanes: negatively charged sulfonate-terminated surfaces were formed from trihydroxysilyl propane-1-sulfonic acid (THSPS); positively charged, ammonium-terminated surfaces were formed from 3-aminopropyltriethoxysilane (APTES); and neutral, methyl-terminated surfaces were formed from trimethoxypropylsilane (TMOPS).

The DPI response from *Mv*BOx adsorbed on bare and silane-modified DPI sensors is shown in Figure 12. Panel A shows the densification of the adlayers with time for each of the different surfaces. Methyl-terminated and bare surfaces give a denser layer than for the sulphonate and ammonium surfaces. Although the layer densities are similar for the acid and ammonium surfaces, the acid has more mass adsorbed and a thicker associated layer.

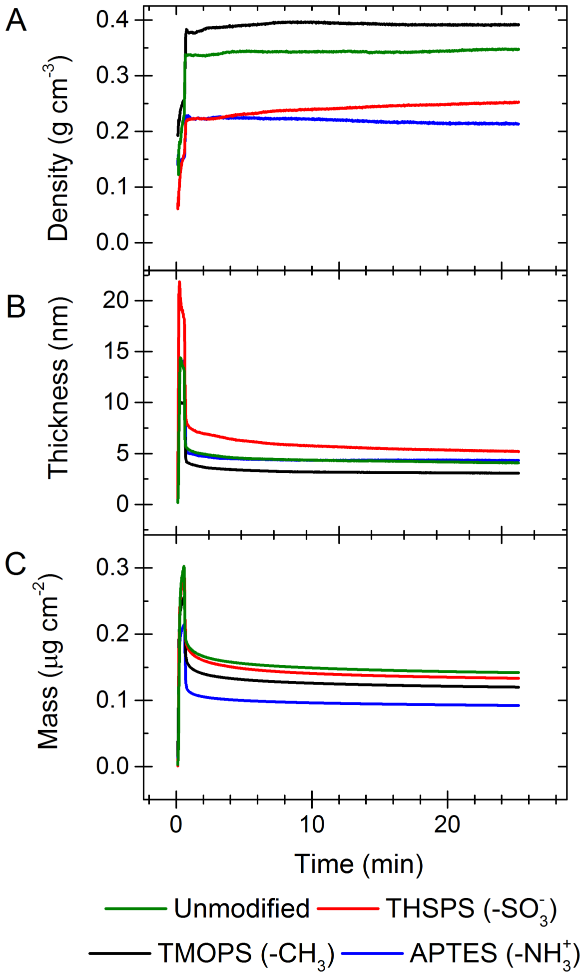

Figure 12. Effect of changing surface functional group on *Mv*BOx adsorption to a silane-modified silicon oxynitride DPI sensor. Panel A shows resolved density, B shows thickness, and C shows adsorbed mass. Conditions: 0.1M sodium phosphate buffer pH 6.0 at 25 °C flowing at 0.05 ml min^{-1}; injection: 25 mg ml^{-1} *Mv*BOx, 25 µl. TM

Data for each layer's final density, thickness and mass are given in Table 2along with their associated time constants. The silica- and methyl-terminated surfaces produced denser and thinner layers with the unmodified surface, which had a larger final adsorbed mass.

Table 2. DPI fitted data for final *Mv*BOx adsorbed on organosilane-modified silicon oxynitride DPI sensors.

Concentration mg ml^{-1}	Density g L^{-1}	Thickness nm	Mass ng mm^{-2}
Unmodified	0.79	1.41	1.18
THSPS	0.29	3.02	0.98
TMOPS	0.70	2.18	0.94
APTES	0.19	3.71	0.75

The lower densities and thicker adsorbed layers for both the charged surfaces suggest the protein structure remains in a soft state, without spreading or denaturation. Comparison with QCM-D data from *Mv*BOx adsorbed on the same surface modifications, showed similar hydrated mass for all adsorbed layers (SI), indicating that the sulfonate and ammonium layers are remaining hydrated, which is why the dry mass is lower from the DPI analysis. This is supported from QCM-D Δ*d*/Δ*f* values, showing more flexible adlayers. The faster time constants associated with densification for TMOPS and particularly unmodified, indicates the spreading is faster for these two surfaces.

Enzyme adsorption mechanistic analysis

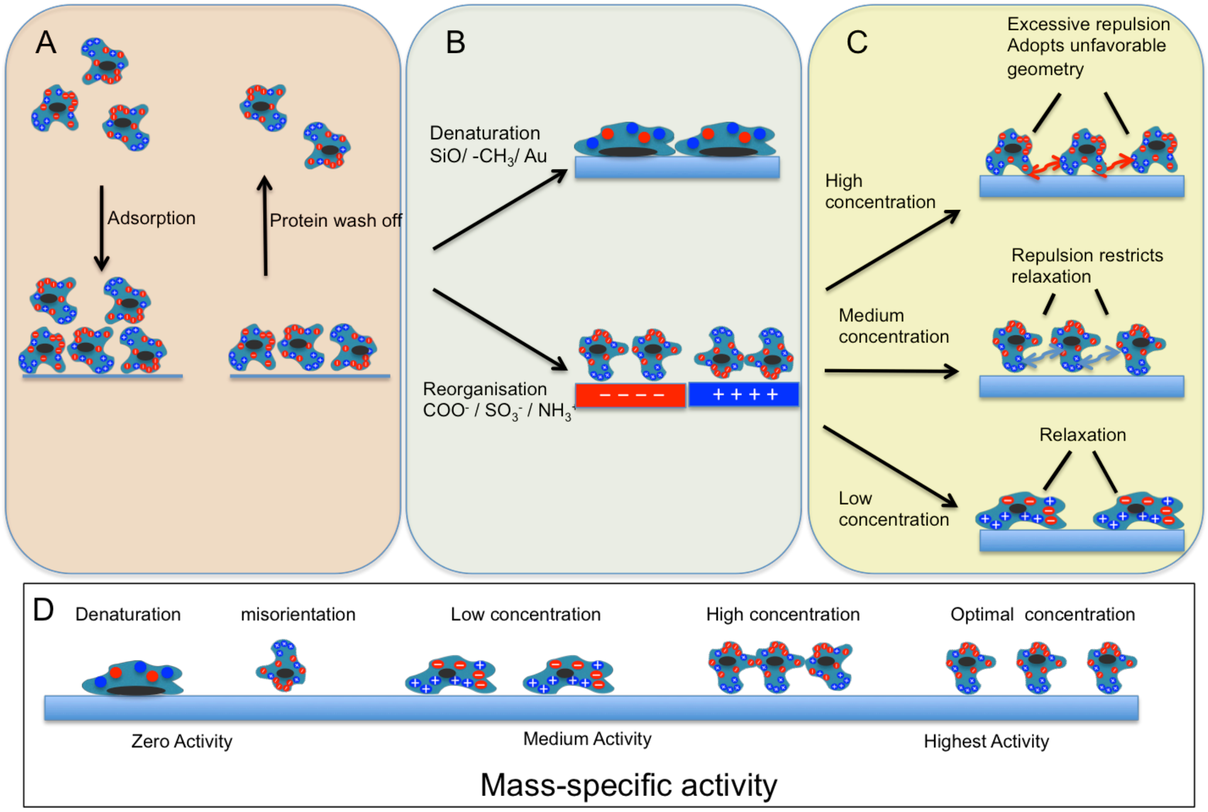

Figure 13. Suggested models for enzyme interactions with electrode surfaces and their relation to activity. Panel A shows adsorption onto electrodes surface, which is governed by a gain in entropy due to displacement of surface bound water and ions. After initial adsorption, loosely bound enzymes are washed off through buffer rinsing. Panel B shows denaturation of the enzyme, where the black hydrophobic center rearranges and comes into contact with the surface. Panel B also shows how the positive (blue) and negative (red) domains of the enzyme can interact with surface charge to induce enzyme re-orientation. Panel C shows the effect of enzyme–enzyme electrostatic repulsion, which effects optimum geometry for catalysis. Panel D indicates how the enzyme-surface interacts correlate to catalytic activity.

TM

At higher concentrations there is a higher competition for adsorption sites and adsorption occurs more rapidly. As each protein is more densely packed, further conformational changes such as spreading are limited. Comparing DPI date with E-QCM-D, we have been able to draw conclusions as to what sort of conformational changes occur when the protein adsorbs to a range of surfaces. How much an enzyme might reorganize on the surface or denature will readily depend on the type of internal structure. Figure 13 visually summarizes the conclusions for *Mv*BOx adsorbing to an electrode surface. QCM data during adsorption showed an excess amount of enzyme is adsorbed before being washed away. Comparing the viscoelastic properties of the adsorbing layers, we can deduce that on hydrophobic surfaces such as methyl-terminated, that the protein readily forms a rigid layer, which is supported by a thin, dense layer seen on DPI. These layers exhibit little or no catalytic ability so the conclusion is that they are readily denaturing. Adsorption to charged hydrophilic surfaces, such as carboxylate- and ammonium-terminated surfaces retain a higher hydrated mass, as seen by a low density and high thickness in DPI measurements and through dissipation analysis using QCM-D. These surfaces show a high degree of surface reorganization during the second stage of adsorption and form a stable bound layer. The effect of concentration on adsorption to these surfaces showed that an optimum concentration allowed for adsorption that limits spreading, but also does not affect activity due to strong electrostatic repulsion forces from overcrowding on the surface.

Conclusion

*Mv*BOx adsorption onto bare gold and 3MPA modified surfaces showed an optimum concentration of 15 mg ml^{-1} gave the largest specific activity for the adlayer. This is due to the effects of high enzyme loading and surface charge, which limits the rate of surface spreading. This is one of the first studies that has correlated E-QCM-D to DPI to give related surface adsorption and adlayer morphology and simultaneously relate this to the mass specific activity. A key observation in all of this work is that the initial stage (1) adsorption monitored by E-QCM-D seems to suggest a lower $\Delta d/\Delta f$ produces higher current densities. Shorter surface modifiers show higher catalytic activity compared to longer equivalents, but at a cost of reduced stability By incorporating modeling into DPI and QCM data, we have been able to suggest that at low concentrations, *Mv*BOx undergoes surface spreading and mass conservation, yet higher concentrations require a mass loss parameter, which is accounted for by slow surface spreading pushing off adsorbed enzymes. Therefore initial protein concentration is critical to reduce surface spreading by faster adsorption. Longer protein contact time showed a detrimental effect, for mass adsorption and activity, which is reinstates the requirement to control the rate and amount of protein adsorbing to the surface.

Author contributions

TM collected all the experimental results and wrote the manuscript with input from CFB. KS designed the modified E-QCM-D flow cell. TPM modeled the QCM-D responses.

Acknowledgements

This research was funded by the UK's Engineering and Physical Sciences Research Council through grant EP/G00434X/2, the NOWNANO Centre for Doctoral Training (TM), and the University of Manchester's School of Materials' Doctoral Training Account (TPM). We are grateful to Marcus Swann for valuable discussions on DPI, and to Nicola Tirelli for use of his viscometer.

Supporting information and data availability

Supporting information available: Modified flow module, adsorption onto 3MPA and bare gold, activity loss with potential cycling, QCM adsorption of BSA on silica sensors, normalized current to frequency response for different MvBOx concentrations on bare gold and 3MPA-coated QCM sensors, longer protein solution contact times, QCM adsorption measurements of *Mv*BOx on modified silica sensors, *Mv*BOx crystal structure analysis, viscosity measurements, additional results from Kelvin-Voigt modelling. The data associated with the paper are openly available from The University of Manchester eScholar Data Repository: http://dx.doi.org/10.12157/1.123456. The computer code associated with this paper is available from Github: http://dx.doi.org/10.5281/zenodo.10395.

References

1. Leech, D.; Kavanagh, P.; Schuhmann, W., Enzymatic fuel cells: Recent progress. *Electrochim. Acta* **2012,** *84*, 223-234.

2. Heller, A.; Feldman, B., Electrochemical glucose sensors and their applications in diabetes management. *Chem. Rev. (Washington, DC, U. S.)* **2008,** *108* (7), 2482-2505.

3. Norde, W.; Zoungrana, T., Surface-induced changes in the structure and activity of enzymes physically immobilized at solid/liquid interfaces. *Biotechnol. Appl. Biochem.* **1998,** *28*, 133-143.

4. van der Veen, M.; Stuart, M. C.; Norde, W., Spreading of proteins and its effect on adsorption and desorption kinetics. *Colloids and Surfaces B-Biointerfaces* **2007,** *54* (2), 136-142.

5. Rabe, M.; Verdes, D.; Seeger, S., Understanding protein adsorption phenomena at solid surfaces. *Adv. Colloid Interface Sci.* **2011,** *162* (1–2), 87-106.

6. Olejnik, P.; Palys, B.; Kowalczyk, A.; Nowicka, A. M., Orientation of Laccase on Charged Surfaces. Mediatorless Oxygen Reduction on Amino- and Carboxyl-Ended Ethylphenyl Groups. *J. Phys. Chem. C* **2012,** *116* (49), 25911-25918.

7. Pankratov, D.; Sotres, J.; Barrantes, A.; Arnebrant, T.; Shleev, S., Interfacial Behavior and Activity of Laccase and Bilirubin Oxidase on Bare Gold Surfaces. *Langmuir* **2014,** *30* (10), 2943-2951.

8. Singh, K.; McArdle, T.; Sullivan, P. R.; Blanford, C. F., Sources of activity loss in the fuel cell enzyme bilirubin oxidase. *Energy Environ. Sci.* **2013,** *6* (8), 2460-2464.

9. Mano, N.; Soukharev, V.; Heller, A., A laccase-wiring redox hydrogel for efficient catalysis of O-2 electroreduction. *J. Phys. Chem. B* **2006,** *110* (23), 11180-11187.

10. Blanford, C. F.; Foster, C. E.; Heath, R. S.; Armstrong, F. A., Efficient electrocatalytic oxygen reduction by the 'blue' copper oxidase, laccase, directly attached to chemically modified carbons. *Faraday Discuss.* **2008,** *140*, 319-335.

11. Mano, N.; Edembe, L., Bilirubin oxidases in bioelectrochemistry: Features and recent findings. *Biosens. Bioelectron.* **2013,** *50*, 478-485.

12. dos Santos, L.; Climent, V.; Blanford, C. F.; Armstrong, F. A., Mechanistic studies of the 'blue' Cu enzyme, bilirubin oxidase, as a highly efficient electrocatalyst for the oxygen reduction reaction. *Physical Chemistry Chemical Physics* **2010,** *12* (42), 13962-13974.

13. Salaj-Kosla, U.; Poeller, S.; Schuhmann, W.; Shleev, S.; Magner, E., Direct electron transfer of Trametes hirsuta laccase adsorbed at unmodified nanoporous gold electrodes. *Bioelectrochemistry* **2013,** *91*, 15-20.

14. Solomon, E. I.; Sundaram, U. M.; Machonkin, T. E., Multicopper oxidases and oxygenases. *Chem. Rev. (Washington, DC, U. S.)* **1996,** *96* (7), 2563-2605.

15. Page, C. C.; Moser, C. C.; Chen, X. X.; Dutton, P. L., Natural engineering principles of electron tunnelling in biological oxidation-reduction. *Nature* **1999,** *402* (6757), 47-52.

16. Gray, H. B.; Winkler, J. R., Long-range electron transfer. *Proc. Natl. Acad. Sci. U. S. A.* **2005,** *102* (10), 3534-3539.

17. Norde, W., Adsorption of proteins from solution at the solid-liquid interface. *Adv. Colloid Interface Sci.* **1986,** *25* (4), 267-340.

18. Herrera, E.; Giacomelli, C. E., Surface coverage dictates the surface bio-activity of D-amino acid oxidase. *Colloids and Surfaces B-Biointerfaces* **2014,** *117*, 296-302.

19. Prime, K. L.; Whitesides, G. M., Self-assembled organic monolayers - model systems for studying adsorption of proteins at surfaces. *Science* **1991,** *252* (5009), 1164-1167.

20. Vallee, A.; Humblot, V.; Al Housseiny, R.; Boujday, S.; Pradier, C. M., BSA adsorption on aliphatic and aromatic acid SAMs: Investigating the effect of residual surface charge and sublayer nature. *Colloids and Surfaces B-Biointerfaces* **2013,** *109*, 136-142.

21. Ulyanova, Y.; Babanova, S.; Pinchon, E.; Matanovic, I.; Singhal, S.; Atanassov, P., Effect of enzymatic orientation through the use of syringaldazine molecules on multiple multi-copper oxidase enzymes. *Phys. Chem. Chem. Phys.* **2014,** *16* (26), 13367-13375.

22. Singh, K.; Blanford, C. F., Electrochemical Quartz Crystal Microbalance with Dissipation Monitoring: A Technique to Optimize Enzyme Use in Bioelectrocatalysis. *Chemcatchem* **2014,** *6* (4), 921-929.

23. Voinova, M. V.; Rodahl, M.; Jonson, M.; Kasemo, B., Viscoelastic acoustic response of layered polymer films at fluid-solid interfaces: Continuum mechanics approach. *Phys. Scr.* **1999,** *59* (5), 391-396.

24. Dixon, M. C., Quartz crystal microbalance with dissipation monitoring: enabling real-time characterization of biological materials and their interactions. *Journal of biomolecular techniques : JBT* **2008,** *19* (3), 151-8.

25. Hook, F.; Kasemo, B.; Nylander, T.; Fant, C.; Sott, K.; Elwing, H., Variations in coupled water, viscoelastic properties, and film thickness of a Mefp-1 protein film during adsorption and cross-linking: A quartz crystal microbalance with dissipation monitoring, ellipsometry, and surface plasmon resonance study. *Anal. Chem.* **2001,** *73* (24), 5796-5804.

26. Rodahl, M.; Hook, F.; Fredriksson, C.; Keller, C. A.; Krozer, A.; Brzezinski, P.; Voinova, M.; Kasemo, B., Simultaneous frequency and dissipation factor QCM

measurements of biomolecular adsorption and cell adhesion. *Faraday Discuss.* **1997,** *107*, 229-246.

27. Hook, F.; Rodahl, M.; Kasemo, B.; Brzezinski, P., Structural changes in hemoglobin during adsorption to solid surfaces: Effects of pH, ionic strength, and ligand binding. *Proc. Natl. Acad. Sci. U. S. A.* **1998,** *95* (21), 12271-12276.

28. Swann, M. J.; Peel, L. L.; Carrington, S.; Freeman, N. J., Dual-polarization interferometry: an analytical technique to measure changes in protein structure in real time, to determine the stoichiometry of binding events, and to differentiate between specific and nonspecific interactions. *Anal. Biochem.* **2004,** *329* (2), 190-198.

29. Cross, G. H.; Reeves, A. A.; Brand, S.; Popplewell, J. F.; Peel, L. L.; Swann, M. J.; Freeman, N. J., A new quantitative optical biosensor for protein characterisation. *Biosens. Bioelectron.* **2003,** *19* (4), 383-390.

30. Caruso, F.; Furlong, D. N.; Kingshott, P., Characterization of ferritin adsorption onto gold. *J. Colloid Interface Sci.* **1997,** *186* (1), 129-140.

31. Cowsill, B. J.; Coffey, P. D.; Yaseen, M.; Waigh, T. A.; Freeman, N. J.; Lu, J. R., Measurement of the thickness of ultra-thin adsorbed globular protein layers with dual-polarisation interferometry: a comparison with neutron reflectivity. *Soft Matter* **2011,** *7* (16), 7223-7230.

32. Frost, R.; Jonsson, G. E.; Chakarov, D.; Svedhem, S.; Kasemo, B., Graphene Oxide and Lipid Membranes: Interactions and Nanocomposite Structures. *Nano Lett.* **2012,** *12* (7), 3356-3362.

33. Coffey, P. D.; Swann, M. J.; Waigh, T. A.; Mu, Q. S.; Lu, J. R., The structure and mass of heterogeneous thin films measured with dual polarization interferometry and ellipsometry. *Rsc Advances* **2013,** *3* (10), 3316-3324.

34. Xu, K.; Ouberai, M. M.; Welland, M. E., A comprehensive study of lysozyme adsorption using dual polarization interferometry and quartz crystal microbalance with dissipation. *Biomaterials* **2013,** *34* (5), 1461-1470.

35. Thourson, S. B.; Marsh, C. A.; Doyle, B. J.; Timpe, S. J., Quartz crystal microbalance study of bovine serum albumin adsorption onto self-assembled monolayer-functionalized gold with subsequent ligand binding. *Colloids and Surfaces B-Biointerfaces* **2013,** *111*, 707-712.

36. Rodgers, C. J.; Blanford, C. F.; Giddens, S. R.; Skamnioti, P.; Armstrong, F. A.; Gurr, S. J., Designer laccases: a vogue for high-potential fungal enzymes? *Trends Biotechnol.* **2010,** *28* (2), 63-72.

37. Online software ProtParam – Expasy Proteomics Server (http://www.expasy.ch/tools/protparam.html) (10-09-14).

38. Rodahl, M.; Kasemo, B., Frequency and dissipation-factor responses to localized liquid deposits on a QCM electrode. *Sensors and Actuators B: Chemical* **1996,** *37* (1–2), 111-116.

39. Fischer, H.; Polikarpov, I.; Craievich, A. F., Average protein density is a molecular-weight-dependent function. *Protein Sci.* **2004,** *13* (10), 2825-2828.

40. Katano, H.; Uematsu, K.; Hibi, T.; Ikeda, T.; Tsukatani, T., Application of Poly oxyethylene(dimethylimino)propyl(dimethylimino)ethylene as Enzyme Stabilizer for Bilirubin Oxidase Immobilized Electrode. *Anal. Sci.* **2009,** *25* (9), 1077-1081.

41. Fraser, S. J.; Mulet, X.; Martin, L.; Praporski, S.; Mechler, A.; Hartley, P. G.; Polyzos, A.; Separovic, F., Surface Immobilization of Bio-Functionalized Cubosomes: Sensing of Proteins by Quartz Crystal Microbalance. *Langmuir* **2012,** *28* (1), 620-627.

42. Shovsky, A.; Bijelic, G.; Imre, V.; Makuska, R.; Claesson, P. M., Adsorption Characteristics of Stoichiometric and Nonstoichiometric Molecular Polyelectrolyte Complexes on Silicon Oxynitride Surfaces. *Langmuir* **2011,** *27* (3), 1044-1050.

43. Escorihuela, J.; González-Martínez, M. Á.; López-Paz, J. L.; Puchades, R.; Maquieira, Á.; Gimenez-Romero, D., Dual-Polarization Interferometry: A Novel Technique To Light up the Nanomolecular World. *Chem. Rev. (Washington, DC, U. S.)* **2015,** *115* (1), 265-294.

44. Pomorska, A.; Shchukin, D.; Hammond, R.; Cooper, M. A.; Grundmeier, G.; Johannsmann, D., Positive Frequency Shifts Observed Upon Adsorbing Micron-Sized Solid Objects to a Quartz Crystal Microbalance from the Liquid Phase. *Anal. Chem.* **2010,** *82* (6), 2237-2242.

45. Johannsmann, D.; Reviakine, I.; Richter, R. P., Dissipation in Films of Adsorbed Nanospheres Studied by Quartz Crystal Microbalance (QCM). *Anal. Chem.* **2009,** *81* (19), 8167-8176.

46. Chao, C.-H.; Li, K.-L.; Wu, C.-S.; Lee, C.-C.; Chiang, H.-P.; Yang, Y.-S.; Pan, T.-M.; Ko, F.-H., Surface Effect of Assembling Enzyme and Modulation of Surface Enzyme Activity with Electric Potential Stress. *Int. J. Electrochem. Sci.* **2012,** *7* (6), 5100-5114.

47. Ge, C. W.; Liao, J. H.; Yu, W.; Gu, N., Electric potential control of DNA immobilization on gold electrode. *Biosens. Bioelectron.* **2003,** *18* (1), 53-58.

Supplementary information for

Optimizing the mass-specific activity of bilirubin oxidase adlayers through combined electrochemical quartz crystal microbalance and dual polarization interferometry analyses

Trevor McArdle, Thomas P. McNamara, Kulveer Singh and Christopher F. Blanford

Table of Contents

S1. Modified flow module for E-QCM-D

E-QCM-D measurements used a modified Q-Sense QEM401 module (100µl sample chamber volume). A redesigned flow module is shown in Figure S1.[1] Panel A shows the side view of the redesigned cell detailing the fluid inlet and outlet holes along with the new reference electrode reservoir at the top of the module. Panel B shows the fluid flow path for the inlet and outlet and how the new reference reservoir maintains an ionic connection with the fluid. Panel C shows a photograph of the constructed module machined out of poly(oxomethylene) (Delrin). Panel D shows the opposite side view to panel A with an arrow indicating where the counter electrode connection is housed. Panel E shows the upper counter electrode housing where the metal contact sits and the lower housing which contains the screw and gold contact pin which makes contact with the platinum sheet. Panel F shows how the counter electrode connection is constructed. Panel G shows the individual components for assembling the cell including the platinum sheet, which is positioned to align the two holes above the inlet and outlet holes. This allows fluid to pass over the platinum sheet. The gasket sits on top of the sheet and an O-ring is placed in the spacing (shown in Panel H). Panel I shows an assembled module with working electrode and reference electrode connections in place. The pin for the counter electrode from the potentiostat fits in the hole marked.

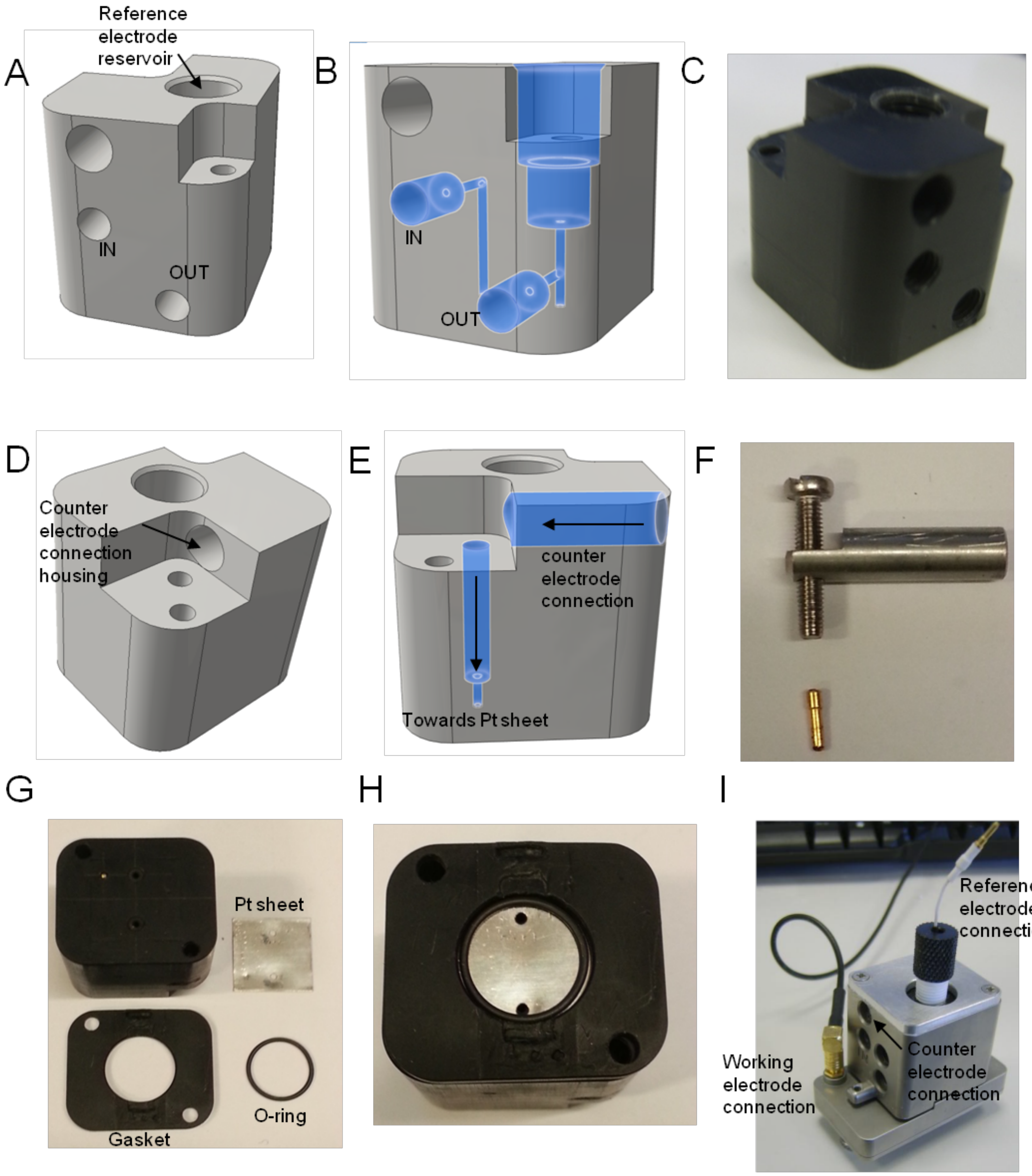

Figure S1. Images showing a redesigned Q-sense 401 flow module. The images in A, B, D and E were designed using AutoCAD 2013 and Inventor Fusion 2013. Figure adapted from ref 1. KS

S2. Adsorption of *Mv*BOx on 3MPA-coated and bare gold QCM sensors

Adsorption data for *Mv*BOx adsorbed on to unmodified and 3MPA-coated QCM sensors is given in Table S1. As the concentration is increased, Δf_{max} and Δd_{max} increased. The value of $\Delta d/\Delta f$ increased monotonically with concentration for region (2) on both unmodified and 3MPA-modified surfaces. This was only the case for 3MPA-modified surfaces for region (1).

Table S1. QCM-D data for *Mv*BOx adsorbed onto 3MPA-coated and bare gold QCM sensors. Stages (3) and (4) were affected by the oscillations caused by cyclic voltammetry and thus are not shown.

Surface	**Concentration** mg ml^{-1}	Δf_{max} Hz	Δd_{max} ppm	Δf_{∞} Hz	Δd_{∞} ppm	$\Delta d/\Delta f$ (Stage 1) ppm Hz^{-1}	$\Delta d/\Delta f$ (Stage 2) ppm Hz^{-1}
3MPA	1	–10	0.17	*	*	–0.0067	–0.011
	5	–161	0.53	–99	0.31	–0.0051	–0.0003
	10	–207	0.49	–116	0.32	–0.012	–0.068
	15	–215	1.3	–157	0.61	–0.024	–0.14
	25	–286	4.0	–190	0.73	–0.057	–0.16
	50	–353	6.1	–274	3.4	–0.043	–0.19
Gold	1	–29	0.14	–20	0.05	*	*
	5	–199	1.51	–140	1.29	–0.016	–0.074
	10	–233	1.62	–173	0.64	–0.021	–0.065
	15	–242	1.95	–197	1.60	–0.014	–0.10
	25	–249	1.84	–172	1.09	–0.018	–0.13
	50	–277	4.74	–191	1.88	–0.0068	–0.035

* Value cannot be determined because of oscillations induced by cyclic voltammetry.

S3. Activity loss with potential cycling

After *Mv*BOx adsorption, the potential was cycled 25 times between 0.7 and 0.1 V vs. Ag|AgCl|3M NaCl. After each scan the overall current decayed. Figure S2 shows two typical examples of activity loss over scans for bare gold and 3MPA-coated QCM sensors.

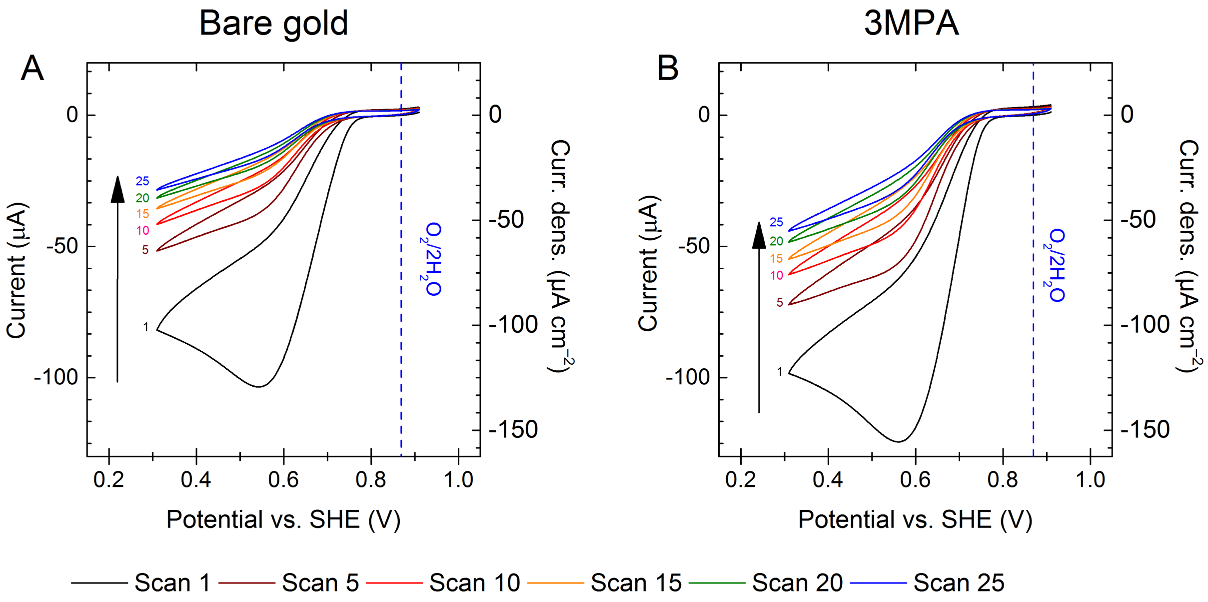

Figure S2 .Typical cyclic voltammetry from E-QCM-D measurements showing the activity loss of *Mv*BOx adsorbed on (A) bare gold and (B) 3MPA-coated QCM sensors. Graphs show CV scans 1, 5, 10, 15, 20 and 25, with an arrow indicating the reduction in current. Conditions: 0.1M sodium phosphate buffer pH 6.0 (pre-saturated with O_2) at 25 °C flowing at 0.1 ml min^{-1}, 15 mg ml^{-1} *Mv*BOx 25 µl sample volume, 0.8 cm^{2} working electrode area. TM

The initial scan shows a typical wave starting at around 0.7 V vs. SHE before a current maximum is reached at around 0.55 V vs. SHE. After this point the current is mass-transport limited and decreases. For subsequent scans, the activity loss results in mass transport no longer being an issue. In this example, the 3MPA-coated surface (Figure S2B) shows a lower activity loss (76%) compared to the gold (84%) for similar concentrations. The adlayer on the 3MPA-coated surface also produced a larger current magnitude then for *Mv*BOx adsorbed on bare gold. Table S2 presents both catalytic O_2-reduction currents and ratios or currents to frequency changes, which are proportional to mass-specific enzyme activity. Adlayers formed from 15 mg ml^{-1} solutions had the highest current per amount of adsorbed enzyme.

Table S2. *Mv*BOx activity for adsorption onto unmodified and 3MPA-modified gold-coated QCM sensors. The subscript "max" refers to the highest magnitude O_2-reduction current or frequency change. The symbols i_∞ and Δf_∞ refer to the highest magnitude reductive current or frequency shift, respectively, during the final CV cycle.

Surface	**Concentration**	$\boldsymbol{i_{max}}$ (scan 1)	$\boldsymbol{i_\infty}$ (scan 25)	$\boldsymbol{i_{max}/\Delta f_{max}}$	$\boldsymbol{i_\infty/\Delta f_\infty}$
	mg ml^{-1}	µA	µA	µA Hz^{-1}	µA Hz^{-1}
Unmodified	1	–1.7	–1.3	–0.060	–0.066
	5	–15.3	–4.5	–0.077	–0.032
	10	–23.0	–2.8	–0.099	–0.016
	15	–103.4	–16.6	–0.426	–0.085
	25	–58.1	–8.4	–0.233	–0.049
	50	–20.8	–3.4	–0.075	–0.018
3MPA	1	–37.9	– 8.9	–0.236	–0.089
	10	–105.4	–14.7	–0.510	–0.127
	15	–124.1	–29.4	–0.578	–0.188
	25	–55.5	–11.2	–0.194	–0.059
	50	–11.2	–1.6	–0.032	–0.006

S4. Adsorption of BSA on silica-coated sensors

Bovine serum albumin (BSA), a globular protein of similar size to *Mv*BOx, was adsorbed onto silica-coated QCM sensors, made hydrophilic by treating with piranha solution and ozone, to compare the effect of varying the concentration on adsorption, and to compare the effect of changing sensor surface. Seven concentrations of BSA (0.01–100 mg ml^{-1}, 25 µl) were flowed over the sensors (Figure S3). The greatest magnitude change for frequency is seen for the largest concentration (100 mg ml^{-1}) at around –410 Hz (1.03 µg cm^{-2}) before forming a stable layer at –210 Hz (0.53 µg cm^{-2}). This is similar for 10 mg ml^{-1}, however smaller frequency changes are seen for 50 and 20 mg ml^{-1}.

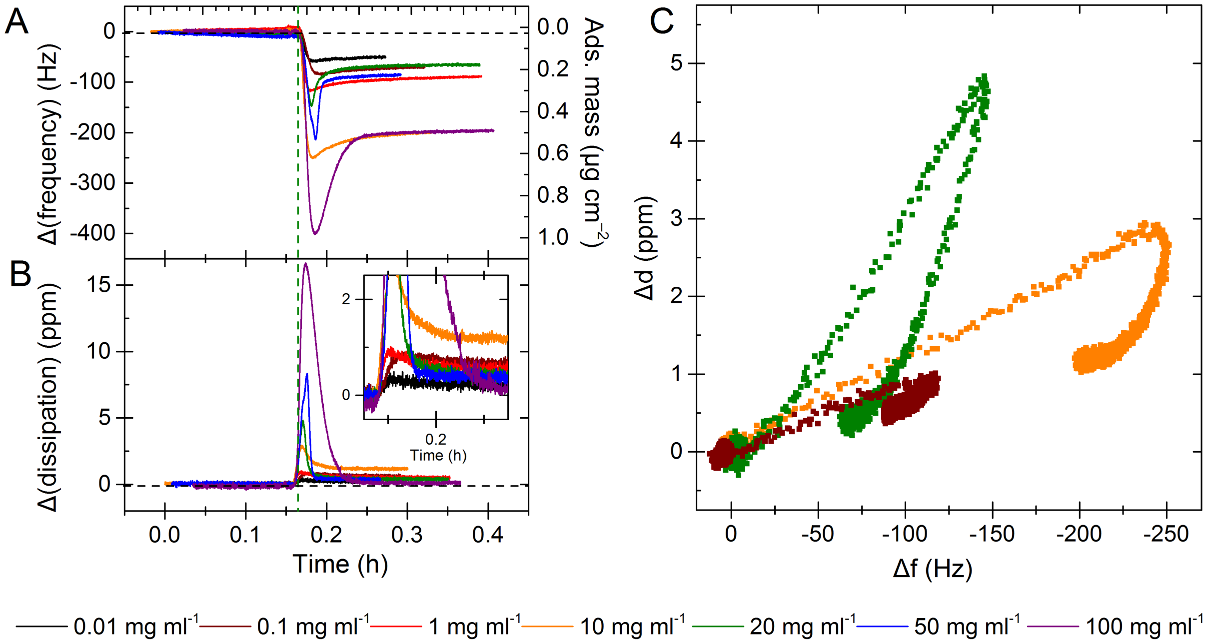

Figure S3. Effect of varying BSA concentration on adlayer formation on bare silicon oxide–coated QCM sensors. Frequency (A) and dissipation (B) responses for addition of BSA. Inset shows a closer view of just after adsorption. Panel C shows Δ*d* vs. Δ*f* plot for 0.1, 10 and 20 mg ml^{-1}. Green dashed lines show adsorption of BSA. 0.1M sodium phosphate buffer pH 6.0 at 25 °C flowing at 0.1 ml min^{-1}, traces are for the seventh harmonic. 25 µl BSA sample volume. TM

The dissipation traces shown in Figure S3B display an overshoot for concentrations above 10 mg ml^{-1}. The Δ*d* trace for 10 mg ml^{-1} BSA shows a markedly higher dissipation (1.2 ppm) following rinsing than the higher concentrations (0.15 ppm for 100 mg ml^{-1}) with similar frequency changes. Table S3 shows QCM-D responses for each concentration. Above 20 mg ml^{-1}, there are large changes in magnitude for both Δ*f* and Δ*d* from the initial maximum values to the final adlayer. Figure S3C shows Δ*d* vs. Δ*f* plots for three selected concentrations to show the change in gradients for each of the four regions. BSA QCM adsorption only has one initial region, instead of two seen for *Mv*BOx. In Table S3, data for each of the adsorption regions is given, with region 1+2 treated as a single stage. Adsorption regions (1)+(2) and (3) showed a monotonic increase in slope with increasing concentration.

Table S3. QCM-D data for BSA adsorbed on to bare, hydrophilic silica sensors with concentrations ranging from 0.1–100 mg ml^{-1}. Symbols and subscripts are illustrated in Fig. 1.

Concentration mg ml^{-1}	Δf_{max} Hz	Δd_{max} ppm	Δf_{∞} Hz	Δd_{∞} ppm	**Δ*d* vs. Δ*f*** Stage 1+2 ppm Hz^{-1}	**Δ*d* vs. Δ*f*** Stage 3 ppm Hz^{-1}	**Δ*d* vs. Δ*f*** Stage 4 ppm Hz^{-1}
0.1	–61	0.36	–51	0.21	–0.011	–0.006	–0.011
1	–86	0.90	–69	0.59	–0.009	–0.014	–0.010
10	–119	1.01	–92	0.53	–0.011	–0.049	–0.008
20	–251	2.95	–200	1.17	–0.037	–0.074	–0.017
50	–147	4.83	–66	0.52	–0.044	–0.069	–0.009
100	–214	8.33	–85	0.34	–0.054	–0.082	–0.019

S5. Correlation between frequency, dissipation and electrocatalytic activity

To correlate the frequency and dissipation response to the electrocatalytic activity, *i/i*$_{max}$ vs. $\Delta f/\Delta f_{max}$ and *i/i*$_{max}$ vs. $\Delta d/\Delta d_{max}$ are plotted in Figure S4. Deceasing activity is always seen with a decrease in frequency (mass loss). Decreases in dissipation with activity show a rearrangement of the enzyme on the surface, however the traces shown in Figure S4 are affected strongly by the cycling potential, especially for the low concentrations.

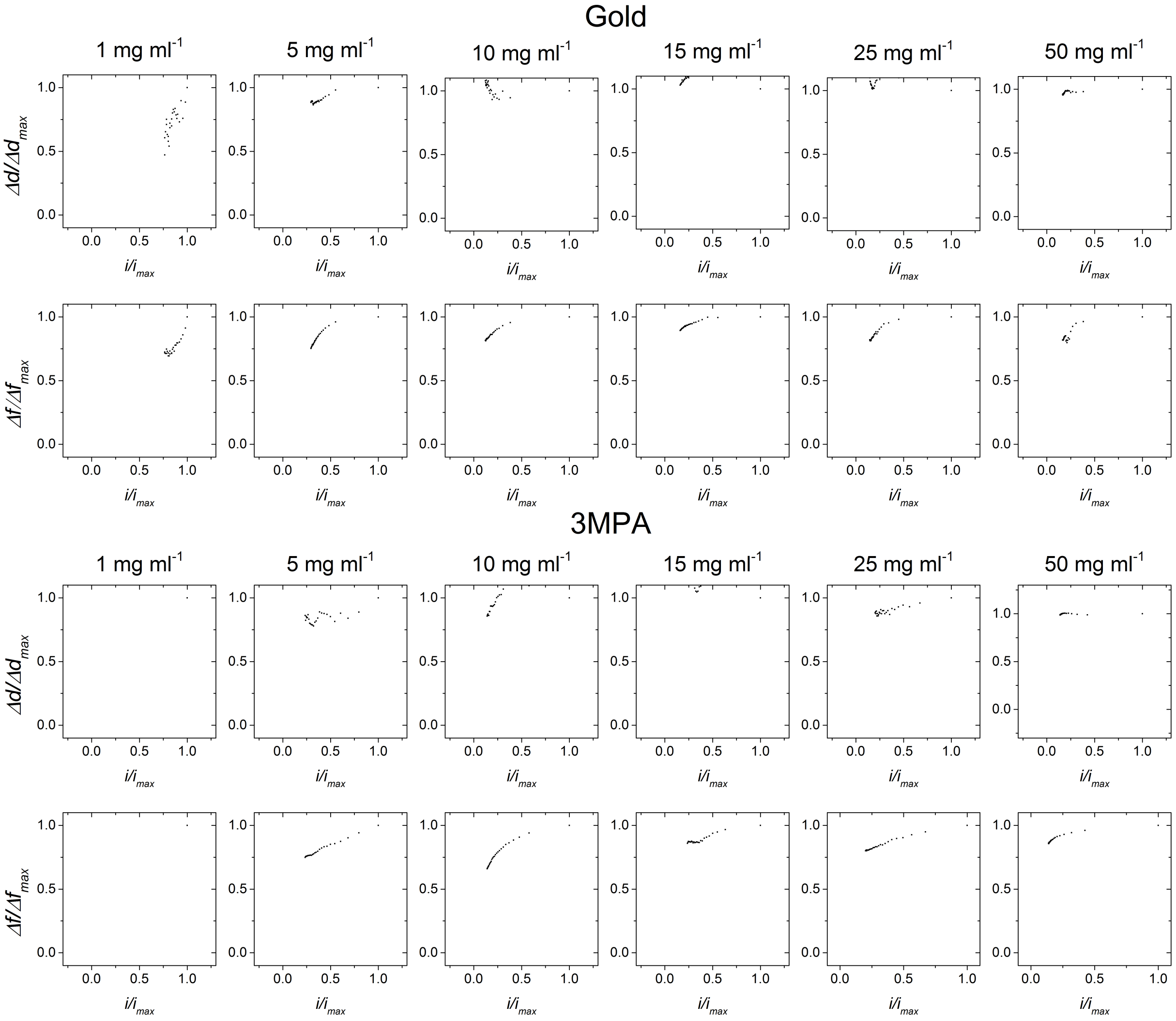

Figure S4. Normalized currents to normalized frequency for concentrations 5–50 mg ml^{-1} for *Mv*BOx adsorbed on gold and 3MPA. i_{max} is taken at 0.55V vs. SHE for each successive CV scan along with the frequency or dissipation change at that time.

TM

S6. Longer protein solution contact times

To test whether the initial overshoot at higher concentrations could be attributed to a bulk solution effect, the injection volume was tripled to 75 µl to increase the protein solutions' contact time to 45 s. Concentrations of 5, 10, 15, 25 mg ml^{-1} were adsorbed onto 3MPA-coated sensors and then were investigated using CVs, as shown in Figure S5.

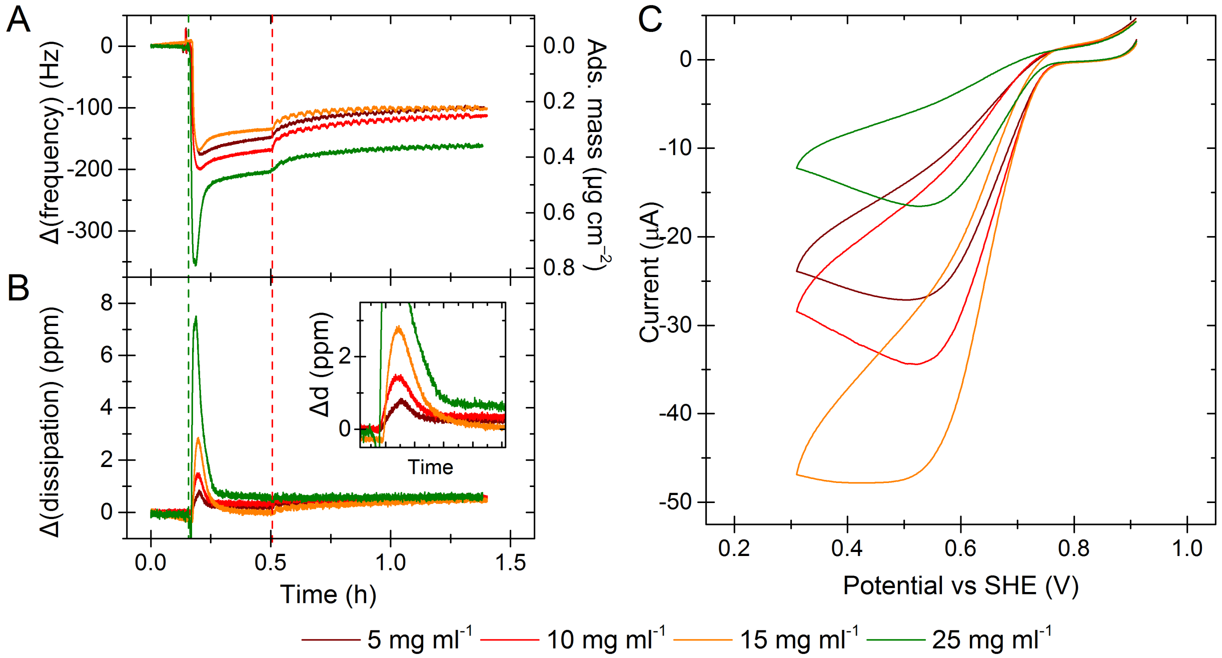

Figure S5. Effect of increasing slug time for *Mv*BOx inside E-QCM chamber. Adsorption for concentrations 5–25 mg ml^{-1}. Panel A shows frequency response, B shows dissipation response and C shows CVs. Green dashed lines show adsorption of *Mv*BOx. Red dashed lines show start of CVs. Panel B shows the first scan for each concentration. Conditions: Oxygen-saturated 0.1M sodium phosphate buffer pH 6.0 at 25 °C flowing at 0.1 ml min^{-1}, QCM traces are for the seventh harmonic, 75 µl *Mv*BOx sample volume, potential cycled between 0.91–0.31 V *vs*. SHE at 10 mV s^{-1}.

TM

The Δf_{max} response showed the largest magnitude change for the highest concentration 25 mg ml^{-1}, however the lowest frequency change was seen for 15 mg ml^{-1}. The Δd_{max} responses follow a linear increase for increasing concentrations. First CV scans for each concentration are shown in Figure S5C and show the highest reductive current to be generated from the 15 mg ml^{-1} concentration, with the smallest being from the highest concentration, 25 mg ml^{-1}. QCM-D data for *Mv*BOx on bare gold and 3MPA-coated surfaces is given in

Table S4. For both surfaces, the maximum and final frequency and dissipation responses were similar, and both increased monotonically with increased concentration. Table S5 lists the $\Delta d/\Delta f$ values for the different adsorption stages for gold and 3MPA. In region (1), no concentration dependence was observed, unlike that for region (1) in the 3MPA-coated sensor. Both surfaces' region (2) showed an increase in $\Delta d/\Delta f$ with concentration, with adlayers formed on gold being less rigid than those formed on 3MPA.

Table S4. QCM-D data for *Mv*BOx adsorbed onto bare gold and 3MPA-modified QCM sensors for longer adsorption times of 45 seconds (75 µl).

Surface	**Concentration** mg ml^{-1}	**Δ*f*$_{max}$** Hz	**Δ*d*$_{max}$** ppm	**Δ*f*$_{\infty}$** Hz	**Δ*d*$_{\infty}$** ppm
Gold	5	–176	0.92	–119	0.17
	10	–221	2.35	–142	0.64
	15	–257	4.18	–174	0.68
	25	–317	5.40	–189	0.62
3MPA	5	–176	0.85	–100	0.55
	10	–205	1.53	–117	0.61
	15	–178	3.14	–109	0.82
	25	–350	7.81	–155	0.94

Table S5 QCM-D adsorption stages for *Mv*BOx adsorbed onto bare gold and 3MPA-modified QCM sensors for longer adsorption times of 45 seconds (75 µl).

Surface	**Concentration** mg ml^{-1}	**Δ*d* vs. Δ*f*** Stage 1 ppm Hz^{-1}	**Δ*d* vs. Δ*f*** Stage 2 ppm Hz^{-1}	**Δ*d* vs. Δ*f*** Stage 3 ppm Hz^{-1}	**Δ*d* vs. Δ*f*** Stage 4 ppm Hz^{-1}
Gold	5	–0.0043	–0.0090	0.106	0.0053
	10	–0.0062	–0.025	–0.10	0.0017
	15	–0.0067	–0.034	–0.080	–0.0042
	25	–0.0050	–0.042	–0.091	–0.0011
3MPA	5	–0.0020	–0.011	–0.053	–0.0030
	10	–0.0034	–0.019	–0.079	–0.0023
	15	–0.0089	–0.033	–0.095	–0.019
	25	–0.0093	–0.049	–0.049	-0.0035

S7. *Mv*BOx adsorption on bare DPI sensors

The changes with time of the density, thickness and mass of *Mv*BOx adlayers on silicon oxynitride DPI sensors were fit to a first-order exponential (Equation S1) and are tabulated in Table S6.

$$x(t) = x_0 - \Delta x \exp[(t_0 - t)/\tau_x] \quad \text{(S1)}$$

In Equation S1, x represents the time-dependent variable (that is, density, thickness or mass) being fitted, t represents time, t_0 is the time at the start of the fitted region, x_0 is the value of the dependent variable when $t = t_0$, Δx is the change in the dependent variable between its initial and asymptotic value, and τ_x is the exponential decay constant for that value

Layer properties appeared to show some positive correlation with the concentration of the deposition solution, but only the thickness and mass of the 1 mg ml^{-1} was significantly different.

Table S6. Density (ρ), thickness (h) and mass (m) of layers of *Mv*BOx adsorbed onto silicon oxynitride DPI sensor from 0.1–15 mg ml^{-1} solutions. Values for each parameter were determined by a non-linear least squares fit to the calculated DPI response using Equation S1.

Concentration mg ml^{-1}	ρ_0 g cm^{-3}	$\Delta\rho$ g cm^{-3}	τ_ρ s	h_0 nm	Δh nm	τ_h s	m_0 ng mm^{-2}	Δm ng mm^{-2}	τ_m s
0.1	0.61	–0.118	442	3.01	0.87	264	1.98	0.36	286
1	0.62	–0.055	408	4.40	1.03	387	2.76	0.46	435
3	0.64	–0.049	521	4.28	1.16	413	2.75	0.60	416
5	0.66	–0.023	241	4.40	1.27	525	2.91	0.79	608
10	0.65	–0.068	419	4.91	1.27	400	3.20	0.59	444
15	0.75	–0.058	666	4.82	1.26	456	3.06	0.61	438

S8. *Mv*BOx adsorption on modified silica-coated QCM sensors

QCM measurements of organosilane-modified silicon oxide–coated sensors with *Mv*BOx are shown in Figure S6 and summarized in

Table S7. The bare silica and modified methyl-terminated surface show similar responses for Δ*f* and Δ*d* traces, and similar Δ*d* vs. Δ*f* plots.

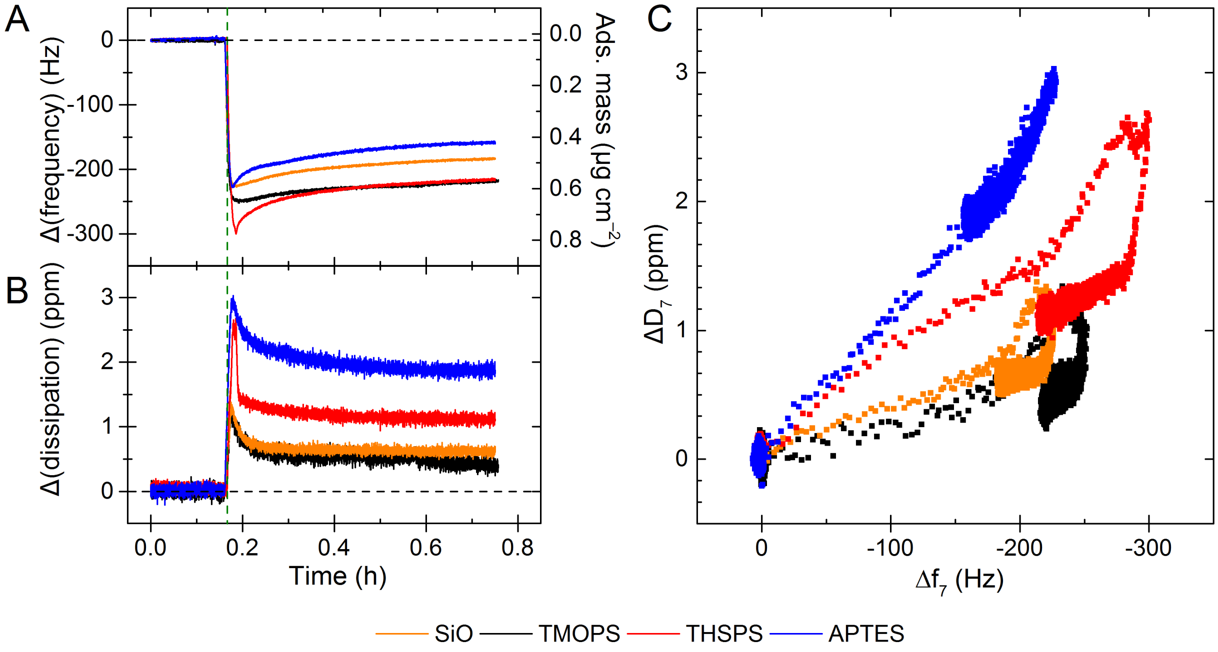

Figure S6. *Mv*BOx adsorption on silane-modified silicon oxide–coated QCM sensors. Panels A and B show the frequency and dissipation responses, respectively, for the addition of *Mv*BOx. Panel C shows Δ*d* vs. Δ*f* plot. Green dashed lines show when *Mv*BOx was injected. Conditions: 0.1M sodium phosphate buffer pH 6.0 at 25 °C flowing at 0.1 ml min^{-1}, traces are for the seventh harmonic. 25 µl, 15 mg ml^{-1} *Mv*BOx sample. TM

The THSPS surface has the largest magnitude Δf_{max}, however the mass loss after adsorption is the largest for any surface. For the THSPS surface also showed a large dissipation loss after adsorption, suggesting fast surface reorientation. The ammonium surface shows lowest Δf_{max} , but the highest Δd_{max} suggesting an adlayer with high conformational. Comparing Δ*d* vs. Δ*f* shows only one region of adsorption for the ammonium surface compared to two regions for the bare silica, methyl- and sulfonate-terminated.

Table S7. QCM-D data for *Mv*BOx adsorbed on to organosilane modified silica QCM sensors.

Surface	**$\Delta f_{\max}$** Hz	**$\Delta d_{\max}$** ppm	**Δf_{∞}** Hz	**Δd_{∞}** ppm
Bare silica	–228	1.38	-–84	0.62
TMOPS	–252	1.34	–218	0.40
SOOOH	–300	2.68	–216	1.12
APTES	–228	3.03	-–59	1.88

Table S8. QCM-D data for adsorption stages of *Mv*BOx adsorbed on to organosilane modified silica QCM sensors.

Surface	**Δd vs. Δf** Stage 1 ppm Hz^{-1}	**Δd vs. Δf** Stage 2 ppm Hz^{-1}	**Δd vs. Δf** Stage 3 ppm Hz^{-1}	**Δd vs. Δf** Stage 4 ppm Hz^{-1}
Bare silica	–0.0034	–0.0184	–0.0222	–0.0026
TMOPS	–0.0027	–0.0126	–0.0269	–0.0085
SOOOH	–0.0067	–0.0168	–0.0770	–0.0050
APTES	–0.0125		–0.0243	–0.0111

S9. Surface change and chain length effects on adsorption of *Mv*BOx

QCM-D responses for *Mv*BOx adsorbed to organothiol-modified sensors with different modifier lengths are given in Table S9.

Table S9. QCM-D data for *Mv*BOx adsorbed on to organothiol modified silica QCM sensors.

Modifier	Δf_{max} Hz	Δd_{max} ppm	Δf_{∞} Hz	Δd_{∞} ppm	$\Delta d/\Delta f$ Stage 1 ppm Hz^{-1}	$\Delta d/\Delta f$ Stage 2 ppm Hz^{-1}
3MPA	–286	3.99	–190	0.73	–0.0069	–0.025
2MP	–260	5.54	–148	0.69	–0.0042	–0.044
2AE	–226	2.64	–162	1.30	–0.0041	–0.021
6MAH	–358	7.10	–298	3.02	–0.015	–0.025
6MH	–249	3.92	–206	0.93	–0.0031	–0.035
6AH	–354	10.1	–248	2.34	–0.016	–0.025

S10. *Mv*BOx crystal structure analysis

Protein crystal structure for *Mv*BOx (pdb 2xll)[2] was sourced from the Protein Data Bank at http://www.rcsb.org/pdb/home/home.do and the molecular modeling program PyMOL was downloaded from http://pymol.sourceforge.net/ and used to show protein crystal structures and the coordination of the copper sites in bilirubin oxidase (*Mv*BOx). The approximate dimensions for height, width and length are given in Figure S7.

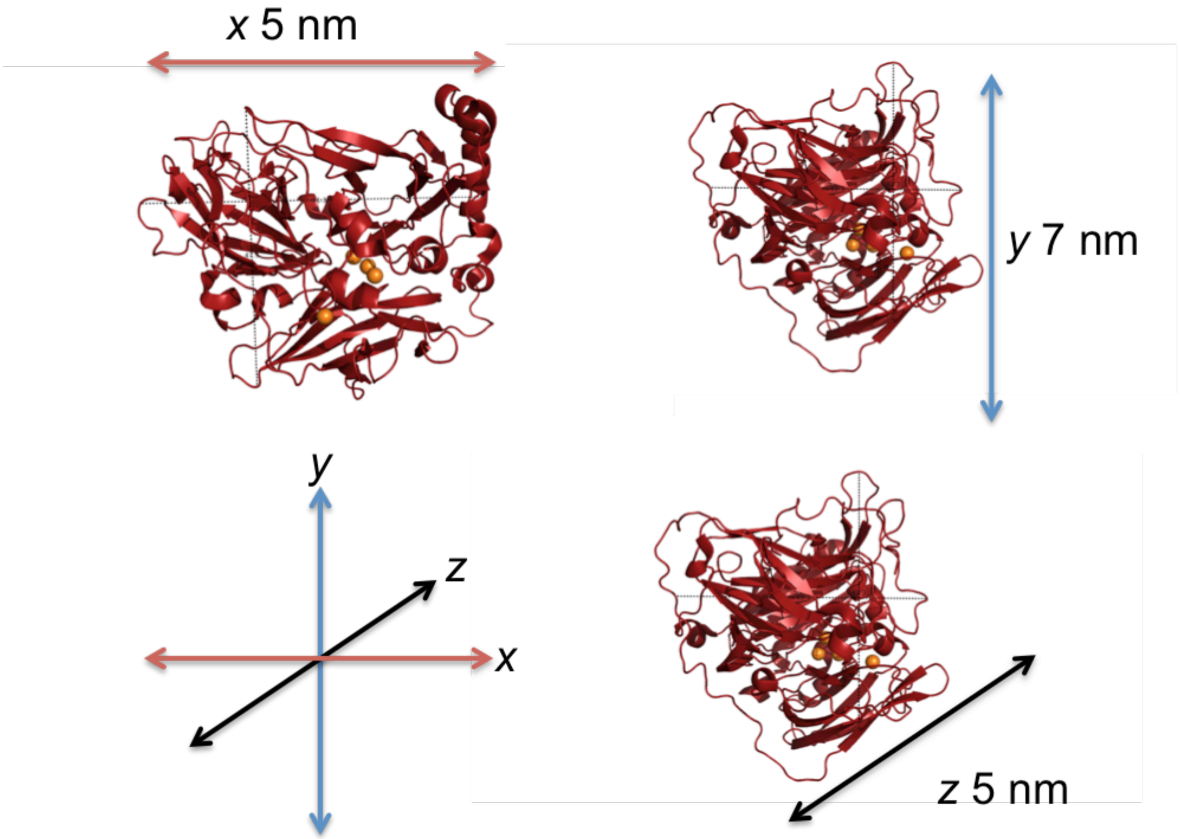

Figure S7 PyMOL visualization of the dimensions for *Mv*BOx (PDB code 2xll)[2]. The polypeptide backbone is shown as the brown cartoon ribbon. The coppers are shown as yellow spheres. The approximate dimension for each of the three axis are given.

TM

S11. Measurements of protein solution viscosities

Viscosity measurements were run for *Mv*BOx concentrations from 1 to 30 mg ml^{-1}. The measurements were fit to the Huggins model (Equation S2) and Kraemer model (Equation S3) and used to calculate the intrinsic viscosity.[3-4]

$$\frac{\eta_{\mathrm{sp}}}{c} = [\eta] + K_{\mathrm{H}}\,[\eta]^2\,c \tag{S2}$$

$$\frac{\eta_{\mathrm{r}}}{c} = [\eta] - K_{\mathrm{K}}\,[\eta]^2\,c \tag{S3}$$

In these equations, η_{sp} is the specific viscosity, $[\eta]$ is the intrinsic viscosity, η_r is the relative viscosity, and K_H and K_K are the Huggins constant and Kramer constant, respectively. The fitting parameters are listed in Table S10, and the measurements and fits are plotted in Figure S8.

Table S10. Huggins and Kraemer calculated data for fitted intrinsic viscosity measurements.

Model	**[η]** dL g^{-1}	***K*_H or *K*_K**
Huggins	0.04782	1.93
Kraemer	0.04781	–1.24

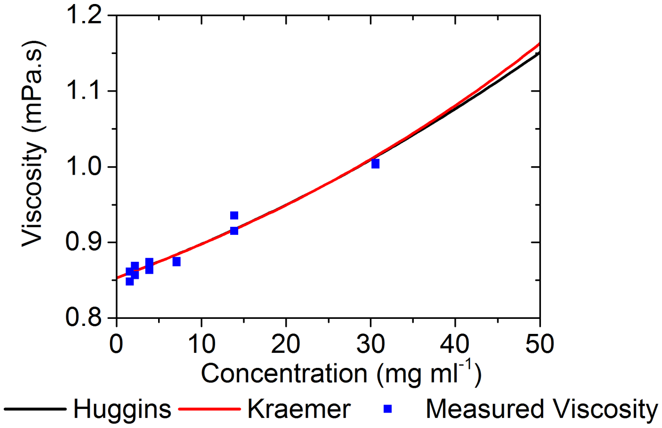

Figure S8. Dynamic viscosity measurements for *Mv*BOx for concentrations ranging from 2–30 mg ml^{-1}. Intrinsic viscosity measured using fitted data for both Huggins and Kraemer methods. Conditions: 0.1M sodium phosphate buffer pH 6.0 at 25 °C.

TM

S12. Voigt modeling of QCM response to protein adsorption.

Figure S9 shows the modeled QCM-D response for an adlayer formation from a 15 mg ml^{-1} solution of *Mv*BOx. In Figure S10, the frequency responses are shown for layer thinning and mass loss respectively. The inset in Figure S9 shows the point where the bulk solution is changed from a protein-containing buffer back to protein-free buffer. At this point the change in the density and viscosity of the bulk solution at both decrease which increases the magnitude of the frequency response (that is, it becomes more negative). This is the opposite of the response observed experimentally and means that bulk solution effects are not responsible for these observations.

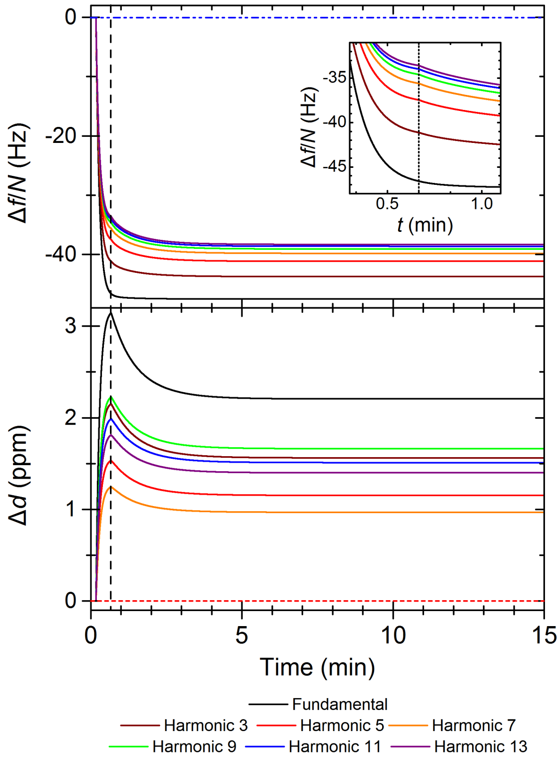

Figure S9. Simulated frequency and dissipation response from protein absorption onto a QCM sensor surface. The model includes an initial 10s baseline where just buffer is present, the solution is then changed to a 15 mg ml^{-1} protein solution for 30 seconds before the solution is changed back to buffer and the concentration of the enzyme in the bulk solution decreases as a first-order exponential with a time constant of 60s. The inset shows an enlarged section of the frequency response where the solution is changed back to buffer. The properties of the layer are: viscosity: 3.2 × 10^{-3} Pa s; shear modulus: 3.2 × 10^{5} Pa; film density: 1 450 kg m^{-3}; fundamental frequency: 4.95 MHz; solution density: 1.0 × 10^{3} kg m^{-3}; solution viscosity 8.5 × 10^{-4} Pa s. TMcN

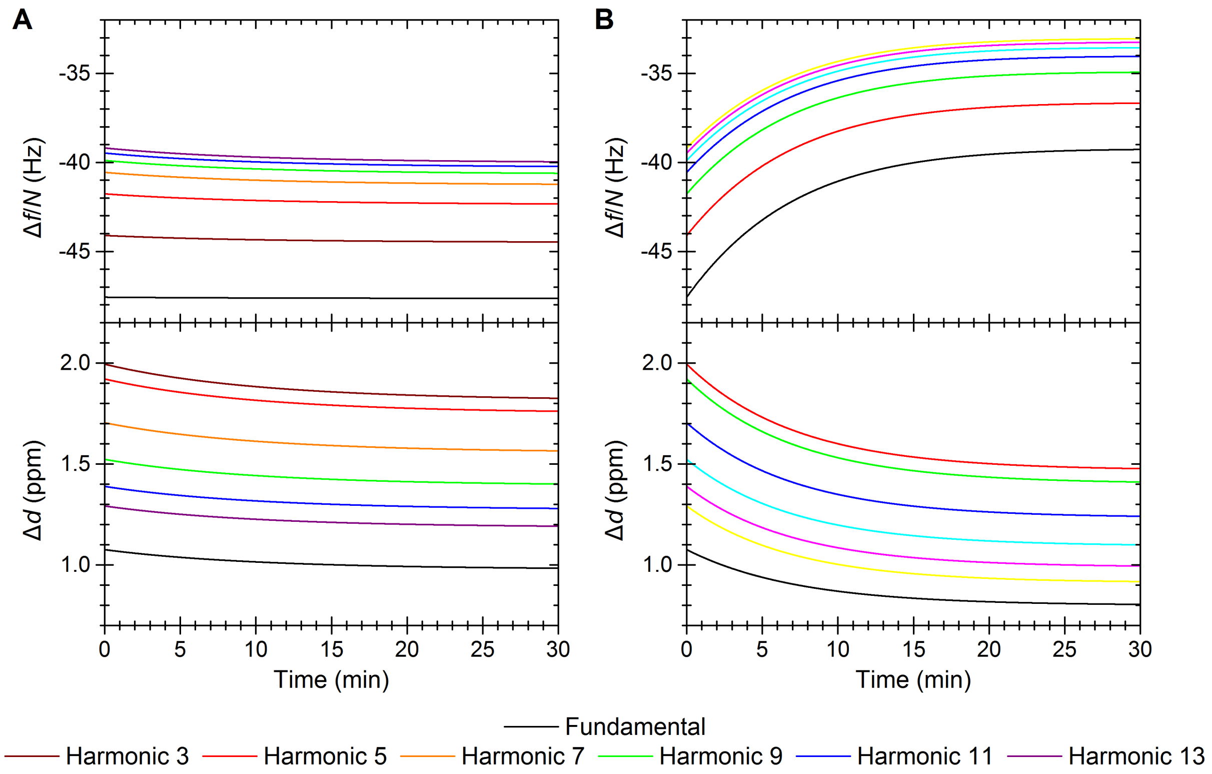

Figure S10. Simulated frequency and dissipation responses from a QCM-D that would result from the thinning of an absorbed protein layer like that generated from a 15 mg ml^{-1} solution of *Mv*BOx. The adlayer viscosity and shear modulus remain constant. Panel A shows the response where the surface protein concentration remains constant (i.e., adlayer thinning is matched by densification). Panel B shows the response when thinning is accompanied by mass loss. Frequency responses are normalized by dividing the frequency by the harmonic number (*N*). Adlayer changes are modeled as first-order exponentials. Adlayer properties: viscosity 3.2 × 10^{-3} Pa s; shear modulus 3.16 × 10^{5} Pa; initial density 1 450 kg m^{-3}; final density 1 595 kg m^{-3}; densification time constant 660 s; initial thickness 6 × 10^{-9} m; final thickness 4.5 × 10^{-9}; thinning time constant 440 s; fundamental frequency 4.95 MHz; solution density 1 × 10^{3} kg m^{-3}; solution viscosity 8.5 × 10^{-4} Pa s. `TMcN`

S13. References

1. Singh, K. Structure-function studies of the oxidoreductase bilirubin oxidase from *Myrothecium verrucaria* using an electrochemical quartz crystal microbalance with dissipation University of Oxford, Department of Chemistry, D.Phil. thesis, 2014.
2. Cracknell, J.; McNamara, T.; Lowe, E.; Blanford, C. F., Bilirubin oxidase from Myrothecium verrucaria: X-ray determination of the complete crystal structure and a rational surface modification for enhanced electrocatalytic O(2) reduction. *Dalton Trans.* **2011,** *40* (25), 6668-6675.
3. Huggins, M. L., The Viscosity of Dilute Solutions of Long-Chain Molecules. IV. Dependence on Concentration. *J. Am. Chem. Soc.* **1942,** *64* (11), 2716-2718.
4. Kraemer, E. O., Molecular Weights of Celluloses and Cellulose Derivates. *Industrial & Engineering Chemistry* **1938,** *30* (10), 1200-1203.

Chapter 5

The effect of applied potential on adsorption and mass-specific activity of bilirubin oxidase

5 The effect of applied potential on adsorption and mass-specific activity of bilirubin oxidase

In this paper, adsorption and specific activity of bilirubin oxidase adsorbed to gold electrodes were investigated before and after a potential was applied to the surface. E-QCM-D measurements showed that under an applied potential, adsorption rates were slower and produced a more flexible layer than adsorption in the absence of an applied potential. Specific activity was greater when the enzyme layer was allowed to adsorb under no electrostatic interference. QCM-D measurements suggested the enzyme was mis-orientated rather than denatured on the surface. Increasing the concentration of the enzyme during adsorption was shown to also affect the specific activity of the enzyme layer.

I wrote the paper and completed all experimental work.

Chapter 6

A versatile route to edge-specific bioconjugation of pristine graphene

6 A versatile route to edge-specific bioconjugation of pristine graphene

In this paper, covalent chemical functionalisation to edge sites of pristine graphene were described, with minimal disturbance of the extended graphene π system. Functionalised graphene was subsequently decorated with proteins and nanoparticles, a key step in the direction of electrochemical sensing and bioelectroatalysis on single graphene flakes.

I produced suspended graphene flakes through liquid sonication and characterised all graphene samples through Raman spectroscopy and scanning electron microscopy before and after chemical funcationalisation.

Throughout this thesis, work has focused on improvement of stability and current density of immobilised *Mv*BOx to gold modified electrodes. This work links to the overall aims of the thesis, by looking for future materials that can improve the main limitations of enzymatic electrocatalysis. Introducing functional groups to graphene, can allow for subsequent attachment of *Mv*BOx through anchored physical adsorption and covalent attachment. Previous studies have focused on attaching multicopper oxidases to functionalised carbon nanotubes, to improve orientation and stability, although chemical modification can disrupt the electrical conductivity.[137-138] This work therefore can aid the immobilisation of a range of bio-catalysts in the future.

.

The effect of applied potential on the adsorption and mass-specific activity of bilirubin oxidase

Trevor McArdle and Christopher F. Blanford
School of Materials and Manchester Institute of Biotechnology, 131 Princess Street,
Manchester, M1 7DN, UK.
*E-mail: christopher.blanford@manchester.ac.uk

Abstract

An electrochemical quartz crystal microbalance with dissipation monitoring (E-QCM-D) was used to follow the effect of applied potential on the adsorption and bioelectrocatalytic activity of bilirubin oxidase from *Myrothecium verrucaria* (*Mv*BOx) at pH 6. Potentials of 100 mV and 400 mV vs. Ag|AgCl|3M NaCl were applied to the unmodified gold QCM sensor surface, which doubled as the system's working electrode. Adsorbed mass was a third higher when the surface was biased to 400 mV than when the surface was biased to 100 mV. The electrocatalytic activity of the system toward the four-electron reduction of dioxygen to water was greater when adsorbed at open circuit potential and decreased as adsorption occurred at a more negative applied potential. QCM-D analysis showed that under an applied potential, the adlayer had increased conformational flexibility compared with OCP. An optimum concentration of 15 mg ml^{-1} give the highest mass specific activity when adsorbed at +100 mV, reinforcing the electrostatic interactions between enzyme-enzyme, and enzyme electrode are of fundamental importance for efficient DET.

Introduction

Immobilization of redox-active enzymes onto electrodes has many technological applications, particularly in the field of biosensors and biofuel cell catalysis.[1-2] Enzymes exhibit bioelectroactivity on a wide range of surfaces, but control over how they are immobilized is required to ensure high current densities and long-term stability.[3-4] Multicopper oxidases (MCO) are a family of enzymes that can catalyze the four-electron reduction of O_2 to water.[3] Here, we have used the MCO bilirubin oxidase from *Myrothecium verrucaria* (*Mv*BOx) as a model protein to investigate the adsorption mechanisms and resulting bioactivity under a constant applied potential to an electrodes surface during the adsorption phase.

Proteins generally have a high affinity for adsorption, due to a gain in entropy occurring from the release of surface water and ions, although adsorption can be controlled either through internal factors such as solvent, pH, surface choice, or external factors such as electric or magnetic fields.[5-7] Benavidez et al. looked at potential assisted adsorption of bovine serum albumin (BSA) onto optically transparent carbon electrodes.[6] They showed BSA had increased adsorption kinetics when an external potential was applied, increasing the surface saturation of the adsorbing protein. This was attributed to the polarization of the incoming BSA, which improved dipole-dipole interactions of the adsorbed layer.

Studies have shown that efficient bioelectrocatalysis of adsorbed proteins are dependent on the distance between the electrode and the enzyme's primary electron entry point.[3, 8-9] Due to the size of proteins, and their catalytic center, careful control of orientation is required.[10] Studies of MCO's immobilization strategies usually focus on selecting electrode surfaces that can be modified with specific functional groups to either increase adsorption, or alter enzyme orientation to the surface.[11] Olejnik et al. showed how a change in surface charge, through ammonium- and carboxylate-terminated SAMs, alters the orientation of adsorbed laccase, which directly affects the bioactivity. The carboxylate surface positioned the laccase in a suitable geometry for fast electron transfer, yet no catalytic current was observed when adsorbed onto the ammonium surface.[12] McArdle et al. showed that *Mv*BOx adsorbed to bare gold and carboxylate-terminate surfaces produced an optimum concentration for mass specific activity of adsorbed. They proposed that careful control of the adsorption rate through concentration of the deposition solution, allowed protein-protein interactions to inhibit spreading on the surface, but not force the enzyme to adopt an orientation unfavorable for electron transfer.[13]

An electrochemical quartz crystal microbalance with dissipation analysis (E-QCM-D) permits the simultaneous measurement of adsorbed hydrated mass of a protein adlayer, its mechanical coupling to the sensor surface, and its catalytic activity with respect to an externally applied potential.[14] This was used investigate how the applied potential affects the adsorption and resulting biocatalytic activity of *Mv*BOx. Electrode potential was shown to influence the adsorption mechanics of the enzyme layer. A range of concentrations of the deposition solution were tested, to see if the affect of an applied potential, would change a previously seen optimum concentration for adsorption to gold QCM sensors.[13] The motivation was to optimize the immobilization of *Mv*BOx for electron–transfer catalysts, through an external influence ,to improve the mass–specific catalytic activity.

The influence of external applied potential, can give understanding towards catalysis failures, and allow us to further develop methods to combat these failure processes and fine tune operating conditions for increased long–term performance.

Experimental

Materials and reagents

Lyophilized *Mv*BOx powder (Amano Enzyme EU, Chipping Norton, UK) was dissolved in 0.1 M sodium phosphate buffer pH 6.0 at 4 °C. The solution was purified by centrifugation through polyethersulfone membrane (Vivaspin, 30 kDa MWCO) to remove small molecular weight contaminants. Protein concentration was calculated by UV absorption , using $\varepsilon_{280\ \mathrm{nm}} = 9.52 \times 10^4\ \mathrm{M^{-1}\ cm^{-1}}$, calculated from the enzyme's amino acid sequence.[15] Solutions of *Mv*BOx were prepared from dilutions of higher concentration stock solutions, which were stored in the gaseous phase above liquid nitrogen.

Hydrochloric acid (37%, Fisher), sodium dihydrogen orthophosphate dihydrate (99.0–101.0%, Fisher), disodium hydrogen orthophosphate anhydrous (99.5+%, Fisher), sulfuric acid ($1.83\ \mathrm{g\ ml^{-1}}$, >95%, Fisher) and hydrogen peroxide (30% w/v, Scientific Laboratory Supplies) were used as received without further purification. Water was purified via reverse osmosis and ion exchange to a resistivity of 18.2 MΩ cm at 25 °C using a MilliQ water purifier.

Electrochemical quartz crystal microbalance with dissipation

A Q-sense E1 system was used to measure protein adsorption along with Qsoft data acquisition software (version 2.5.18.682). E-QCM-D measurements used a modified Q-Sense QEM401 module with a 0.1 ml sample chamber volume.[13] Sensors (Q-Sense) were gold-coated 14mm diameter AT-cut quartz crystals with a fundamental frequency of 4.95 ±0.05 MHz. The flow module and fluid handling system were positioned on an aluminum plate maintained at 25 °C using an internal water flow. The temperature of the flow module was stabilized to within 10 mK using the module's integrated Peltier device.

QCM measurements started with a flow of buffer a stable response was obtained. Aliquots of *Mv*BOx and BSA were pulled through the measurement cell at $0.1\ \mathrm{min^{-1}}$ using. Time between sample loading and sensor interaction was 2 minutes. The flow of buffer was left for a minimum of 30 minutes after injection (longer for E–QCM–D measurements to measure activity loss) to measure surface changes and desorption.

An Ivium CompactStat potentiostat was used for electrochemical measurements. A three-electrode system was used: the gold-coated QCM sensors acted as the working electrode (surface area 0.8 cm^2), a 0.2mm thick 2.25 cm^2 rectangle of platinum located 0.7–0.8 mm from the working electrode acted as counter electrode, and a Ag|AgCl|3M NaCl system (BASi RE–6, $E_{\mathrm{SHE}} = E_{\mathrm{ref}} + 0.209$ V at 25 °C) was use for the reference electrode. The buffer was pre-oxygenated for at least 20 minutes.

Results and discussion

In order evaluate the effect of working electrode potential on the adsorption and activity of *Mv*BOx, potentials of 100 and 400 mV vs. reference were applied during the adsorption phase. Figure 1 shows the comparison of the E-QCM-D response to enzyme adsorption when the sensor surface is held at 100 mV (panel A) to its response when this potential is applied ~25 min. after adsorption (panel B). The frequency response (Δf, top panels) starts with a baseline response when only buffer is flowing. About 2 min. after protein injection an increase in the magnitude of Δf is seen, indicative of an increase in mass on the sensor surface. The areal mass densities given on the right-hand axes are based on the Sauerbrey equation, which assumes a rigid, well-coupled adlayer.[16] Protein adlayers, however, are soft, which causes the sensor's vibrational energy stored to be lost to viscous damping.[17] This change in energy dissipation of the loaded versus the unloaded crystal (Δd) is plotted in the middle panels. The ratio of dissipation change to frequency change effectively normalizes dissipation to adsorbed mass, so plots of Δd vs. Δf, such as those shown in the insets, give information about changes in protein orientation or conformation on the surface.[14] *Mv*BOx adsorption always follows a four-stage pattern:[13] (1) the rapid formation of a relatively stiff initial layer region, (2) the formation of less rigid layer or layers, (3) a rapid loss of mass (increase in Δf) and stiffening (decrease in Δd) of the film, and (4) a more gradual increase in Δf and decrease in Δd. The bottom panel shows the electrocatatlyic O_2 current, which is negative for reduction by convention, and is proportional to both enzyme activity and surface coverage.[14] There was always a lag between the peak in adsorbed mass (Δf_{max}) peak in catalytic response (i_{max}) which may be due to enzyme activation effects. In this work, the subscript "max" refers to the points of greatest magnitude for these three measurements, and the subscript ∞ is used for their final layer values.

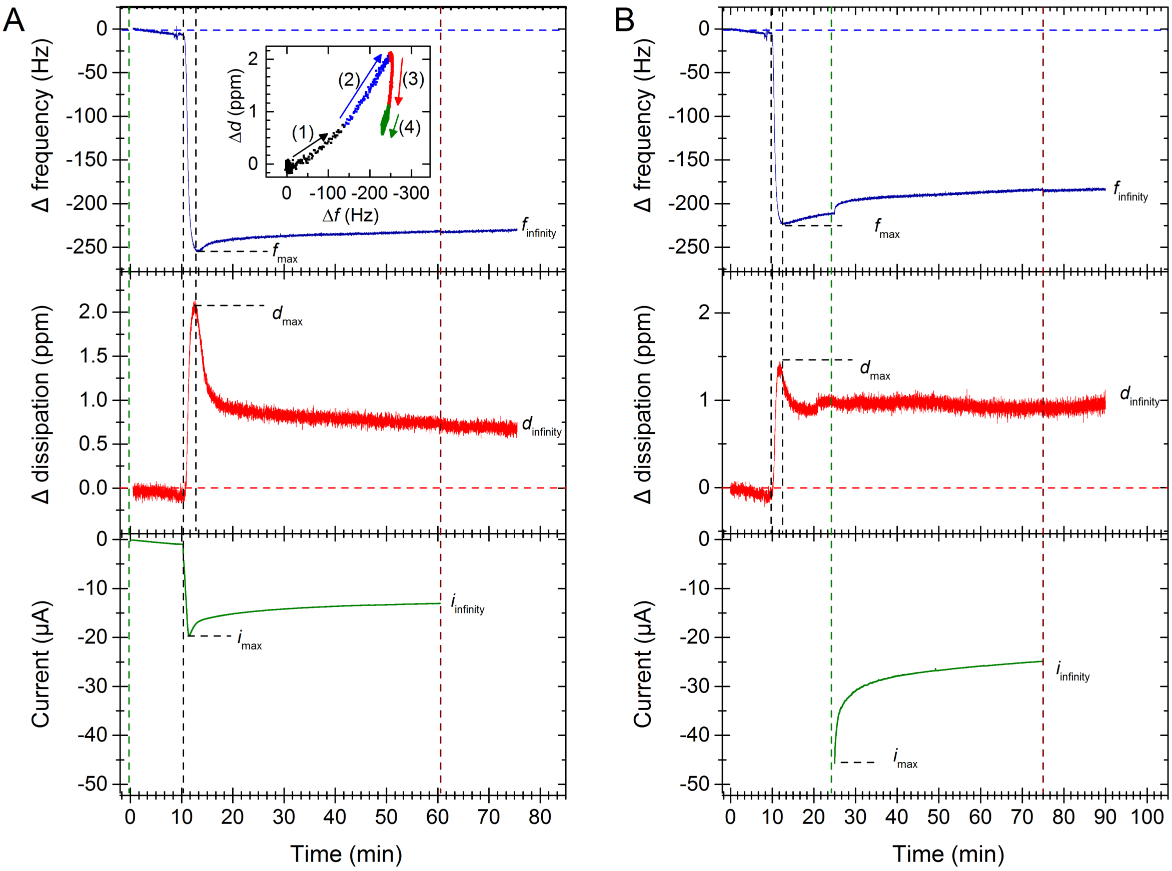

Figure 1. Typical QCM–D response for *Mv*BOx adsorbed onto a bare gold QCM sensors applied at a constant potential at +400 mV (left) and OCP (right). Top panel shows frequency response, middle panel shows the dissipation and the bottom panel shows O_2 reduction current. Inset in A Top shows Δ*d* vs. Δ*f* plot labeled into four distinct adsorption regions, (1), shown in black, region (2), shown in blue, region (3) in red and region (4) in green. Green dashed lines show the start of applied potential. Between the black dashed lines is where the adsorption regions (1) and (2) occur. Brown dashed line shows when the potential is switched off. Conditions: 0.1M sodium phosphate buffer pH 6.0 at 25 °C with continuous O_2 bubbling, 15 mg ml^{-1}, 25 µl *Mv*BOx sample volume, seventh harmonic shown. Flow rate 0.1 ml min^{-1}.

TM

Comparing the adsorption in the presence of 400 mV potential shows higher mass loading that the OPC adsorption shown in Figure 1. Dissipation is also lower for the OPC adsorption, suggesting a more rigid stable layer, with less surface reorganization is formed. In Figure 2, adsorption at two potentials +100 mV and +400 mV for *Mv*BOx (25 µl, 15 mg ml^{-1} is compared to *Mv*BOx adsorbed to bare gold at OCP. After adsorption without an applied potential, once a stable layer had formed, +100 mV and +400 mV were applied to see observe changes in activity as a result of the different adsorption conditions.

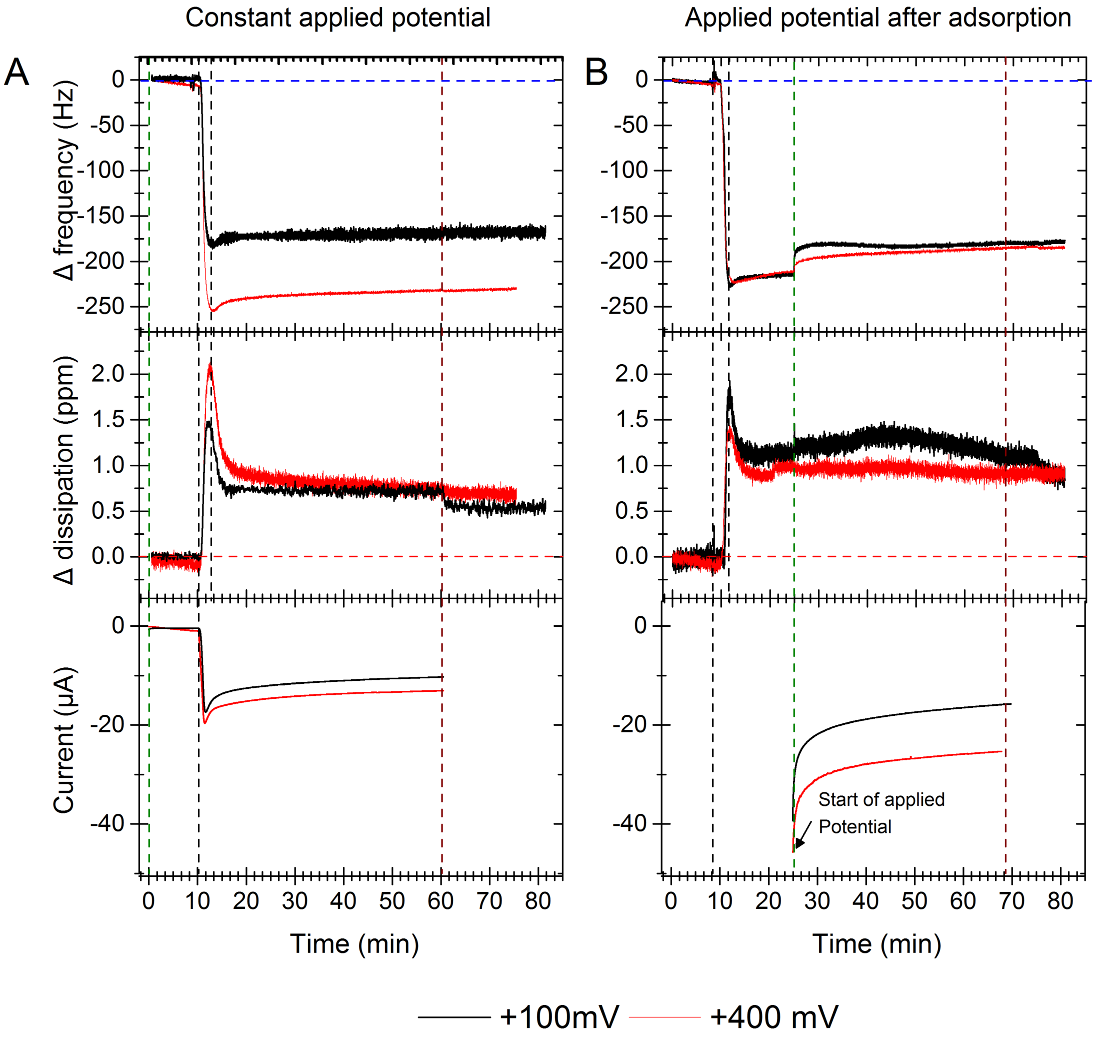

Figure 2. E-QCM–D response for *Mv*BOx adsorbed onto a bare gold QCM sensors. Left shows adsorption when a potential is applied to the electrode surface during the adsorption phase. Right shows adsorption in the absence of a potential, but with a reductive potential of 0.1 and 0.4 V being applied 15 minutes after adsorption. Row A shows the frequency responses. Panel B shows dissipation responses. Panel C shows the O_2 reduction current. Black dashed lines show the adsorption stages (1) and (2), green dashed line shows the start of applied potential and brown dashed lines show the end of applied potential. Conditions: 0.1M sodium phosphate buffer pH 6.0 at 25 °C with continuous O_2 bubbling, 15 mg ml^{-1}, 25 μl *Mv*BOx sample volume, seventh harmonic shown. Flow rate 0.1 ml min^{-1}. TM

In Figure 2A, frequency responses are shown for adsorption during applied potentials and for applied potential after adsorption. Mass loading is seen to be smallest for +100 mV applied during the adsorption phase, and largest for +400 mV applied during adsorption. Traces on the right shown a jump in the frequency response when the potential is applied at 25 minutes, which is more prominent for +100 mV.

The mass required for *Mv*BOx surface saturation can be calculated by using the macromolecular footprint of the enzyme (ca. 40 nm^2) and the active area of the electrodes surface.[18] For the QCM sensors used, the electrodes surface area is 0.8 cm^2 and has a roughness factor or 1.5-1.6, giving a closely packed monolayer of 0.78- 0.8 μg cm^2. This corresponds to a frequency change of 306- 308 Hz, or 7.2 pmol cm^{-2}. From the experimentally determine frequency shifts, we can see that in each case, there is not a fully saturated monolayer formed. The adsorption at an applied potential of +100 mV only shows a frequency response of 175 Hz, well below surface saturation.

Mass normalized to dissipation values for the two stages of adsorption are displayed in Table 1. Normalized stage (1) adsorption shows that *Mv*BOx forms a less rigidly bound surface when there is an applied potential, with a slightly larger value for +100 mV. Stage (1) and Stage (2) for the runs where the potential is not turned on until after the enzyme has adsorbed, show similar values, as is to be expected, as the adsorption conditions are the same. Adsorption for stage (2) shows an increase in viscoelastic nature of the adsorbed layer in all cases.

Table 1 Ratio of dissipation response to frequency response for the first two adsorption stages of *Mv*BOx to unmodified gold QCM sensors with and without an applied potential. Times are relative to the start of each adsorption stage, to the inflection point of the next stage. ___.

Adsorption conditions	**$\Delta d/\Delta f$** Stage 1 ppm Hz^{-1}	**Time** s	**$\Delta d/\Delta f$** Stage 2 ppm Hz^{-1}	**Time** s
+100 mV pre-adsorption	–0.0070	32	–0.011	73
+400 mV pre-adsorption	–0.0060	32	–0.013	78
Open circuit, +100 mV post-adsorption	–0.0043	14	–0.012	65
Open circuit, +400 mV post-adsorption	–0.0037	10	–0.010	69

For adsorption under an applied potential, higher Δd vs. Δf stage (1) shows a more flexible layer being produced on the surface. The time taken for both adsorption stages were longer for applied potentials compare to absence of potentials cases, so surface saturation is slower.

At pH 6, *Mv*BOx will have an overall negative charge, with a pI of 4.1. When a surface potential is applied, the adsorption at each stage is longer showing that electrostatics repulsions are decreasing the rate of adsorption. To assess the activity of the adsorbed layer, the reductive current produced from the enzymatically catalyzed O_2 reduction is compared for the adsorption during applied potential, and for adsorption at open circuit voltage and are shown in Figure 2C. A maximum reductive current, i_{max} was measured for each of the adlayers along with a final fitted current decay, denoted as i_∞ and are given in Table 2. A larger i_{max} can be expected for the layers that have been adsorbed under no potential, because the saturated surface will have fully oxygenated buffer above it, whereas in the case of the adsorption under applied potential, the buffer immediately above the adlayer starts to be depleted of O_2 as soon as the first proteins adsorb. Therefore by the time of surface saturation, mass transport limitations are already seen.

To relate adsorbed mass to the generated reductive current, i_{max} and i_{∞} were divided by the respective frequency response to give an activity per adsorbed amount of enzyme.[13] Adsorption under an applied potential shows a lower activity for both values compared to the adsorption in the absence of an applied potential. Table 2 gives values for the initial activity per adsorbed mass of enzyme along with a resting activity. Both +100 mV and +400 mV show a very similar activity per adsorbed mass for maximum and final adsorbed layers although adsorption at +400 mV showed higher mass loading. The layers, which were allowed to adsorb under no applied potential, showed higher activity, with +400 mV having the highest activity of all four adsorption conditions.

Table 2. Specific activity of MvBOx adsorbed in the presence and absence of applied potential.

Adsorption conditions	i_{max} μA	i_{∞} μA	$i_{max}/\Delta f_{max}$ μA Hz^{-1}	$i_{\infty}/\Delta f_{\infty}$ μA Hz^{-1}
+100 mV pre-adsorption	–17.4	–10.5	0.09	0.06
+400 mV pre-adsorption	–19.6	–16.6	0.08	0.07
Open circuit, +100 mV post-adsorption	–39.3	–15.7	0.17	0.09
Open circuit, +400 mV post-adsorption	–45.7	–25.3	0.20	0.14

Adsorption under applied potential showed that a more positive potential give a higher overall adsorption, therefore a higher current. However the adsorbed layer shows no difference in activity per adsorbed amount of enzyme. This is not true for *Mv*BOx adsorbed in the absence of an applied potential. In all cases, less than a saturated monolayer is being formed, which suggests that the enzyme is spreading on the surface. In Figure 3, the initial adsorption process is shown for an applied potential, and open-circuit potential. QCM-D experiments show us that the applied potential slows down the rate of adsorption. As a potential is applied to the surface, a change in the electrical double layer will occur to counteract the increasing charge at the electrode. This will change the composition of ions located at the surface of the electrode, which in turn affect the enzyme-electrode interaction. The effective electrical field that is generated at the surface will also change, slowing down the approach of the adsorbing enzyme.[19] Once an enzyme has adsorbed, the electrostatic interactions between the electrode and neighboring enzymes, can induce surface re-orientation, producing a lower activity per adsorbed mass. QCM-D suggests this is happening when the enzyme adsorbs at an applied potential, as dissipation analysis shows the layer to retain conformational flexibility.

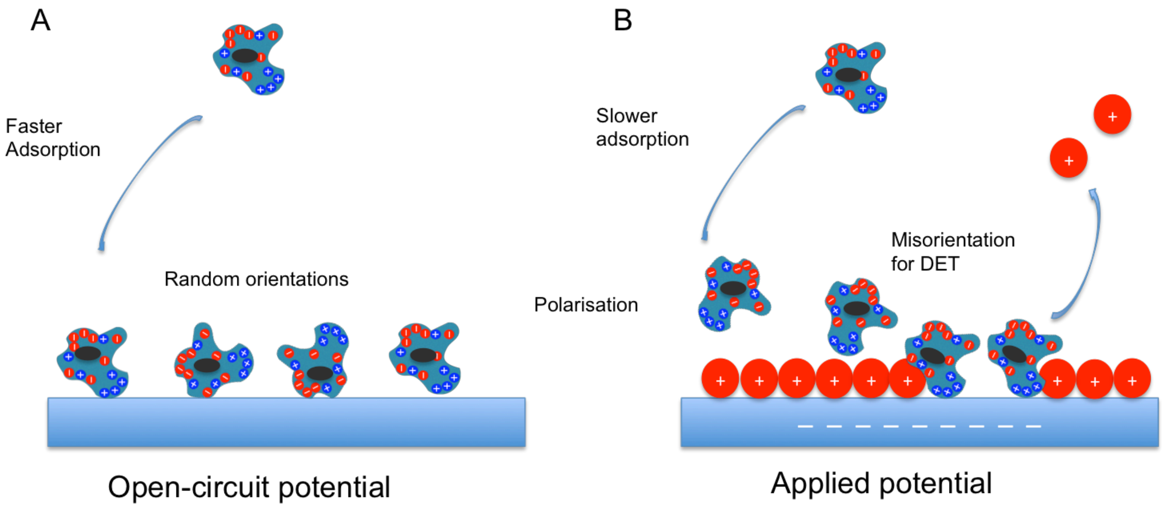

Figure 3. Proposed mechanism of initial adsorption processes of *Mv*BOx to a surface at open-circuit potential and at an applied potential. A shows adsorption at an open circuit potential, where the enzyme is free to adsorbed in several orientations. B shows the effect of an applied electrical field, that changes the composition of the electrical double layer, and polarizes the enzyme for unfavorable DET. TM

Increasing concentrations of *Mv*BOx adsorbed at an applied potential was investigated to observe the influence on the adsorption and activity of the resting layer Concentrations ranging from 10–50 mg ml^{-1} were adsorbed at a constant potential of + 100 mV which was applied before adsorption. The frequency, dissipation and catalytic reduction of O_2 are shown in Figure 4.

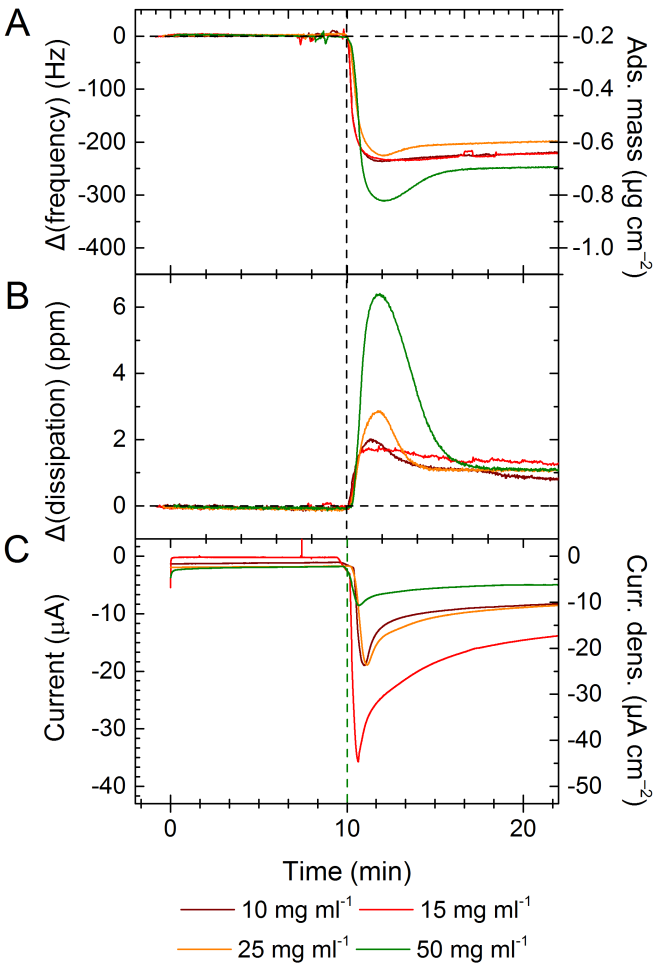

Figure 4 E–QCM–D traces for *Mv*BOx adsorbed onto bare gold QCM sensors with concentration ranging from 10–50 mg ml^{-1}. Panel A shows the frequency response, panel B shows the dissiaption response and panel C showsO_2 reductive current at a applied potential of 0.1 V vs. Ag|AgCl|3 M NaCl. Conditions: 0.1M sodium phosphate buffer pH 6.0 at 25 °C with continuous O_2 bubbling, 25 µl *Mv*BOx sample volume, seventh harmonic shown. Flow rate 0.1 ml min^{-1} TM

The frequency responses for the increasing concentrations all give similar surface saturations. Concentrations of 25 and 50 mg ml^{-1} both have an overshoot in the frequency response before forming a stable layer. This is due to an excess of loosely bound protein, which desorbs from the surface as the layer is rinsed with buffer. Dissipation traces show similar Δd_∞, but again observes an overshoot, which increases with increasing concentration. Figure 4C shows the variation in the catalytic current generated by the catalytic oxygen reduction. For each concentration, the maximum frequency, dissipation and current is displayed in Figure 5 as a function of enzyme concentration.

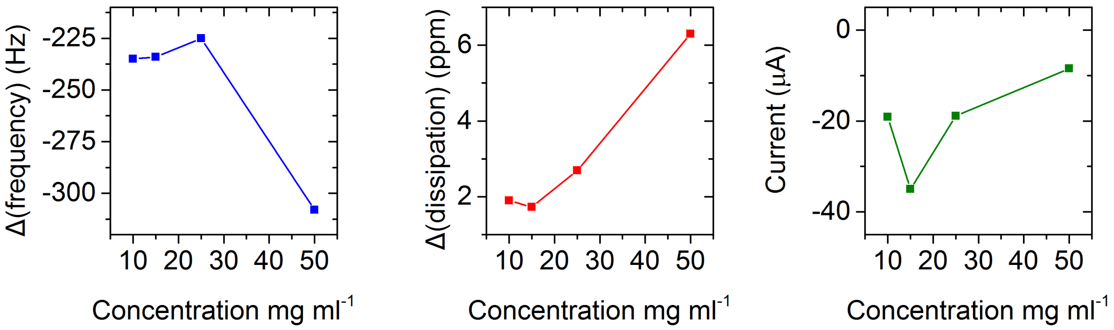

Figure 5. E-QCM-D analyses for *Mv*BOx adsorption to bare gold QCM sensor at an applied potential of +100 mV for concentrations ranging from 10–50 mg ml^{-1}. Maximum frequency, dissipation and current are shown as a function of enzyme solution concentration.

TM

The trace for15 mg ml^{-1} exhibits the largest current generated at the electrode, with 50 mg ml^{-1} being least active. The current decay was calculated and shows that 15 mg ml^{-1} has the longest decay time constant, suggesting the layer is more susceptible to the influence of the applied potential on enzyme deactivation.

Table 3 shows the Δd vs. Δf responses for the increasing concentrations, along with the activity maximum and end activity per adsorbed amount of enzyme.

Table 3. *Mv*BOx adsorption analysis and specific activity with increasing concentration.

Concentration	**Δd vs. Δf**	**Stage 1**	**Δd vs. Δf**	**Stage 2**	**$i_{max}/\Delta f_{max}$**	**$i_\infty/\Delta f_\infty$**
	Stage 1		Stage 2			
mg ml^{-1}	ppm Hz^{-1}	s	ppm Hz^{-1}	s	μA Hz^{-1}	μA Hz^{-1}
10	–0.006	22	–0.016	56	–0.08	0.05
15	–0.003	16	–0.020	49	–0.15	0.07
25	–0.007	33	–0.024	71	–0.08	0.05
50	–0.017	46	–0.037	74	–0.03	0.02

During the adsorption stage 15 mg ml^{-1} shows the lowest response for stage (1) along with both the highest activity and the shortest adsorption time for both stages. At higher concentrations, the rate for competing surface sites increases, which will lower the extent of protein spreading on the surface. This could lead to a more flexible layer being formed, as adsorption would be above the critical surface coverage where electrostatics from neighboring proteins inhibits spreading.[20]

The lower the conformational flexibility of the layer, i.e. the more rigid, it is during stage (1) of adsorption – the higher the resulting specific activity was observed. However, the viscoelastic nature of the layer does not scale linearly with increasing concentration, and neither does the time frame for each adsorption. Stage (2) shows linear increase with protein concentration. Stage (1) has a non–linear response with increasing concentration suggesting that there is an optimum concentration of adsorbed protein This has been previously seen in earlier work, where 15 mg ml^{-1} was shown to be an optimum concentration for non-equilibrium adsorption onto bare gold and carboxylate-terminated surfaces.[13]

Conclusion

The adsorption and activity of *Mv*BOx has been shown to be strongly dependent on the applied potential during the adsorption. Applied potential also affected the surface coverage of the adsorbed *Mv*BOx. The enzyme-electrode interaction at more negative potential suggested the enzyme was orientated in a way, which was less suitable for DET. However stability was not compromised which rules out that an applied electric field increases surface denaturation at the applied potential investigated. Increasing the concentration showed that orientation governed initially by electrode–enzyme interactions become more susceptible to enzyme-enzyme electrostatic interactions, which can further orientate the enzyme into a more favorable geometry. This could have large implications due industrial adsorption process that usually require the minimum amount of material for adsorption. Although in the case of *Mv*BOx, adsorption during an applied potential was detrimental to activity, this is only the case for this enzyme under the electrode potentials tested. Further investigation into other enzyme-electrode interactions may show favorable improvements. This therefore shows a possible method for improvement of enzyme assisted adsorption for applications such as biofuel cells or biosensors.

Acknowledgements

This research was funded by the UK's Engineering and Physical Sciences Research Council through grant EP/G00434X/2 and the NOWNANO Centre for Doctoral Training (TM).

Data availability

The data associated with the paper are openly available from The University of Manchester eScholar Data Repository: http://dx.doi.org/10.12157/1.123456.

References

1. Yang, X.-Y.; Tian, G.; Jiang, N.; Su, B.-L., Immobilization technology: a sustainable solution for biofuel cell design. *Energy Environ. Sci.* **2012,** *5* (2), 5540-5563.
2. Armstrong, F. A., Recent developments in dynamic electrochemical studies of adsorbed enzymes and their active sites. *Curr. Opin. Chem. Biol.* **2005,** *9* (2), 110-117.
3. Mano, N.; Edembe, L., Bilirubin oxidases in bioelectrochemistry: Features and recent findings. *Biosens. Bioelectron.* **2013,** *50*, 478-485.

4. Leech, D.; Kavanagh, P.; Schuhmann, W., Enzymatic fuel cells: Recent progress. *Electrochim. Acta* **2012,** *84*, 223-234.

5. Borges, J.; Campina, J. M.; Fernando Silva, A., Probing the Contribution of Different Intermolecular Forces to the Adsorption of Spheroproteins onto Hydrophilic Surfaces. *J. Phys. Chem. B* **2013,** *117* (51), 16565-16576.

6. Benavidez, T. E.; Garcia, C. D., Potential-Assisted Adsorption of Bovine Serum Albumin onto Optically Transparent Carbon Electrodes. *Langmuir* **2013,** *29* (46).

7. Rabe, M.; Verdes, D.; Seeger, S., Understanding protein adsorption phenomena at solid surfaces. *Adv. Colloid Interface Sci.* **2011,** *162* (1–2), 87-106.

8. Leger, C.; Bertrand, P., Direct electrochemistry of redox enzymes as a tool for mechanistic studies. *Chem. Rev. (Washington, DC, U. S.)* **2008,** *108* (7), 2379-2438.

9. Page, C. C.; Moser, C. C.; Chen, X. X.; Dutton, P. L., Natural engineering principles of electron tunnelling in biological oxidation-reduction. *Nature* **1999,** *402* (6757), 47-52.

10. Blanford, C. F.; Foster, C. E.; Heath, R. S.; Armstrong, F. A., Efficient electrocatalytic oxygen reduction by the 'blue' copper oxidase, laccase, directly attached to chemically modified carbons. *Faraday Discuss.* **2008,** *140*, 319-335.

11. Ulyanova, Y.; Babanova, S.; Pinchon, E.; Matanovic, I.; Singhal, S.; Atanassov, P., Effect of enzymatic orientation through the use of syringaldazine molecules on multiple multi-copper oxidase enzymes. *Phys. Chem. Chem. Phys.* **2014,** *16* (26), 13367-13375.

12. Olejnik, P.; Palys, B.; Kowalczyk, A.; Nowicka, A. M., Orientation of Laccase on Charged Surfaces. Mediatorless Oxygen Reduction on Amino- and Carboxyl-Ended Ethylphenyl Groups. *J. Phys. Chem. C* **2012,** *116* (49), 25911-25918.

13. McArdle, T. M., T.; Singh, K.; Blanford, C. F., Combining electrochemical quartz crystal microbalance with dissipation analysis and dual polarization interferometry analyses to optimize the mass-specific activity of bilirubin oxidase adlayers. *In preperation* **2015**.

14. Singh, K.; Blanford, C. F., Electrochemical quartz crystal microbalance with dissipation monitoring: A technique to optimize enzyme use in bioelectrocatalysis. *Chemcatchem* **2014,** *6* (4), 921-929.

15. Online software ProtParam – Expasy Proteomics Server (http://www.expasy.ch/tools/protparam.html) (10-09-14).

16. Sauerbrey, G., Verwendung von schwingquarzen zur wagung dunner schichten und zur mikrowagung *Zeitschrift Fur Physik* **1959,** *155* (2), 206-222.

17. Hook, F.; Kasemo, B.; Nylander, T.; Fant, C.; Sott, K.; Elwing, H., Variations in coupled water, viscoelastic properties, and film thickness of a Mefp-1 protein film during adsorption and cross-linking: A quartz crystal microbalance with dissipation monitoring, ellipsometry, and surface plasmon resonance study. *Anal. Chem.* **2001,** *73* (24), 5796-5804.

18. McNamara, T. P., Electrochemical Studies and X-ray Structure Determination of Bilirubin Oxidase from Myrothecium verrucaria. *University of Oxford, Inorganic Chemistry* **2010**.

19. Sugimoto, Y.; Kitazumi, Y.; Tsujimura, S.; Shirai, O.; Yamamoto, M.; Kano, K., Electrostatic interaction between an enzyme and electrodes in the electric double layer examined in a view of direct electron transfer-type bioelectrocatalysis. *Biosens. Bioelectron.* **2015,** *63*.

20. van der Veen, M.; Stuart, M. C.; Norde, W., Spreading of proteins and its effect on adsorption and desorption kinetics. *Colloids and Surfaces B-Biointerfaces* **2007,** *54* (2), 136-142.

19

A Versatile Route to Edge-Specific Bioconjugation of Pristine Graphene

Mirja Hartmann,[a,b] Philippa M. Shellard,[a,b] Ashley M. Shepherd,[d] Trevor McArdle,[b,c] Robert M.J. Jacobs,[d] Christopher F. Blanford[b,c,*] and Sabine L. Flitsch[a,b,*]

[a] School of Chemistry, University of Manchester, Oxford Road, Manchester, M13 9PL, UK
[b] Manchester Institute of Biotechnology, University of Manchester, 131 Princess Street, Manchester, M1 7DN, UK [c] School of Materials, University of Manchester, Oxford Road, Manchester, M13 9PL, UK [d] Department of Chemistry, Chemical Research Laboratory, University of Oxford, 12 Mansfield Road, Oxford, OX1 3TA,UK
[*]christopher.blanford@manchester.ac.uk;sabine.flitsch@manchester.ac.uk

Graphene, an aromatic graphite monolayer first isolated in 2004,[GEIM] has become famous as a versatile material with superlative mechanical strength, electrical conductivity and thermal conductivity.[GEIM] In particular the high carrier mobilities of graphene[MOROSOV] are desirable for electrochemical and electronic sensing and release applications.

Chemical modifications of graphene-family nanomaterials (GFNMs) are able to fine-tune electrical properties,[CHEN] water dispersibility[SI] and introduce functional groups. Several modification strategies begin with the GFNM graphene oxide (GO), a graphene analogue rich in reactive, synthetically useful oxygen-containing defects. These defects introduce many sp^3 carbon sites, disrupting graphene's π system, presenting a significant disadvantage for electronic biosensing; the electron mobility of GO is orders of magnitude lower than graphene, even in its reduced form.[EIGLER] Herein we describe covalent chemical functionalisations based upon electrophilic aromatic substitution (EArS) directly to the edges and defect sites of pristine graphene, resulting in minimal disturbance of the extended graphene π-system. Functionalised graphene sheets can be subsequently decorated with tracers and biomolecules such as nanoparticles, proteins and fluorophores, setting a foundation for dispersible 'lab-on-a-flake' devices, which link stimulus-induced electrochemical events to the release of therapeutic agents.

EArS has been used since the nineteenth century to introduce functional groups in carbon-based compounds, initially to produce nitrobenzene for azo dye manufacture.[MITSCHERLISCH] EArS should only be achievable at edges and defect sites (the 'internal edges') of graphene, where hydrogen atoms are found. Graphene, which is functionalised by EArS should maintain good electrical conductivity, lending itself to use in sensing applications. This EArS substitution strategy has been shown with the aromatic nitration and sulphonation of carbon materials, such as graphitised nanodiamond[HARTMANN] and carbon nanotubes.[WANG] On graphene, to the best of our knowledge, only Friedel-Crafts reactions have been reported.[CHUA] A number of other edge-specific functionalisations exist, such as ball milling of graphite in the presence of various gases,[JEON] chlorination of nanographenes, [TAN] Diels-Alder reactions[SARKAR] and diazonium coupling[KOEHLER]. With a set of edge-specific reactions available, we can fine-tune the chemical properties of graphene flakes in suspension, or graphene films on solid supports.

Graphene suspensions were produced from graphite by sonication in *N*-methyl-2-pyrrolidone (NMP) and centrifugation, based on the method of Hernandez.[HERNANDEZ] Graphene films, produced by chemical vapour deposition ('CVD graphene') and transferred to silica-coated silicon wafers, were obtained commercially. We prepared four differently modified graphene materials (Fig. 1), which are outlined in the reaction schemes below.

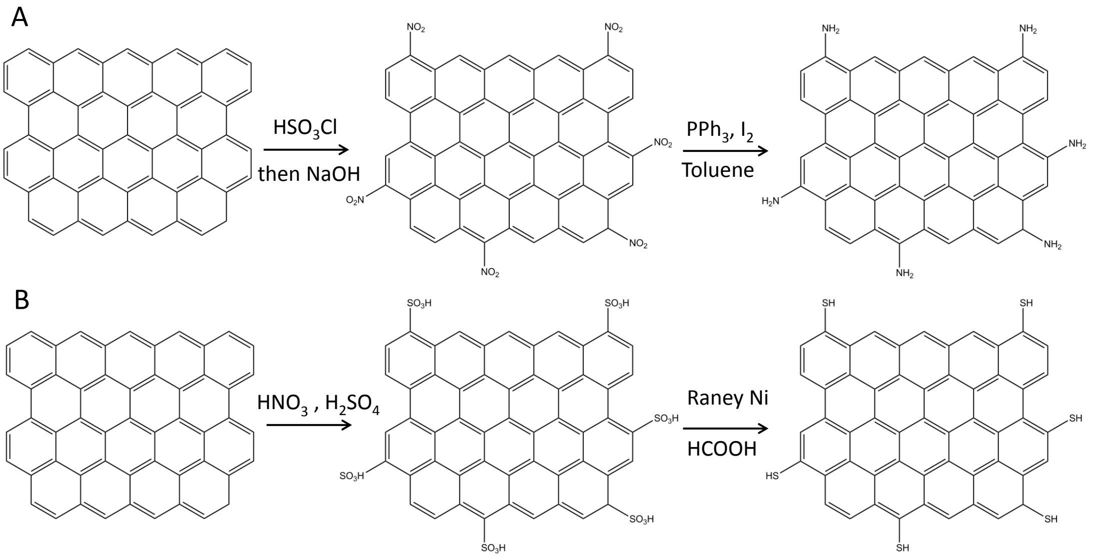

Figure 1: Reaction schemes for the chemical modification of graphene materials: A: sulphographene and thiographene B: nitrographene and aminographene

MH

Amino-functionalised graphene is a versatile material as it shows higher hydrophilicity than pristine graphene or nitrographene (Fig. 2C). As a weak base it can be protonated at low pH to obtain a positively charged graphene material. Furthermore, an amino functionality allows conjugation to organic compounds and biomolecules via standard peptide coupling reactions. Characterisation of the nitrographene and aminographene via XPS, FTIR, TGA, Raman, contact angle measurements can be found in the SI.

The sulphonic acid groups significantly increase the water dispersibility of the graphene (Fig. 2C). Also, negative charges make the material potentially useful as coating material for biocompatible surfaces. Sulphonate groups are strongly negatively charged and repel blood cells and proteins away from the surface of the device, consequently reducing blood cell and protein deposition (thrombogenesis). Similarly amino groups attached to graphene have been found to display no induction of thromboembolisms.[SINGH] The thio functionality can form disulphide bonds or be used in 'thiol-ene' coupling reactions.[DONDONI] Disulphides are largely found on natural proteins to stabilise their three-dimensional structure, through bridges between cysteine side chains on the exterior. Disulphides are formed under oxidative conditions and break apart upon reduction, making thiographene a suitable material for applications where release under reductive conditions is desirable. The reduction of the sulphonic acid groups was monitored by treatment with Ellman's reagent. (Fig.S6, SI). Characterisations of sulphographene and thiographene via XPS, FTIR, TGA, Raman contact angle measurements and chemical assays can be found in the SI. The XPS spectra for sulphographene and thiographene can be seen below (Fig. 2A and Fig. 2B respectively), and clearly show some successful reduction of sulphographene to thiographene.

Water dispersibility of graphene is desired for future applications under physiological conditions, e.g. as drug carrier or theranostics device or as membrane in filtration devices. Dispersibility measurements for all functionalisations can be found in Fig. 2C.

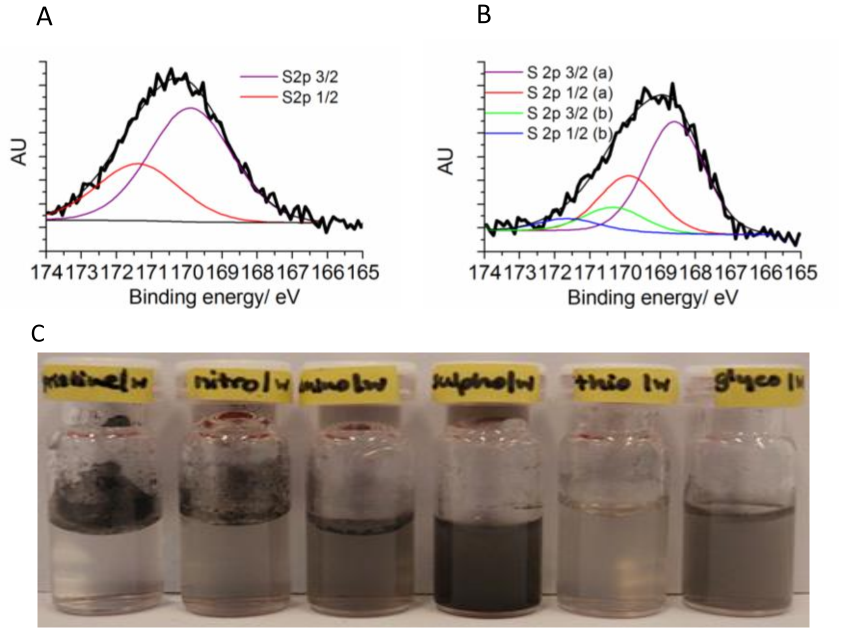

Figure 2: A: XPS S2p spectra of sulphographene, showing two peaks corresponding to the spin-orbit coupling (SOC) of the S2p orbitals B: XPS S2p spectra of thiographene, showing four peaks, from SOC of S2p orbitals. The two peaks at higher binding energy are residual sulphographene peaks and the two at lower binding energy those of thiographene. C: Tuneable water dispersibility of edge-modified graphene produced by ultrasonic exfoliation. Graphene type (L to R): unfunctionalised graphene, nitrographene, aminographene, sulphographene, thiographene, glycographene. Approximate concentration: 1 mg mL^{-1}. MH

Biologically active molecules with terminal double or triple bonds can be bound to thiols via click chemistry. To demonstrate the edge-specificity of the thiol modification, we covalently conjugated thiographene with a carbohydrate, allyl α-D-mannopyranoside, via an irreversible radical addition reaction, as outlined in Fig. 3A i). The resulting 'glycographene' shows increased water dispersibility compared to pristine graphene and thiographene (Fig. 2C). CVD glycographene was used to bind a fluorescently-labelled glycan-binding protein, Concanavalin A (ConA), its presence at the edges of the CVD glycographene sheet confirmed by fluorescence microscopy (Fig. 3B). The introduction of ligands for specific proteins is an interesting feature of glycographene, as cell-surface carbohydrates and their corresponding glycan-binding proteins have importance as cancer biomarker systems.

We also made use of the ability of sulphur to form stable covalent bonds to gold. After incubation of a CVD thiographene sample with gold nanoparticles (AuNPs) and thorough washing, the attachment of AuNPs to the edge of the graphene sheet was confirmed by scanning electron microscopy (Fig. 3C). The realisation of a reversible attachment of gold to the edges of thiographene could be used in gold recovery from electronic devices.

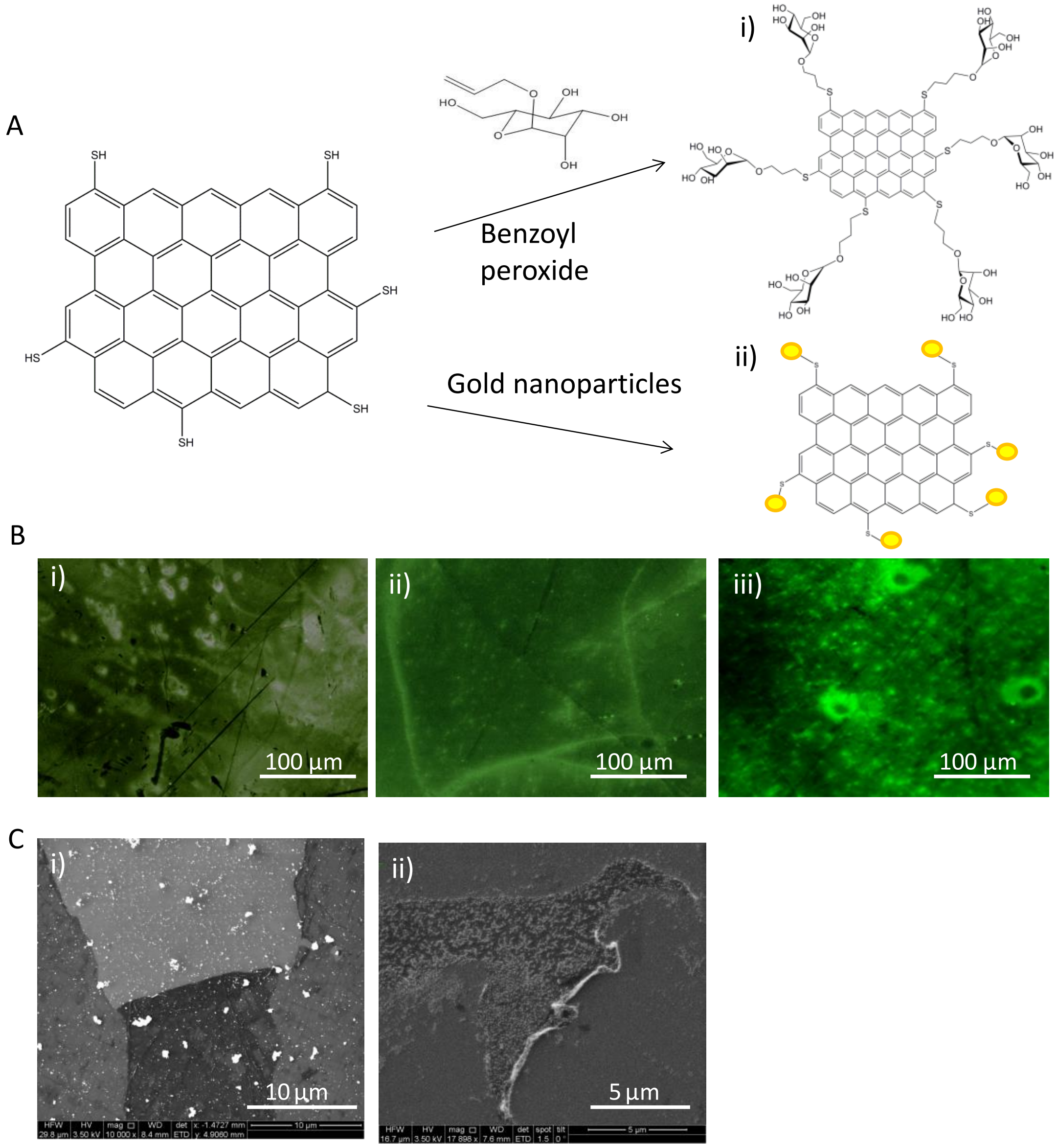

Figure 3: A: Reaction schemes showing attachment of mannose sugar to thiographene to form 'glycographene' (i) and attachment of gold nanoparticles to thiographene (ii) B: fluorescence microscopic images of pristine CVD graphene (i) and CVD glycographene (ii), on SiO_2 wafers, after incubation with fluorescein isothiocyanate (FITC)-labelled ConA (FITC-ConA). Pristine graphene only shows background fluorescence (i). FITC-ConA can be detected around the edges of the glycographene flake (ii). After incubation of the CVD glycographene/FITC-ConA with excess methyl mannoside (inhibitor of mannose-specific binding), only background fluorescence is observed, and stronger fluorescence along the edges of CVD glycographene can no longer be detected (ii). C: SEM images of chemically modified CVD graphene on SiO_2 wafers. Gold nanoparticles incubated on CVD sulphographene only show non-specific adsorption to

MH/TM

the sample (i). Sulphhydryl groups predominantly localised at the edges of CVD thiographene covalently bind the nanoparticles through Au-S bonds, leading to observed bright clusters at the edges (ii).

In summary, we have successfully applied two strategies for the covalent chemical modification of pristine graphene in dispersion and on surfaces. We have shown how the material's dispersibility in different solvents (or wettability properties in case of graphene-coated surfaces) can be fine-tuned by simple chemical modification. The reaction mechanism ensures edge-specific modification. The great advantage of this topological specificity is that the two-dimensional structure of the material is preserved and the electronic properties should not be modified by introduction of defect sites, as it is the case when reduced graphene oxide, rather than pristine graphene, is used for the production of functional graphene. The functionalities are in direct proximity to the graphene sheet itself and no linker molecule is required, which is an important prerequisite for future application of the material in electronically driven biosensing.

Acknowledgements

EPSRC (EP/G00434X/2), UoM Confidence in Concept, EU (GlycoBioM). Polly Greensmith TGA.

References

1. [GEIM] Novoselov, K. S., Geim, A. K., Morozov, S. V., Jiang, D., Zhang, Y., Dubonos, S. V., Grigorieva, I. V. & Firsov, A.A. Electric Field Effect in Atomically Thin Carbon Films, *Science,* **306***,* 666-669 (2004). *DOI: 10.1126/science.1102896*
2. [MOROZOV] Morozov, S. V. *et al*. Giant intrinsic carrier mobilities in graphene and its bilayer. *Physical Review Letters* **100**, 0166021-0166024, doi:10.1103/PhysRevLett.100.016602 (2008).
3. [BERRY] Berry, V. Impermeability of Graphene and its applications. *Carbon* **62**, 1-10 (2013).
4. [CHEN] Chen, D., Tanga, L. & Li J. Graphene-based materials in electrochemistry. *Chem. Soc. Rev.* **39**, 3157–3180 (2010).
5. [SI] Si, Y. & Samulski E. T. *Nano Lett.* **8**, 1679-1682 (2008).
6. [EIGLER] Eigler, S. *et al*. Wet Chemical Synthesis of Graphene. **26**, 3583-3587 (2013).
7. [HUMMERS] Hummers, W. S., Offeman, E. R. Preparation of Graphitic Oxide. *J. Am. Chem. Soc.* **80**, 1339–1339 (1958). DOI: 10.1021/ja01539a017
8. [CHUA] Chua, C. K. & Pumera, M. Chemical reduction of graphene oxide: a synthetic chemistry viewpoint. *Chem. Soc. Rev.* **43**, 291-312 (2014).
9. [JEON]
   Jeon, I.-Y. *et al*. Edge-carboxylated graphene nanosheets via ball milling. *Proceedings of the National Academy of Sciences of the United States of America* **109**, 5588-5593 (2012).

Jeon, I.-Y. *et al*. Edge-Selectively Sulphurized Graphene Nanoplatelets as Efficient Metal-Free Electrocatalysts for Oxygen Reduction Reaction: The Electron Spin Effect. *Advanced Materials* **25**, 6138-6145 (2013).
Jeon, I.-Y. *et al*. Large-Scale Production of Edge-Selectively Functionalized Graphene Nanoplatelets via Ball Milling and Their Use as Metal-Free Electrocatalysts for Oxygen Reduction Reaction. *Journal of the American Chemical Society* **135**, 1386-1393 (2013).

10. [TAN] Tan, Y.-Z. *et al*. Atomically precise edge chlorination of nanographenes and its application in graphene nanoribbons. *Nature Communications* **4**, doi:10.1038/ncomms3646 (2013).
11. [SARKAR] Sarkar, S., Bekyarova, E., Niyogi, S. & Haddon, R. C. Diels-Alder Chemistry of Graphite and Graphene: Graphene as Diene and Dienophile. *J. Am. Chem. Soc.* **133**, 3324–3327 (2011).
12. [KOEHLER] Koehler, F. M., & Stark, W. J. Organic Synthesis on Graphene. *Acc. Chem. Res.* **46**, 2297–2306 (2013).
13. [HERNANDEZ] Hernandez, Y. *et al*. High-yield production of graphene by liquid-phase exfoliation of graphite. *Nature Nanotechnology* **3**, 563-568 (2008).
14. [LeGOFF] Le Goff, A., Reuillard, B., & Cosnier, S., A Pyrene-Substituted Tris(bipyridine)osmium(II) Complex as aVersatile Redox Probe for Characterizing and Functionalizing Carbon Nanotube- and Graphene-Based Electrodes. *Langmuir* **29**, 8736−8742 (2013).
15. [HIRSCH] Kozhemyakina, N. V., Englert, J. M., Yang, G., Spiecker E., Schmidt, C. D., Hauke, F. & Hirsch, A., Non-Covalent Chemistry of Graphene: Electronic Communication with Dendronized Perylene Bisimides. *Adv. Mater.* **22**, 5483–5487 (2010).
16. [MITSCHERLICH] Mitscherlich, E., Über das Benzin und die Verbindungen desselben. (1898).
17. [CHUA] Chua, C. K., & Pumera, M. Covalent chemistry on graphene. *Chem. Soc. Rev.*, **42**, 3222-3233 (2013).
18. [HARTMANN] Hartmann, M., Betz, P., Sun, Y., Gorb, S. N., Lindhorst, T. K. & Krueger, A., Saccharide-Modified Nanodiamond Conjugates for the Efficient Detection and Removal of Pathogenic Bacteria. *Chem. Eur. J.* **18**, 6485-6492 (2012).
19. [WANG] Wang, L. *et al*. A facile method to modify carbon nanotubes with nitro/amino groups. *Appl. Surf. Sci* .**20,**6060‑6064 (2010).
20. [SINGH] Singh, S. K. *et al*. Amine-Modified Graphene. Thrombo-Protective Safer Alternative to Graphene Oxide for Biomedical Applications. *Acs Nano* **6**, 2731-2740 (2012).
21. [DONDONI] Dondoni, A. & Marra, A. Recent applications of thiol–ene coupling as a click process for glycoconjugation. *Chem. Soc. Rev.* **41**, 573–586 (2012).

Supplementary materials for
A Versatile Route to Edge-Specific Bioconjugation of Pristine Graphene

Mirja Hartmann,[a,b] Philippa M. Shellard,[a,b] Ashley M. Shepherd,[d] Trevor McArdle,[b,c] Robert M.J. Jacobs,[d] Christopher F. Blanford[b,c,*] and Sabine L. Flitsch[a,b,*]

Materials and equipment

All chemicals were purchased and used without further purification. Primary amines were detected on Merck silica TLC plates with ninhydrin dispersion (300 mg ninhydrin dissolved in 100 mL butanol and 3 mL conc. acetic acid), followed by heat treatment. Sulphhydryl groups were detected using Ellman's reagent (5,5'-dithio-bis-(2-nitrobenzoic acid)): 39.6 mg of Ellman's reagent were dissolved in 10 mL phosphate-buffered saline (pH 7.4, 0.01 M phosphate, 0.138 M NaCl, 2.7 mM KCl) and the 10 mM dispersion was used immediately.

FTIR spectra were recorded on a Nicolet 5700 FTIR spectrometer (Thermo electron corporation), by mixing approximately 0.1mg lyophilised samples of graphene with 10mg KBr powder (FTIR grade, >99%, Sigma Aldrich) and pressed into a pellet.

Raman spectra were recorded on a Renishaw RM System 1000 Mk1 spectrometer with 633nm (1.96 eV) illumination. The shift of the G peak is insensitive to the number of layers of graphene.[1]

Scanning electron microscopy images were acquired using an FEI Quanta 650 FEG-SEM operating at 1-5 kV. CVD graphene samples on SiO_2/Si were mounted on 12.5mm aluminium stubs. No surface coatings were applied.

Fluorescence images were collected on an Olympus BX51 upright microscope using UPlanFLN objectives and captured using a Coolsnap camera (Photometrics) through MetaVue Software (Molecular Devices). A specific band pass filter set for FITC (excitation BP480/40, dichroic Q505LP, emission 535/50) was used.

Thermogravimetric analyses (TGA) were collected from a TA Instruments Q500. Samples of 1–3 mg were heated at 10 °C min^{-1} in a nitrogen atmosphere. Powdered samples were acquired from aqueous dispersions by lyophilising.

X-ray photoelectron spectroscopy (XPS) data were acquired on a VG Escalab II, using an Al Kα source (1486.6 eV) at 10 kV anode potential with 20 mA emission current and hemispherical analyser. Peak fitting was carried out using CasaXPS peak fitting software, calibration carried out by setting the C1s peak for sp2 carbon at 284.5 eV.

Chemical modifications of graphene in dispersion

Preparation of dispersed graphene flakes

Graphene dispersions were prepared from natural graphite flakes (Branwell Graphite, Ltd Grade 2369). Following the method of Hernandez,[2] 2 g graphite were sonicated in 500 mL *N*-methyl-2-pyrrolidone (NMP) at 37 Hz for 48 h in an ultrasonic bath (Elmasonic PH750EL). Remaining graphite was removed by cetrifugation (3 × 20 min at 4000 rpm). The supernatant was a graphene dispersion (ca. 0.4 g L^{-1}). Graphene reaction dispersions were vacuum filtered through 0.02μm

Whatman Anodisc membrane filters to create graphene laminates. For analysis, samples were dried as laminates on the filter membrane or re-dispersed in water by sonication and freeze-dried (HETO Powderdry LL1500 Freeze Dryer, Thermo Electron Corporation). For long-term storage the samples were kept in a desiccator at room temperature.

Synthesis of sulphographene dispersion

25 mL chlorosulphonic acid and 100 mL NMP were cooled with ice and 175 mL graphene dispersion were added in drops while the ice was allowed to thaw. Vigorous stirring is crucial to keep the mixture from gelation. The mixture was stirred at 55 °C for 20 h, poured on ice and filtered. Chlorosulphonated graphene was washed with water until the filtrate was neutral. The product was re-dispersed in water by sonication.

15 g sodium hydroxide were dissolved in 19.5 mL of chlorosulphonated graphene in water and the mixture was sonicated for 2 h. The product war filtered and washed with water until the filtrate was neutral. Sulphographene was re-dispersed in water by sonication and freeze dried in aliquots.

Synthesis of thiographene dispersion

Dry sulphographene (freeze dried from 12 ml of sulphographene in water) was suspended in anhydrous benzene by sonication in a N_2-atmosphere. 4.6 g (10 mmol) triphenylphosphine and 300 mg (0.6 mmol) iodine were added and the mixture was stirred under a N_2 atmosphere at 90 °C for 21 h. The product was washed with 500 mL toluene, 200 mL acetone, 100 ml sodium thiosulphate dispersion and 1000 mL water. Thiographene was re-dispersed in 12 mL water by sonication.

Synthesis of α-D-mannopyranoside graphene ('glycographene') dispersion

Allyl alcohol (125 mL, 1.84 mol) was cooled to 0 °C, acetyl chloride (10 mL, 14.0 mmol) was added in drops, and the mixture was stirred at 0 °C for 1 h. After heating to 70 °C, mannose (10.0 g, 55.6 mmol) was added and the reaction was stirred under reflux for 5 h. It was neutralized with sodium hydrogen carbonate and filtrated. After three co-distillations with toluene, the solvent was removed and the crude product was purified by flash column chromatography on silica (EtOAc/MeOH, 8:2).

To 12 mL of thiographene in water 200 mg (909 µmol) allyl mannoside and 1 spatula benzoyl peroxide were added and the mixture was stirred at 65 °C for 21 h. The mixture was filtered and washed with ethanol, dichloromethane, ethanol and water and re-dispersed in 15 mL water by sonication.

Synthesis of nitrographene dispersion

20 mL 100 % nitric acid and 28 mL concentrated sulphuric acid were carefully mixed and cooled with ice. 75 ml graphene dispersion in NMP were added in drops, while the ice was allowed to thaw. The mixture is stirred overnight, poured on 200 mL ice, filtered and washed with 700 mL

water until the filtrate was pH neutral. The filter was transferred in a round bottom flask and the nitrographene sonicated in 75 mL NMP.

Synthesis of aminographene dispersion

20 mL of nitrographene were mixed with 7 mL of Raney-Ni suspension in water. 20 mL formic acid were added and the mixture was stirred for 20 h. Decanting several times with the help of a strong magnet facilitated the removal of the catalyst. The remaining mixture was filtered and washed with 500 mL concentrated sodium hydroxide dispersion, 500 mL water and 500 mL ethanol. The product was sonicated in 20 mL water and kept in dispersion until further use.

Chemical modification of CVD graphene on SiO_2 wafers

Uniform polycrystalline films of single layer graphene were grown by chemical vapour deposition and transferred to Si wafers with a surface layer of thermally grown oxide, of 290nm thickness (2-D Tech, Ltd).

Synthesis of CVD sulphographene

8 mL anhydrous DMF and 2 mL chlorosulphonic acid were mixed in a glass vial. The CVD graphene sample was left to react in the mixture overnight. The CVD graphene sample was rinsed with acetone and water and transferred immediately into the next reaction vial for hydrolysis of the chlorosulphonates.

A sodium hydroxide dispersion, pH 10 was prepared and 10 mL were transferred to a glass vial. The chlorosulphonated CVD graphene sample was left in the sodium hydroxide dispersion for 15 min and rinsed immediately with water and acetone. The sample was dried in a nitrogen gas stream and stored at ambient temperature.

Synthesis of CVD thiographene

4.6 g (10 mmol) triphenylphosphine were dissolved in anhydrous toluene and heated up to 90 °C. 300 mg (0.6 mmol) iodine were added under stirring. The stirrer was stopped, the flask was opened keeping a strong nitrogen counterflow and the sulphonated CVD graphene sample was added. The mixture was kept in a nitrogen atmosphere and heated to 90 °C overnight. The CVD graphene sample was rinsed with acetone, water and ethanol and then dried in a nitrogen gas stream and stored at ambient temperature.

Synthesis of CVD glycographene

150 mg (682 µmol) allyl mannoside and 1 spatula benzoyl peroxide were dissolved in ethanol. A CVD thiographene sample was added to the reaction vial and the mixture was heated to 65 °C overnight. The CVD graphene sample was rinsed with ethanol, water and acetone and then dried in a nitrogen gas stream and stored at ambient temperature.

Binding of gold nanoparticles to CVD thiographene

Gold nanoparticles (20 nm diameter in 0.1mM phosphate-buffered saline, reagent free, ~7.2 × 10^{11} particles mL^{-1}, Aldrich/CytoDiagnostics) were diluted in phosphate-buffered saline (PBS pH 7.4, 0.01 M phosphate, 0.138 M NaCl, 2.7 mM KC) by tenfold. 10 mL of this suspension were transferred to a glass vial. A sample of CVD thiographene (or CVD sulphographene as a negative control) was immersed in the nanoparticle suspension overnight at ambient temperature. The sample was rinsed with water and acetone and then dried in a nitrogen gas stream and stored at room temperature.

ConA binding to CVD glycographene

FITC-ConA was dissolved in binding buffer (20 mM Tris, 500 mM NaCl, 1 mM $CaCl_2$, 1 mM $MgCl_2$, pH 7.2) in a glass vial wrapped in aluminium foil. The CVD glycographene sample was added to the vial incubated at 37 °C for 2 h. The CVD graphene sample was rinsed with water and then dried in a nitrogen gas stream and examined under a fluorescence microscope.

Synthesis of CVD nitrographene

5 mL 100 % nitric acid and 7 mL concentrated sulphuric acid were carefully mixed in a glass vial cooled with ice. A CVD graphene sample was added to the glass vial and left to react overnight. The sample was rinsed with dilute sodium hydroxide solution, water and acetone and then dried in a nitrogen gas stream and stored at ambient temperature.

Synthesis of CVD aminographene

To 1.5 mL of an aqueous suspension of Raney Ni in a glass vial 8 mL formic acid were added slowly. A CVD nitrographene sample was transferred to the vial and left to react overnight. The sample was rinsed with water and acetone and then dried in a nitrogen gas stream before being stored at ambient temperature.

Additional characterisation

X-ray photoelectron spectroscopy

Fig. S1 shows the XPS full scans and C1s for graphene, sulphographene and thiographene. S2p spectra are shown for sulphographene and thiographene and peak positions tabulated in Table S1.

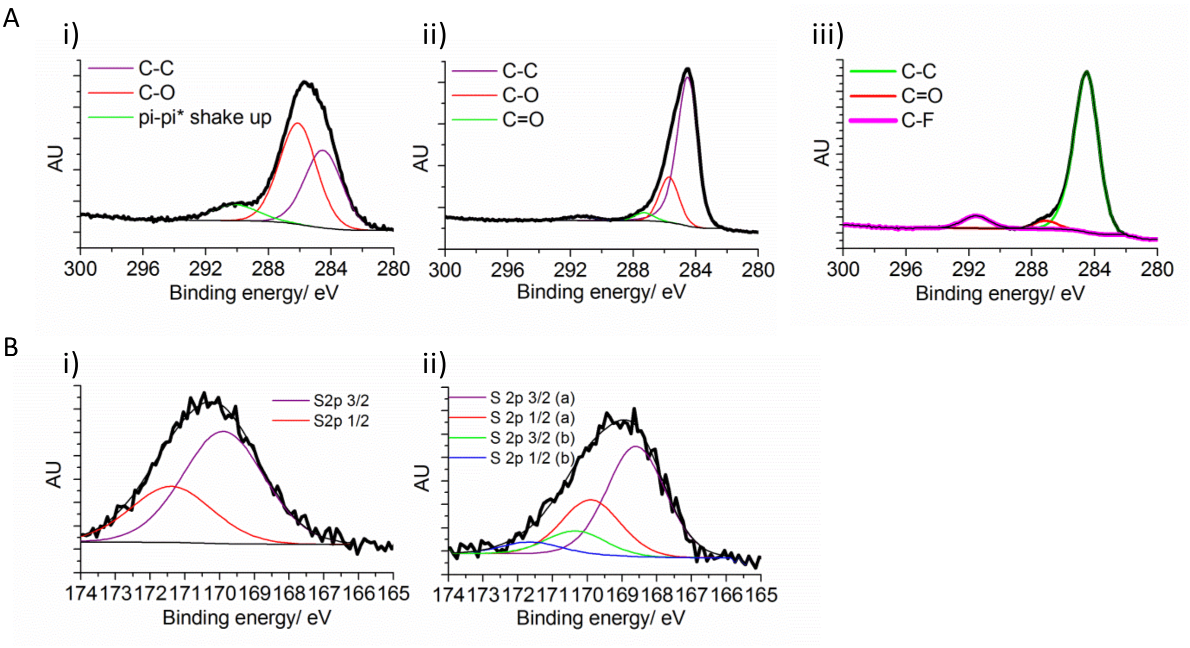

Figure S1. A: C1s spectra for sulphographene (i), thiographene (ii) and pristine graphene (iii) B: S2p spectra for sulphographene (i) and thiographene (ii). MH

Table S1. Tabulated data for XPS peaks for graphene, sulphographene and thiographene. N/O=not observed

	C1s				S2p 3/2	S2p 1/2	I(C-C)/I(C-O)	I(C-C)/((C=O)
Material	C-C	C-O	C=O	C-F				
graphene	284.5	N.O	287.1	291.7	N/O	N/O	N/O	6.37
sulphographene	284.5	286.1	N/O	N/O	169.8	171.0	0.86	N/O
thiographene	284.5	285.7	287.3	N/O	170.0 168.5	171.2, 169.7	2.38	4.72

For pristine graphene there is a small degree of oxygen-containing functionality. There is also a C-F peak observed which is at an energy consistent with an aliphatic fluorine. This indicates that it is not bound to graphene but instead could be some artefact or contaminant. Likely sources include vacuum grease or fluorine containing compounds from inside Schott bottles, in which the graphene dispersion is stored.

The C-O peak from sulphographene decreases in area in comparison to thiographene, in conjunction with the reducing conditions used to achieve thiographene. When comparing the I(C-C)/I(C=O) to pristine graphene, there is still a large amount of oxygen functionality remaining, indicative of some remaining oxidised functionality. Upon transformation to sulphographene it is clear that the magnitude of the C-O peak fit is much larger, most likely due to a degree of oxidation introduced by the chlorosulphonation (strongly acidic conditions). This C-O peak becomes much smaller again for thiographene as a result of the reduction conditions.

The appearance of a clear shoulder in the thiographene sample indicates that there are now two different sulphur species present. Comprison of binding energies between the samples suggest there is some unreduced sulphographene remaining in the thiographene sample. The peaks highlighted in red, in the thiographene section of the table are those peaks which at higher binding energy which are conserved from sulphographene, as there is little shift in binding energy (within the margins of error). The ratio of these two peaks is 0.17:0.83 (for the S2p 3/2) indicating approximately an 83%conversion to thiographene. The sulphur component shifts to lower binding energy in thiographene. In sulphographene, the sulphur is attached to particularly electron withdrawing groups, in turn causing electrons to possess increased binding energies. Fig. S2 displays the XPS spectra for nitrographene and aminographene. The positions of the peaks and further information are tabulated in Table S2.

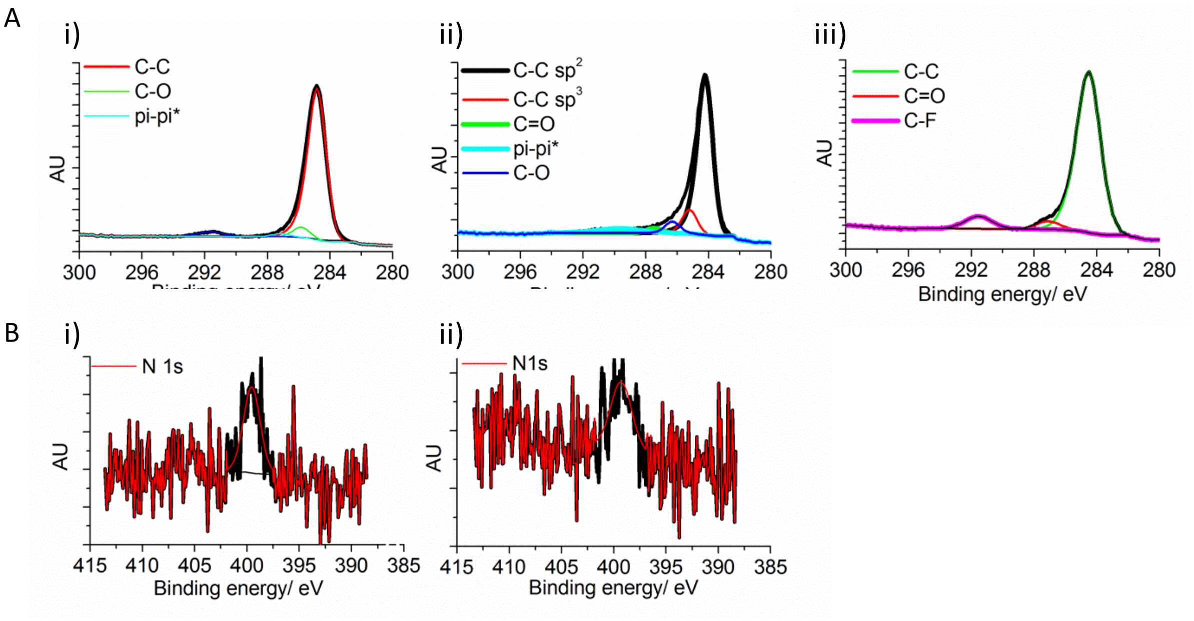

Figure S2. A: C1s spectra for nitrographene (i), aminographene (ii) and pristine graphene (iii) B: N1s spectra for nitrographene (i) and aminographene (ii).

MH

Table S2. Tabulated data for XPS peaks for graphene, nitrographene and aminographene. N/O = not observed

	C1s				N1s	I(C-C)/I(C-O)	I(C-C)/((C=O)
Material	C-C	C-O	C=O	C-F			
graphene	284.5	N/O	287.1	291.7	N/O	N/O	6.37
nitrographene	284.5	285.5	286.7	N/O	399.6	5.3	N/O
aminographene	284.5	285.6	286.9	N/O	399.7	6	7.38

There is little shift between the position of the N1s peak from nitro to aminographene, however this is likely due to the factN1s is a core level and as such will be affected in a smaller way by the local environment of the nitrogen. The S2p shifts are altered much more, as they are at a higher energy and are thus more sensitive to local electronic effects. There appears to be more oxygen-containing functionality in nitrographene than in aminographene, indicating that some reduction has occurred, but it is still unclear from looking at the XPs data whether full reduction took place.. There still appears to be a high proportion of oxygen containing functionality in the aminographene sample, suggesting incomplete reduction.

Raman spectroscopy

Fig. S3 Shows Raman spectra of CVD graphene samples before and after thiolation. Table S1 tabulates the peak positiong and G/D ratio of the Raman peaks observed.

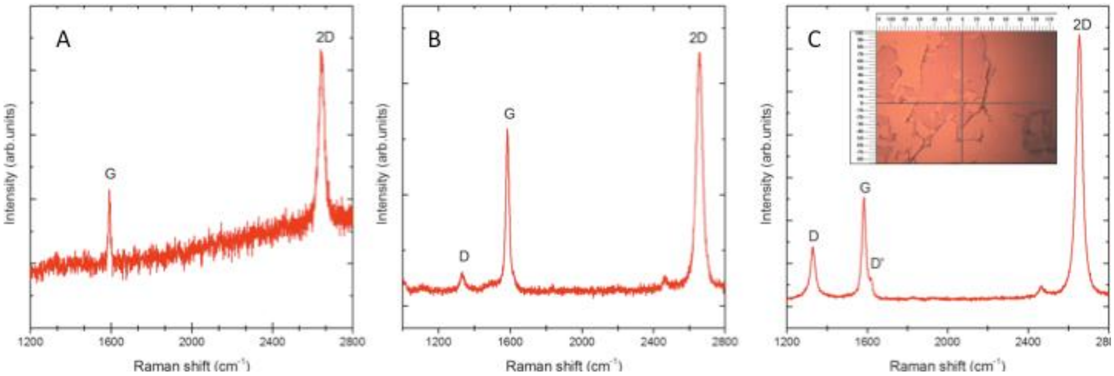

Figure S3 Raman spectra of CVD graphene samples:(a) unmodified CVD graphene, spectrum taken in the center of the sample; (b) unmodified CVD graphene, spectrum taken at the edge of the sample; (c) CVD thiographene, spectrum taken at the crosshairs shown in the inset image. TM

Table S3. Location of Raman peaks shown in Figure S1. Position of the G peak was set to 1581 cm^{-1}. N/O = not observed

Sample	**D / cm^{-1}**	**G/D ratio**[a]	**D′ / cm^{-1}**	**D″ + D / cm^{-1}**	**2D / cm^{-1}**
(a) pristine CVD centre	N/O	N/O	N/O	N/O	2631
(b) pristine CVD edge	1329	6.33	1620	2462	2656
(c) thiolated CVD centre	1326	1.89	1617	2468	2652

[a]Based on counts above baseline after fitting peaks to Gaussian functions.

The Raman spectra for CVD graphene shows a clear change upon functionalisation. Thiolation visibly increases the number of defects (Figure S1 inset), producing a drop in the G/D ratio consistent with this. The D′ at ca. 1620 cm^{-1} also becomes more prominent. Spectra taken from the edges of the CVD graphene show more features and a greater number of defects (Table S1). Fig. S4 shows the Raman spectra for liquid phase exfoliated graphene, taken on films of fuctionalised graphene on anodisk filter membranes.

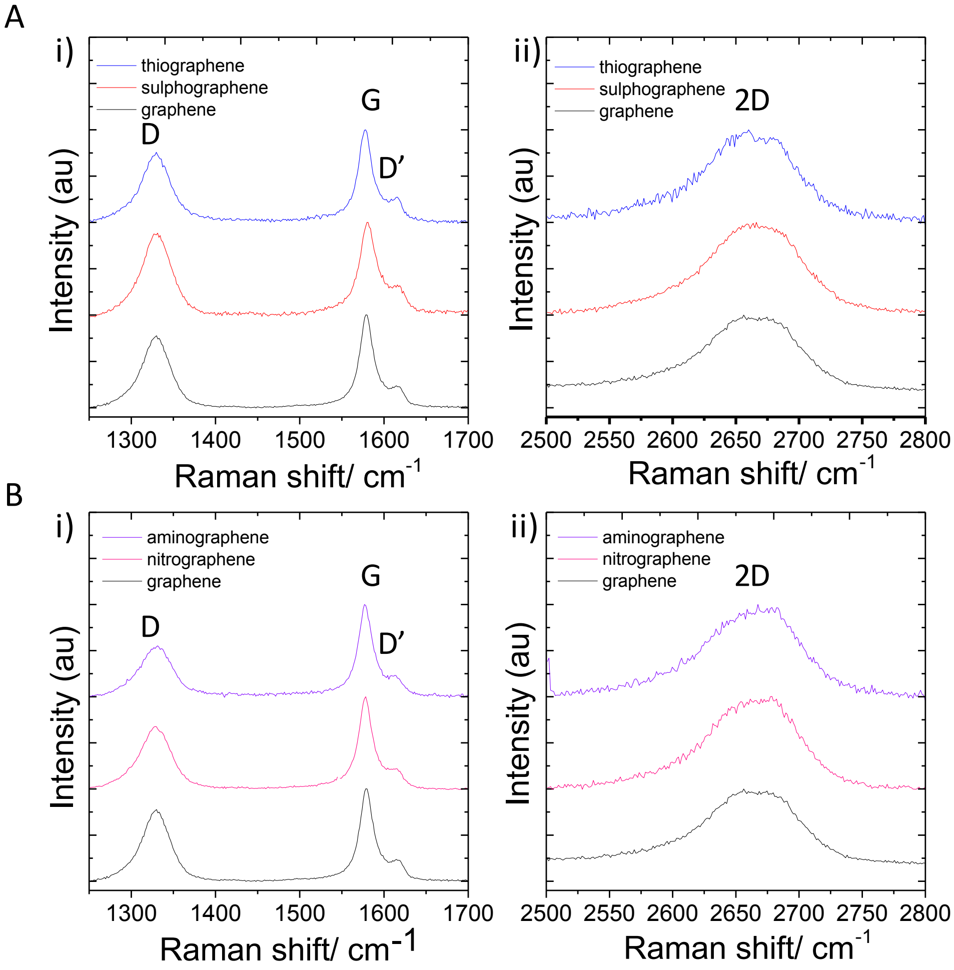

Figure S4: Raman spectra of functionalised graphene from liquid-phase exolfiation. A: Raman spectra for graphene (black), sulphographene (red) and thiographene (blue). B: Raman spectra for graphene (black), nitrographene (pink) and aminographene (purple). TM

The number of defects does not increase significantly over the reaction sequence. This shows that the exfoliation has been successful, as no further AB stacking is seen. The I_D/I_G ratio was found by Coleman and co-workers to scale with the lateral dimensions of the flakes, with I_D/I_G increasing as the flakes become smaller.[3] For nitrogen containing functionalisations, the lateral dimensions appear to increase slightly from pristine graphene (possibly due to some agglomeration of flakes), consistent with the asymmetry of the 2D band. For sulphographene the lateral dimensions appear to decrease. This may be due to the harsh reaction conditions breaking apart flakes into smaller pieces. For thiographene the size again increases, which may be due to the agglomeration of flakes in this step, or may also be due to dispersibility differences.

The FWHM of the Raman peaks here is increased, versus CVD graphene due to the sonication process, which causes an increase in edge-character for the graphene films.[4]

The position of the 2D peak indicatesthat the exfoliation process was successful as there is no obvious peak splittings from AB stacking of graphitic layers. However the layers may agglomerate and therefore it is difficult to determine whether the Raman shows few layered graphene or turbostatic graphite.

Thermogravimetric analysis

Fig. S5 displays the thermal gravimetric analysis (TGA) plots for the functionalised graphene materials.

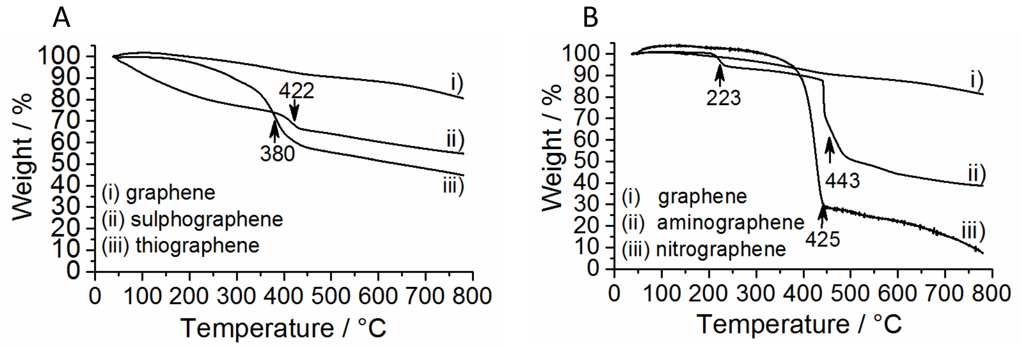

Figure S5 TGA analysis of graphene samples produced by ultrasonic exfoliation: A: pristine graphene (i), sulphographene (ii) and thiographene (iii) B: pristine graphene (i), aminographene (ii) and nitrographene (iii) The number by the arrow shows the point of the minimum in dm/dT. `PS/TM`

All functionalisations of graphene result in the lowering of thermal stability, with all functionalised graphene samples undergoing significant mass loss below 800°C. Pristine graphene shows no significant mass loss over the temperature range. It is unclear whether the mass losses are simply due to the removal of the edge groups, or whether the presence of these groups labilises the remaining graphene structure, meaning that it anneals at a much lower temperature. Aminographene has two distinct mass losses, one at 223°C, which may be from residual carbon species remaining from the Raney Ni, and a larger mass loss at 443°C from the amine groups. Nitrographene only has one mass loss at 425°C. The temperature for the major mass losses in sulphographene occurs at 422°C as compared to 380°C for thiographene. These TGA plots indicate changes in thermal stability upon each functionalisation, and thus support the modification of the graphene sheets.

The TGA used for this analysis was calibrated for samples over 10mg (the mass calibration for the instrument uses a 20mg weight). As a result, the percentage mass losses shown are not quantitative, as graphene samples were typically 1 mg or less. This also explains the portion of the plots where the mass is over 100%.

Ellman's assay

Ellman's reagent was employed as a colorimetric assay for the presence of sulphhydryl groups in modified graphene samples. Figure S6 shows the effect of the Ellman's reagent on graphene with sulphur-containing groups.

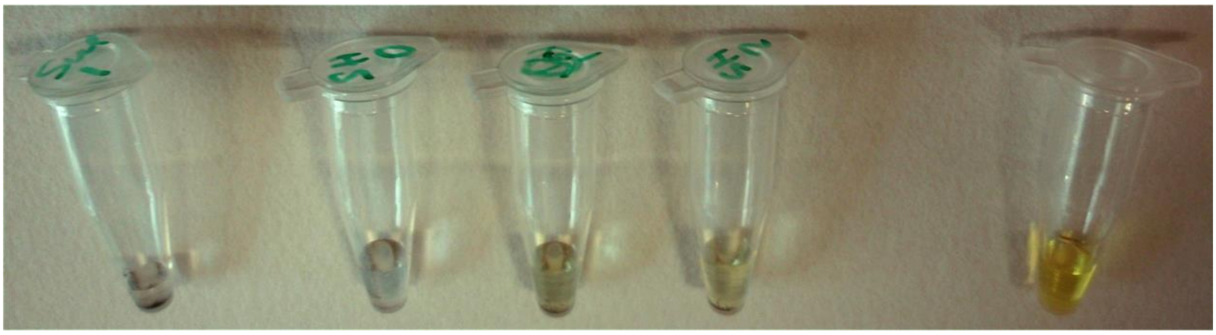

Figure S6: Ellman's assay applied to edge-modified graphene. From left to right: negative control containing 30 µl of sulphographene + 10 µl Ellman's reagent dispersion; 30 µl thiographene + 0 µl Ellman's dispersion; 30 µl thiographene + 5 µl Ellman's dispersion; 30 µl thiographene + 10 µl Ellman's dispersion; positive control containing 30 µl 260 mM cysteine + 10 µl Ellman's dispersion. Compounds with free sulphydryl groups react with Ellman's reagent to release a yellow dye. C: Sulphographene dispersion stayed colourless, while D: edge-thio groups in thiographene induce a colour change to yellow. Concentration of graphene suspensions: ca. 0.5 mg cm^{-3}.

MH

The negative controls on the right show no colour in the presence of sulphographene (i.e., before reduction to the thiol) nor in the absence of Ellman's reagent. Upon addition of Ellman's reagent to thiographene a yellow colouration is observed. The positive control at the right shows the colour associated with disulphide exchange when the Ellman's reagent is mixed with a 78-fold excess of cysteine. This positively confirms the presence of thiol groups in thiographene.

Solvent dispersibility of edge-modified graphene

Fig. S7 shows the dispersibility of functionalised graphenes in different solvents. Table S5 tabulates the dispersibility of each functionalisation in each solvent.

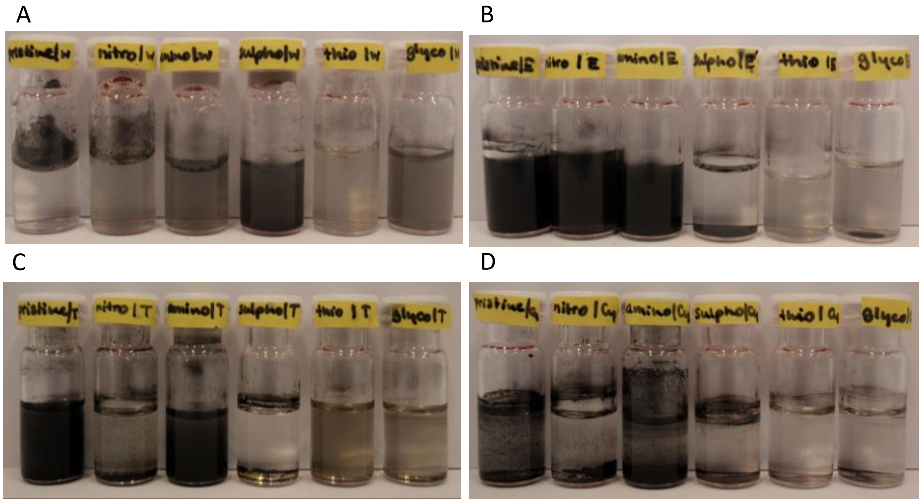

Figure S7. Tuneable dispersibility of edge-modified graphene produced by ultrasonic exfoliation. Solvent (from top to bottom): A: water, B: ethanol, C: toluene, D: cyclohexane. Graphene type (left to right): un-functionalised graphene, nitrographene, aminographene, sulphographene, thiographene, glycographene. Approximate concentration: 1 g L^{-1}.

MH

Table S5. Dispersibility of functionalised graphene materials in different solvents

	Dispersibility			
Material	Water	Ethanol	Toluene	Cyclohexane
Graphene	Poor	Good	Good	Good
Nitrographene	Moderate	Good	Moderate	Poor
Aminographene	Moderate	Good	Good	Poor
Sulphographene	Good	Poor	Poor	Poor
Thiographene	Poor	Poor	Moderate	Poor
Glycographene	Moderate	Poor	Moderate	Poor

Graphene modified with sulphonate groups shows the best dispersion in water. Nitrogen functionalised graphene samples disperse well in ethanol. Amino-, thio- and glycographene samples are moderately dispersible in toluene.

Contact angle measurements on functionalised graphene samples

Fig. S8 shows the contact angle measurements for the functionalised graphene sheets.

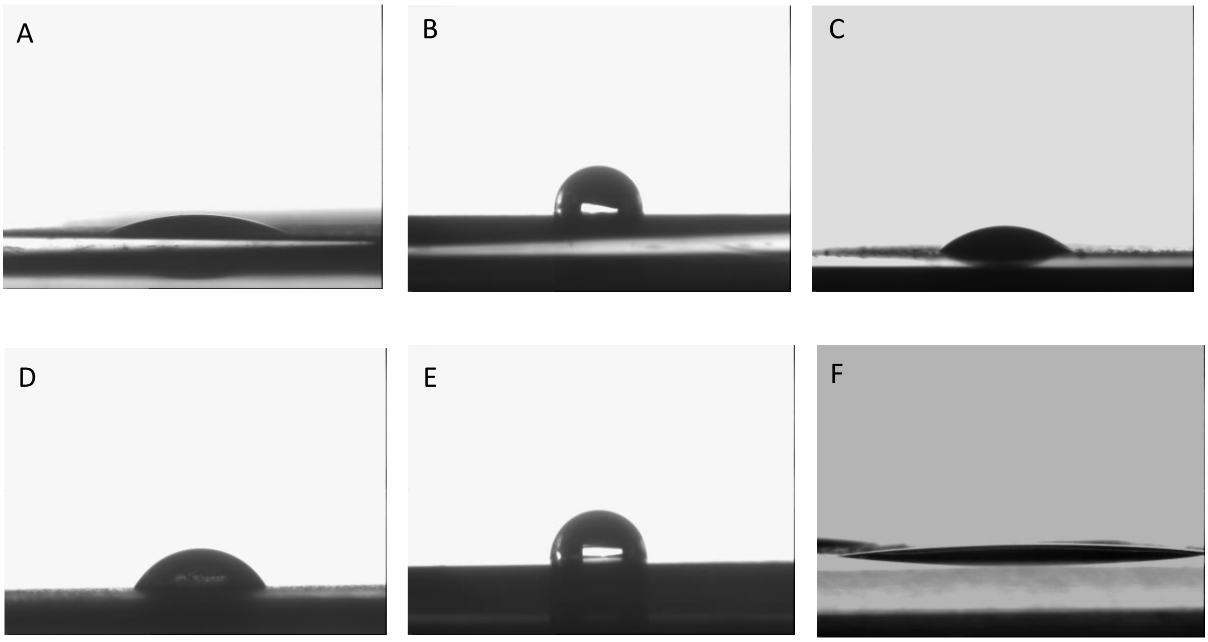

Figure S8. Contact angle measurements of water on Anodisc filters coated with a thin film of functionalised graphene. A: Anodisc control 26° B: graphene (105.1±7.67°) C: sulphographene (45.9±5.71°) D: thiographene (66.2±3.6°) E: nitrographene (75.2±4.47°) F: aminographene. N.O PS

All functionalised graphene sheets were found to have a smaller contact angle than that of pristine graphene. The contact angle for graphene was in good agreement with the published value for few layered graphene.[5] These angles provide information regarding the wettability of the functionalised graphenes, further indication that changes occur between the materials; they are not identical. From these studies it appears that sulphographene and aminographene are the most water compatible of the functionalised graphene samples.

Infrared spectroscopy

Fig. S9 displays the FTIR spectra recorded for the functionalised graphene materials

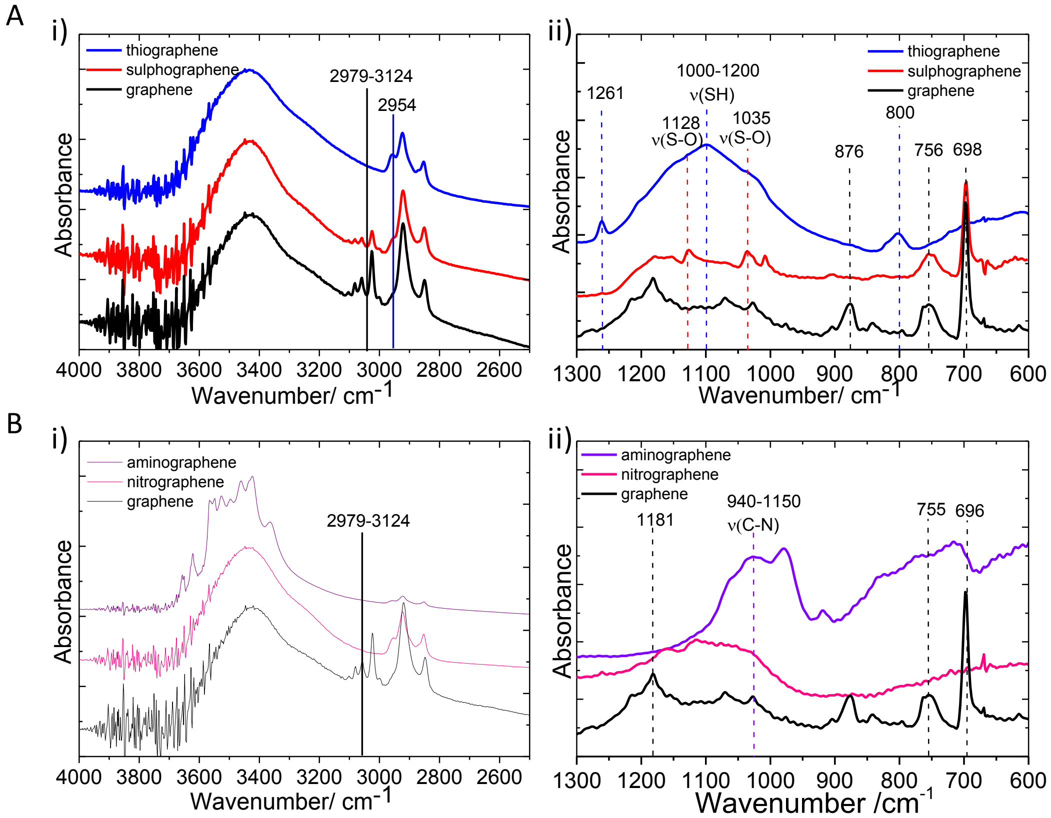

Figure S9. FTIR spectra of functionalised graphene. A: Graphene (black line), sulphographene (red line) and thiographene (blue line) at high energy (i) and low energy (ii). B: Graphene (black line), nitrographene (pink line) and aminographene (purple line) at high energy (i) and low energy (ii).

`PS/MH`

The S–H stretch of thiol group should be at around 2550-2600 cm^{-1}, but are not observed (Fig.S9 Ai)). The S-H thiol peaks are typically weak.[6] A small shoulder is observed at 2954 cm^{-1} for thiographene, which is not present in either sulphographene and pristine graphene. The disappearance of peaks between 2979-3134 cm^{-1} from sulphographene to thiographene is indicative of a reduction process.

Peaks at 1124 and 1034 cm^{-1} for sulphographene can be attributed to the two ν(S-O) stretches of the -SO_3H bond,[7,8] which are not observed in the graphene IR spectra (Fig.S9 Aii)).[9] It is difficult to see whether these peaks have disappeared in the case of thiographene, as there is a strong, broad absorbance centred at 1097 cm^{-1} which would obscure these peaks. It is reasonable to assume that these peaks still would exist as the XPS has shown that there is still some residual SO_3H functionality in the thiographene sample. There are peaks at both 1261 cm^{-1} and approximately 800 cm^{-1} for thiographene, which are present in neither graphene nor sulphographene and have been observed in thiol group grafted to GO,[10] although it is not clear to which modes these can be assigned. Peaks at 698 cm^{-1} and 756 cm^{-1} which are present in both graphene and sulphographene must be due to some oxygen functionality as these disappear for thiographene.

The shape of the peak from 3300-3600 cm^{-1} changes significantly for aminographene, compared to graphene and nitrographene (Fig.S9 Bi)). There is a broad stretch centred between 3300-3600 cm^{-1} but with spikes, which is typical for amine N-H stretches. There appear to be two distinct peaks at around 3463 cm^{-1} and 3421 cm^{-1}, which could correspond to the symmetric and anti-symmetric NH_2 stretches of a aromatic primary amine.[6] Two peaks can be observed round 3400 cm^{-1} in the spectra of aniline indicating that the two peaks observed for aminographene are likely to be due to these NH_2 stretches.[11] The broad, smooth O-H band from 3000-3600 cm^{-1} disappears, which could arise as a result of the reduction conditions.

Nitrographene display absorption peaks between 900-1200 cm^{-1}, which are likely to be attributable to C-N stretching modes (Fig S9 Bii)). There is a broad absorption between about 700-900 cm^{1}, which could be assigned to an NH wagging mode,[6] which is not present for the nitrographene IR. For aminographene however, there is no observed peak between 1550-1650 cm^{-1} corresponding to the NH bending vibration,[6,12] but this usually produces a weak stretch so it is possible it is lost in graphene signals. Similarly, for aromatic nitro groups, there should be symmetric and anti-symmetric NO_2 stretches at 1500-1550 cm^{-1} and 1285-1350 cm^{-1} respectively,[6,13] but these are not observed for nitrographene.

1 Ferrari, A. C. & Basko, D. M. Raman spectroscopy as a versatile tool for studying the properties of graphene. *Nature Nanotechnology* **8**, 235-246, doi:10.1038/nnano.2013.46 (2013).
2 Hernandez, Y. *et al*. High-yield production of graphene by liquid-phase exfoliation of graphite. *Nature Nanotechnology* **3**, 563-568, doi:10.1038/nnano.2008.215 (2008).
3 Khan, U., O'Neill, A., Lotya, M., De, S. & Coleman, J. N. High-Concentration Solvent Exfoliation of Graphene. *Small* **6**, 864-871, doi:10.1002/smll.200902066 (2010).
4 Eckmann, A. *et al*. Probing the Nature of Defects in Graphene by Raman Spectroscopy. *Nano Letters* **12**, 3925-3930, doi:10.1021/nl300901a (2012).
5 Taherian, F., Marcon, V., van der Vegt, N. F. A. & Leroy, F. What Is the Contact Angle of Water on Graphene? *Langmuir* **29**, 1457-1465, doi:10.1021/la304645w (2013).
6 Silverstein, R. M., Clayton Bassler, G. & Morrill, T. C. (John Wiley and sons, inc., New York).
7 Chen, G. *et al*. Preparation of sulfonic-functionalized graphene oxide as ion-exchange material and its application into electrochemiluminescence analysis. *Biosensors & Bioelectronics* **26**, 3136-3141, doi:10.1016/j.bios.2010.12.015 (2011).
8 Hu, X.-j. *et al*. Removal of Cu(II) ions from aqueous solution using sulfonated magnetic graphene oxide composite. *Separation and Purification Technology* **108**, 189-195, doi:10.1016/j.seppur.2013.02.011 (2013).
9 Shen, J. *et al*. Fast and Facile Preparation of Graphene Oxide and Reduced Graphene Oxide Nanoplatelets. *Chemistry of Materials* **21**, 3514-3520, doi:10.1021/cm901247t (2009).
10 Langner, R. & Zundel, G. FTIR investigation of O center dot center dot center dot H center dot center dot center dot O hydrogen bonds with large proton polarizability in sulfonic acid-N-oxide systems in the middle and far-IR. *Journal of the Chemical Society-Faraday Transactions* **94**, 1805-1811, doi:10.1039/a801000e (1998).
11 Yadav, L. D. S. *Organic spectroscopy*. (Kluwer Academic publishers, 2005).
12 Anderson, R. J., Bendell, D. J. & Groundwater, P. W. *Organic Spectroscopic analysis*. (Royal Society of Chemistry, 2004).
13 Robinson, J. W., Skelly Frame, E. M. & Frame II, G. M. *Undergraduate Instrumental Analysis, Sixth Edition*. (Marcel Dekker, 2005).

Chapter 7

Conclusion

7 Conclusion

This thesis has shown how an E-QCM-D can be combined with DPI analysis to optimize the adsorption, immobilisation and mass-specific catalytic activity of the fuel cell enzyme *Mv*BOx. Relating activity to the structural changes upon adsorption, densification and dehydration can allow for conclusions to be drawn about the mechanistic properties of the enzyme adlayer.

The first key finding of this thesis showed that potential cycling, which mimics changing the current load on a fuel cell, showed an increase in the rate of activity loss, suggesting it has a destabilisation effect on the enzyme that rests near the surface of the electrode. Covalent attachment of the enzyme did not mitigate this loss in activity and positioned the enzyme in an orientation exhibiting poor electron transfer. This infers an operational disadvantage to *Mv*BOx for use in fuel cells if it is unable to operate under a variety of current demands. Although this may not be the case for alternatives, it shows another failure mechanism that will affect overall stability in real-life devices. This observed behaviour for *Mv*BOx depends on the overall protein structure, operating conditions, and electrode surface. It has been shown by others that covalent attachment of other metalloenzymes, such as [FeFe] hydrogenases can improve activity decay from hours to days, by changing immobilisation methods.[139]

Improvements to stability and current generation were made though optimising the adsorption process via carefully deposition solution concentrations, and through electrode surface modifications. Overall activity of the adsorbed layer could be optimised by controlling the concentration of enzyme during the adsorption phase. The normal procedure for protein immobilisation is usually low concentrations and longer adsorption times, but for *Mv*BOx, this method produced low enzyme stability and low power output. This key finding can have implications throughout all protein immobilisation strategies, which aim at retaining biofunctionality after adsorption. Further studies to improve activity by controlling the adsorption showed that adsorption during an applied potential, misorientated the enzyme, which resulted in reduced catalytic activity. Yet this approach showed the possibility to manipulate protein orientation via and external, controllable factor, which may lead to, improved geometries for DET of other enzymes.

Despite improvements towards increasing stability and power output, these limitations of enzymatic fuel cells still limit their potential uses as a suitable commercial route to low temperature power generation. Enzymatic fuel cells specificity and ability to be minimised do suggested they could be use in niche markets, such as short term biofuel cells that can operate in the body, however several key challenges still need to be overcome before commercialisation. Electrode choice is a key area for materials to be used within the body. Functionalised graphene was shown as a potential suitable substrate for bioelectrocatalysis. Although attachment of only simple biomolecules has been shown, the potential for further work to attach larger biomolecules such as enzymes could pave the way for stable single flake devices. These have the potential for low power implantable devices, which can use the body's own sugar as a fuel supply. Functionalised graphene shows promise over alternative carbon nanomaterial's such as carbon nanotubes, due to increased density of functional groups, which can facilitate immobilization of enzymes.[140] Although similar practical limitations may still need to be overcome, such as high current densities and long-term operational life.

7.1 Future work

There is scope for several lines of research from this work to be pursued. We have shown how an applied potential reduced the activity of one MCO, bilirubin oxidase, but this could be extended to include others to test if similar process occur.

The initial work using an applied potential on adsorption showed how the orientation of the enzyme changes. This could be investigated using techniques such as E-SPR to compare the adsorption on a surface, which orientates the enzymes correctly, to that which orientates it to exhibit poor electron transfer. The E-SPR would be able to detect the changes in the orientation during adsorption and relate these back to the catalytic activity of the enzyme. There is also a need for further understanding of the specific protein–surface interactions, to improve surface immobilisation and reduce the rate of denaturation which are the main factors behind successfully incorporating redox enzymes such as *Mv*BOx use in real biofuel cell systems. Circular dichroism is one technique that could be used to distinguish the types of structural rearrangements observed when adsorbing to a surface. When comparing bilirubin oxidase to the more common studied laccases, it is clear further work is required in order to decipher the mechanisms of adsorption on the factors which affect activity specifically for this enzyme, notably surface functionality, rate of adsorption and spreading.

Incorporating new electrode materials into fuel cells or biosensors, to improve output and efficiency has been a key area of research, with graphene a cheap and effective substitute for precious metals. Continuing the research into biocompatible devices will require more precise and inventive ways, to specifically immobilise biomolecules in a supportive but functional state. This may require engineering enzymes to be more stable upon immobilisation, yet retaining high activity.

Chapter 8

References

8 References

1. Boardman, N. K., Comparative photosynthesis of sun and shade plants *Annu. Rev. Plant Physiol. Plant Mol. Biol.* **1977,** *28*, 355-377.

2. Norskov, J. K.; Rossmeisl, J.; Logadottir, A.; Lindqvist, L.; Kitchin, J. R.; Bligaard, T.; Jonsson, H., Origin of the overpotential for oxygen reduction at a fuel-cell cathode. *J. Phys. Chem. B* **2004,** *108* (46), 17886-17892.

3. Lewis, N. S.; Nocera, D. G., Powering the planet: Chemical challenges in solar energy utilization. *Proc. Natl. Acad. Sci. U. S. A.* **2006,** *103* (43), 15729-15735.

4. Bard, A. J.; Faulkner, L. R., *Electrochemical Methods: Fundamentals and Applications, New York: Wiley, 2001, 2nd ed.* **2001**; Vol. 38, p 1364-1365.

5. Mano, N.; Fernandez, J. L.; Kim, Y.; Shin, W.; Bard, A. J.; Heller, A., Oxygen Is Electroreduced to Water on a “Wired” Enzyme Electrode at a Lesser Overpotential than on Platinum. *J. Am. Chem. Soc.* **2003,** *125* (50), 15290-15291.

6. Gasteiger, H. A.; Kocha, S. S.; Sompalli, B.; Wagner, F. T., Activity benchmarks and requirements for Pt, Pt-alloy, and non-Pt oxygen reduction catalysts for PEMFCs. *Applied Catalysis B-Environmental* **2005,** *56* (1-2), 9-35.

7. Demir, F.; Erdogmus, A.; Koca, A., Oxygen reduction reaction catalyzed with titanyl phthalocyanines in nonaqueous and aqueous media. *Phys. Chem. Chem. Phys.* **2013,** *15* (38), 15926-15934.

8. Hijazi, I.; Bourgeteau, T.; Cornut, R.; Morozan, A.; Filoramo, A.; Leroy, J.; Derycke, V.; Jousselme, B.; Campidelli, S., Carbon Nanotube-Templated Synthesis of Covalent Porphyrin Network for Oxygen Reduction Reaction. *J. Am. Chem. Soc.* **2014,** *136* (17), 6348-6354.

9. Wei, C.; Yu, L. H.; Cui, C. L.; Lin, J. D.; Wei, C.; Mathews, N.; Huo, F. W.; Sritharan, T.; Xu, Z., Ultrathin MnO2 nanoflakes as efficient catalysts for oxygen reduction reaction. *Chem. Commun. (Cambridge, U. K.)* **2014,** *50* (58), 7885-7888.

10. Wang, C. H.; Hsu, H. C.; Wang, K. C., Iridium-decorated Palladium-Platinum core-shell catalysts for oxygen reduction reaction in proton exchange membrane fuel cell. *J. Colloid Interface Sci.* **2014,** *427*, 91-97.

11. Malmstrom, B. G., Cytochrome -c-oxidase as a redox-linked proton pump. *Chem. Rev.* **1990,** *90* (7), 1247-1260.

12. Holm, R. H.; Kennepohl, P.; Solomon, E. I., Structural and functional aspects of metal sites in biology. *Chem. Rev.* **1996,** *96* (7), 2239-2314.

13. Klema, V. J.; Solheid, C. J.; Klinman, J. P.; Wimot, C. M., Structural Analysis of Aliphatic versus Aromatic Substrate Specificity in a Copper Amine Oxidase from Hansenula polymorpha. *Biochemistry* **2013,** *52* (13), 2291-2301.

14. Kishishita, S.; Okajima, T.; Kim, M.; Yamaguchi, H.; Hirota, S.; Suzuki, S.; Kuroda, S.; Tanizawa, K.; Mure, M., Role of copper ion in bacterial copper amine oxidase: Spectroscopic and crystallographic studies of metal-substituted enzymes. *J. Am. Chem. Soc.* **2003,** *125* (4), 1041-1055.

15. Ikemoto, H.; Mossin, S. L.; Ulstrup, J.; Chi, Q. J., Probing structural and catalytic characteristics of galactose oxidase confined in nanoscale chemical environments. *Rsc Advances* **2014,** *4* (42), 21939-21950.

16. Lewis, E. A.; Tolman, W. B., Reactivity of dioxygen-copper systems. *Chem. Rev. (Washington, DC, U. S.)* **2004,** *104* (2), 1047-1076.

17. Liu, S. J.; Chen, S. S., Function and structure of peptide alpha-amidating monooxygenase. *Progress in Biochemistry and Biophysics* **1999,** *26* (3), 195-197.

18. Thorseth, M. A.; Letko, C. S.; Rauchfuss, T. B.; Gewirth, A. A., Dioxygen and Hydrogen Peroxide Reduction with Hemocyanin Model Complexes. *Inorg. Chem.* **2011,** *50* (13), 6158-6162.

19. Popovic, D. M.; Leontyev, I. V.; Beech, D. G.; Stuchebrukhov, A. A., Similarity of cytochrome c oxidases in different organisms. *Proteins-Structure Function and Bioinformatics* **2010,** *78* (12), 2691-2698.

20. Salaj-Kosla, U.; Poller, S.; Schuhmann, W.; Shleev, S.; Magner, E., Direct electron transfer of Trametes hirsuta laccase adsorbed at unmodified nanoporous gold electrodes. *Bioelectrochemistry* **2013,** *91*, 15-20.

21. Pankratov, D.; Sotres, J.; Barrantes, A.; Arnebrant, T.; Shleev, S., Interfacial Behavior and Activity of Laccase and Bilirubin Oxidase on Bare Gold Surfaces. *Langmuir* **2014,** *30* (10), 2943-2951.

22. Vashchenko, G.; MacGillivray, R. T. A., Multi-Copper Oxidases and Human Iron Metabolism. *Nutrients* **2013,** *5* (7), 2289-2313.

23. Kjaergaard, C. H.; Qayyum, M. F.; Augustine, A. J.; Ziegler, L.; Kosman, D. J.; Hodgson, K. O.; Hedman, B.; Solomon, E. I., Modified Reactivity toward O-2 in First Shell Variants of Fet3p: Geometric and Electronic Structure Requirements for a Functioning Trinuclear Copper Cluster. *Biochemistry* **2013,** *52* (21), 3702-3711.

24. Durand, F.; Gounel, S.; Kjaergaard, C. H.; Solomon, E. I.; Mano, N., Bilirubin oxidase from Magnaporthe oryzae: an attractive new enzyme for biotechnological applications. *Appl. Microbiol. Biotechnol.* **2012,** *96* (6), 1489-1498.

25. Murao, S.; Tanaka, N., A new enzyme bilirubin oxidase produced by myrothecium-verrucaria mt-1 *Agric. Biol. Chem.* **1981,** *45* (10), 2383-2384.

26. Solomon, E. I.; Sundaram, U. M.; Machonkin, T. E., Multicopper oxidases and oxygenases. *Chem. Rev. (Washington, DC, U. S.)* **1996,** *96* (7), 2563-2605.

27. Sakurai, T.; Kataoka, K., Structure and function of type I copper in multicopper oxidases. *Cell. Mol. Life Sci.* **2007,** *64* (19-20), 2642-2656.

28. Cracknell, J.; McNamara, T.; Lowe, E.; Blanford, C. F., Bilirubin oxidase from Myrothecium verrucaria: X-ray determination of the complete crystal structure and a rational surface modification for enhanced electrocatalytic O(2) reduction. *Dalton Trans.* **2011,** *40* (25), 6668-6675.

29. Shleev, S.; Shumakovich, G.; Morozova, O.; Yaropolov, A., Stable 'Floating' Air Diffusion Biocathode Based on Direct Electron Transfer Reactions Between Carbon Particles and High Redox Potential Laccase. *Fuel Cells* **2010,** *10* (4), 726-733.

30. Shleev, S.; Andoralov, V.; Falk, M.; Reimann, C. T.; Ruzgas, T.; Srnec, M.; Ryde, U.; Rulisek, L., On the Possibility of Uphill Intramolecular Electron Transfer in Multicopper Oxidases: Electrochemical and Quantum Chemical Study of Bilirubin Oxidase. *Electroanalysis* **2012,** *24* (7), 1524-1540.

31. Lee, S. K.; George, S. D.; Antholine, W. E.; Hedman, B.; Hodgson, K. O.; Solomon, E. I., Nature of the intermediate formed in the reduction of O-2 to H2O at the trinuclear copper cluster active site in native laccase. *J. Am. Chem. Soc.* **2002,** *124* (21), 6180-6193.

32. dos Santos, L.; Climent, V.; Blanford, C. F.; Armstrong, F. A., Mechanistic studies of the 'blue' Cu enzyme, bilirubin oxidase, as a highly efficient electrocatalyst for the oxygen reduction reaction. *Phys. Chem. Chem. Phys.* **2010,** *12* (42), 13962-13974.

33. Marshall, N. M.; Garner, D. K.; Wilson, T. D.; Gao, Y.-G.; Robinson, H.; Nilges, M. J.; Lu, Y., Rationally tuning the reduction potential of a single cupredoxin beyond the natural range. *Nature* **2009,** *462* (7269), 113-U127.

34. Lamberg, P.; Shleev, S.; Ludwig, R.; Arnebrant, T.; Ruzgas, T., Performance of enzymatic fuel cell in cell culture. *Biosens. Bioelectron.* **2014,** *55*, 168-173.

35. Filip, J.; Monosik, R.; Tkac, J., Poly(lactic acid)-based Nanocomposite for Construction of Efficient Bilirubin Oxidase-Based Biocathodes and Stable Biofuel Cells. *Int. J. Electrochem. Sci.* **2014,** *9* (5), 2491-2506.
36. Koikeda, S.; Ando, K.; Kaji, H.; Inoue, T.; Murao, S.; Takeuchi, K.; Samejima, T., Molecular-cloning of the gene for bilirubin oxidase from myrothecium-verrucaria and its expression in yeast. *J. Biol. Chem.* **1993,** *268* (25), 18801-18809.
37. Quintanar, L.; Stoj, C.; Taylor, A. B.; Hart, P. J.; Kosman, D. J.; Solomon, E. I., Shall we dance? How a multicopper oxidase chooses its electron transfer partner. *Acc. Chem. Res.* **2007,** *40* (6), 445-452.
38. Hakulinen, N.; Andberg, M.; Kallio, J.; Koivula, A.; Kruus, K.; Rouvinen, J., A near atomic resolution structure of a Melanocarpus albomyces laccase. *J. Struct. Biol.* **2008,** *162* (1), 29-39.
39. Eddowes, M. J.; Hill, H. A. O., Novel method for the investigation of the electrochemistry of metalloproteins: cytochrome c. *J. Chem. Soc., Chem. Commun.* **1977,** (21), 771b-772.
40. Yeh, P.; Kuwana, T., Reversible electrode-reaction of cytochrome-c. *Chem. Lett.* **1977,** (10), 1145-1148.
41. Varfolomeev, S. D.; Yaropolov, A. I.; Berezin, I. V.; Tarasevich, M. R.; Bogdanovskaya, V. A., Bioelectrocatalysis. Hydrogenase as catalyst of electrochemical hydrogen ionization. *Bioelectrochemistry and Bioenergetics* **1977,** *4* (3), 314-326.
42. Armstrong, F. A., Protein Film Voltammetry: Revealing the Mechanisms of Biological Oxidation and Reduction. *Russ. J. Electrochem.* **2002,** *38* (1), 49-62.
43. Klis, M.; Maicka, E.; Michota, A.; Bukowska, J.; Sek, S.; Rogalski, J.; Bilewicz, R., Electroreduction of laccase covalently bound to organothiol monolayers on gold electrodes. *Electrochim. Acta* **2007,** *52* (18), 5591-5598.
44. Ulman, A., Formation and structure of self-assembled monolayers. *Chem. Rev. (Washington, DC, U. S.)* **1996,** *96* (4), 1533-1554.
45. Laredo, T.; Leitch, J.; Chen, M. H.; Burgess, I. J.; Dutcher, J. R.; Lipkowski, J., Measurement of the charge number per adsorbed molecule and packing densities of self-assembled long-chain monolayers of thiols. *Langmuir* **2007,** *23* (11), 6205-6211.
46. Walczak, M. M.; Popenoe, D. D.; Deinhammer, R. S.; Lamp, B. D.; Chung, C. K.; Porter, M. D., Reductive desorption of alkanethiolate monolayers at gold - a measure of surface coverage *Langmuir* **1991,** *7* (11), 2687-2693.
47. Schreiber, F., Structure and growth of self-assembling monolayers. *Prog. Surf. Sci.* **2000,** *65* (5-8), 151-256.
48. Love, J. C.; Estroff, L. A.; Kriebel, J. K.; Nuzzo, R. G.; Whitesides, G. M., Self-assembled monolayers of thiolates on metals as a form of nanotechnology. *Chem. Rev. (Washington, DC, U. S.)* **2005,** *105* (4), 1103-1169.
49. Tarasevich, M. R.; Yaropolov, A. I.; Bogdanovskaya, V. A.; Varfolomeev, S. D., 293 - Electrocatalysis of a cathodic oxygen reduction by laccase. *Bioelectrochemistry and Bioenergetics* **1979,** *6* (3), 393-403.
50. Vincent, K. A.; Parkin, A.; Armstrong, F. A., Investigating and exploiting the electrocatalytic properties of hydrogenases. *Chem. Rev. (Washington, DC, U. S.)* **2007,** *107* (10), 4366-4413.
51. Olejnik, P.; Palys, B.; Kowalczyk, A.; Nowicka, A. M., Orientation of Laccase on Charged Surfaces. Mediatorless Oxygen Reduction on Amino- and Carboxyl-Ended Ethylphenyl Groups. *J. Phys. Chem. C* **2012,** *116* (49), 25911-25918.
52. Tominaga, M.; Ohtani, M.; Taniguchi, I., Gold single-crystal electrode surface modified with self-assembled monolayers for electron tunneling with bilirubin oxidase. *Phys. Chem. Chem. Phys.* **2008,** *10* (46), 6928-6934.

53. Ramírez, P.; Mano, N.; Andreu, R.; Ruzgas, T.; Heller, A.; Gorton, L.; Shleev, S., Direct electron transfer from graphite and functionalized gold electrodes to T1 and T2/T3 copper centers of bilirubin oxidase. *Biochimica et Biophysica Acta (BBA) - Bioenergetics* **2008,** *1777* (10), 1364-1369.

54. de Groot, M. T.; Evers, T. H.; Merkx, M.; Koper, M. T. M., Electron transfer and ligand binding to cytochrome c' immobilized on self-assembled monolayers. *Langmuir* **2007,** *23* (2), 729-736.

55. Blanford, C. F.; Foster, C. E.; Heath, R. S.; Armstrong, F. A., Efficient electrocatalytic oxygen reduction by the 'blue' copper oxidase, laccase, directly attached to chemically modified carbons. *Faraday Discuss.* **2008,** *140*, 319-335.

56. Brady, D.; Jordaan, J., Advances in enzyme immobilisation. *Biotechnol. Lett.* **2009,** *31* (11), 1639-1650.

57. Balland, V.; Hureau, C.; Cusano, A. M.; Liu, Y.; Tron, T.; Limoges, B., Oriented immobilization of a fully active monolayer of histidine-tagged recombinant laccase on modified gold electrodes. *Chemistry-a European Journal* **2008,** *14* (24), 7186-7192.

58. Singh, K.; McArdle, T.; Sullivan, P. R.; Blanford, C. F., Sources of activity loss in the fuel cell enzyme bilirubin oxidase. *Energy Environ. Sci.* **2013,** *6* (8), 2460-2464.

59. Armstrong, F. A.; Hill, H. A. O.; Oliver, B. N.; Walton, N. J., Direct electrochemistry of redox proteins at pyrolytic-graphite electrodes. *J. Am. Chem. Soc.* **1984,** *106* (4), 921-923.

60. Leger, C.; Bertrand, P., Direct electrochemistry of redox enzymes as a tool for mechanistic studies. *Chem. Rev. (Washington, DC, U. S.)* **2008,** *108* (7), 2379-2438.

61. Farver, O.; Wherland, S.; Koroleva, O.; Loginov, D. S.; Pecht, I., Intramolecular electron transfer in laccases. *FEBS J.* **2011,** *278* (18), 3463-3471.

62. A.Fisher, *Electrode Dynamics*. Oxford University Press: **1996**.

63. Avila, K.; Moxey, D.; de Lozar, A.; Avila, M.; Barkley, D.; Hof, B., The Onset of Turbulence in Pipe Flow. *Science* **2011,** *333* (6039), 192-196.

64. Hush, N. S., Adiabatic theory of outer sphere electron-transfer reactions in solution *Transactions of the Faraday Society* **1961,** *57* (4), 557-&.

65. Chou, M.; Creutz, C.; Sutin, N., Rate constants and activation parameters for outer-sphere electron-transfer reactions and comparisons with predictions of marcus theory. *J. Am. Chem. Soc.* **1977,** *99* (17), 5615-5623.

66. Wherland, S.; Gray, H. B., Metalloprotein electron-transfer reactions - analysis of reactivity of horse heart cytochrome-c with inorganic complexes. *Proc. Natl. Acad. Sci. U. S. A.* **1976,** *73* (9), 2950-2954.

67. Ikeuchi, H.; Kanakubo, M., Determination of diffusion coefficients of the electrode reaction products by the double potential step chronoamperometry at small disk electrodes. *J. Electroanal. Chem.* **2000,** *493* (1-2), 93-99.

68. Page, C. C.; Moser, C. C.; Chen, X. X.; Dutton, P. L., Natural engineering principles of electron tunnelling in biological oxidation-reduction. *Nature* **1999,** *402* (6757), 47-52.

69. Blanford, C. F., The birth of protein electrochemistry. *Chem. Commun. (Cambridge, U. K.)* **2013,** *49* (95), 11130-11132.

70. Norde, W., Adsorption of proteins from solution at the solid-liquid interface. *Adv. Colloid Interface Sci.* **1986,** *25* (4), 267-340.

71. Zoungrana, T.; Findenegg, G. H.; Norde, W., Structure, stability, and activity of adsorbed enzymes. *J. Colloid Interface Sci.* **1997,** *190* (2), 437-448.

72. Norde, W., Driving forces for protein adsorption at solid surfaces. *Biopolymers at Interfaces* **1998,** *75*, 27-54.

73. Kamitaka, Y.; Tsujimura, S.; Kataoka, K.; Sakurai, T.; Ikeda, T.; Kano, K., Effects of axial ligand mutation of the type I copper site in bilirubin oxidase on direct electron transfer-type bioelectrocatalytic reduction of dioxygen. *J. Electroanal. Chem.* **2007,** *601* (1–2), 119-124.

74. Shleev, S.; El Kasmi, A.; Ruzgas, T.; Gorton, L., Direct heterogeneous electron transfer reactions of bilirubin oxidase at a spectrographic graphite electrode. *Electrochem. Commun.* **2004,** *6* (9), 934-939.

75. Gupta, G.; Rajendran, V.; Atanassov, P., Bioelectrocatalysis of oxygen reduction reaction by laccase on gold electrodes. *Electroanalysis* **2004,** *16* (13-14), 1182-1185.

76. Koutsopoulos, S.; van der Oost, J.; Norde, W., Structural features of a hyperthermostable endo-beta-1,3-glucanase in solution and adsorbed on "invisible" particles. *Biophys. J.* **2005,** *88* (1), 467-474.

77. van der Veen, M.; Norde, W.; Stuart, M. C., Electrostatic interactions in protein adsorption probed by comparing lysozyme and succinylated lysozyme. *Colloids and Surfaces B-Biointerfaces* **2004,** *35* (1), 33-40.

78. Tan, W.; Norde, W.; Koopal, L. K., Interaction between lysozyme and humic acid in layer-by-layer assemblies: Effects of pH and ionic strength. *J. Colloid Interface Sci.* **2014,** *430*.

79. Galassi, V. V.; Villarreal, M. A.; Posada, V.; Montich, G. G., Interactions of the fatty acid-binding protein ReP1-NCXSQ with lipid membranes. Influence of the membrane electric field on binding and orientation. *Biochimica Et Biophysica Acta-Biomembranes* **2014,** *1838* (3), 910-920.

80. Vogler, E. A., Protein adsorption in three dimensions. *Biomaterials* **2012,** *33* (5), 1201-1237.

81. Cracknell, J. A.; Blanford, C. F., Developing the mechanism of dioxygen reduction catalyzed by multicopper oxidases using protein film electrochemistry. *Chemical Science* **2012,** *3* (5), 1567-1581.

82. Rabe, M.; Verdes, D.; Seeger, S., Understanding protein adsorption phenomena at solid surfaces. *Adv. Colloid Interface Sci.* **2011,** *162* (1–2), 87-106.

83. Anand, G.; Sharma, S.; Dutta, A. K.; Kumar, S. K.; Belfort, G., Conformational Transitions of Adsorbed Proteins on Surfaces of Varying Polarity. *Langmuir* **2010,** *26* (13), 10803-10811.

84. Clark, A. J.; Kotlicki, A.; Haynes, C. A.; Whitehead, L. A., A new model of protein adsorption kinetics derived from simultaneous measurement of mass loading and changes in surface energy. *Langmuir* **2007,** *23* (10), 5591-5600.

85. vanOss, C. J., Hydrophobicity and hydrophilicity of biosurfaces. *Curr. Opin. Colloid Interface Sci.* **1997,** *2* (5), 503-512.

86. Thorum, M. S.; Anderson, C. A.; Hatch, J. J.; Campbell, A. S.; Marshall, N. M.; Zimmerman, S. C.; Lu, Y.; Gewirth, A. A., Direct, Electrocatalytic Oxygen Reduction by Laccase on Anthracene-2-methanethiol-Modified Gold. *Journal of Physical Chemistry Letters* **2010,** *1* (15), 2251-2254.

87. Thourson, S. B.; Marsh, C. A.; Doyle, B. J.; Timpe, S. J., Quartz crystal microbalance study of bovine serum albumin adsorption onto self-assembled monolayer-functionalized gold with subsequent ligand binding. *Colloids and Surfaces B-Biointerfaces* **2013,** *111*, 707-712.

88. Lebec, V.; Landoulsi, J.; Boujday, S.; Poleunis, C.; Pradier, C. M.; Delcorte, A., Probing the Orientation of beta-Lactoglobulin on Gold Surfaces Modified by Alkyl Thiol Self-Assembled Monolayers. *J. Phys. Chem. C* **2013,** *117* (22), 11569-11577.

89. Awsiuk, K.; Budkowski, A.; Psarouli, A.; Petrou, P.; Bernasik, A.; Kakabakos, S.; Rysz, J.; Raptis, I., Protein adsorption and covalent bonding to silicon nitride surfaces

modified with organo-silanes: Comparison using AFM, angle-resolved XPS and multivariate ToF-SIMS analysis. *Colloids and Surfaces B-Biointerfaces* **2013,** *110*, 217-224.

90. Wertz, C. F.; Santore, M. M., Fibrinogen adsorption on hydrophilic and hydrophobic surfaces: Geometrical and energetic aspects of interfacial relaxations. *Langmuir* **2002,** *18* (3), 706-715.

91. Ramsden, J. J., Puzzles and paradoxes in protein adsorption. *Chem. Soc. Rev.* **1995,** *24* (1), 73-78.

92. Wei, Y.; Thyparambil, A. A.; Latour, R. A., Quantification of the influence of protein-protein interactions on adsorbed protein structure and bioactivity. *Colloids and Surfaces B-Biointerfaces* **2013,** *110*, 363-371.

93. Zhao, X.; Pan, F.; Garcia-Gancedo, L.; Flewitt, A. J.; Ashley, G. M.; Luo, J.; Lu, J. R., Interfacial recognition of human prostate-specific antigen by immobilized monoclonal antibody: effects of solution conditions and surface chemistry. *J. Royal Soc. Interface* **2012,** *9* (75), 2457-2467.

94. P, A. J., Paula, *Physical Chemistry*. 9th ed.; W.H. Freeman: 2009.

95. Szilagyi, I.; Trefalt, G.; Tiraferri, A.; Maroni, P.; Borkovec, M., Polyelectrolyte adsorption, interparticle forces, and colloidal aggregation. *Soft Matter* **2014,** *10* (15), 2479-2502.

96. Dejardin, P.; Le, M. T.; Wittmer, J.; Johner, A., Adsorption rate in the convection-diffusion model *Langmuir* **1994,** *10* (10), 3898-3901.

97. Ohshima, H.; Fujita, N.; Kondo, T., Adsorption-kinetics with time-delay *Colloid Polym. Sci.* **1992,** *270* (7), 707-710.

98. Krishnan, A.; Siedlecki, C. A.; Vogler, E. A., Mixology of protein solutions and the Vroman effect. *Langmuir* **2004,** *20* (12), 5071-5078.

99. Vroman, L.; Adams, A. L.; Klings, M., Interactions among human blood proteins at interfaces *Fed. Proc.* **1971,** *30* (5), 1494-&.

100. Langmuir, I., Vapor pressures, evaporation, condensation and adsorption. *J. Am. Chem. Soc.* **1932,** *54*, 2798-2832.

101. Swendsen, R. H., Dynamics of random sequential adsorption. *Phys. Rev. A* **1981,** *24* (1), 504-508.

102. Feder, J., Random sequential adsorption. *J. Theor. Biol.* **1980,** *87* (2), 237-254.

103. Cowsill, B. J.; Coffey, P. D.; Yaseen, M.; Waigh, T. A.; Freeman, N. J.; Lu, J. R., Measurement of the thickness of ultra-thin adsorbed globular protein layers with dual-polarisation interferometry: a comparison with neutron reflectivity. *Soft Matter* **2011,** *7* (16), 7223-7230.

104. Rabe, M.; Verdes, D.; Rankl, M.; Artus, G. R. J.; Seeger, S., A comprehensive study of concepts and phenomena of the nonspecific adsorption of beta-lactoglobulin. *ChemPhysChem* **2007,** *8* (6), 862-872.

105. Rodahl, M.; Hook, F.; Krozer, A.; Brzezinski, P.; Kasemo, B., Quartz-crystal microbalance setup for frequency and q-factor measurements in gaseous and liquid environments *Rev. Sci. Instrum.* **1995,** *66* (7), 3924-3930.

106. Singh, K.; Blanford, C. F., Electrochemical quartz crystal microbalance with dissipation monitoring: A technique to optimize enzyme use in bioelectrocatalysis. *Chemcatchem* **2014,** *6* (4), 921-929.

107. Du, B. Y.; Johannsmann, D., Operation of the quartz crystal microbalance in liquids: Derivation of the elastic compliance of a film from the ratio of bandwidth shift and frequency shift. *Langmuir* **2004,** *20* (7), 2809-2812.

108. Sauerbrey, G., Verwendung von schwingquarzen zur wagung dunner schichten und zur mikrowagung *Zeitschrift Fur Physik* **1959,** *155* (2), 206-222.

109. Rodahl, M.; Hook, F.; Fredriksson, C.; Keller, C. A.; Krozer, A.; Brzezinski, P.; Voinova, M.; Kasemo, B., Simultaneous frequency and dissipation factor QCM measurements of biomolecular adsorption and cell adhesion. *Faraday Discuss.* **1997,** *107*, 229-246.

110. Bingen, P.; Wang, G.; Steinmetz, N. F.; Rodahl, M.; Richter, R. P., Solvation Effects in the Quartz Crystal Microbalance with Dissipation Monitoring Response to Biomolecular Adsorption. A Phenomenological Approach. *Anal. Chem.* **2008,** *80* (23), 8880-8890.

111. Hook, F.; Rodahl, M.; Kasemo, B.; Brzezinski, P., Structural changes in hemoglobin during adsorption to solid surfaces: Effects of pH, ionic strength, and ligand binding. *Proc. Natl. Acad. Sci. U. S. A.* **1998,** *95* (21), 12271-12276.

112. Voinova, M. V.; Jonson, M.; Kasemo, B., 'Missing mass' effect in biosensor's QCM applications. *Biosens. Bioelectron.* **2002,** *17* (10), 835-841.

113. Mieure, J. P.; Jones, J. L., Electrogravimetric trace analysis on a piezoelectric detector. *Talanta* **1969,** *16* (1), 149-150.

114. Jones, J. L.; Mieure, J. P., Piezoelectric transducer for determination of metals at the micromolar level. *Anal. Chem.* **1969,** *41* (3), 484-490.

115. Kamitaka, Y.; Tsujimura, S.; Ikeda, T.; Kano, K., Electrochemical quartz crystal microbalance study of direct bioelectrocatalytic reduction of bilirubin oxidase. *Electrochemistry* **2006,** *74* (8), 642-644.

116. Cross, G. H.; Reeves, A. A.; Brand, S.; Popplewell, J. F.; Peel, L. L.; Swann, M. J.; Freeman, N. J., A new quantitative optical biosensor for protein characterisation. *Biosens. Bioelectron.* **2003,** *19* (4), 383-390.

117. Heideman, R. G.; Lambeck, P. V., Remote opto-chemical sensing with extreme sensitivity: design, fabrication and performance of a pigtailed integrated optical phase-modulated Mach-Zehnder interferometer system. *Sensors and Actuators B-Chemical* **1999,** *61* (1-3), 100-127.

118. Cross, G. H.; Ren, Y. T.; Freeman, N. J., Young's fringes from vertically integrated slab waveguides: Applications to humidity sensing. *J. Appl. Phys.* **1999,** *86* (11), 6483-6488.

119. Cross, G.; Freeman, N.; Swann, M., Hanbook of Biosensors and Biochps. **2007**.

120. P, C. Interfacial Measurements of Colloidal and Bio-colloidal Systems in Real-Time. University of Manchester, 2011.

121. Lin, S.; Lee, C.-K.; Lin, Y.-H.; Lee, S.-Y.; Sheu, B.-C.; Tsai, J.-C.; Hsu, S.-M., Homopolyvalent antibody-antigen interaction kinetic studies with use of a dual-polarization interferometric biosensor. *Biosens. Bioelectron.* **2006,** *22* (5), 715-721.

122. Xu, P. P.; Huang, F. J.; Liang, H. J., Real-time study of a DNA strand displacement reaction using dual polarization interferometry. *Biosens. Bioelectron.* **2013,** *41*, 505-510.

123. Lu, J. R.; Swann, M. J.; Peel, L. L.; Freeman, N. J., Lysozyme adsorption studies at the silica/water interface using dual polarization interferometry. *Langmuir* **2004,** *20* (5), 1827-1832.

124. McCrackin, F. L.; Passaglia, E.; Stromberg, R. R.; Steinber.Hl, Measurememt of thickness and refractive index of very thin films and optical properties of surfaces by ellipsometry *Journal of Research of the National Bureau of Standards Section a-Physics and Chemistry* **1963,** *A 67* (4), 363-+.

125. Hook, F.; Voros, J.; Rodahl, M.; Kurrat, R.; Boni, P.; Ramsden, J. J.; Textor, M.; Spencer, N. D.; Tengvall, P.; Gold, J.; Kasemo, B., A comparative study of protein adsorption on titanium oxide surfaces using in situ ellipsometry, optical waveguide lightmode spectroscopy, and quartz crystal microbalance/dissipation. *Colloids and Surfaces B-Biointerfaces* **2002,** *24* (2), 155-170.

126. Mrksich, M.; Sigal, G. B.; Whitesides, G. M., Surface-plasmon resonance permits in-situ measurement of protein adsorption on self-assembled monolayers of alkanethiolates on gold *Langmuir* **1995,** *11* (11), 4383-4385.

127. Brockman, J. M.; Nelson, B. P.; Corn, R. M., Surface plasmon resonance imaging measurements of ultrathin organic films. *Annu. Rev. Phys. Chem.* **2000,** *51*, 41-63.

128. Lubarsky, G. V.; Davidson, M. R.; Bradley, R. H., Hydration-dehydration of adsorbed protein films studied by AFM and QCM-D. *Biosens. Bioelectron.* **2007,** *22* (7), 1275-1281.

129. Kovacs, N.; Patko, D.; Orgovan, N.; Kurunczi, S.; Ramsden, J. J.; Vonderviszt, F.; Horvath, R., Optical Anisotropy of Flagellin Layers: In Situ and Label-Free Measurement of Adsorbed Protein Orientation Using OWLS. *Anal. Chem.* **2013,** *85* (11), 5382-5389.

130. ExPASy, Bioinformatics Resource Portal - Proteomics Server (11-09-14). *Bioinformatics Resource Portal - Proteomics Server* http://www.expasy.ch/tools/protparam.html.

131. Shin, K. S.; Lee, Y. J., Purification and characterization of a new member of the laccase family from the white-rot basidiomycete Coriolus hirsutus. *Arch. Biochem. Biophys.* **2000,** *384* (1), 109-115.

132. Singh, K. Structure-function studies of the oxidoreductase bilirubin oxidase from *Myrothecium verrucaria* using an electrochemical quartz crystal microbalance with dissipation University of Oxford, Department of Chemistry, D.Phil. thesis, 2014.

133. Q-Sense http://www.q-sense.com/file/q-sense-e1-folder.pdf (11-09-14).

134. Q-Sense http://www.q-sense.com/products/q-sense-sensors.

135. Farfield, http://www.farfield-group.com/pdfs/4D_product_specification_sheet-dual_autosampler.pdf (16-08-14).

136. Farfield, http://www.farfield-group.com/pdfs/Dual_Polarisation_Interferometry_-_sensors_and_immobilisation_strat.pdf (16-8-14).

137. Ulyanova, Y.; Babanova, S.; Pinchon, E.; Matanovic, I.; Singhal, S.; Atanassov, P., Effect of enzymatic orientation through the use of syringaldazine molecules on multiple multi-copper oxidase enzymes. *Phys. Chem. Chem. Phys.* **2014,** *16* (26), 13367-13375.

138. Minson, M.; Meredith, M. T.; Shrier, A.; Giroud, F.; Hickey, D.; Glatzhofer, D. T.; Minteer, S. D., High Performance Glucose/O-2 Biofuel Cell: Effect of Utilizing Purified Laccase with Anthracene-Modified Multi-Walled Carbon Nanotubes. *J. Electrochem. Soc.* **2012,** *159* (12), G166-G170.

139. Baffert, C.; Sybirna, K.; Ezanno, P.; Lautier, T.; Hajj, V.; Meynial-Salles, I.; Soucaille, P.; Bottin, H.; Léger, C., Covalent Attachment of FeFe Hydrogenases to Carbon Electrodes for Direct Electron Transfer. *Anal. Chem.* **2012,** *84* (18), 7999-8005.

140. Karimi, A.; Othman, A.; Uzunoglu, A.; Stanciu, L.; Andreescu, S., Graphene based enzymatic bioelectrodes and biofuel cells. *Nanoscale* **2015,** *7* (16), 6909-6923.